APPLIED COMPUTATIONAL ELECTROMAGNETICS SOCIETY JOURNAL

June 2024
Vol. 39 No. 6
ISSN 1054-4887

The ACES Journal is abstracted in INSPEC, in Engineering Index, DTIC, Science Citation Index Expanded, the Research Alert, and to Current Contents/Engineering, Computing & Technology.

The illustrations on the front cover have been obtained from the ARC research group at the Department of Electrical Engineering, Colorado School of Mines

Published, sold and distributed by: River Publishers, Alsbjergvej 10, 9260 Gistrup, Denmark

JUNE 2024 REVIEWERS

Hristos T. Anastassiu
Alireza Baghai-Wadji
Chakravarthy
Peiyao Chen
Yogesh Kumar Coukiker
Arkaprovo Das
Alfredo Gomes Neto
Hatem Oday Hanoosh
Yaqdhan Mahmood Hussein
William Kefauver
Lida Kouhalvandi
Anubhav Kumar
Gang Liu
Matteo Bruno Lodi
Yuchen Ma
Hacene Mellah
Ali Madani Mohammadi
Jafar Mohammed
Antonino Musolino
Sathishkumar N.
Mahdi Oliaei
Oscar Quevedo-Teruel
Alain Reineix
Michael Saville
M. Mohammadi Shirkolaei
Shu Wang
Shihyuan Yeh
Xiaoyan Zhang

THE APPLIED COMPUTATIONAL ELECTROMAGNETICS SOCIETY JOURNAL

Vol. 39 No. 6 June 2024

TABLE OF CONTENTS

Performance Analysis and Design Considerations of the Near-Field-Focused Rotman Lens Antennas

Salem M. Otman, Mehmet Kuşaf, and Abdullah Y. Öztoprak

Department of Electrical and Electronic Engineering
Cyprus International University, Nicosia 99258, Northern Cyprus
22007405@student.ciu.edu.tr, mkusaf@ciu.edu.tr, aoztoprak@ciu.edu.tr

Abstract – This study investigates the application of Rotman lens antennas in the near field. The design equations of these antennas have been derived in the near field and demonstrated to be highly effective. By considering specific examples, the shapes of the inner surfaces of these lens antennas have been analyzed and discussed, revealing how practically realizable lens surfaces can be designed. As these Rotman lenses are perfect at only three points in the near field, they exhibit phase errors at other points along a line connecting the three near-field focal points, resulting in deterioration of the near-field patterns. It has been shown that by selecting the lens parameters appropriately, these phase errors can be kept to a minimum, causing only minimal beam deterioration. Compared to far-field-focused Rotman lens antennas, near-field-focused Rotman lens antennas achieve significantly higher power levels, having 3.8 to 6.3 dB improvement for different beams of a 17-element array. The study has demonstrated the potential of Rotman lenses as multiple beamforming antennas for near-field applications.

Index Terms – Beamforming, near-field-focusing, Rotman lenses.

I. INTRODUCTION

Near-field-focused antennas have been extensively used for applications requiring high concentrations of electromagnetic fields in the nearby regions of the antennas [1–9] some applications such as radio frequency identification (RFID) [10–12] and industrial inspection systems [13]. In the case of hyperthermia applications [4, 14–16], concentrating the power on the unhealthy tissues avoids heating and damaging healthy tissues.

On the other hand, only a limited region can be covered with a single focused beam. To increase the coverage area the focused beam should be scanned or multi-beam antenna techniques should be used. Although beam scanning and multiple beamforming is well known and widely published for far-field-focused beams [17–25], there has been a limited number of publications for near-field-focused beams. In [22] the near-field-focused beam is scanned by changing the frequency by introducing progressively increasing multiple additional transmission lines into the system. In [26] the authors compare an electronic scanning antenna using phase shifters and power dividers, with multiple beamforming antennas using Butler matrix and Rotman lens for near-field-focused fields. Butler matrixes are well established beam forming networks using phase shifters and power dividers [27], feeding linear array antennas. Rotman lens beamforming antennas are two dimensional multi-focal constrained lens antennas using a parallel plate region, with several input and output ports, and different lengths of transmission lines.

In this paper we establish the design equations of the Rotman lens beamforming antenna when focusing at three points in the near field instead of three far-field directions. The shape and feasibility of the lens curves have been investigated for different lens parameters. The near-field performance of the near-field-focused lens has been studied for different parameters and compared with the far-field-focused lens.

II. LENS DESIGN

The mathematical model of the near-field-focused Rotman lens is given in Fig. 1. The two-dimensional coordinate system (x,y) centered at O_1 and the coordinate system (X,Y) centered at O_2 are independent of each other. The feed array curve and the inner array curve are represented by the coordinate system centered at O_1 and the radiating array and the target points are represented by the coordinate system centered at O_2. In this study, all lengths are expressed in terms of wavelengths to have frequency independent equations.

The Rotman lens is a two-dimensional lens characterized by constrained paths, or transmission lines, connecting its two surfaces. These surfaces are represented by two curves - the inner lens curve and the outer lens curve - which forms the radiating array. In this study, a linear radiating array is employed, but curved arrays can also be utilized. The Rotman lens's focal points are located at F_1, F_0, and F_2 along the feed array curve, where all feed antenna elements are situated. Points B_1,

Submitted On: December 15, 2023
Accepted On: August 27, 2024

https://doi.org/10.13052/2024.ACES.J.390601

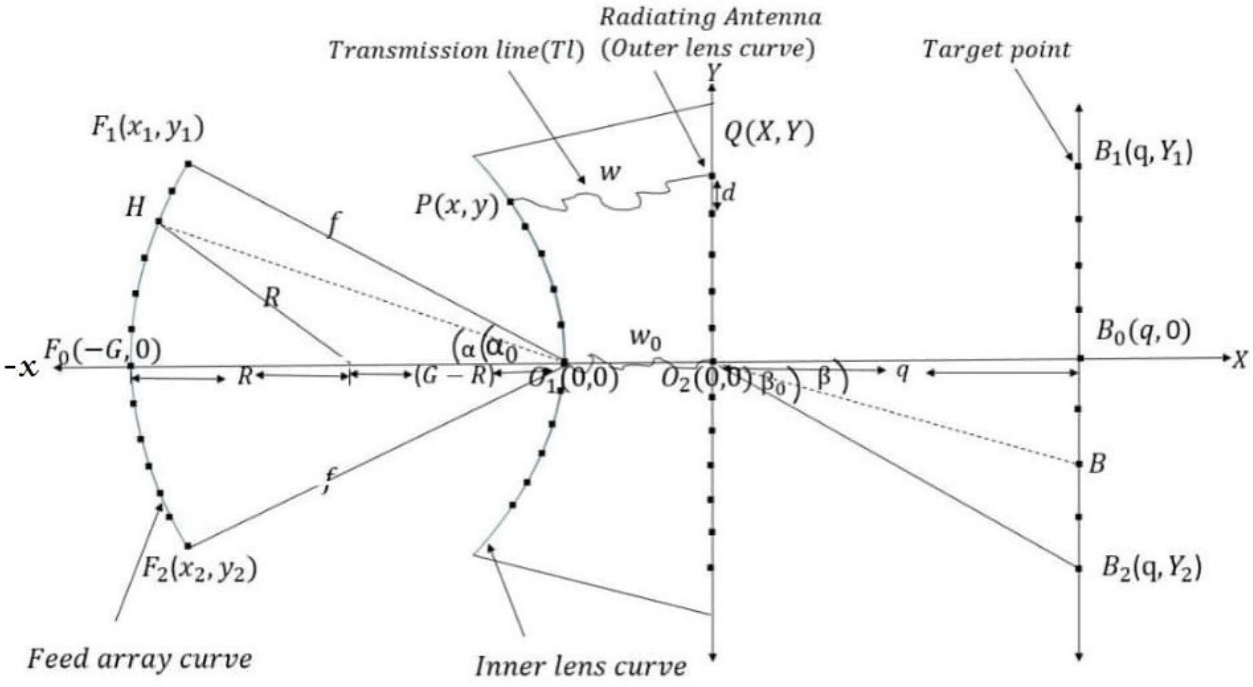

Fig. 1. Geometry of near-field-focused Rotman lens.

B_0, and B_2 in the radiating array's near field represent the locations where the antenna elements at the three lens focal points focus their fields. Element F_1 focuses at B_2, element F_0 focuses at B_0, and element F_2 focuses at B_1. G is the distance from O_1 to the central focal point at F_0.

A general point on the lens's inner curve is denoted by $P(x,y)$, and its corresponding point on the radiating array is represented by $Q(X,Y)$. An antenna element at P receives the field from the feed array elements and relays it to the corresponding element Q at the radiating array via a transmission line of length w .

For a field launched at focal point F_1 to focus at B_2:

$$\left(\vec{F_1P}\right)+w+\left(\vec{QB_2}\right)=(\vec{F_1O_1})+w_0+\left(\vec{O_2B_2}\right). \quad (1)$$

For a field launched at focal point F_2 to focus at B_1:

$$(\vec{F_2P})+w+\left(\vec{QB_1}\right)=(\vec{F_2O_1})+w_0+\left(\vec{O_2B_1}\right). \quad (2)$$

For a field launched at focal point F_0 to focus at B_0 :

$$\left(\vec{F_0P}\right)+w+\left(\vec{QB_0}\right)=G+w_0+\left(\vec{O_2B_0}\right), \quad (3)$$

where w_0 is the transmission line length for the center element.

$$\left(\vec{F_1P}\right)=\sqrt{(x-x_1)^2+(y-y_1)^2}, \quad (4)$$

$$\left(\overline{F_2P}\right)=\sqrt{(x-y_2)^2+(y-y_2)^2}, \quad (5)$$

$$\left(\overline{F_0P}\right)=\sqrt{(x+G)^2+y^2}, \quad (6)$$

$$\left(\overline{QB_2}\right)=\sqrt{(q-X)^2+(Y_2-Y)^2}, \quad (7)$$

$$\left(\overline{O_2B_2}\right)=\sqrt{(q)^2+(Y_2)^2}, \quad (8)$$

$$\left(\overline{QB_1}\right)=\sqrt{(q-X)^2+(Y_1-Y)^2}, \quad (9)$$

$$\left(\overline{O_2B_1}\right)=\sqrt{(q)^2+(Y_1)^2}, \quad (10)$$

$$\left(\overline{QB_0}\right)=\sqrt{(q-X)^2+(Y)^2}, \quad (11)$$

$$\left(\overline{O_2B_0}\right)=\sqrt{(q)^2}, \quad (12)$$

where $x_1 = x_2 = -f\cos\alpha_0$, $y_1 = f\cos\alpha_0$, $y_2 = -f\cos\alpha_0$. Here, f is the distance from O_1 to the off-center focal point at F_1, and α_0 is the angle subtended by off axis lens focal points from O_1.

Equations 1, 2, and 3 are solved simultaneously to determine the variables x, y, and w for each position of Q on the radiating array. The Q positions correspond to the locations of the radiating array antenna elements. The values of x and y define the inner lens curve of the lens, and each point on the inner curve is associated with a corresponding value of w.

In practice the region between feed array and inner lens is a parallel plate region and a TEM wave propagates in this region. The Rotman lenses are usually implemented on microstrip substrates for low power applications and air-filled parallel conducting plates for high power applications. The varying length transmission lines between the inner lens curve elements and radiating elements are usually microstrip lines for the microstrip implementation and co-axial transmission lines for the conducting plate implementation. Usually small V- shaped or stepped transitions [28] are used between the transmission lines and parallel plate region. The transitions act as two-dimensional aperture antennas into the parallel plate region. The field at the target point is obtained by summing the fields of each element at this point.

III. SHAPE OF THE INNER LENS CURVES

The lens design principles outlined above utilize optical principles to generate inner lens curves. Not all inner lens curves obtained in this manner are suitable for practical applications. Given that Rotman lenses operate at microwave frequencies, the shape of the inner lens curves must facilitate efficient power transfer between antenna elements on the feed array curve and those on the inner lens curve. Sample inner lens curves are presented in this section to illustrate the significance of their shapes.

The positions of the lens focal points F_1, F_2, and F_0, the focusing points in the near field B_1, B_2, and B_0, and the length of the radiating array are parameters selected in advance according to the specific application requirements. The parameters for this lens shape study are as follows: the lens focal points are located at $F_1(x_1, y_1)$, $F_2(x_2, y_2)$, and $F_0(-G, 0)$. F_1 and F_2 subtend an angle of 25° (α_0) degrees from the origin O_1. The linear radiating array comprises 17 elements with a separation (d) of 0.5 between them.

The three focusing points in the near field are positioned on a line perpendicular to the $X-$axis and passing through $B_0(q, 0)$. The near-field-focusing points are located at $B_1(q, Y_1)$, $B_0(q, 0)$, and $B_2(q, Y_2)$, where $q = 10$ and $Y_1 = -Y_2 = q * \tan(\beta_o)$. The angle of the off-axis near-field-focusing point is defined as β_o. Here, β_0 is chosen to be 35°. All lens parameters were selected such that the lens is symmetric around the x-axis.

Examples of the inner lens curves, obtained through numerical solutions to equations 1, 2, and 3, have been generated for different values of g, where $g = G/f$. Table 1 shows the G, g, and f values used to obtain the inner lens curves. Figure 2 depicts the shapes of the inner curves for $g = 1.0, 1.05, 1.10, 1.15, 1.20, 1.25, 1.30$, and 1.35 respectively.

The shape of the inner lens curve significantly impacts the illumination of antenna elements and the overall effectiveness of the lens antenna. As shown in Fig. 2 (g=1.35), the inner lens curve bends backward at both the upper and lower end points. This positioning blocks any antenna elements at these locations by those placed before them. Consequently, the antenna elements at the upper end of the inner curve receive very low illumination from the lower end feed elements, and the elements at the lower end of the inner curve receive incomplete illumination from the upper end feed elements.

Table 1: Parameters of the lens design

G	g	f
10.5	1.00	10.5
10.5	1.05	9.52
10.5	1.10	9.09
10.5	1.15	8.69
10.5	1.20	8.33
10.5	1.25	8.00
10.5	1.30	7.69
10.5	1.35	6.66

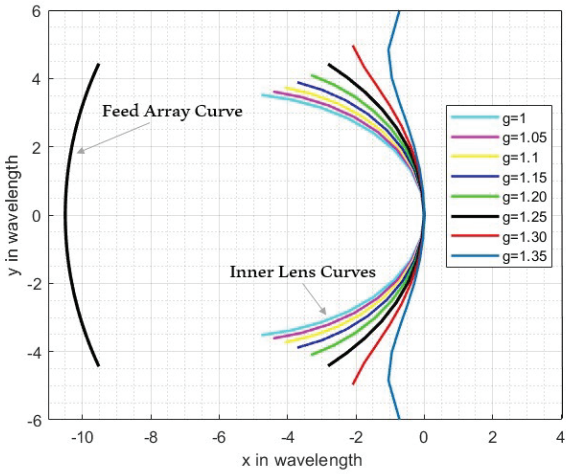

Fig. 2. Lens curves for g=1, 1.05, ..., 1.35.

Conversely, in Fig. 2 (g=1.0), the end elements of the inner curve are bent forward, so the inner curve's lower endpoints will not be illuminated by the lower elements of the feed array curve. Similarly, the inner curve's upper elements will not be illuminated by the upper elements of the feed array curve.

In contrast, Fig. 2 (g=1.25) demonstrates a design where the antenna elements on the feed array curve and inner curve directly face each other without any blockage. This alignment ensures efficient power transfer and maximizes the lens antenna's performance.

The lens antenna shapes presented in Fig. 2 highlight the criticality of selecting appropriate lens parameters for optimal design. Factors such as the positions of the near-field-focusing points and the spacing between radiating array elements can significantly alter the shape of the inner lens curve. Therefore, careful selection of lens parameters is essential for each design to achieve practical realization of these lens antennas.

In summary, the shape of the inner lens curve and the selection of appropriate lens parameters are crucial aspects in designing efficient and high-performance lens antennas. Careful consideration of these factors can optimize power transfer and minimize blockage, leading to enhanced lens antenna performance.

Achieving the strongest possible near-field intensity with a given amount of power requires careful planning of the radiating array. First, the size of the array needs to be estimated based on the target intensity and available input power. This initial design consideration ensures efficient use of the available energy. Next, the spacing between elements within the array must be carefully calculated to eliminate unwanted interference patterns known as grating lobes. These lobes can significantly reduce the intensity at the target point, so their elimination is crucial. Finally, a realizable lens is designed, as discussed above, to achieve the required phase distribution for each radiating element. Since lens design relies on principles of optics, the dimensions for the lens, (G, f) are typically no smaller than four to five wavelengths.

IV. PATH LENGTH ERROR AND RADIATION PATTERNS OF FEED ELEMENTS AT NON-FOCAL POSITIONS ON THE FEED ARRAY CURVE

Since the path length from each of the lens focal points to the corresponding focusing points in the near field is equal for all radiating array elements, the phases are identical at these points. This means that maximum possible power is achieved at B_1, B_2, and B_0 for feed antenna elements at F_2, F_0, and F_1, respectively. In practice, we may need to focus the field at other points in the near field, which requires placing feed antennas at non-focal positions on the feed array curve.

Any antenna placed at a non-focal point will concentrate the field at specific points but, due to phase errors caused by path length discrepancies, there will be some degradation in the focused field, resulting in lower gain, a wider beam, and higher sidelobes. By carefully selecting the parameters of the Rotman lens, these phase errors can be minimized.

The path length error for a point on the feed array curve can be calculated for each radiating array element relative to the center radiating array element using the following formula:

$$Path\ length\ error\,(\Delta L) = \left(\vec{HP}\right) + w + \left(\vec{QB}\right) - \left(\vec{HO_1}\right) - w_0 - \left(\vec{O_2B}\right) . \quad (13)$$

Figure 3 illustrates the path length errors for the lens design given in Fig. 2 (g=1.25) for various values of α, including 0°, 5°, 10°, 15°, 20°, and 25°, where α represents the angle subtended by points on the feed array curve from O_1. The errors for each feed element were determined at the maximum power point along the line connecting B_1 and B_2.

As evident from Fig. 3, the phase errors for the focal points, as anticipated, are zero for all radiating elements. Conversely, path length errors increase as the distance of the feed element from the focal points increases, reaching a maximum path length error of 0.0512 for the feed element located at α=15°. The phase errors can be minimized by selecting the appropriate parameters for a Rotman lens based on the specific design requirements.

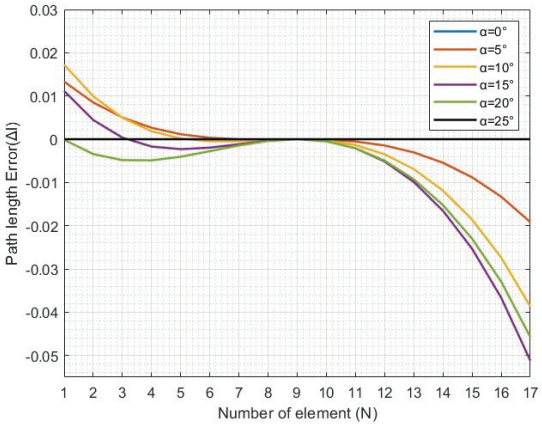

Fig. 3. Path length errors along the radiating array for six points on the feed array curve.

An optical method was employed first to determine the patterns along the line connecting B1 and B2 for the lens design (g=1.25) in Fig. 2. Figure 4 presents these results for various feed port angles (α): 0° (port6), 5° (port7), and so on, up to 25° (port11). Notably, isotropic radiating elements were assumed for this analysis. Due to parameter selection minimizing phase errors, the patterns exhibit minimal degradation.

Next, the design was implemented as a microstrip circuit and simulated using the commercial software CST. Figure 5 depicts the CST implementation of the lens. The design parameters are detailed in Table 2. The radiation patterns of the microstrip lens were then obtained using CST, with the results presented in Fig. 6.

A comparison of Figs. 4 and 6 reveals a high degree of similarity between the radiation patterns obtained

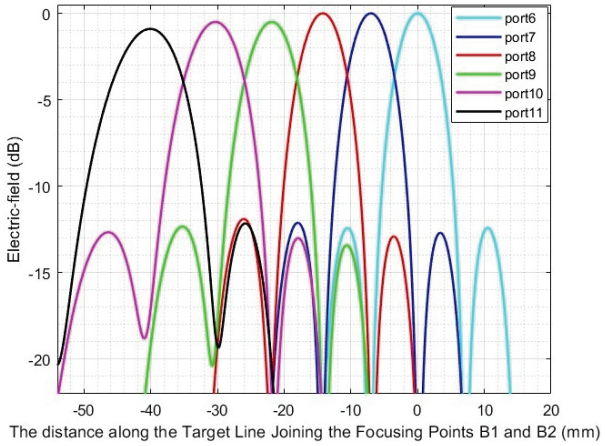

Fig. 4. Radiation patterns for the lens design in Fig. 2 (g=1.25) using optical method.

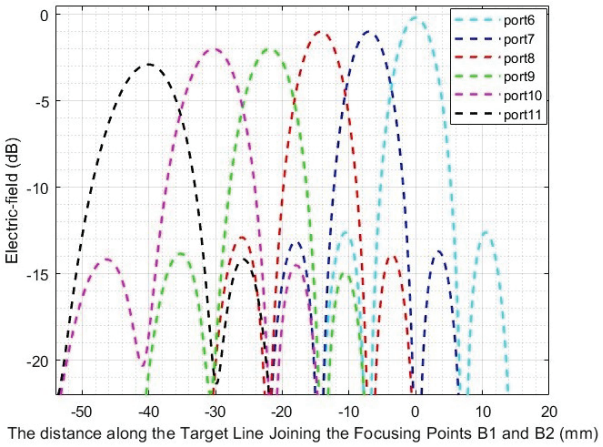

Fig. 6. Radiation patterns for the lens design in Fig. 2 (g=1.25) using CST method.

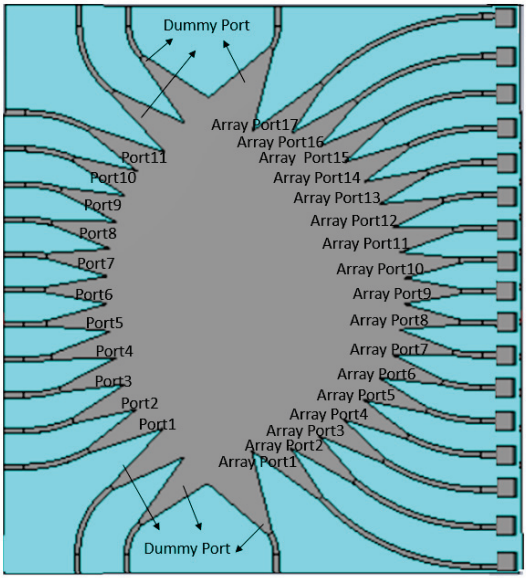

Fig. 5. CST implementation of the lens design.

Table 2: Parameters of the CST lens design

Central frequency	27.5 GHz
ε_r	6.15
Substrate thickness	1.5 mm
Length of feed port and array port tapered lines	18.8 mm
Radiating elements	8 mm × 8 mm
G	60.58 mm
F	48 mm
q	57.70 mm

through the optical and CST methods. However, a key difference exists: the peak electric field strength of the outer feed elements is lower in the CST implementation. This discrepancy arises because the optical analysis assumed isotropic elements for both the feed array and inner lens elements, while the actual CST implementation utilizes aperture elements with directional patterns.

V. COMPARISON OF NEAR-FIELD PERFORMANCES OF ROTMAN LENSES DESIGNED FOR NEAR FIELD AND FAR FIELD

As has already been stated, achieving the highest field intensity is essential when using electromagnetic fields in the near field for a given input power, therefore a study was conducted to compare the field intensities of two Rotman lens antenna types in the near field. For this comparison, the design of Fig. 2 (g=1.25) was utilized for the near-field-focusing Rotman lens. The far-field-focusing Rotman lens, while maintaining the same parameters, is focused at angles of -35°, 0°, and +35°, corresponding to the angles subtended by the near-field-focusing points B_2, B_0, and B_1.

To calculate total field intensity at a target point, we first determine the phase distribution of each radiating element using lens calculations. Then, we account for the varying distances between the elements and the target point by incorporating a $1/r$ factor when summing the individual field intensities. Although the design of the far-field-focusing lens was carried out for far-field focal points, for fair comparison the field intensity of this lens is also calculated at the same near-field target points.

Figure 7 depicts the electric field intensity for both lenses under identical input power conditions. The fields are positioned along the line joining B_1 and B_2 at the peak points of the near-field-focused Rotman lens, with α values ranging from 0° to 25°. It is clear that the power density of the near-field-focusing lens is 3.8 to 6.3 dB

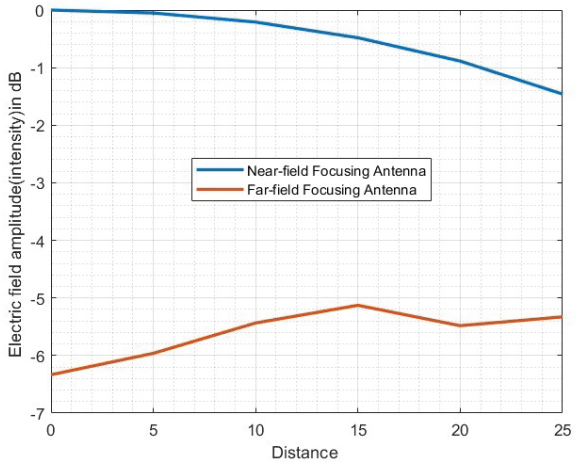

Fig. 7. Maximum electric field intensity along $X=q$ for different positions of feed angle.

higher. These results indicate that the near-field-focusing Rotman lens offers a substantial advantage over the far-field-focusing lens in the near field.

VI. CONCLUSION

Rotman lenses have been demonstrated to be effective multiple beamforming antennas for near-field applications. The design equations for these lenses have been derived, and the inner lens curves and transmission line path lengths have been determined for sample design parameters. These results provide a foundation for the practical realization of Rotman lenses with desired performance characteristics.

The study has shown that by selecting the lens parameters appropriately, the phase errors can be minimized for non-focal points, resulting in only minimal beam deterioration. This is a significant advantage for near-field applications, as it ensures that the Rotman lens can achieve the desired beamforming performance even when the target is not located at the focal point.

A comparison of the power density in the near field has been made for far-field- and near-field-focusing Rotman lenses having the same lens parameters. The results indicate that the power densities of the near-field-focused lens are 3.8 to 6.3 dB higher. This is a significant improvement and makes the near-field-focusing Rotman lens a promising candidate for a wide range of near-field applications.

REFERENCES

[1] P. Nepa and A. Buffi, "Near-field-focused microwave antennas; near-field shaping and implementation," *IEEE Antenna and Propagation Magazine*, vol. 59, no. 3, pp. 42-53, 2017.

[2] A. Buffi, P. Nepa, and G. Manara, "Design criteria for near-field-focused planar arrays," *IEEE Antennas Propag. Mag.,* vol. 54, no. 1, pp. 40–50, Feb. 2012.

[3] S. M. Mikki and Y. M. M. Antar, "A theory of antenna electromagnetic near field-Part I," *IEEE Transactions on Antennas and Propagation*, vol. 59, no. 12, pp. 4691-4705, 2011.

[4] S. M. Mikki and Y. M. M. Antar, "A theory of antenna electromagnetic near field-Part II," *IEEE Transactions on Antennas and Propagation*, vol. 59, no. 12, pp. 4706-4724, 2011.

[5] J. T. Loane III and S.-W. Lee, "Gain optimization of a near-field focusing array for hyperthermia applications," *IEEE Trans. on Microwave Theory and Techniques*, vol. 37, no. 10, pp. 1629–1635, Oct. 1989.

[6] F. Tofigh, J. Nourinia, M. Azarmanesh, and K. M. Khazaei, "Near-field focused array microstrip planar antenna for medical applications," *IEEE Antennas and Wireless Propagation Letters*, vol. 13, pp. 951-954, 2014.

[7] H. Chen, Z. Zhang, and J. Yu, "Near-field scattering of typical targets illuminated by vortex electromagnetic waves," *The Applied Computational Electromagnetics Society Journal (ACES),* vol. 35, no. 2, pp. 129-134, Feb. 2023.

[8] H. Chen, Z. Zhang, and J. Yu, "Resolution of near-field beamforming and its impact on NOMA," *IEEE Wireless Commun. Lett.*, vol. 13, no. 2, pp. 456-460, Feb. 2024.

[9] F. Paredes, C. Herrojo, R. Escudé, E. Ramon, and F. Martin, "High data density near-field chipless-RFID tags with synchronous reading," *IEEE Journal of Radio Freq. Ident.*, vol. 4, no. 4, pp. 517-524, Dec. 2020.

[10] S. H. Zainud-Deen, H. A. Malhat, and K. H. Awadalla, "Dielectric resonator antenna phased array for fixed RFID reader in near field region," in *Japan-Egypt Conference on Electronics, Communications and Computers,* Alexandria, Egypt, pp. 102-107, 2012.

[11] A. Buffi, A. A. Serra, P. Nepa, H. T. Chou, and G. Manara, "A focused planar microstrip array for 2.4 GHz RFID readers," *IEEE Transactions on Antennas and Propagation*, vol. 58, no. 5, pp. 1536-1544, 2010.

[12] Y. Wang, L. Shen, C. Huang, J. Zhu, and W. Tang, "Series-fed dipole array for near-field RFID application," *The Applied Computational Electromagnetics Society Journal (ACES),* vol. 33, no. 11, pp. 1190-1195, Nov. 2018.

[13] M. Bogosanovic and A. G. Williamson, "Microstrip antenna array with a beam focused in the near-field zone for application in non-contact microwave industrial inspection," *IEEE*

Transactions on Instrumentation and Measurement, vol. 56, no. 6, pp. 2186-2195, 2007.

[14] S. Singh and S. P. Singh, "Microstrip slot antenna for hyperthermia applications," in *Applied Electromagnetic Conference (AEMC 2015)*, Guwahati, India, 18-21 Dec. 2015.

[15] W. C. Choi, K. J. Kim, J. Kim, and Y. J. Yoon, "Compact microwave radiator for improving heating uniformity in hyperthermia system," *IEEE Antennas Wireless Propag. Lett.,* vol. 13, pp. 1345-1348, 2014.

[16] W. C. Choi, S. Lim, and Y. J. Yoon, "Design of noninvasive hyperthermia system using transmit-array lens antenna configuration," *IEEE Antennas and Wireless Propagation Letters,* vol. 15, pp. 857-860, 2016.

[17] P. Nayeri, F. Yang, and A. Z. Elsherbeni, "Beam-scanning reflectarray antennas: An overview," in *USNC-URSI National Radio Science Meeting*, Chicago, IL, July 2012.

[18] L. Stark, "Microwave theory of phased-array antennas: a review," *Proc. the IEEE*, pp. 1661-1701, 1974.

[19] W. Rotman and R. F. Turner, "Wide-angle microwave lens for line source applications," *IEEE Trans. Antennas Propag.,* vol. AP-11, no. 6, pp. 623-632, Nov. 1963.

[20] M. J. Maybell, K. K. Chan, and P. S. Simon, "Rotman lens recent developments 1994–2005," in *Proceedings of the 2005 IEEE Antennas and Propagation Society International Symposium*, Washington, DC, 3-8 July 2005.

[21] D. H. Archer and M. J. Maybell, "Rotman lens development history at Raytheon Electronic Warfare Systems 1967-1995," in *Proceeding of the IEEE Antennas and Propagation Society International Symposium,* Washington, DC, pp. 31-34, 2005.

[22] M. Sohail, R. Uyguroğlu, and A.Y. Öztoprak, "Scanning of the near-field focused beam by changing frequency," *The Applied Computational Electromagnetics Society Journal (ACES),* vol. 38, no. 3, pp. 177-183, Mar. 2023.

[23] P. Li, P. Li, P. Yang, Z. Kuang, and X. Luo, "Design of compact Rotman lens with wide-angle scanning using high permittivity substrate," in *2021 International Applied Computational Electromagnetics Society (ACES-China) Symposium*, Chengdu, China, 28-31 July 2021.

[24] T. K. Vo Dai, T. Nguyen, and O. Kilic, "A non-focal Rotman lens design to support cylindrically conformal array antenna," *The Applied Computational Electromagnetics Society Journal (ACES),* vol. 33, no. 2, pp. 240-243, Feb. 2018.

[25] R. Uyguroğlu, A. Y. Öztoprak, and C. Ergün, "Improved phase performance for Rotman lens," *International Journal of RF and Microwave Computer-Aided Engineering,* vol. 23, no. 6, pp. 634-638, Oct. 2013.

[26] H.-T. Chou and D. Torrungrueng, "Development of 2-D generalized tri focal Rotman lens beam-forming network to excite conformal phased arrays of antennas for general near/far-field multi-beam radiations," *IEEE Access,* vol. 9, pp. 49176–49188, 2021.

[27] A.K. Vallappil, M. K. A. Rahim, B. A. Khawaja, N. A. Murad, M. M. Gajibo, "Butler matrix based beamforming networks for phased array antenna systems: A comprehensive review and future directions for 5G applications," *IEEE Access*, vol. 9, pp. 3970-3987, 2021.

[28] R. Uyguroğlu and A. Y. Niazi, "Designing microstrip transitions into parallel plate regions using the FDTD method," *Microwave and Optical Technology Letters*, vol. 22, pp. 81-84, 1999.

Salem M. Otman received his bachelor's degree in Electrical and Electronic Engineering from Bright Star University, Albrega Libya, in 2003, and his master's degree from Cyprus International University in 2018 in the same field. He is currently a Ph.D. student in the Department of Electrical and Electronic Engineering at Cyprus International University. His current research interests include planar antennas, arrays, and near-field-focusing of planar arrays.

Mehmet Kuşaf was born in Larnaca, Cyprus, in December 1973. He received the Ph.D. degree in Electrical and Electronic Engineering from Eastern Mediterranean University in 2005. From 2005 to 2006, he worked as Assistant Professor with the Department of Electrical and Electronics Engineering, European University of Lefke. His academic journey at Cyprus International University began in 2006 as an Assistant Professor, followed by his promotion to Associate Professor in 2009, and culminated as Professor position in 2019. He is currently serving as the Head of Electrical and Electronic Engineering Department. He is the author of many research articles published in esteemed journals. His research expertise includes computational electrodynamics, antennas, and power systems.

Abdullah Y. Öztoprak earned his Ph.D. in Electrical and Electronic Engineering from University College London, University of London, UK, in 1977. He joined Eastern Mediterranean University (EMU) as an Assistant Professor in 1986, became an Associate Professor in 1988, and progressed to Professor in 1997. During his tenure at EMU, he held various leadership positions, including Chairman of the Department of Electrical and Electronic Engineering (1989-1992), Vice-Rector for Academic Affairs (1992-2003), and Rector (2009-2014). Professor Oztoprak's research focuses on beam forming networks, Rotman lenses, microwave antennas, split-step finite-difference time-domain methods, and unconditionally stable finite-difference time-domain methods.

Design of a Radar Signature Measurement Model of an Unmanned Aerial Vehicle with Low Radar Signature

Harmen van der Ven[1], David Escot Bocanegra[2], Jesús Álvarez González[2], Mehmet Erim İnal[3], Askin Altinoklu[3], Alper Kürşat Öztürk[4], Ulrich Jakobus[5], Andrey Osipov[6], Øystein Lie-Svendsen[7], Frank Weinmann[8], Åsa Andersson[9], Henrik Edefur[9], Jan-Ove Hall[9], David Poyatos Martínez[10], Tolga Çiftçi[11], and Şükrü Tarık Kostak[11]

[1]Royal National Aerospace Center (NLR)
A. Fokkerweg 2, Amsterdam, The Netherlands
harmen.van.der.ven@nlr.nl

[2]Airbus Defence and Space
Calle Aviocar, 2 28906 Getafe, Spain
david.escot@airbus.com, jesus.g.alvarez@airbus.com

[3]Aselsan Inc.
Konya Yolu 8.km Ogulbey Mah, 3051. Sokak No:3, 06830 Ankara, Turkiye
inal@aselsan.com.tr, aaltinoklu@aselsan.com.tr

[4]RAPIDEM LLC
Bilkent CyberPark B-222, Cankaya, Ankara, Turkiye
alperkozturk@gmail.com

[5]Altair Engineering GmbH
Calwer Str. 7, D-71034 Böblingen, Germany
jakobus@altair.com

[6]German Aerospace Center (DLR)
DLR Microwaves and Radar Institute, Muenchener Strasse 20, 82234 Wessling, Germany
andrey.osipov@dlr.de

[7]Norwegian Defence Research Establishment (FFI)
P.O. Box 25, NO-2027 Kjeller, Norway
oystein.lie-svendsen@ffi.no

[8]Fraunhofer Institute for High Frequency Physics and Radar Techniques FHR
Fraunhoferstraße 20, 53343 Wachtberg, Germany
frank.weinmann@fhr.fraunhofer.de

[9]Swedish Defence Research Agency (FOI)
SE-164 90 Stockholm, Sweden
asa.andersson@foi.se, henrik.edefur@foi.se, jan-ove.hall@foi.se

[10]National Institute of Aerospace Technology (INTA)
Ctra. de Ajalvir, Km. 4,5, 28850 Torrejón de Ardoz, Madrid, Spain
poyatosmd@inta.es

[11]Turkish Aerospace
Fethiye Mahallesi, Havacilik Bulvari No:17, Kahramankazan Ankara, Turkiye
tolga.ciftci@tai.com.tr, sukrutarik.kostak@tai.com.tr

Submitted On: January 21, 2024
Accepted On: August 7, 2024

https://doi.org/10.13052/2024.ACES.J.390602

Abstract – Existing databases of RCS benchmarks lack a complex, low-observable target. This paper describes the design of such a complex and low-observable measurement model. Starting point of the design is the so-called Muldicon model, developed by the NATO/STO/AVT panel. Hot spots of the original model are identified and treated with radar-absorbing materials. Simulations on the treated model demonstrate that the model is indeed low observable. The effect of the manufacturing process of 3D-printing and separable parts is assessed experimentally on a cone-sphere; the effect is found to be negligible. These results give confidence that the model, when built, satisfies the requirements of being complex and low observable; and that artefacts of the manufacturing process will not impair its signature.

Index Terms – Low observable, measurement model, radar signature.

I. INTRODUCTION

With the ever-increasing use of computational electromagnetics, there is a constant need to validate the computational tools with measurement data. The pioneering work of Woo et al. [1] presented a first set of canonical test cases which still serve as benchmarks for the validation of computational tools [2]. More databases for validation followed [3][4]. The publicly available Austin RCS benchmark suite [4] is the most recent; it contains canonical geometries, but also a generic military aircraft. Moreover, the suite not only contains perfectly electrically conducting (PEC) bodies, but also (fully homogeneous) dielectric bodies [5].

Military aircraft generally are designed to have low radar signature by shaping and the application of radar-absorbing materials. This type of target is missing in the above databases: complex targets with doubly curved surfaces, sharp edges, concealed inlet, with radar-absorbing materials. The resulting low signature (typically one or two orders of magnitude less than the size would suggest) poses challenges to computational tools, since the correct modelling of small details becomes important.

This paper presents the design of a low-observable unmanned aerial combat vehicle (UCAV) measurement model. In future, it could serve as a standard problem for validation (in the formulation of the IEEE standard on validation [6]). Starting point of the design is the so-called Muldicon model developed by the NATO/STO/AVT panel [7], as a paper exercise for multidisciplinary design (aerodynamic and structural properties were considered). Figure 1 presents both the outer mold of the aircraft and the inlet and outlet. The aircraft has certain features which may lead to a low signature, such as a concealed air intake. Nonetheless, the aircraft shape has not been driven, nor comprised, by its radar signature, so its signature has not been optimized. Changing the outer mold will require a new design loop to assure the aerodynamic characteristics of the aircraft. Its signature can only be reduced by the application of radar absorbing materials (RAM).

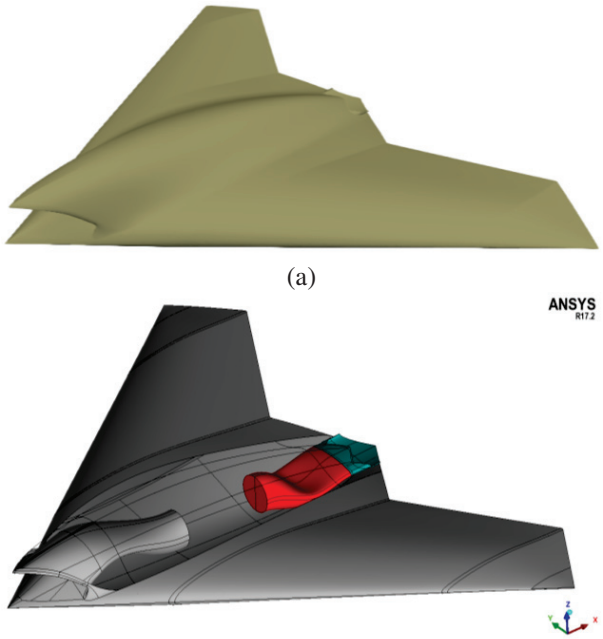

(a)

(b)

Fig. 1. Geometry of the unmanned aerial vehicle Muldicon [7]: (a) outer mold and (b) inlet and outlet.

This paper will address some of the topics in the design process. The design and manufacturing of the measurement model has been the task of the NATO/STO/SET-252 Task Group [8]. It was a five-year effort of the authors of the present paper. Obviously, there is not enough space to incorporate all details of the design process.

The structure of this paper is as follows. In Section II the design requirements and an overall design of the model is presented. Section III contains a hot spot analysis which will be used to reduce the nose-on signature. Parts of the model will be 3D printed; the required accuracy of the printing process is assessed experimentally in Section IV. Section V contains a computational assessment of the low observability characteristics of the measurement model. Finally, Section VI draws the conclusions of the study.

II. OVERALL DESIGN OF THE MEASUREMENT MODEL

As stated in the introduction the overall objective is to design a low-observable, complex, radar signature

measurement model. The requirement on geometrical complexity of the model is satisfied for the Muldicon. Modeling complexity will be satisfied by the application of radar-absorbing material which shall reduce the RCS by at least 10 dB in the nose section. The model will be measured at different sites, so must be transportable.

The measurement model will be measured at a center frequency of 10 GHz. RAM is applied to certain parts of the aircraft to reduce the radar signature. The RAM can be narrowband RAM since no broadband measurements are foreseen.

The span of the model will be 3 meters. The size is a compromise. On the one hand, the model should be sufficiently large to correspond to the objects of practical interest (UCAV, drones), and the field scattered by the model should be sufficiently strong to be registered by the receiving system of an RCS measurement facility with enough signal-to-noise ratio to ensure high accuracy of the results and good dynamic range. On the other hand, its electrical size should permit numerical evaluation of RCS with commercial EM solvers and fit into the quiet zone of a typical compact test range RCS measurement facility. The weight of the model (which is directly related to its size) should be acceptable for the supporting and positioning structures of the measurement facilities and allow uncomplicated transportation between measurement sites. Moreover, RCS measurement of a three meters object can also be performed on outdoor test ranges which will provide further benchmarking activities.

Because of the transportation requirement, the model consists of three separable parts: two wings and a midsection. The midsection is 3D printed because of the level of geometrically detail required for the inlet, outlet, turntable insert, and the spars connecting to the wings. This level of detail can also be obtained through milling, but at a higher cost. Since the wings are large smooth surfaces, they are milled from foam. A nickel paint is applied to the full aircraft to ensure a PEC surface.

This design prompts the following research questions: (1) what are the appropriate locations for the RAM patches to reduce the signature and (2) what are the resolution requirements for the 3D-printing process?

III. HOT SPOT ANALYSIS

To ascertain the radar signature of the untreated, fully PEC, model, the monostatic RCS for both vertical and horizontal polarization is computed. Computations are performed using RAPID [9], with the combined field integral equation (CFIE) formulation and multilevel fast-multipole (MLFMM) acceleration. Results are shown in Fig. 2.

The HH polarization shows two spiky maxima at $\phi = 53^\circ$ and $\phi = 150^\circ$. These azimuthal angles are the

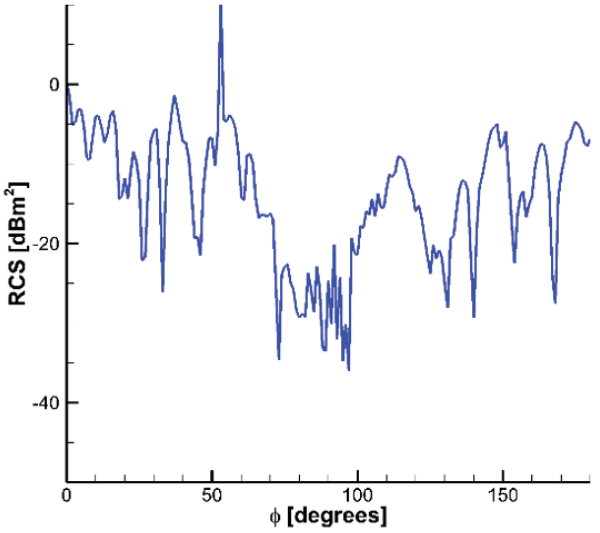

(a)

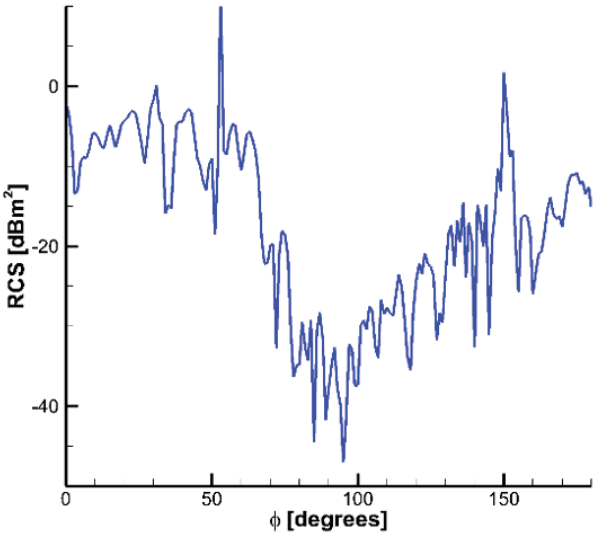

(b)

Fig. 2. RCS at 10 GHz of the untreated Muldicon as a function of azimuth angle ϕ in the zero elevation plane, where $\phi = 0^\circ$ corresponds to nose-on illumination: (a) VV polarization and (b) HH polarization.

starboard leading edge and the trailing edges of the delta wing. It is also obvious from the RCS characteristics for both polarizations that a significant RCS increase accumulates around the nose sector. As the future measurements will be performed for frontal aspects, it is worthy to investigate the RCS contributors of the illumination angles $\phi = 0^\circ$ and $\phi = 53^\circ$.

In order to calculate the hot spots on the 3D surface model for a given illumination angle, the currents induced on the surface of the mesh model are post-processed through a specific method [10]: the RCS contribution of the induced currents within a certain

neighborhood of each point on the surface of the mesh model is calculated and this value is assigned to the associated point. This yields a color map of RCS contribution surfaces of the mesh model, namely, the hot spot areas on the surface.

Results are shown in Fig. 3. It is clear that the leading edge of the wing and the inlet are the dominant RCS contributors for $\phi = 53°$. The dominant RCS contributor for nose on is the inlet. These two regions will be treated with a commercially available narrowband magnetic absorber which is effective at 10 GHz.

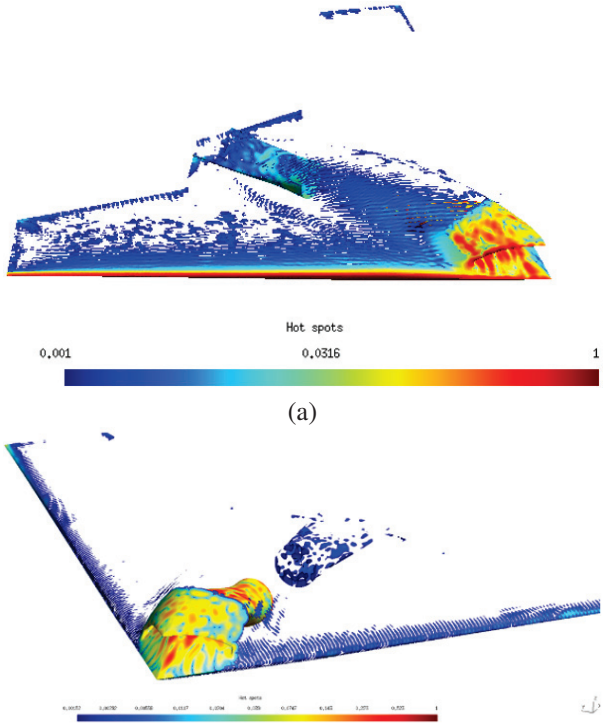

(a)

(b)

Fig. 3. Hot spot areas (in red) for horizontal polarization: (a) hot spot analysis for $\phi = 53°$ and (b) hot spot analysis for $\phi = 0°$ (nose on).

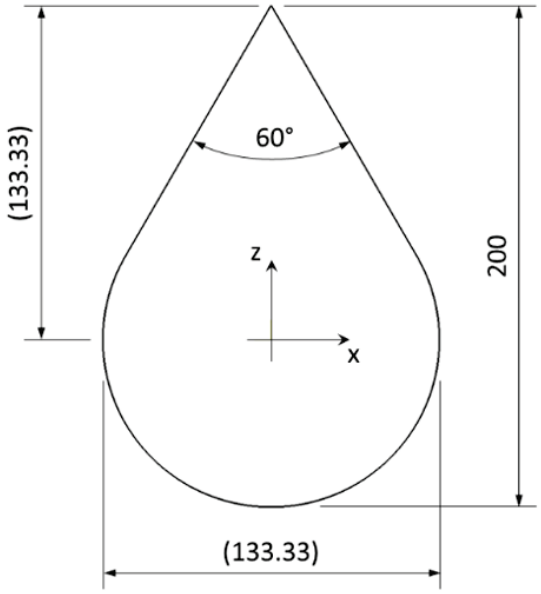

Fig. 4. Cone-sphere dimensions (in mm).

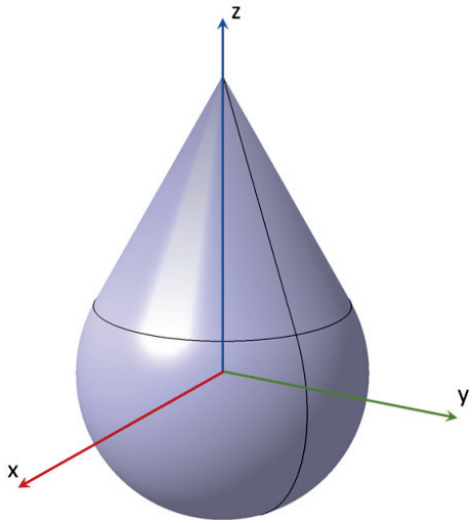

Fig. 5. Cone-sphere coordinate system.

IV. 3D PRINTING

The midsection of the Muldicon will be 3D printed. This process will not result in a smooth surface as the filament is applied in layers. In order to assess the effect of the surface roughness on the radar signature, four different 3D cone-spheres are fabricated with different finishes and conductivity, in addition to an aluminum cone-sphere as reference. The dimensions are defined in Fig. 4 and the coordinate system is shown in Fig. 5.

The objective of this study is to assess the effect of geometrical impurities on the radar signature. It is expected that if the print resolution is high enough in relation with the radar frequency, the surface can be considered to be smooth; and hence can be modeled as a smooth surface in the validation simulations. Therefore, radar signatures of the impure rough geometries will be compared directly with the signature of a smooth cone-sphere and no effort is made to quantify the surface roughness. The interested reader is referred to [11, 12], which measure and assess the surface roughness due to 3D-printing. The current study is performed at the same frequency which will be used for the Muldicon measurements. Since the cone-sphere has a low signature in the cone section, it is reasonable to expect that the results can be extrapolated to the Muldicon.

A. Model definition

A conventional fused filament fabrication (FFF) [13] 3D-printer is used to manufacture the cones at FOI. A thermoplastic material, in the form of a continuous filament, is fed from a large spool through a moving heated extruder head and deposited layer by layer on a growing object. The head is moved in two dimensions under computer control depositing one layer at a time to define the printed shape. The print head is then moved vertically by a small amount to begin the next layer. Increased layer thickness and/or larger nozzle diameter reduces the time it takes to print the object, but it also increases the surface roughness, potentially affecting the scattering of electromagnetic waves, or increasing the manual work needed afterwards. Hence, print time and surface roughness tolerance must be balanced.

The cone-spheres are printed in two sections (see Fig. 6) to avoid print support. The sections have a small central hole where a peg is placed to align the cone and sphere section during assembly. This peg also increases the bond between the parts when glued together.

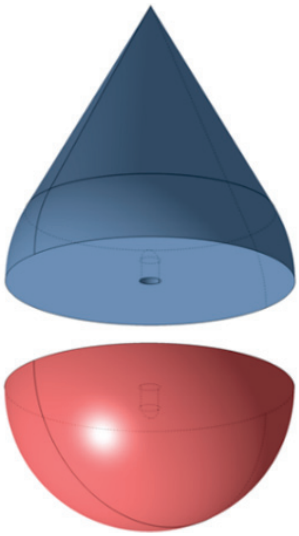

Fig. 6. Cone-sphere print sections.

To give the cone-spheres a PEC surface, the models are spray-painted with several layers of copper-based paint (Kontakt Chemie EMI 35 [14]). The surfaces are cleaned and degreased before painting to maintain the surface imperfections resulting from the print process.

The five models are:

- Cone-sphere A: Nozzle size 0.4 mm, layer height 0.2 mm. Standard PLA-filament (PrimaCreator EasyPrint PLA). Pieces glued together and then PEC-coated, which gives a "seamless" cone-sphere.
- Cone-sphere B: Nozzle size 0.8 mm, layer height 0.4 mm. Standard PLA-filament (PrimaCreator EasyPrint PLA). Pieces glued together and then PEC-coated, which gives a "seamless" cone-sphere.
- Cone-sphere C: Nozzle size 0.4 mm, layer height 0.2 mm. Standard PLA-filament (PrimaCreator EasyPrint PLA). Pieces PEC-coated and then glued together to simulate wing-fuselage joint.
- Cone-sphere D: Nozzle size 0.4 mm, layer height 0.2 mm. Electric conducting PETG-filament [15] (resistivity 106-109 ohm-cm). Pieces joined with a central metal screw.
- Cone-sphere E: fully metallic with smooth surface.

Cone-spheres A and B were designed to investigate the effect of surface roughness due to layer height but also other minor print artifacts. Figures 7 and 8 show a close-up of the surfaces after coating with electric conducting copper paint. Cone-sphere C was designed to investigate if there are any effect on the RCS due to a non-perfect joint between two PEC surfaces, similar to the joint between the wing and central fuselage sections of the Muldicon. To simulate this kind of joint, the spherical and cone section of the cone-sphere were

Fig. 7. Cone-sphere A.

Fig. 8. Cone-sphere B.

coated with copper paint separately (including the joining surface) and glued together afterwards. The purpose of cone-sphere D is to investigate if PETG could be a viable alternative to PLA coated with conductive paint.

B. Measurements

The measurements were carried out in the INTA Compact Antenna Test Range (CATR) at 10 GHz, the Muldicon frequency, and for cone-to-sphere aspects (polar angle $0^\circ < \theta < 180^o$).

C. Simulation

With the aim of comparing in a better way the measurements made, a smooth PEC cone-sphere is also simulated with Methods of Moments CFIE using FEKO [16].

D. Comparison and evaluation

Results will be shown for vertical ($\theta\theta$) polarization. The results for horizontal polarization are similar. Figure 9 (a) compares the measurement and simulation for the smooth PEC cone-sphere. The agreement is very good, except near the tip ($\theta = 0^o$). These discrepancies could be explained by the fact that, in the tip, the reflected field is very weak and the signal-to-noise ratio at the receiver is low, limiting the accuracy of the measurement results. Nevertheless, the overall agreement provides confidence in the measurement setup.

Measurements at 10 GHz for vertical polarization are shown in Fig. 9 (b). The objective is to see if different manufacturing techniques have significant effects and if the different specimens have comparable signature to the perfect metallic specimen E.

Negligible differences between specimen A (nozzle size 0.4 mm) and specimen B (nozzle size 0.8 mm) can be seen, except for the tip ($\theta = 0^o$). It can be concluded that the reduction in nozzle size is only relevant for very small and sharp geometrical details. It is not expected to find any effect on the fabricated Muldicon due to the nozzle size.

Studying specimen B (nozzle size 0.8 mm, layer height 0.4 mm) in detail and comparing with the metallic specimen E, again only the tip of the cone-sphere displays higher RCS. Hence the layer height will not cause any relevant effect on the final fabricated Muldicon.

Also, there are negligible differences between specimen A (pieces glued together and then PEC-coated) and specimen C (pieces PEC-coated and then glued together). PEC paint seems to work fine in both cases. It can be concluded that no effect on the Muldicon RCS is expected due to the joint between the wing and central fuselage sections when fabricated separately and joined afterwards as planned.

Finally, specimen D (PETG material) shows a lower RCS due to the low conductivity of the raw material.

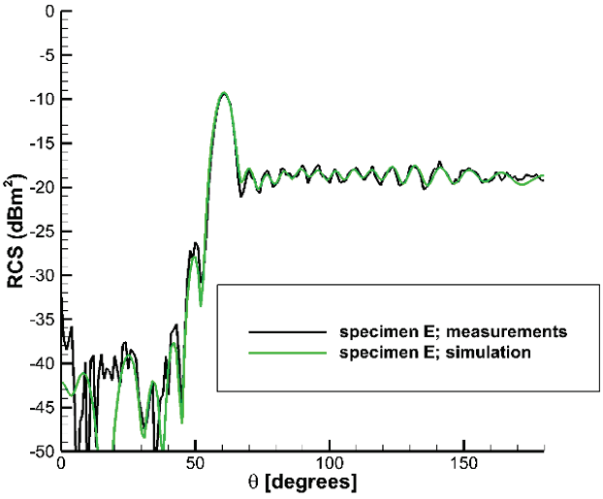

(a)

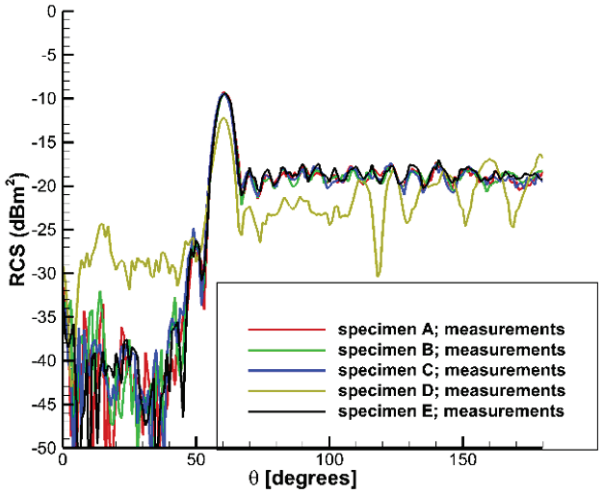

(b)

Fig. 9. Comparison of simulation and measurement results on the cone-sphere at 10 GHz for vertical polarization: (a) results comparison of measurement and simulation for the PEC cone-sphere and (b) comparison of the measurements.

Thus, this material is not an alternative for fabrication purposes.

V. SIMULATION OF TREATED MULDICON

Figure 10 shows a closeup of the model, depicting the areas where RAM is applied. Note that the leading edge of the right wing is not treated. For the physical model Laird SF-10 RAM [17] will be used. The tiles have a thickness of 1.35 mm and material properties: $\varepsilon_r = 13.29\text{-}0.25$ j and $\mu_r = 1.64\text{-}1.2$ j. There is no tapering of the tiles at their edges.

Two common meshes have been generated (but not used by all authors). Mesh A: a single layer mesh with a mesh width of $\lambda_0/10$ (where λ_0 is the wave length in vac-

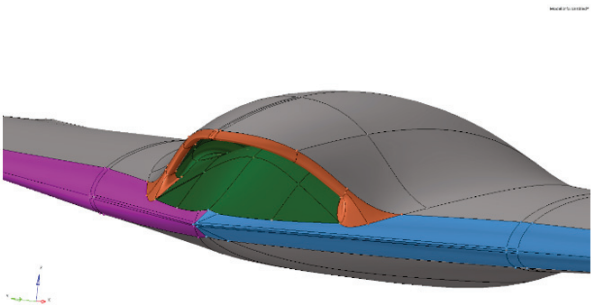

Fig. 10. Computational model of the treated Muldicon. The green and blue areas are treated with a narrowband RAM. The orange, purple and grey areas are PEC.

uum) when impedance boundary conditions (IBC) are used. Mesh B: a standard double layer mesh with a mesh width of $\lambda_0/10$ when the RAM is modeled as a dielectric. A brief overview of the simulation settings is given in Table 1, all (but one) using integral equation solvers with MLFMM acceleration. The impedance η in the IBC is computed as $\eta = j\sqrt{\frac{\mu_r}{\varepsilon_r}}\tan(k_0 d\sqrt{(\varepsilon_r \mu_r)})$, where ε_r, μ_r, d, and k_0 are the relative permittivity of the dielectric, its relative permeability, the thickness of the dielectric layer, and the free-space wave number. The motivation for using different meshes is, on the one hand, that the mesh structure is dictated by the method (IBC does not require a double layer; the finite-element boundary integral method requires a volume mesh in the RAM). On the other hand, the experience from different partners with their method of choice leads to different meshing strategies which produce the best results for the method considered.

The simulation results at elevation zero are shown in Fig. 11. It is clear from the difference between the left and right wing aspects that the treatment of the leading

Table 1: Overview of simulation settings

Partner	Method	Mesh
Airbus	in-house tool; both IBC and full dielectric [18]	A & B
Altair	FEKO [16]; IBC	A
Aselsan	in-house tool [9]; both IBC and full dielectric; JMCFIE formulation of [19]	own
FHR	in-house tool [20]: coupled boundary integral with finite element for dielectric	own
FOI	FEKO; IBC	A
INTA	FEKO; IBC	own
NLR	in-house tool [21]: full dielectric (Müller formulation)	B

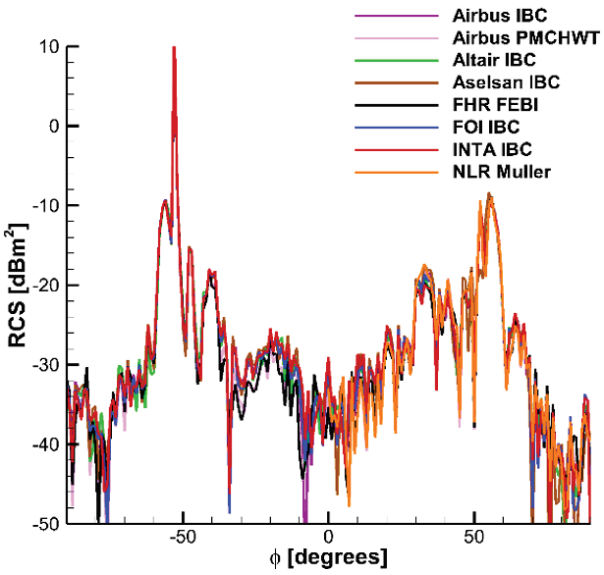

(a)

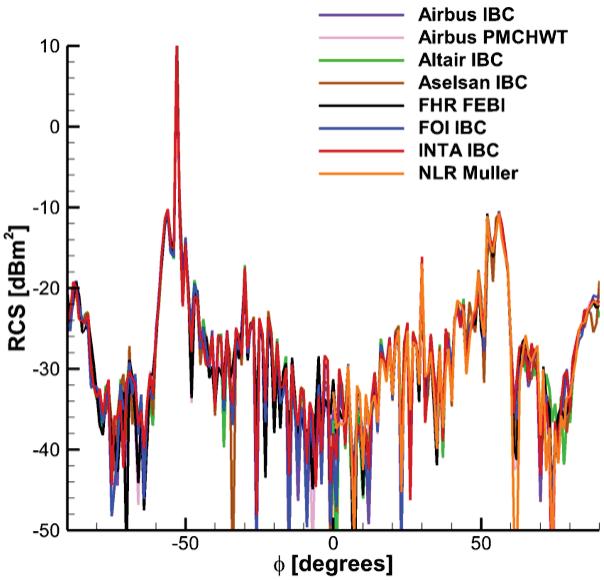

(b)

Fig. 11. Comparison of simulations of the treated model at zero elevation. RCS in dB m^2: (a) horizontal polarization and (b) vertical polarization.

edge reduces the RCS by 20 dB around $\phi = 53^o$. Also, and more importantly, the nose-on RCS is reduced significantly, even without treatment of the rim of the inlet. Scatter in the simulation results only occurs at low RCS levels, below -30dBm^2. It is precisely for this reason that the validation model is developed. Despite the large range of methods and meshes, the computational results compare very well even at very low RCS levels.

Figure 12 shows a close-up of the RCS in the nose-on region at higher aspect resolution of 0.2 degrees. At

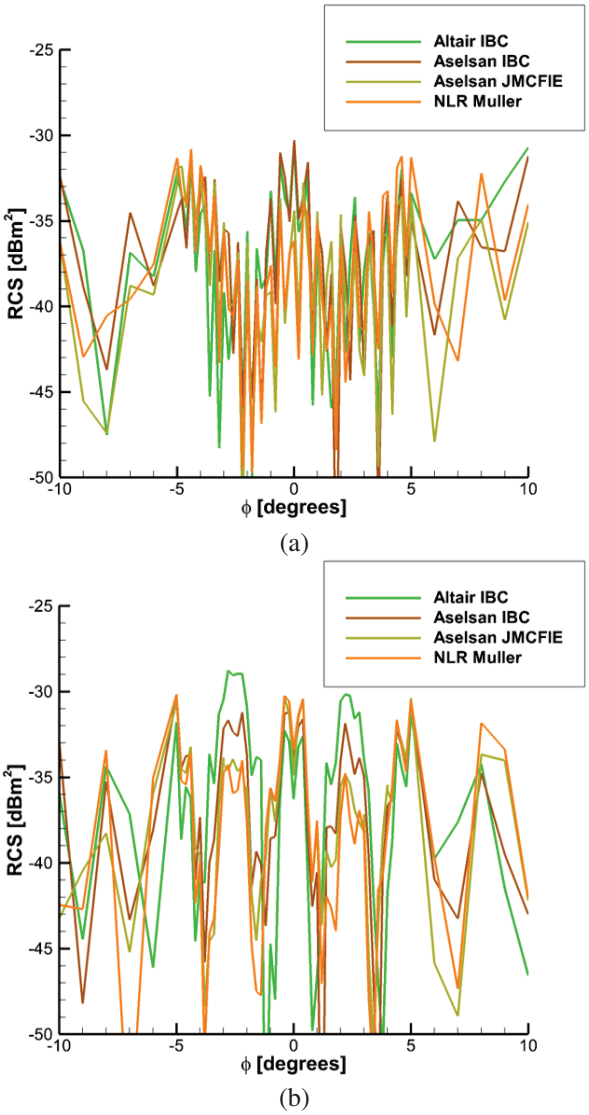

Fig. 12. Comparison of simulations of the treated model. Detail for nose-on aspects: (a) horizontal polarization and (b) vertical polarization.

these low RCS levels, differences of up to 5 dB can be observed. A more consistent cross-comparison of methods and meshes will be executed in the future.

VI. CONCLUSION

A design of a measurement model of an unmanned aerial vehicle which is geometrically complex, applies radar-absorbing material and has a low radar signature has been presented. Numerical simulations have demonstrated that the measurement model is low observable at the center frequency of 10 GHz. Experiments on a variety of cone-sphere specimens have shown that it is reasonable to expect that the surface of the measurement model can be modeled as smooth and contiguous, even though the measurement model consists of three parts and the midsection is 3D printed. Hence, it is expected that the measurement model, once built, will satisfy the design requirements.

REFERENCES

[1] A. C. Woo, H. T. G. Wang, M. J. Schuh, and M. L. Sanders, "EM programmer's notebook - benchmark plate radar targets for the validation of computational electromagnetics programs," *IEEE A&P Magazine*, vol. 34, no. 6, pp. 52-56, 1992.

[2] A. Greenwood, "Electromagnetic code consortium benchmarks," Technical Report AFRL-DE-TR-2001-1086, Air Force Research Laboratory, 2001.

[3] R. Fernandez-Recio, A. Jurado-Lucena, B. Errasti-Alcala, D. Poyatos-Martinez, D. Escot-Bocanegra, and I. Montiel-Sanchez, "RCS measurements and predictions of different targets for radar benchmark purpose," in *2009 International Conference on Electromagnetics in Advanced Applications*, Turin, Italy, 2009.

[4] J. W. Massey, J. T. Kelley, C. Courtney, D. A. Chamulak, and A. E. Yilmaz, "A benchmark suite for quantifying RCS simulation performance on modern computers," in *Proc. USNC/URSI Radio Science Meeting*, July 2018.

[5] J. T. Kelley, A. E. Yilmaz, D. A. Chamulak, and C. C. Courtney, "Increasing the material diversity in the Austin RCS benchmark suite using thin plates," in *Antenna Measurement Techniques Association Symposium (AMTA),* Newport, RI, 2020.

[6] IEEE Standard for Validation of Computational Electromagnetics Computer Modeling and Simulations, in IEEE Std 1597.1-2022 (Revision of IEEE Std 1597.1-2008), pp. 1-52, 8 Sep. 2022.

[7] R. Nangia, M. Ghoreyshi, M. P. C. van Rooij, and R. M. Cummings, "Aerodynamic design assessment and comparison of the MULDICON UCAV concept," *Aerospace Science and Tech.,* vol. 93, 2019.

[8] NATO/STO/SET-252 on *Development of a validation model of a stealth UCAV* [Online]. Available: https://www.sto.nato.int/publications/STO%20Technical%20Reports/Forms/Technical%20Report%20Document%20Set/docsethomepage.aspx?ID=5162&FolderCTID=0x0120D5200078F9E87043356C409A0D30823AFA16F6010066D541ED10A62C40B2AB0FEBE9841A61&List=92d5819c-e6ec-4241-aa4e-57bf918681b1&RootFolder=%2Fpublications%2FSTO%20Technical%20Reports%2FSTO%2DTR%2DSET%2D252

[9] A. Altinoklu, A. K. Ozturk, and M. E. Inal, "Radar cross section reduction for air vehicles based on MLFMA and surface integral equations using RAPID" in *Proceedings of ASELSAN REHIS TTEK Conference*, Ankara, Turkiye, 2021.

[10] A. Altınoklu, A. K. Ozturk, E. Sever, and M. E. İnal, "3-D scattering center determination algorithm for detecting primary radar cross-section contributing regions on a radar target," in *Proc. IEEE Int. Symp. Antennas Propag. (APSURSI),* Oregon, Portland, July 2023.

[11] E. R. Biglete, M.C.E. Manuel, J. C. Dela Cruz, M. S. Verdadero, J. M. B. Diesta, D. N. G. Miralpez, R. A. C. Javier, and J. I. C. Picato, "Surface roughness analysis of 3D printed parts using response surface modeling," in *2020 11th IEEE Control and System Graduate Research Colloquium (ICSGRC),* Shah Alam, Malaysia, pp. 191-196, 2020.

[12] R. Rakshit, A. Ghosal, P. K. S. Podder, D. Misra, and S. C. Panja, "An experimental investigation of surface roughness and print duration on FDM printed polylactic acid (PLA) parts," in *2022 Interdisciplinary Research in Technology and Management (IRTM),* Kolkata, India, pp. 1-5, 2022.

[13] Fused filament fabrication [Online]. Available: https://en.wikipedia.org/wiki/Fused_filament_fabrication

[14] Kontakt Chemie [Online]. Available: http://www.kontaktchemie.com/KOC/KOCproductdetailV2.csp?product=EMI%2035

[15] North 3D Filament [Online]. Available: https://addnorth.com/product/ESD%20PETG/ESD%20PETG%20-%201.75mm%20-%20750g%20-%20Black

[16] Altair Feko [Online]. Available: https://www.altair.com/feko

[17] Laird [Online]. Available: https://www.laird.com/products/microwave-absorbers/microwave-absorbing-elastomers-and-films/eccosorb-fgm/21191167

[18] J. Alvarez, J. M. Alonso-Rodriguez, H. Carbajosa-Cobaleda, M. R. Cabello, R. Gomez-Martin, and S. G. Garcia, "DGTD for a class of low-observable targets: A comparison with MoM and (2,2) FDTD," *IEEE Ant. and Wireless Propag. Letters*, vol. 13, pp. 241-244, 2014.

[19] P. Ylä-Oijala, M. Taskinen, and S. Järvenpää, "Surface integral equation formulations for solving electromagnetic scattering problems with iterative methods," *Radio Science*, vol. 40, no. 6, p. RS6002, 2005.

[20] A. Tzoulis and T. F. Eibert, "A hybrid FEBI-MLFMM-UTD method for numerical solutions of electromagnetic problems including arbitrarily shaped and electrically large objects," *IEEE Trans. Antennas Propag.,* vol. 53, pp. 3358-3366, Oct. 2005.

[21] H. van der Ven, C. A. Liontas, K. Cools, and D. R. van der Heul, "On the accuracy of different boundary integral formulations for dielectric bodies using RWG and BC functions," in *Proceedings of EuCAP 2016,* Davos, Switzerland, 2016.

Harmen van der Ven received his Ph.D. in Mathematics in 1993 from Utrecht University. In the same year he joined the Netherlands National Aerospace Laboratory NLR where he develops numerical algorithms for fluid dynamics and electromagnetics. His main research interest is in radar signature prediction. He is also program manager Emerging Technologies at NLR. He was the chairman of the NATO/STO group SET-252.

David Escot Bocanegra was born in Madrid, Spain. He received the M.Sc. and Ph.D. degrees in telecommunication engineering from the University of Alcala, Madrid, Spain, in 2002 and 2012, respectively. He has worked in Telecom Bretagne, Brest, France (2002-2003) and the National Institute for Aerospace Technology (INTA), Spain (2004-2019). He is since 2019 in Airbus Defence and Space, Spain. His current research interests are related to stealth technologies, radar cross section, computational electromagnetics and materials characterization.

Jesús Álvarez González was born in Leon, Spain. He received the Ph.D. degree from the University of Granada, Granada, Spain, in 2013. Since 2006, he has been working as an RCS, Antenna and EMC Engineer with Airbus Defense and Space, Getafe, Spain. His research interests include computational electrodynamics in time domain, the method of moments and fast algorithms for integral equations in frequency domain and computational electromagnetics applied to electromagnetic compatibility, antenna, and radar cross section.

Mehmet Erim İnal was born on 8 June 1971 in Mardin, Turkiye. He received the B.S. and M.S. degrees in electrical and electronics engineering from Middle East Technical University at Ankara, Turkiye, in 1993 and 1997, respectively. From 1993 till today he is employed by ASELSAN, Ankara, Turkiye. During his 30 years in the defense industry, his work mainly spans research, development and design activities of radar and electronic warfare (EW) systems, active and passive microwave devices, antennas, radomes, absorbers, frequency selective surfaces, advanced engineering materials and low observable (LO) solutions. His interest areas are interdisciplinary development cycles of critical hardware related to electromagnetics, RF and microwaves, mechanical engineering and material science. He holds several patents on antennas, absorbers and computational electromagnetics. Currently he is working as the head of "Radomes, Low Observables and Advanced Engineering Materials Design Division" in Aselsan, Ankara, Turkey.

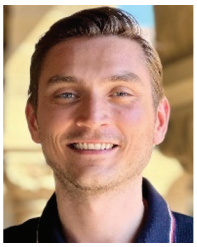

Askin Altinoklu received his B.Sc. and M.Sc. degrees in Electrical and Electronics Engineering from Middle East Technical University, Turkey, in 2016 and 2019, respectively. From July 2016 to November 2023, he worked as an RF/Microwave design engineer at ASELSAN, Turkey, where he served as a team leader for the electromagnetic analysis team from 2019 to 2023. Currently, he is a Doctoral Research Fellow in the School of Computer Science and Electronic Engineering at the University of Essex, UK, where he is involved in the research and development activities in the SCION project funded by the European Commission within the Horizon Europe, Marie Skłodowska-Curie Actions – Doctoral Network Program. His research interests lie in machine-type communications, 6G, Energy Harvesting and SWIPT, and Semantic Communications.

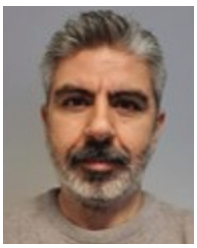

Alper Kürşat Öztürk was born in Yozgat, Turkey. He earned his B.S. and M.S. degrees in electrical and electronics engineering at Bilkent University, Ankara, Turkey, in 2000 and 2002, respectively. He later earned his Ph.D. from Concordia University, Montreal, QC, Canada, in 2009. From 2010 to 2019, he was employed at ASELSAN, Turkey. In 2019, he founded RAPIDEM LLC, Turkey, with a focus on developing electromagnetic simulation software for RCS prediction, scattering, and antenna design. His research interests cover a broad spectrum of applied computational electromagnetics, particularly concerning integral, differential and variational equations.

Ulrich Jakobus graduated in electrical engineering from the University of Stuttgart, Germany, in 1991. He completed his Ph.D. and Habilitation and became Privatdozent at the same university in 1994 and 1997, respectively. His areas of research included numerical techniques in electromagnetics and their hybridization, antennas, EMC and bio-electromagnetics, laying the foundations for the electromagnetics simulation code Feko in 1991. Since 1998, Ulrich has been focusing on the development and commercialization of Feko. Through an acquisition, he joined Altair in 2014, where he currently oversees the development of all electromagnetic and electronic software solutions. He is a member of URSI commission B, the German VDE/ITG, Fellow of IEEE, and Fellow of ACES.

Andrey Osipov received the degrees of Diploma Physicist (with honors), Candidate of Sciences (Ph.D.), and Doctor of Sciences (Habilitation), all in physics of electromagnetic waves, from the St. Petersburg State University, St. Petersburg, Russia, in 1983, 1987 and 1996, respectively. Since 1998 he has been with the Microwaves and Radar Institute of the German Aerospace Center (DLR). His current research interests include radar cross section engineering, theory of electromagnetic scattering by canonical objects, development of high-frequency simulation tools in radar-based remote sensing and applications of metamaterials in defense and security. Dr. Osipov is the author and co-author of two monographs, more than 160 journal and conference papers and two patents.

Øystein Lie-Svendsen received his dr.scient. (Ph.D.) in physics from the University of Oslo, Norway, in 1988. From 1990-1993 he was employed as research associate at the University of Alaska, Fairbanks, working on numerical models of plasma transport in the Earth's ionosphere. From 1993 onwards he has worked at the Norwegian Defence Research Establishment (FFI), currently as principal scientist. His research topics have been space physics, continuing his work on modelling plasma transport in the solar atmosphere and the solar wind, and, more lately, radar.

Frank Weinmann received the Dr.-Ing. degree in electrical engineering from the University of Karlsruhe, Germany, in 2004. Since 2004 he is with the Fraunhofer FHR Research Institute for High Frequency Physics and Radar Techniques in Wachtberg, Germany, as a Research Engineer. In 2009, he became Teamleader of the Electromagnetic Modelling Group, in 2017 he became head of the department Antenna Technology and Electromagnetic Modelling, and since 2023 he is head of the department Antennas & Frontend. Dr. Weinmann's major areas of interest include all aspects of antenna development, metamaterials and metasurfaces, as well as propagation modeling of electromagnetic waves, high-frequency asymptotic techniques, modeling of radar signatures, and studies in the fields of wind turbine scattering as well as automotive radar.

Åsa Andersson received the M.Sc. degree in Applied Physics and Electrical Engineering and the Ph.D. degree in Theoretical Physics from Linköping University, Linköping, Sweden in 1996 and 2002, respectively. Since 2003, she has been with the Swedish Defence Research Agency (FOI), Linköping, Sweden, working with electronic warfare modeling, advanced low observable materials and radar signatures. Her present activities are focused on research and applications of electromagnetic modeling and calculations of radar signatures for military systems.

Henrik Edefur graduated from the Royal Institute of Technology (KTH) in Stockholm 2002 with a master degree in aeronautics. He started working at FOI 2004 as a research engineer and was last year appointed to senior scientist. All this time at FOI he has been working with aircraft conceptual design and analysis.

Jan-Ove Hall obtained his M.Sc. in 2000 and a Ph.D. in space physics in 2004, both from Uppsala University in Sweden. Subsequent to completing his doctoral studies, Dr. Hall embarked on a postdoctoral research position. In 2006, he transitioned to the Swedish Defence Research Agency (FOI), where he conducts research in radar signature management.

David Poyatos received his M.Sc. degree in Telecommunication Engineering from the Universidad Politécnica de Madrid (UPM), Spain, in 1998 and a Ph.D. degree in Computational and Applied Electromagnetics from the University of Alcala, Spain, in 2017. He joined the National Institute of Aerospace Technology (INTA), Spain, in 1997. Since 2015, he is the head of the Radiofrequency Area at INTA. His current research activities are related to the simulation, measurement and analysis of antennas and radar signature and the electromagnetic characterization of materials.

Tolga Çiftçi received the B.Sc. degree in Electrical and Electronics Engineering from Bilkent University, Ankara, Turkey, in 2012, and the M.Sc. degree in Industrial Engineering from Middle East Technical University, Ankara, Turkey in 2019. Since 2016, he has been with Turkish Aerospace Industries, currently working as Lead Engineer. His current research interests include computational electromagnetics, optimization techniques, electromagnetic analysis, electromagnetic compatibility and electromagnetic testing.

Şükrü Tarık Kostak received the B.Sc. degree in Mechanical Engineering from Istanbul Technical University (ITU), Istanbul, Turkey, in 2018. Since 2018, he has been with Turkish Aerospace Industries, currently working as Structural Design Chief Engineer. His current research interest is development of next generation fighter aircrafts.

Analysis of Reader Orientation on Detection Performance of Hilbert Curve-based Fractal Chipless RFID Tags

Muntasir M. Sheikh

King Abdulaziz University, Department of Electrical and Computer Engineering
Jeddah 21589, Saudi Arabia
mshaikh@kau.edu.sa

Abstract – The role of the orientation of the radio frequency identification (RFID) reader is vital in the RFID-based communication system. This study presents the design and analysis of the impact of the orientation of the RFID reader (angle of incidence of the plane wave) on the detection and sensitivity characteristics of fractal chipless RFID tags. Four fractal (irregular) shaped tags are developed using four iterations of the Hilbert curve filling algorithm. The full-wave EM analysis of the designed tags in Matlab is performed by exporting them in Computer Simulation Technologies Micro-Wave Studio (CST MWS) in the frequency range of 2 to 20 GHz. Firstly, the performance of the tags is analyzed by observing the radar cross-section (RCS) of the tag for the fixed orientation of the incident plane wave in three different polarizations (horizontal, vertical, and oblique). Later, the variations in the EM spectrum (RCS results) are analyzed for oblique polarization by varying the incidence plane wave in both elevations (for two cases of 0° and 90°) and azimuth planes (sweeping from 0° to 180° with a step size of 10°). The analysis of the proposed aggregated RCS response for all cases in oblique polarization produces higher coding capacity (169 bits), coding spatial capacity (16.504 bits/cm^2), coding spectral capacity (9.826 bits/GHz), and coding density (0.960 bits/GHz/cm^2) for the realized highly irregular tag using fourth-iteration (4T) of Hilbert curve filling algorithm. The proposed procedure of detection based on aggregated response makes the developed RFID communication system more secure and reliable.

Index Terms – Angle of incidence, chipless RFID, coding den, fractal tags, RFID readers.

I. INTRODUCTION

The popularity of chipless radio frequency identification (RFID) tags has increased over the last decade. Chipless RFID tags are the vital components of a wide range of modern-day applications such as warehouse inventory management, logistics, bio-medical, Internet of Things (IoT), and document security [1–3].

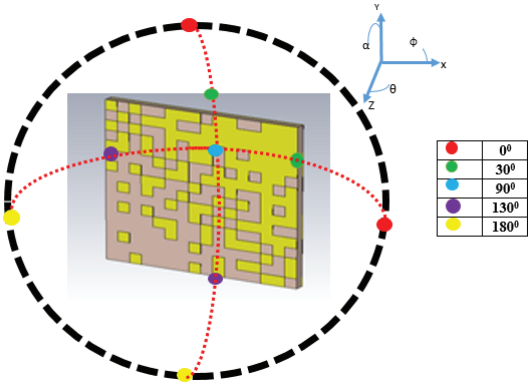

Fig. 1. Analysis framework for different orientations (angle of incidences of illuminating plane waveform of RFID reader on Hilbert curve-based fractal tag).

The action of a chipless RFID tag is based on the backscatter from the tag due to the incident signal from the RFID reader. The RFID reader decodes the features of the backscattered signal which leads to its unique identification. The backscattered signal contains the resonance frequency features (dips or notches) of the tag which are analyzed using both time and frequency domain techniques [4, 5]. Frequency domain tags use the amplitude and phase of the reflected signal or radar cross-section (RCS) of the tag for its characterization and identification [3, 5–7].

Different resonance structures [3, 5, 8–10] of the RFID tags are reported in the literature for different applications. The conventional tag structures [3, 5, 8–10], although providing good performance in terms of coding density, lack in the development of a secure and safe wireless communication system [11, 12]. The scattered tag information could be intercepted and decoded by predators.

Fractal chipless tags have emerged as a good solution to this problem as their resonance characteristics cannot be easily interpreted by a conventional RFID reader due to their inherent irregular structures [7, 13–15]. The commonly reported techniques for the

Submitted On: October 6, 2022
Accepted On: April 2, 2023

https://doi.org/10.13052/2024.ACES.J.390603

generation of fractal tags are fragmented loaded resonators [14], space-curve filling [12, 16–18], the game of life theory [11], irregular natural geometries [7], and shape-optimized fractal structures [19].

Space-filling curved (Peano and Hilbert curves) based RFID tags have compact structures and offer higher encoding densities which depend on the layout of the curves [17]. The developed geometries have an iterative nature and their planar structures offer the additional advantage of cheaper fabrication. Murad et al. [16] developed Hilbert-curve antennas for RFID applications at 2.4 GHz. The authors in [17] proposed RFID tags based on the array of Peano and Hilbert curve elements. Dual band Card-type Hilbert-curve fractal antenna for high and ultra-high frequency range RFID applications is reported in [15].

This study reports a detailed simulation of the impact of the RFID reader orientation on the backscattering of designed Hilbert curve-based fractal RFID tags. Four different irregular-shaped RFID tags are developed using the Hilbert curve filling algorithm in Matlab. The designed tags are then imported into CST MWS using the Matlab-CST API. The 3D geometries of the tags with added FR4 substrate in CST are analyzed in the frequency range of 2 to 20 GHz.

Each tag geometry is illuminated by a plane wave, and its backscattered RCS responses are recorded for the fixed and varying orientations of the illuminating plane wave. For the fixed orientation, all tag RCS results are analyzed in three different polarizations (horizontal, vertical, and oblique). In the second case study analysis, the incident plane wave angle of incidences is varied in both the elevation and azimuth planes, and RCS results are recorded for oblique polarization. Here two different configurations of elevation plane angles, i.e. φ=0° and $\varphi = 90°$ are chosen for the analysis purpose. For each configuration of elevation angle, the azimuth angle (θ) is changed from 0° to 180°, and RCS waveforms are recorded for each case. Figure 1 illustrates the concept of the different angles of incidence of a plane wave (mimicking the different orientations of the RFID reader) on one of the designed fractal tags. Next, aggregated RCS responses for both cases of elevation plane, i.e. $\varphi = 0°$ (case 1) and $\varphi = 90°$ (case 2) are considered to analyze the overall coding performance of tags in terms of coding capacity (bits), coding spatial capacity (bits/cm^2), coding spectral capacity (bits/GHz), and coding density (bits/GHz/cm^2). The details of the design procedure, the EM analysis of realized tags, and the analysis of the tags for the configurations are given in the next sections.

Since there was no fabrication of the tags or experimental validation of the simulation results, we used the same numerical setup that was used in similar previous papers [3, 7] where simulations were validated by experimental results. This gave us confidence that our simulation produces credible results. We intend to fabricate the tags designed in this paper and experimentally validate our results soon.

II. DESIGN OF FRACTAL TAGS

The Hilbert curve filling technique is used for designing different irregular-shaped tags for the proposed study. Four tags are designed using different iterations of the Hilbert curve filling algorithm in MATLAB and then are imported to CST MWS for full-wave EM analysis. The details for the design and implementation steps in MATLAB are as follows:

- CST-MATLAB application interface (API) is installed on the system.
- Develop the Hilbert curve filling algorithm in MATLAB.
- Design the different 2-dimensional (2D) tag shapes in MATLAB by using the developed Hilbert curve filling algorithm.
- Import the designed 2D image into CST MWS using the integrated CST-MATLAB API.

After the first iteration (1T) of the Hilbert space-curve filling, a 2D image is created in MATLAB. Figure 2 (a) depicts the tag's shape after the 1T of the Hilbert curve filling algorithm. The 1T of the algorithm produces only a rectangular-shaped tag.

The second (2T), third (3T), and fourth (4T) iterations of the tag can also be generated, as shown in Figs. 2 (b-d). We note from Figs. 2 (b-d) that the tag shape becomes more irregular in each successive iteration.

A. Simulation environment

The tags designed in MATLAB are imported into CST MWS as a 3D shape using the CST-MATLAB API for the full-wave EM analysis. The full pack of an API is required for the successful interfacing of MATLAB and CST.

Figure 2 depicts the 3D executed tags in CST with the addition of the substrate behind the 2D tag geometry. Each 2D shape of the tag is placed on an FR4 substrate of 32x32x1.6 mm. The 2D tag shape is assigned to copper material with a thickness of 0.04 mm. The horizontal, vertical, and oblique polarization electrical field probes are placed in the far-field region at 140 mm. The far-field distance (z) satisfies the condition of $z>2D2/\lambda$, where D depicts the size of the tag and λ refers to the free-space wavelength at 20 GHz. These probes are used to record the RCS of each tag for all analyzed cases of angular reader orientations. The RCS analysis of all tags is performed in the frequency range of 2-20 GHz.

Each tag geometry is illuminated with the incident plane wave at different angles of incidence, mimicking the angular nature of the reader. Figure 3 presents the

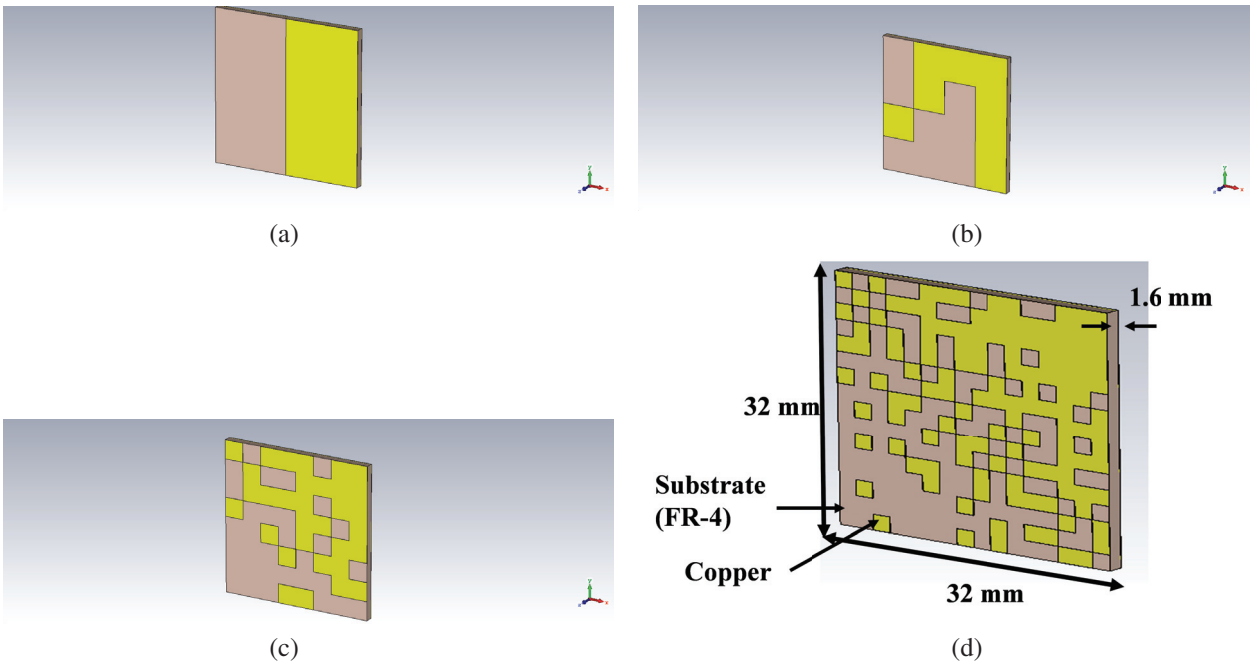

Fig. 2. Designed CST and Matlab structure of applied Hilbert curve filling on the chipless RFID tags: (a) Tag 1 (1T), (b) Tag 2 (2T), (c) Tag 3 (3T), and (d) Tag 4 (4T).

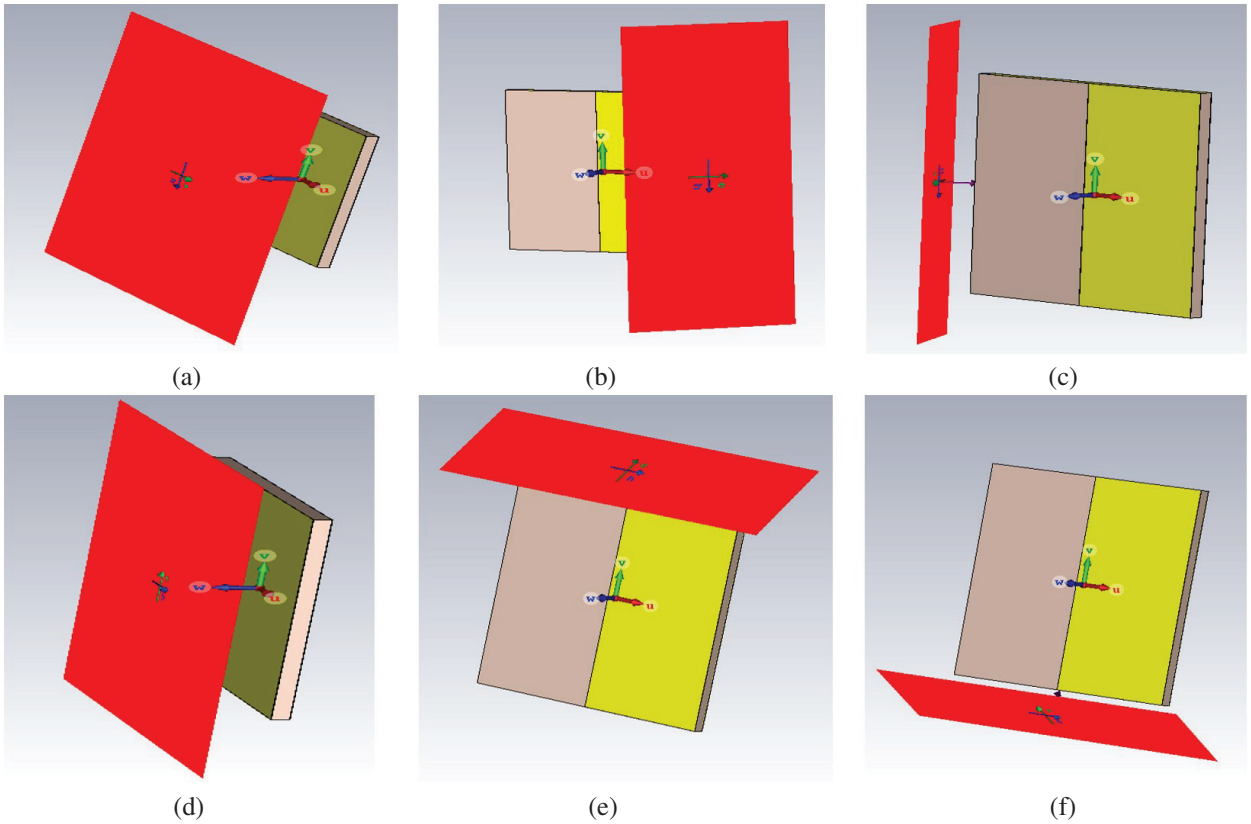

Fig. 3. Tag 1 (1T) with different angle of incidence of plane wave excitations: (a) $\varphi = 0°, \alpha = 0°$, and $\theta = 0°$; (b) $\varphi = 0°$ $\alpha = 0°$, and $\theta = 50°$; (c) $\varphi = 0°, \alpha = 0°$, and $\theta = 150°$; (d) $\varphi = 90°, \alpha = 0°$, and $\theta = 0°$; (e) $\varphi = 90°, \alpha = 0°$, and $\theta = 50°$; (f) $\varphi = 90°$, $\alpha = 0°$, and $\theta = 140°$[11].

selective cases of the different angles of incidence of the angular reader for Tag 1 [11]. Figure 3 (a) refers to the plane wave excitation with φ=0°, α=0°, and θ=0° which represents the case of zero elevation and azimuth angles of the RID reader. The cases of change in azimuth angles to 50° and 150° of the RFID readers are shown in Figs. 3 (b-c) with the fixed elevation orientation of 0°. Figures 3 (d-f) show the simulation environment with a fixed elevation angle of 90° for plane wave excitation (reader orientation) with the change in azimuth angles to 0°, 50°, and 140°, respectively.

The incident plane wave elevation angle (φ) of the angular reader is chosen to be 0^o and 90^o for this study. For each elevation angle, the value of the azimuth angle (θ) of the incident plane wave is changed from 0^o to 180^o with a 10^o step size, as illustrated in Fig. 1 and some selective cases in Fig. 3. The incident elevation angle (φ) configurations of 0^o and 90^o are referred to as case 1 and case 2 for brevity in the onward discussion. Table 1 summarizes the analyzed reader orientation cases.

Table 1: Analysis cases of angular reader orientations

	Reader Orientation
Case # 1	$\varphi = 0°, \alpha = 0°$, and $\theta = 0 - 180° \, (10° \text{ step})$
Case # 2	$\varphi = 90°, \alpha = 0°$, and $\theta = 0 - 180° \, (10° \text{ step})$

The current distribution and RCS results are recorded and analyzed for each case of RFID reader incident angle for horizontal (HH), vertical (VV), and oblique polarization for the four different realized tags of Fig. 2 for each θ and φ combination.

III. ANALYSIS OF REALIZED TAGS WITH FIXED READER ORIENTATION

An RFID reader is a wireless transceiver that reads a code printed on a tag. The reader does not have to scan the tag directly or have a line of sight with it. However, the tag must be within the readers' range (typically 10-100 m) to be successfully read. The reader is a transceiver that utilizes an antenna to emit radiofrequency. There is no integrated circuit on a chipless tag. Instead, a unique pattern is printed or engraved on the tag. This pattern (code) is usually made by metallization on a dielectric (substrate). Thus, the metallization reflects the RF energy to the reader, which is programmed to identify the unique pattern. In this work, we study backscattered, frequency-domain, chipless RFID tags designed using Hilbert curve-based metallization. Specifically, we are studying the effect of RFID reader angular orientation on the encoding capacity of the tag. The analysis is performed for both fixed and angular rotations of the RFID reader.

First, the analysis of the different realized tags is performed in terms of their current distribution and RCS results for the three different polarizations (horizontal, vertical, and oblique) for the fixed reader orientation. The excitation plane wave is incident at fixed angles (H [horizontal]= $\varphi = 0°$, $\alpha = 0°$, and $\theta = 0°$, V [vertical]= $\varphi = 0°$, $\alpha = 90°$, and $\theta = 0°$, Ob [oblique]= $\varphi = 0°$, $\alpha = 0°$, and $\theta = 45°$) and the results for each tag are analyzed.

A. Surface current distribution analysis

Figures 4 (a-d) depict how the current distribution changes as the tag structure changes in horizontal polarization. These results correspond to Tag 1, Tag 2, Tag 3, and Tag 4 at resonance frequencies of 4.25 GHz, 8.16 GHz, 8.25 GHz, and 8.16 GHz, respectively. The RCS peaks can be easily identified by considering the noise level. The used level of noise is around 5-10 dB, which is the difference between the lowest RCS value and the highest RCS value of resonant frequency. With the change in the fractal geometry, we observe significant variations in the spreading of the current around the metallic structures of the tag. The change of the irregular copper shape of the tag with each successive iteration of the Hilbert curve filling algorithm brings out the variations in the resonance characteristics of each tag, as evident from the results of Figs. 5 (a-d) for the fixed horizontal polarization for all tags.

The red color, which represents highly concentrated surface current areas, shows the most exciting parts of the tags at the selected frequencies. The metallic islands of the tags resonate at different frequencies depending on their size compared to the wavelength. The change in the tag's metallic structure varies its electrical size and thus changes its resonance characteristics. The observed maximum value of current J_{max} (corresponding to red color) is 0.114 A/m, 0.060 A/m, 0.106 A/m, and 0.275 A/m for Tag 1, Tag 2, Tag 3, and Tag 4, respectively, at their mentioned unique resonance frequencies.

The change in polarization significantly impacts the current distribution around the metallic islands of the fractal tags. This is observed when the tag's current distributions are analyzed for vertical and oblique polarization under the same settings as the incident plane wave. Figures 5 (e-h) illustrate the current distribution of the realized four tags for vertical polarization. The resonance frequencies of all tags changed to 6.9 GHz (1T), 7.85 GHz (2T), 19.42 GHz (3T), and 6.23 GHz (4T).

A similar observation in the tag's current distribution characteristics is observed for the oblique polarization. The results for the oblique polarization are depicted in Figs. 4 (i-l). The comparison of oblique polarization results with earlier cases confirms that the realized fractal tags are sensitive to polarization changes even with the

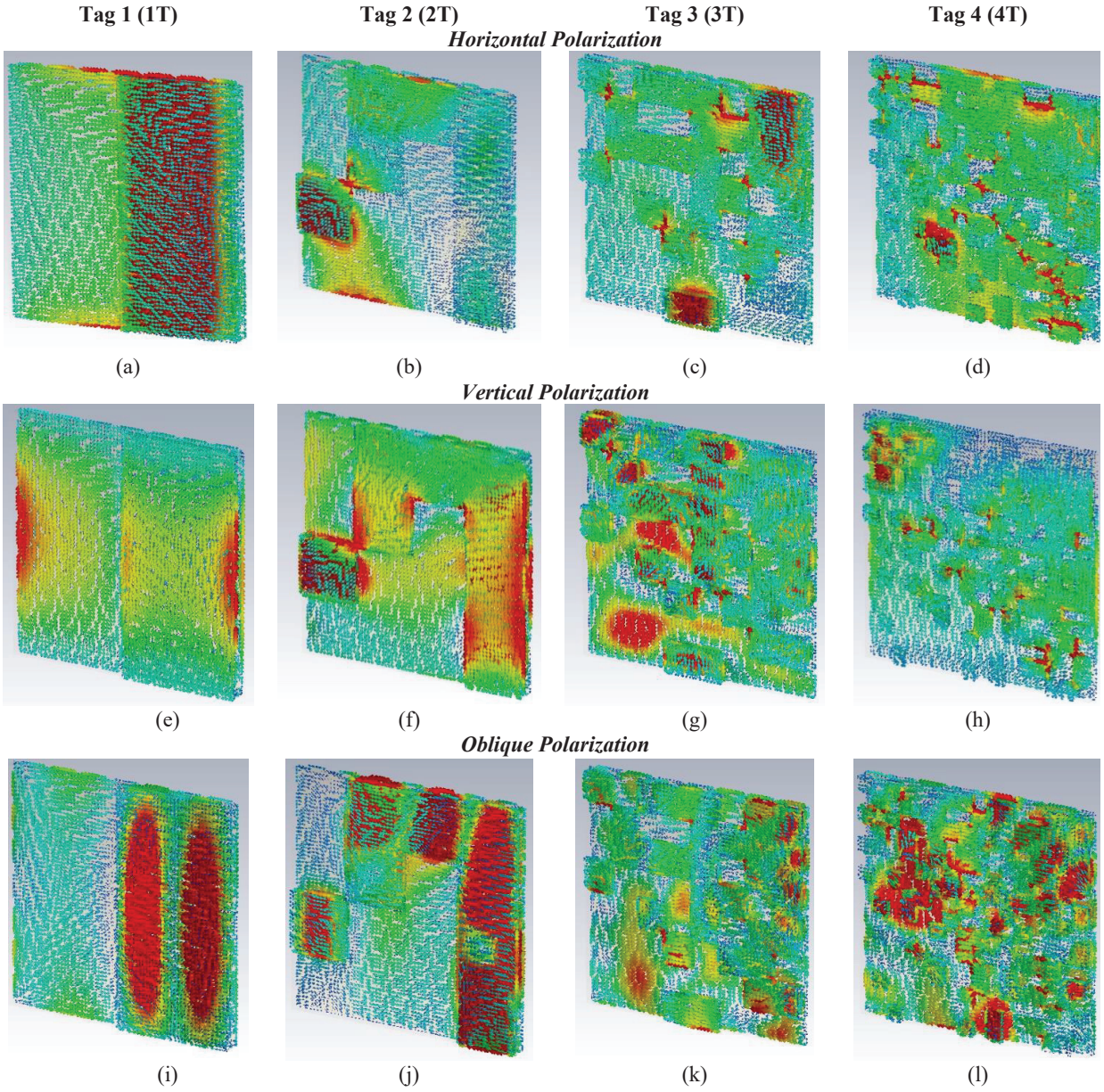

Fig. 4. Surface current distribution of realized chipless RFID tags (Tag 1, Tag 2, Tag 3, and Tag 4) of Fig. 2 with the plane wave illumination angle of $\alpha = 0^{\circ}$. (a) Horizontal polarization: 1T at $f = 4.25$ GHz, $J_{max} = 0.114$ A/m; (b) Horizontal polarization: 2T at $f = 8.16$ GHz, $J_{max} = 0.060$ A/m; (c) Horizontal polarization: 3T at $f = 8.25$ GHz, $J_{max} = 0.106$ A/m; (d) Horizontal polarization: 4T at $f = 8.16$ GHz, $J_{max} = 0.275$ A/m, (e) Vertical polarization: 1T at $f = 6.9$ GHz, $J_{max} = 0.038$ A/m; (f) Vertical polarization: 2T at $f = 7.85$ GHz, $J_{max} = 0.064$ A/m; (g) Vertical polarization: 3T at $f = 19.42$ GHz, $J_{max} = 0.042$ A/m; (h) Vertical polarization: 4T at $f = 6.23$ GHz, $J_{max} = 0.216$ A/m, (i) Oblique polarization: 1T at f=8.41 GHz, $J_{max} = 0.038$ A/m; (j) Oblique polarization: 2T at f=9.00 GHz, $J_{max} = 0.041$ A/m; (k) Oblique polarization: 3T at $f = 19.19$ GHz, $J_{max} = 0.030$ A/m; (l) Oblique polarization: 4T at f=18.78 GHz, $J_{max} = 0.041$ A/m.

fixed angle of incidence of the plane wave for all tags. Therefore, the significant changes in the resonance characteristics of the tag for each polarization increase the coding density of the tags.

B. RCS analysis

The RCS results of the four tags are analyzed for the three horizontal, vertical, and oblique polarizations for the fixed angle of the illuminating plane wave. Figure 5

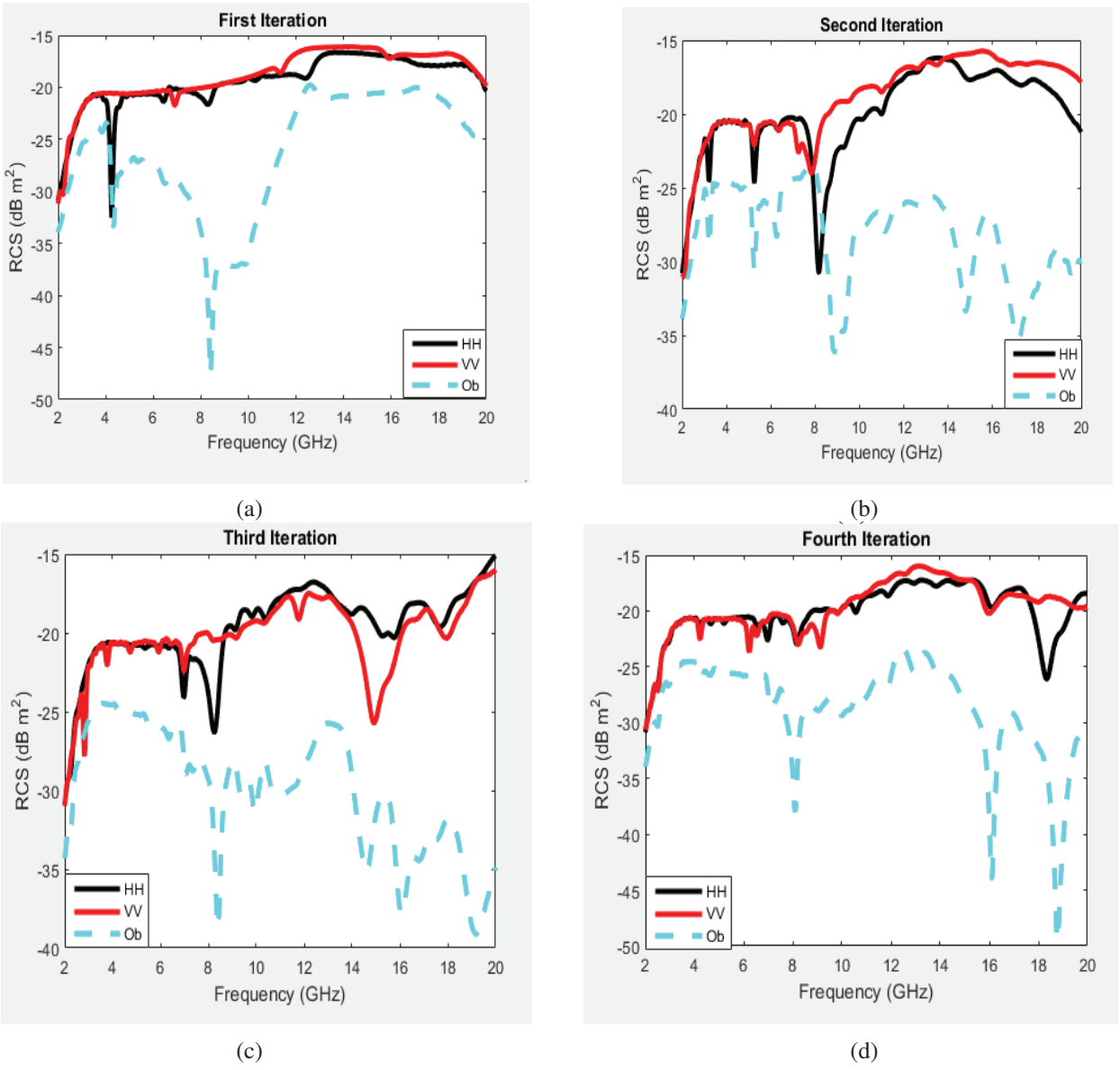

Fig. 5. RCS results of realized chipless RFID tags with the plane wave illumination angle of α=0^o: (a) 1T, (b) 2T, (c) 3T, and (d) 4T.

shows the obtained results of Tag 1, Tag 2, Tag 3, and Tag 4, respectively, in the three analyzed polarizations. The resonance frequencies of each tag can be observed from the dips in the respective waveform results horizontal (HH), vertical (VV), and oblique (Ob) polarizations. We observe that Tag 1 (1T) has resonance frequencies of 4.25 GHz, 6.43 GHz, 8.3 GHz, and 12.4 GHz in horizontal polarization; 6.90 GHz and 11.34 GHz in vertical polarization; and 4.34 GHz, 3.85 GHz, 6.48 GHz, and 8.41 GHz in oblique polarization, respectively. The difference in resonance characteristics in different polarizations is due to the change in the current distribution of the tags, as shown in Figs. 4 (a,e,i), respectively, for Tag 1. The performance of each tag is also analyzed in terms of the coding capacity (bits), coding spatial capacity (bits/cm^2), coding spectral capacity (bits/GHz), and coding density (bits/GHz x cm^2) of the tag.

For the fixed orientation case, the coding capacity is computed by adding all the resonant frequencies (dips in the analyzed RCS spectrum) for all polarizations (horizontal [HH] + vertical [VV] + oblique [Ob]) for the analyzed fixed orientation of the reader as shown in (1):

$$Coding\ Capacity_{fixed\ orientation} = \sum All\ resonance\ frequencies\ (HH+VV+Ob). \quad (1)$$

Table 2: Resonance frequency (in GHz) of characteristics of realized chipless RFID tags of Fig. 1 for fixed orientation of RFID reader

	Polarization		
Tag #	**HH**	**VV**	**Ob**
1	4.25, 6.43, 8.3, 12.4	6.90, 11.34	4.34, 3.85, 6.48, 8.41
2	3.21, 5.26, 6.32, 8.16, 11	5.26, 6.36, 7.24, 7.85	3.22, 5.26, 6.27, 9.00, 11.14, 14.80, 17.08
3	6.97, 8.25, 9.13, 9.83, 10.41, 15.27, 15.77, 17.71	2.83, 3.76, 4.74, 5.92, 6.99, 11.77, 19.42, 17.97	6.36, 7.10, 7.36, 8.41, 9.36, 9.94, 14.6, 16.08, 19.19
4	4.21, 4.64, 5.20, 6.55, 6.97, 7.96, 8.16, 10.57, 11.90, 16.09	4.23, 6.23, 6.54, 8.23, 9.13, 15.99	4.27, 7.11, 8.10, 9.06, 9.99, 10.84, 11.86, 12.91, 16.09, 18.78

Figure 5 (a) shows that for Tag 1, there are 4, 2, and 4 resonance frequencies in the HH, VV, and Ob polarizations, respectively, resulting in a coding capacity of 10 bits for the analyzed frequency range. The coding spatial capacity is computed by dividing the coding capacity by the tag area, as depicted in (2):

$$Coding\ Spatial\ Capacity = \frac{Coding\ Capacity}{Tag\ Area\ (cm^2)}\ . \quad (2)$$

The coding spatial capacity for Tag 1 comes out to be 0.997 bits/cm^2 (10/10.24). The division of coding capacity by the investigated frequency spectrum of dips (resonance frequencies) produces the coding spectral capacity (see (3)):

$$Coding\ Spectral\ Capacity = \frac{Coding\ Capacity}{GHz}\ , \quad (3)$$

$$Coding\ Density = \frac{Coding\ Capacity}{GHz \times Tag\ Area\ (cm^2)}\ . \quad (4)$$

The spectral range of resonance dips for Tag 1 is from 3.85 GHz to 12.4 GHz. Therefore, the coding spectral capacity becomes 1.170 bits/GHz (10/8.55). Lastly, with the help of (4), coding density can be calculated at 0.114 bits/GHz x cm^2 (10/8.55x10.24) for Tag 1.

The results of Tag 2 are depicted in Fig. 5 (b). The observed resonances for this case are 3.21 GHz, 5.26 GHz, 6.32 GHz, 8.16 GHz, and 11 GHz in horizontal polarization; 5.26 GHz, 6.36 GHz, 7.24 GHz, and 7.85 GHz in vertical polarization; and 3.22 GHz, 5.26 GHz, 6.27 GHz, 9.00 GHz, 11.14 GHz, 14.80 GHz, and 17.08 GHz in oblique polarization, respectively. We notice that the change in the tag metallic geometry with the second iteration brings a notable change in the resonance properties of the tag. Also, it is observed that 2T has more unique resonance frequencies as compared to 1T, which increases its coding capacity to 16 bits as to the 10 bits of the 1T tag. Similar observations regarding the enhanced coding capacities of Tags 3 and 4 can be made from the increased number of resonances in their RCS results in Figs. 4 (c) and (d), respectively. Table 1 summarizes the resonance frequency of all four tags in Fig. 5.

The comparison of different characteristics of the realized tags in terms of coding capacity (bits), coding spatial capacity (bits/cm^2), coding spectral capacity (bits/GHz), and coding density (bits/GHz x cm^2) is given in Table 1. We observe that Tag 3 exhibits a coding capacity of 25 bits in the resonance frequency range of 2.83-19.42 GHz. The resonance frequency range of the most complex shape Tag 4 is 4.21-18.78 GHz with the highest coding capacity of 26 bits. Tag 4 also has the highest values of coding spatial capacity (2.539 bits/cm^2), coding spectral capacity (1.784 bits/GHz), and coding density (0.174 bits/GHz x cm^2). These results infer that the increase in the number of iterations of the Hilbert curve filling algorithm makes the tag structure more irregular and thus increases its overall coding properties as compared to earlier iteration tags.

IV. ANALYSIS OF REALIZED TAGS WITH DIFFERENT READER ORIENTATION

The second case study is the investigation of the resonance and coding properties of the four realized tags in oblique polarization with the change in the horizontal angle (theta) of an incident plane wave in the range of 0-180° for two different cases in Table 1. At first (case 1), angles phi (φ) and alpha (α) are fixed at zero degrees (0°), and theta (θ) takes values from 0° to 180°. For case 2, φ and α take the values of 90° and 0° while θ is varied as before.

As with the results for the fixed orientation of the RFID reader in Section III, current distribution and RCS results are analyzed for the four investigated tags with the different outlined orientations of the incident plane wave in oblique polarization.

A. Surface current distribution analysis

The RFID reader orientation, like polarization, plays an important role. The current distribution results of the four realized tags for two selectively different orientations of the RFID reader (orientations of the incident plane wave) are depicted in Fig. 6.

Figures 6 (a) and (b) show the surface current distribution of Tag 1 for illuminating plane wave orientations $\varphi = 0°/\theta = 150°$ and $\varphi = 90°/\theta = 180°$, respectively. Figure 6 (a) shows the result at the resonance frequency of 12.96 GHz with a maximum current value of 0.031 A/m. The change of the incident plane wave elevation

Table 3: Comparison of different characteristics of the realized four iterations of Hilbert curve filling

Tag #	Iteration	Frequency Range (GHz)	Coding Capacity (bits)	Coding Spatial Capacity (bits/cm^2)	Coding Spectral Capacity (bits/GHz)	Coding Density (bits/GHz*cm^2)
1	1T	3.85-12.4	10	0.977	1.170	0.114
2	2T	3.21-17.08	16	1.563	1.154	0.113
3	3T	2.83-19.42	25	2.441	1.507	0.147
4	4T	4.21-18.78	26	2.539	1.784	0.174

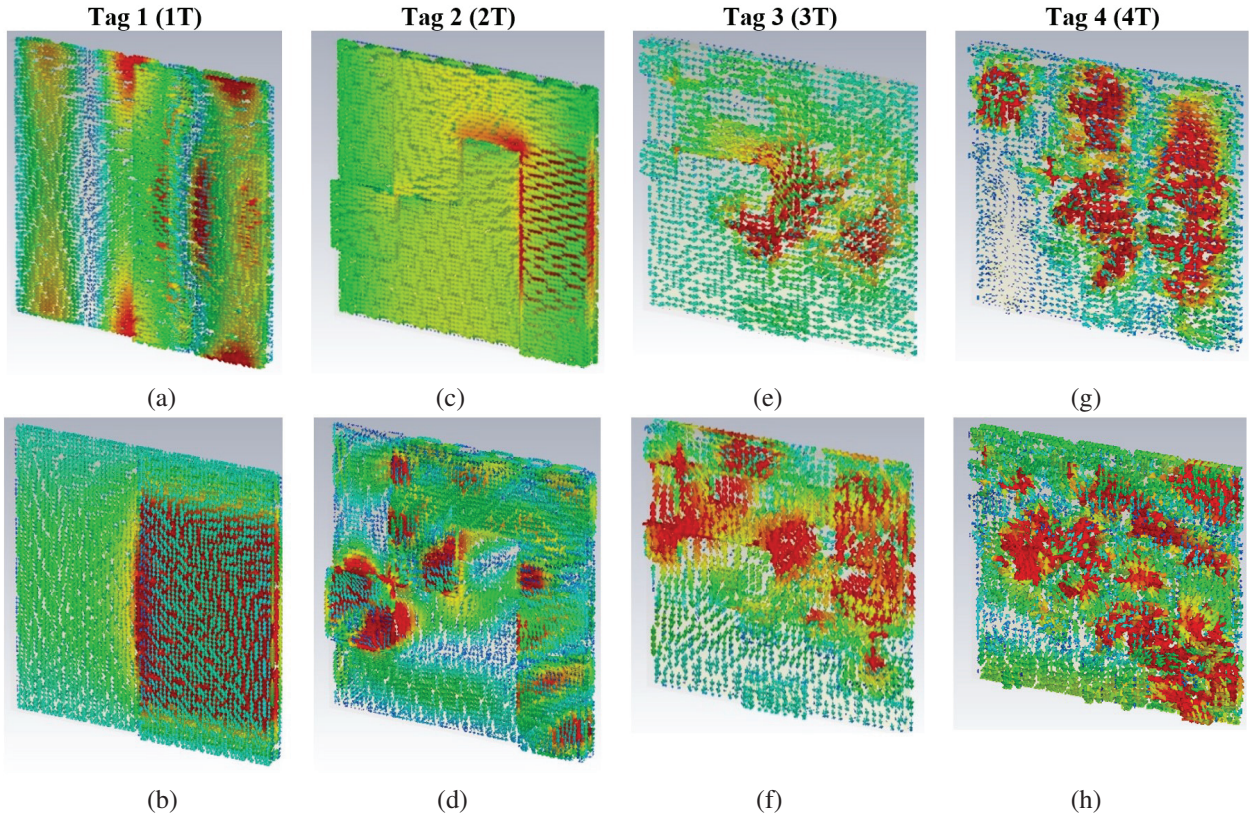

Fig. 6. The surface current distribution of four iterations of tags of Fig. 2 with the plane wave illumination angle of $\alpha = 0\circ$. (a) 1T at 12.96 GHz: $\varphi = 0\circ$ and $\theta = 150\circ$, J_{max} =0.031 A/m; (b) 1T at 2.13 GHz: $\varphi = 90\circ$ and $\theta = 180\circ$, J_{max} = 0.012 A/m; (c) 2T at 2.13 GHz: $\varphi = 0\circ$ and $\theta = 90\circ$, J_{max} = 0.032 A/m; (d) 2T at 13.41 GHz: $\varphi = 90\circ$ and $\theta = 180\circ$, J_{max} = 0.031 A/m; (e) 3T at 2.07 GHz: $\varphi = 0\circ$ and $\theta = 180\circ$, J_{max} = 0.026 A/m; (f) 3T at 3.75 GHz: $\varphi = 90\circ$ and $\theta = 140\circ$, J_{max} = 0.022 A/m; (g) 4T at 6.10 GHz: $\varphi = 0\circ$ and $\theta = 180\circ$, J_{max} =0.078 A/m; (h) 4T at 10.33 GHz: $\varphi = 90\circ$ and $\theta = 180\circ$, J_{max} =0.050 A/m.

angle to 90° and azimuth angle to 180° changes the resonance frequency of the tag to 2.13 GHz.

Figures 6 (c) and (d) represent the distributed current results of the 2T tag (Tag 2). Tag 2 exhibits the resonance frequency of 2.13 GHz for the plane wave having φ=0° and θ=90°, as depicted in Fig. 6 (c). It changes to 13.41 GHz when the reader is oriented to the positions of φ=90° and θ=180°, as shown in the changed pattern of the distributed current of Tag 2 in Fig. 6 (d). The comparison of the surface current distribution of the four tags in Figs. 6 (a-h) reveal significant variation with different orientations of the incident plane wave. Also, we can notice that the metallic shape of the tag impacts the induced current on the structure and thus produces a unique backscattered response for each tag, even for a fixed reader orientation.

B. RCS analysis

Figure 7 shows the RCS results of Tag 1 in oblique polarization for the two defined cases of elevation angles. The RCS results of the 1T tag for an incident plane wave with $\varphi = 0°$ and a change in azimuth angle from 0-180° with a step size of 10° are shown in Figs. 7 (a-c), respectively. The plane wave orientation of $\varphi = 0°$,

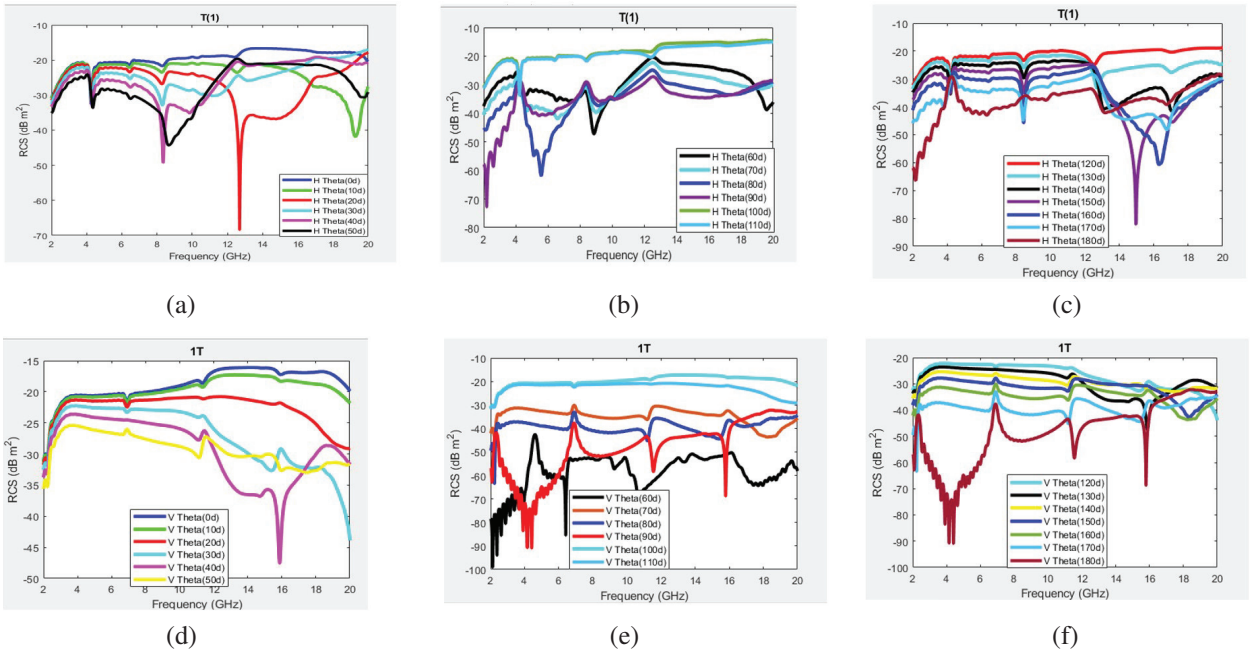

Fig. 7. RCS results of Tag 1 (1T) for oblique polarization with $\alpha = 0°$: (a) $\varphi = 0°$, θ = 0-50°; (b) $\varphi = 0°$, θ = 60-110°; (c) $\varphi = 0°$, θ = 110-180°; (d) $\varphi = 90°$, θ = 0-50°; (e) $\varphi = 90°$, θ = 60-110°; (f) $\varphi = 90°$, θ = 110-180°.

Table 4: Resonance frequency characteristics of Tag 1 (1T) for different angle of incidence of plane wave excitation in azimuth range for φ=90°

Theta	Resonance Frequencies (GHz)	# of Resonance Frequencies	Theta	Resonance Frequencies (GHz)	# of Resonance Frequencies
0°	4.25, 6.45, 8.30	3	100°	4.25, 6.43, 8.39	3
10°	4.27, 6.45, 8.26, 12.57, 19.26	5	110°	4.23, 6.41, 8.41, 12.42	4
20°	4.29, 6.45, 8.28, 12.69	4	120°	4.21, 6.41, 8.44, 12.51	4
30°	4.30, 6.46, 8.30	3	130°	4.21, 6.43, 8.44, 12.71, 17.03	5
40°	4.322, 6.5, 8.354	3	140°	4.20, 8.44, 13.11, 17.08	4
50°	4.34, 6.48, 8.66	3	150°	4.16, 8.44, 12.96, 17.12	4
60°	4.41, 8.86, 19.59	3	160°	4.12, 8.44, 16.31	4
70°	4.68, 6.59, 9.00	3	170°	3.40, 3.82, 8.43, 16.78	6
80°	5.11, 5.58, 9.18	3	180°	2.18, 2.58, 2.99, 6.30, 13.16, 16.76	4
90°	2.20, 2.61, 3.03	3			4

$\theta = 0°$ produces three significant resonance dips at 4.25 GHz, 6.45 GHz, and 8.30 GHz, respectively. The resonance frequencies change to 4.27 GHz, 6.45 GHz, 8.26 GHz, 12.57 GHz, and 19.26 GHz when θ is changed to 10°, as shown in Fig. 6 (a). Table 4 lists all significant resonances of Figs. 7 (a-c) waveforms for the complete sweep of azimuth angles with elevation angle (φ)=0°.

The heights of the resonances are recorded for the azimuth angles of 10° (5), 130° (5), and 180° (6). The metallic islands of the realized fractal tags are sensitive to the angle of incidence of the illuminating plane wave and thus show different resonance behavior even for a slight change in the orientation in the sweep range of the azimuth plane. The angular coding capacity for this case is computed using (5):

All resonance frequencies in oblique polarizations are added together for all different orientations of the reader (i.e. change in α, φ, θ). The coding spatial capacity, spectral capacity, and coding densities are calculated using (2)-(4). For this study, the focus is to demonstrate the proof-of-concept of the angular nature of the RFID reader on its detection performance. For the sake of simplicity, we assumed that angular encoding status was independent in this study. The coding capacity represent-

Table 5: Resonance frequency characteristics of Tag 1 (1T) for different angles of incidence of plane wave excitation in azimuth range for $\varphi = 90^\circ$

Theta	Resonance Frequencies (GHz)	# of Resonance Frequencies	Theta	Resonance Frequencies (GHz)	# of Resonance Frequencies
0°	6.90, 11.34, 15.91, 2.22	4	100°	6.90	2
10°	6.91, 11.36, 2.22	3	110°	6.91	1
20°	6.90, 2.22	2	120°	2.22, 6.90, 15.45	3
30°	2.22, 6.91, 15.41	3	130°	2.22, 11.13, 15.88	3
40°	2.22, 11.11, 15.88	3	140°	2.23, 11.16	2
50°	2.23, 11.14, 15.97	3	150°	2.23, 11.18, 18.36	3
60°	2.13, 2.38, 2.63, 2.88, 3.13, 3.40, 3.66, 3.93, 6.41, 9.25, 10.66, 13.39	12	160°	2.23, 11.20	2
70°	2.23, 11.20	2	170°	2.23, 2.58, 11.20, 15.43	4
80°	2.23, 2.58, 11.20, 15.43	4	180°	2.09, 2.56, 2.77, 3.01, 3.22, 3.46, 3.67, 3.91, 4.16, 4.41, 4.65, 4.86, 5.11, 11.56, 15.79	15
90°	2.09, 2.56, 2.77, 3.01, 3.22, 3.46, 3.67, 3.91, 4.16, 4.41, 4.65, 4.86, 11.56, 15.79	14			

ing the total number of resonance dips for this case is 70 bits, which produces the coding spatial capacity of 6.836 bits/cm^2.

$$\text{Coding Capacity}_{\text{ angular}} = \sum_{\theta=0^\circ}^{360^\circ} \sum_{\varphi=0^\circ}^{360^\circ} \sum_{\alpha=0^\circ}^{360^\circ} \text{All Resonance Frequencies (Oblique (Ob))}. \quad (5)$$

The RCS waveforms of the same tag in oblique polarization for the second case of zapping plane wave elevation angle, i.e., φ=90° are depicted in Figs. 7 (d-f). For the $\theta = 0^\circ$ orientation of the plane wave, the observed resonance frequencies are 6.90 GHz, 11.34 GHz, 15.91 GHz, and 2.22 GHz which are different when compared to the same case resonance of $\varphi = 0^\circ$. Similar observations can be made for the other cases of the azimuth angle by comparing the respective waveforms for each case in Fig. 7. The summary of the resonance frequencies for this case is given in Table 5. A larger number of resonances are obtained when the tag is excited with an incident plane wave with azimuth angles of 60° (12), 90° (14), and 180° (15). The total number of resonances for the complete azimuth sweep with $\varphi = 90^\circ$ is 85. The computed coding spatial capacity for this case is 8.301 bits/cm^2, which is higher than the first case, i.e., $\varphi = 0^\circ$.

Figure 8 illustrates the RCS waveforms of Tag 2 for the two analyzed cases of elevation angles. The first case results with $\varphi = 0^\circ$, and the change in θ is depicted in Figs. 8 (a-c). The observed resonance frequencies of the $\theta = 0^\circ$ waveform in Fig. 8 (a) are 3.21 GHz, 5.26 GHz, 6.32 GHz, 8.16 GHz, and 11 GHz. These frequencies change to 3.24 GHz, 5.29 GHz, 6.34 GHz, 8.36 GHz, and 11 GHz when the incident plane wave is oriented to $\varphi = 0^\circ$ and $\theta = 10^\circ$. Table 6 lists all resonance frequencies for Figs. 8 (a-c) waveforms. We can observe from Table 6 that the number and location of the resonance dip change with the variation in the incident plane wave orientations from $\theta = 0^\circ$ to $\theta = 180^\circ$ with a fixed $\varphi = 0^\circ$. The illuminating plane wave orientations of $\theta = 90^\circ$ and $\theta = 180^\circ$ produce maximum resonances of the metallic tag structures. The coding capacity for this first analyzed case of Tag 2 is 103 bits, which makes the coding spatial capacity 10.059 bits/cm^2.

Table 7 summarizes all observed resonance frequencies for Tag 2's second analyzed configuration i.e., φ=90° and sweeping of azimuth angle from 0° to 180°. Figures 8 (d-f) show the waveforms of the Table 6 results. The observed number of resonance frequencies when Tag 2 is illuminated with an incident plane wave of φ=90° and θ=0° is four (5.24 GHz, 6.36 GHz, 7.24 GHz, and 7.83 GHz). A total of nine resonance frequencies are noted for the case of θ=90°, θ=170°, and θ=180° for this case. The observed number of resonance frequencies for these three cases of θ=90°, θ=170°, and θ=180° is the highest in the complete sweep of azimuth angles. The coding capacity and coding spatial capacity for this second case of Tag 2 are 106 bits and 10.352 bits/cm^2, which are higher than case 1 of the same tag. It is noted that as the Tag 2 geometry is more irregular as compared to the Tag 1 geometry, a higher number of resonances and thus higher coding capacity are observed for Tag 2.

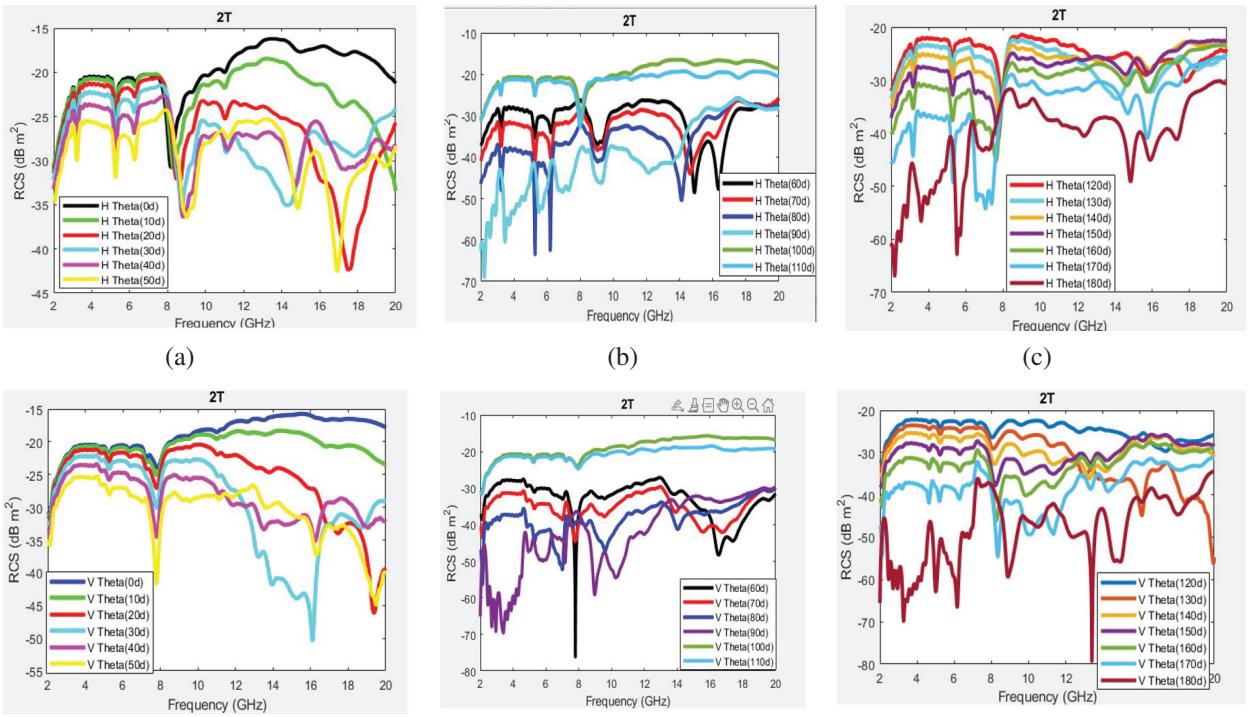

Fig. 8. RCS results of Tag 2 (2T) for oblique polarization with $\alpha = 0°$: (a) $\varphi = 0°$, θ = 0-50°; (b) $\varphi = 0°$, θ = 60-110°; (c) $\varphi = 0°$, θ = 110-180°; (d) $\varphi = 90°$, θ = 0-50°; (e) $\varphi = 90°$, θ = 60-110°; (f) $\varphi = 90°$, θ = 110-180°.

Table 6: Resonance frequency characteristics of Tag 2 for different angles of incidence of plane wave excitation in azimuth range for φ=0°

Theta	Resonance Frequencies (GHz)	# of Resonance Frequencies	Theta	Resonance Frequencies (GHz)	# of Resonance Frequencies
0°	3.21, 5.26, 6.32, 8.16, 11	5	100°	3.21, 5.26, 8.08	3
10°	3.24, 5.29, 6.34, 8.36, 11	5	110°	3.21, 5.26, 7.99	3
20°	3.22, 5.26, 6.28, 11.02, 17.52	5	120°	3.21, 5.26, 7.92, 15.68, 17.79	5
30°	3.22, 5.26, 6.27, 8.73, 11.09, 14.31	6	130°	3.21, 5.26, 7.87, 14.10, 15.93	5
40°	3.22, 5.26, 6.27, 8.80, 11.14, 14.74	6	140°	3.21, 5.28, 7.81, 14.49, 15.91	5
50°	3.22, 5.26, 6.27, 9.00, 11.16, 14.85, 16.92	7	150°	3.19, 5.29, 7.74, 14.60, 15.84	5
60°	3.22, 5.24, 6.25, 9.06, 14.89, 16.35	6	160°	3.17, 5.29,7.63, 14.65, 15.75	5
70°	3.22, 5.26, 6.23, 9.04, 14.64, 16.15	6	170°	3.17, 5.31, 6.57, 7.06, 7.38, 14.67, 15.73	7
80°	3.24, 5.28, 6.19, 9.07, 14.11	5	180°	2.18,2.50, 2.83, 3.60, 5.53, 12.35, 14.83, 15.90, 17.30	9
90°	2.22, 2.56, 2.88, 3.46,9.29	5			

Figures 9 and 10 show the RCS waveforms for both cases of elevation angle for Tags 3 and 4, respectively. The variations in the resonance characteristics of both tags could be noted by comparing the results of successive orientations. Tag 3 has six resonances at 6.97 GHz, 8.25 GHz, 9.13 GHz, 9.81 GHz, 10.39 GHz, and 15.28 GHz for $\varphi = 90°$ and $\theta = 0°$ incident plane wave orientation. While six dips at 6.55 GHz, 6.99 GHz, 8.17

Table 7: Resonance frequency characteristics of Tag 2 for different angles of incidence of plane wave excitation in azimuth range for φ=90°

Theta	Resonance Frequencies (GHz)	# of Resonance Frequencies	Theta	Resonance Frequencies (GHz)	# of Resonance Frequencies
0°	5.24, 6.36, 7.24, 7.83	4	100°	5.26, 7.22, 7.89	3
10°	5.26, 7.24, 7.81	3	110°	6.34, 7.22, 7.98	3
20°	5.26, 7.80, 17.46, 19.37	4	120°	5.24, 6.32, 8.03, 17.37	4
30°	5.26, 7.78, 13.20, 16.11, 18.74	5	130°	5.26, 6.34, 8.10, 12.98, 16.11,19.95	6
40°	5.28, 7.79, 13.52, 16.22	4	140°	4.65, 5.24, 6.32, 8.17,13.27, 14.20, 16.17	7
50°	5.28, 7.80, 13.59, 16.31, 19.48	5	150°	4.65, 5.24, 6.30, 8.21, 9.78, 11.32, 13.32	7
60°	5.29, 7.00, 7.80, 16.51, 17.41	5	160°	2.11, 4.65, 5.22, 6.28, 8.26, 9.85, 13.34, 14.29	8
70°	2.13, 5.29, 7.00, 7.78, 13.88, 15.57	6	170°	2.13, 4.65, 5.20, 6.28, 8.34, 10.14, 11.34, 13.34, 14.29	9
80°	2.13, 5.13, 7.00, 9.61, 14.04	5	180°	2.70, 2.95, 3.28, 5.01, 6.16, 8.89, 13.41,16.13, 18.07	9
90°	2.47, 2.70, 2.95, 3.40, 4.95, 7.17, 8.97, 10.26, 14.17	9			

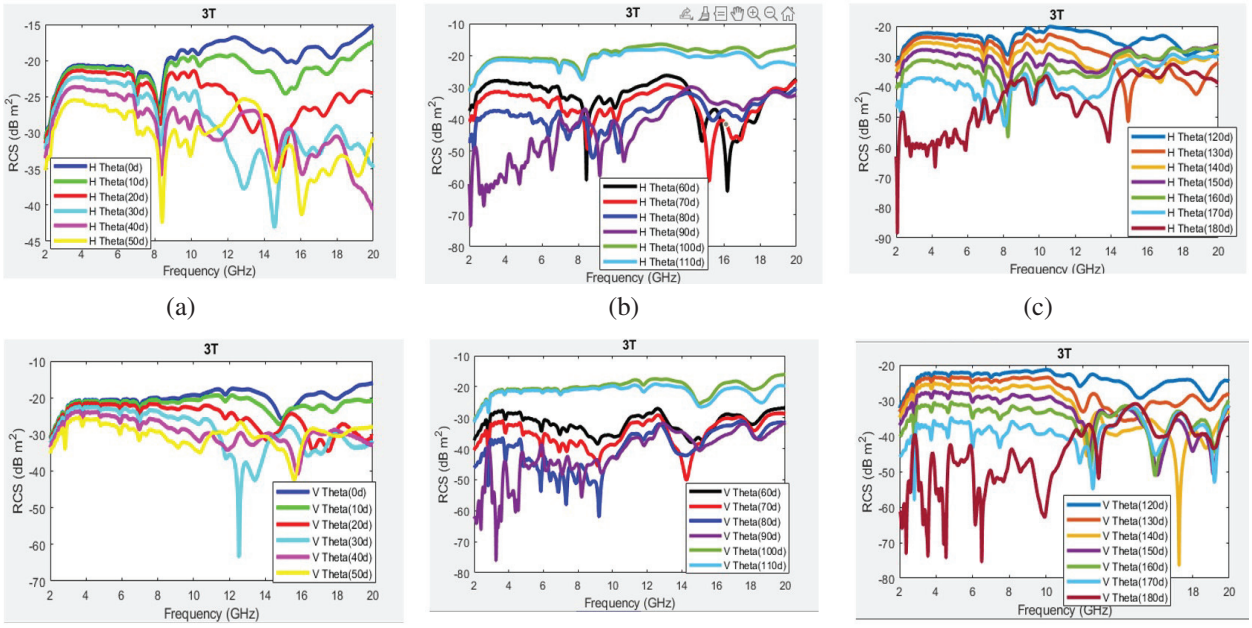

(a) (b) (c)

(d) (e) (f)

Fig. 9. RCS results of Tag 3 (3T) for oblique polarization with α=0°: (a) φ=0°, θ=0-50°; (b) φ=0°, θ=60-110°; (c) φ=0°, θ=110-180°; (d) φ=90°, θ=0-50°; (e) φ=90°, θ=60-110°; (f) φ=90°, θ=110-180°.

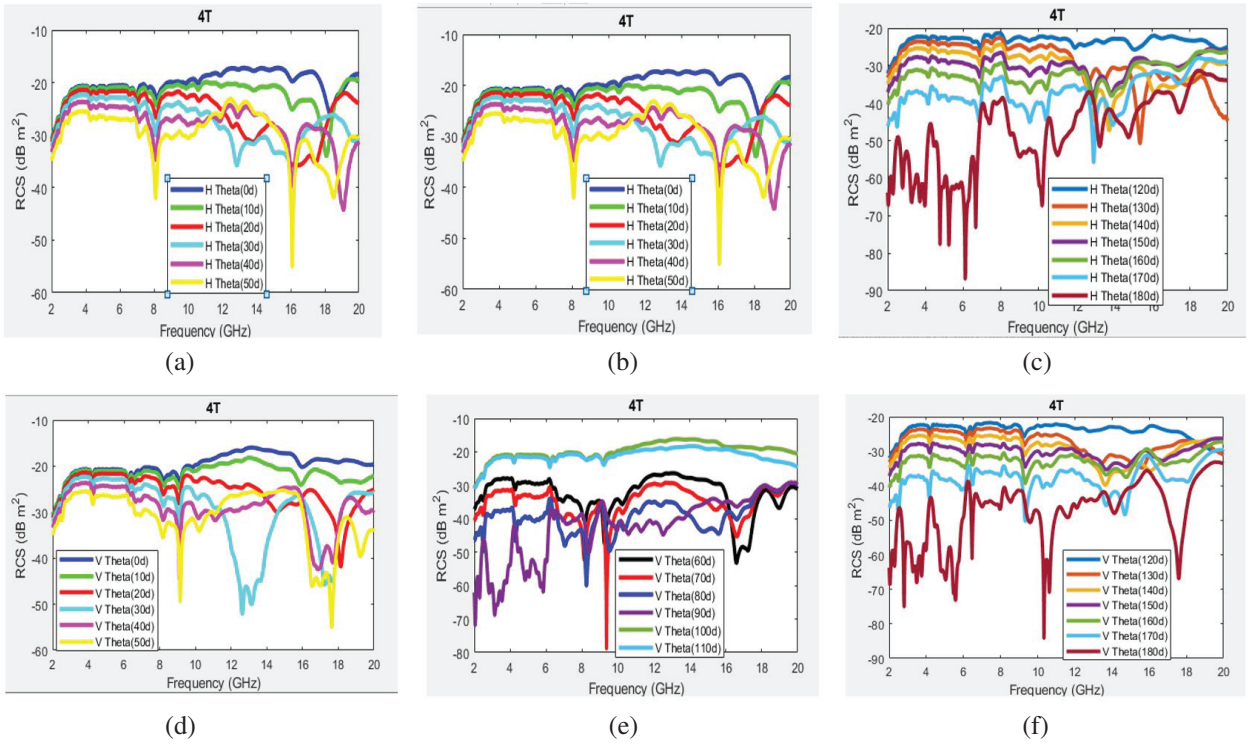

Fig. 10. RCS results of Tag 4 (4T) for oblique polarization with $\alpha = 0^\circ$: (a) $\varphi = 0^\circ, \theta = 0-50^\circ$; (b) $\varphi = 0^\circ, \theta = 60-110^\circ$; (c) $\varphi = 0^\circ$, $\theta = 110-180^\circ$; (d) $\varphi = 90^\circ, \theta = 0-50^\circ$; (e) $\varphi = 90^\circ, \theta = 60-110^\circ$; (f) $\varphi = 90^\circ, \theta = 110-180^\circ$.

Table 8: Comparison between the four realized chipless tags for two different cases of oblique polarization

# Tag	Frequency Range (GHz)	Coding Capacity (bits)	Coding Spatial Capacity (bits/cm^2)	Coding Spectral Capacity (bits/GHz)	Coding Density (bits/GHz x cm^2)
1-case 1	2.18-19.59	70	6.836	4.021	0.393
1-case 2	2.09-18.36	85	8.301	5.224	0.510
2-case 1	2.18-17.79	103	10.059	6.598	0.644
2-case 2	2.11-19.95	106	10.352	5.942	0.580
3-case 1	2.07-18.78	113	11.035	6.762	0.660
3-case 2	2.13-19.21	167	16.309	9.778	0.945
4-case 1	2.04-19.10	138	13.477	8.089	0.790
4-case 2	2.04-19.24	169	16.504	9.826	0.960

GHz, 10.55 GHz, 16.09 GHz, and 18.34 GHz in the RCS waveform of Tag 4 are observed for the same case as shown in Fig. 10 (a). As for Tag 2, the maximum number of resonances in RCS waveforms is noted for the zapping plane wave orientation of θ=180° for both configurations of elevation angle for both Tags 3 and 4, respectively. The tabular summaries of Figs. 9 and 10 results as in Tables 4–8 are not reported here for brevity. Table 8 presents the comparison of the performance of all analyzed tags for both cases of elevation angles (φ=0° for case 1 and φ=90° for case 2) in terms of their frequency range of the resonance spectrum, coding capacity (bits), coding spatial capacity (bits/cm^2), coding spectral capacity (bits/GHz), and coding density (bits/GHz x cm^2).

The coding capacities for Tags 3 and 4 are 113 bits and 167 bits and 138 bits and 169 bits for case 1 and case 2, respectively. It is observed that, as expected, the higher the irregularity in tag geometry, the higher the coding density. The highest coding capacity of 169 bits is noted for case 2 of Tag 4. The spectrum range of 2.04-19.24 GHz of Tag 4 is also wider as compared to less-fractal tags.

The observed coding spatial capacity for the second case of Tag 1 is 8.301 bits/cm^2, which changes to 10.352 bits/cm^2 for Tag 2, 16.309 bits/cm^2 for Tag 3, and

16.504 bits/cm^2 for Tag 4, respectively. A similar trend is observed for the increase in the fractal nature of the tag with increasing coding spectral capacity. The heights of the coding densities are observed for Tag 4, which are 0.790 bits/GHz x cm^2 and 0.960 bits/GHz x cm^2 for cases 1 and 2, respectively. The lowest levels of coding densities (0.393 bits/GHz x cm^2 and 0.510 bits/GHz x cm^2) are noted for Tag 1, owing to its simplified structure in the 1st iteration of the Hilbert curve filling algorithm. Due to its highly irregular tag geometry, Tag 4 performance is the best in terms of all compared parameters for all tags.

Table 8 results depict that the coding performance of the fractal (and even simple) tags can be comprehensively increased by incorporating the effect of reader orientation in the detection process. Lowering the step size of the azimuth sweep or adding more cases of elevation angle in the incident plane wave orientation will further enhance the coding capacity and coding density of the tag with the increased number of overall resonances in the analyzed spectral range.

The comparison of RCS results for realized fractal chipless RFID tags reveals that coding and detection performance is affected by reader orientation. The detection using different orientations of an RFID reader (different angles of incidence of the illuminating plane wave) further increases the security of the communication between the reader and the tag.

Although the fractal geometry of chipless RFID tags provides inherent advantages for secure communication, such tag responses are difficult to decode using a standard RFID reader. The detection of the tag based on the collected backscattered tag response with different orientations of the reader further increases the security of the communication as the backscattered RCS response is highly sensitive to slight variations in the reader orientation. The coding capacity and security performance of the realized tags could be further enhanced by incorporating the effect of the polarization factor into the analyzed RCS response of the tag along with the plane wave orientation factor without any change in the tag geometry.

V. CONCLUSION

The study has presented a comprehensive analysis of the impact of the RFID reader orientation (angle of incidence of an illuminating plane wave) on the sensing and detection capabilities of the realized fractal chipless RFID tags. The analysis is performed on four irregular chipless RFID tags developed based on the Hilbert curve filling algorithm for the two different elevation angles of an incident plane wave in oblique polarization. The analysis suggested that higher coding and detection performance of the tag in terms of coding capacity, coding spatial capacity, coding spectral capacity, and coding density is obtained when the aggregated backscattered RCS responses of the tag are analyzed in the azimuth range of 0° to 180° for two cases of elevation angles (0° and 90°). The detection based on the proposed aggregated analysis approach not only enhanced the coding and sensing performance of the tag but also made the communication highly secure. The proposed strategy could be used for the development of future highly secured RFID-based communication systems for smart cities, confidential documents, and Internet of Things (IoT) applications.

ACKNOWLEDGMENT

This project was funded by the Deanship of Scientific Research (DSR), King Abdulaziz University, under grant No. (21-135-35-HiCi). The authors, therefore, acknowledge the technical and financial support of KAU.

REFERENCES

[1] Q. H. Sultan and A. M. Sabaawi, "Design and implementation of improved fractal loop antennas for passive UHF RFID tags based on expanding the enclosed area," *Progress in Electromagnetics Research C*, vol. 111, pp. 135-145, 2021.

[2] M. Borgese, S. Genovesi, G. Manara, and F. Costa, "Radar cross section of chipless RFID tags and BER performance," *IEEE Transactions on Antennas and Propagation*, vol. 69, no. 5, pp. 2877-2886, 2021.

[3] H. Rmili, B. Oussama, J. Yousaf, B. Hakim, R. Mittra, T. Aguili, and S. Tedjini, "Robust detection for chipless RFID tags based on compact printable alphabets," *Sensors*, vol. 19, no. 21, p. 4785, 2019.

[4] C. Herrojo, M. Moras, F. Paredes, A. Nunez, E. Ramon, J. Mata-Contreras, and F. Martin, "Very low-cost 80-bit chipless-RFID tags inkjet printed on ordinary paper," *Technologies*, vol. 6, no. 2, 2018.

[5] K. Issa, Y. Alshoudokhi, M. Ashraf, M. Alshareef, H. Behairy, S. Alshebeili, and H. Fathallah, "A high-density L-shaped backscattering chipless tag for RFID bistatic systems," *International Journal of Antennas and Propagation* vol. 2018, p. 10, 2018.

[6] L. M. Arjomandi, G. Khadka, Z. Xiong, and N. C. Karmakar, "Document verification: A cloud-based computing pattern recognition approach to chipless RFID," *IEEE Access*, vol. 6, pp. 78007-78015, 2018.

[7] H. Rmili, D. Oueslati, L. Ladhar, and M. Sheikh, "Design of a chipless RFID tags based on natural fractal geometries for security applications," *Microwave and Optical Technology Letters*, vol. 58, no. 1, pp. 75-82, 2016.

[8] H. Huang and L. Su, "A compact dual-polarized chipless RFID tag by using nested concentric square loops," *IEEE Antennas and Wireless Propagation Letters*, vol. 16, pp. 1036-1039, 2017.

[9] M. Polivka, J. Havlicek, M. Svanda, and J. Machac, "Improvement in robustness and recognizability of RCS response of U-shaped strip-based chipless RFID tags," *IEEE Antennas and Wireless Propagation Letters*, vol. 15, pp. 2000-2003, 2016.

[10] O. Necibi, S. Beldi, and A. Gharsallah, "Design of a chipless RFID tag using cascaded and parallel spiral resonators at 30 GHz," in *2015 2nd World Symposium on Web Applications and Networking (WSWAN)*, pp. 1-5, 2015.

[11] J. Y. Mohammad, N. Zaqumi, M. Zarouan, M. A. Hussaini, and H. Rmili, "Passive fractal chipless RFID tags based on cellular automata for security applications," *Applied Computational Electromagnetics Society (ACES) Journal*, vol. 36, no. 5, pp. 559-567, May 2021.

[12] E. Motovilova and S. Y. Huang, "Hilbert curve-based metasurface to enhance sensitivity of radio frequency coils for 7-T MRI," *IEEE Transactions on Microwave Theory and Techniques*, vol. 67, no. 2, pp. 615-625, 2019.

[13] M. E. Mousa, H. H. Abdullah, and M. E. d. A. El-Soud, "Compact chipless RFID tag based on fractal antennas and multiple microstrip open stub resonators," in *2018 Progress in Electromagnetics Research Symposium (PIERS-Toyama)*, pp. 1332-1338, 2018.

[14] L. Wang, T. Liu, J. Sidén, and G. Wang, "Design of chipless RFID tag by using miniaturized open-loop resonators," *IEEE Transactions on Antennas and Propagation*, vol. 66, no. 2, pp. 618-626, 2018.

[15] M. Alibakhshi-Kenari, M. Naser-Moghadasi, R. A. Sadeghzadeh, B. S. Virdee, and E. Limiti, "Dual-band RFID tag antenna based on the Hilbert-curve fractal for HF and UHF applications," *IET Circuits, Devices & Systems*, vol. 10, no. 2, pp. 140-146, 2016.

[16] N. A. Murad, M. Esa, M. F. M. Yusoff, and S. H. A. Ali, "Hilbert curve fractal antenna for RFID application," in *2006 International RF and Microwave Conference*, pp. 182-186, 2006.

[17] J. McVay, A. Hoorfar, and N. Engheta, "Space-filling curve RFID tags," in *2006 IEEE Radio and Wireless Symposium*, pp. 199-202, 2006.

[18] L. Velho and J. D. M. Gomes, "Digital halftoning with space filling curves," *Proc. Of the 18th ann. Conf. on Computer Graphics and Interactive Techniques*, vol. 25, no. 4, pp. 81-90, 1991.

[19] Y. Watanabe and H. Igarashi, "Shape optimization of chipless RFID tags comprising fractal structures," *International Journal of Applied Electromagnetics and Mechanics,* vol. 52, no. 1-2, pp. 609-616, 2016.

Muntasir Sheikh received his B.Sc. from King Abdulaziz University, Saudi Arabia, in Electronics and Communications Engineering, M.Sc. in RF Communications Engineering from the University of Bradford, UK, and Ph.D. in Electromagnetics Engineering and Applications from the University of Arizona, USA. Since then, he has been teaching in the Electrical and Computer Engineering Dept. in KAU. His research interests are antenna theory and design, radar applications, and electromagnetic metamaterials.

3D Marine Controlled-Source Electromagnetic Numerical Simulation Considering Terrain and Static Effect

Chunying Gu[1], Suyi Li[1], Wanyue Zhang[1], and Silun Peng[2,*]

[1]College of Instrumentation and Electrical Engineering
Jilin University, Changchun 130061, China
cygu20@mails.jlu.edu.cn, lsy@jlu.edu.cn, wanyue22@mails.jlu.edu.cn

[2]College of Automotive Engineering
Jilin University, Changchun 130022, China
*pengsilun@jlu.edu.cn

Abstract **–** The marine controlled-source electromagnetic (CSEM) method is an important geophysical method for the exploration of marine hydrocarbon resources. In marine CSEM forward modeling the uplift terrain, such as submarine hills and seamounts, the static effects caused by polymetallic nodules and hydrothermal sulfide are ignored which can lead to the deviation of marine CSEM data. To improve the accuracy of data processing and interpretation, this study realizes efficient 3D numerical simulation considering submarine uplift terrain and static effect based on the finite difference (FD) algorithm in a fictitious wave domain. First, based on the correspondence principle between the fictitious wave domain and a real diffusive domain, we derive the FD electromagnetic field iteration equations of the fictitious wave domain, and apply the fictitious emission source and the boundary condition of complex frequency shifted-perfectly matched layer (CFS-PML). We use the inverse transformation method to convert the electromagnetic response to the diffusive domain. Then, we carry out simulations on typical 1D and 3D reservoir models to verify the correctness and effectiveness of the algorithm. Furthermore, we design an uplift terrain model and a static effect model and study the influence of parameters such as top width, bottom width, height and volume of uplift terrain on the CSEM field response characteristics through the forward modeling of multiple models and discuss the influence of parameters such as electrical conductivity, length, width, thickness, depth and volume of a shallow anomaly on the marine CSEM response. Finally, we analyze the characteristics and rules of electromagnetic field propagation of uplift terrain and static effect, which provides theoretical guidance for the design of marine CSEM exploration systems.

Index Terms **–** 3D numerical simulation, fictitious wave domain, marine controlled-source electromagnetic (CSEM), static effect, uplift terrain.

I. INTRODUCTION

The marine controlled-source electromagnetic (CSEM) is an important technology for deep-sea oil exploration, marine geological investigation and marine environment survey [1]. The marine CSEM method usually uses an antenna located tens of meters above the seabed to emit low-frequency electromagnetic signals, and a receiver located on the seabed continuously recording electromagnetic signals. By analyzing the collected electromagnetic signals, the resistivity distribution characteristics and electrical structure of the submarine medium can be inferred [1]. Marine CSEM technology can effectively identify high-resistivity oil reservoirs, reduce exploration risk and improve drilling success rate, which has been widely used in offshore oil exploration. After decades of vigorous development, it has achieved considerable success and economic benefits in instrument and equipment research and development, data processing and interpretation, and commercial exploration applications [2, 3]. Nowadays, the inversion interpretation of marine CSEM data is stepping into the 3D practical stage [4]. However, due to its complexity, 3D inversion technology is not mature yet, and the calculation accuracy and efficiency of the inversion algorithm needs to be improved. Moreover, 3D inversion studies considering seabed static effects are lacking [5]. 3D numerical simulation is the premise and theoretical basis of measured data inversion, and the accuracy and efficiency of inversion interpretation mainly depend on a numerical simulation algorithm. Therefore, it is of great theoretical significance and practical value to study the high-efficiency and high-precision 3D marine CSEM numerical simulation method.

With the improvement of computer performance, 3D numerical simulation technology has developed and advanced rapidly [6, 7]. Marine CSEM numerical simulation algorithms mainly include the integral equation (IE) method [8, 9], FD method [10, 11], finite volume

Submitted On: April 2, 2024
Accepted On: July 13, 2024

https://doi.org/10.13052/2024.ACES.J.390604

(FV) method [12, 13] and finite element (FE) method [14, 15]. The FD method is currently the more used algorithm in marine electromagnetic forward modeling and inversion because of the advantages of simple calculation, strong applicability, high computational efficiency and sufficient computational accuracy [16]. To improve the computational efficiency, in recent years scholars have proposed a numerical simulation method based on wave field transformation technology, which uses correspondence between the fictitious wave domain and the real diffusive domain to convert the governing equation of the electromagnetic field in the diffusive domain to the fictitious wave domain, and then calculate the electromagnetic response in the fictitious wave domain. Finally, the electromagnetic response in the diffusive domain is obtained through inverse transformation [17–19]. This transformation method makes the electromagnetic field fluctuate in the "fictitious wave domain" and slows down the propagation speed of the electromagnetic wave. Thus, it is easy to meet the stability conditions of the FD time-domain (FDTD) calculation, obtain a larger fictitious time step, and ensure that limited computing resources can be used to achieve efficient numerical calculation. Therefore, this method is widely used in the field of geophysical numerical simulation at present [20–22].

In marine CSEM exploration, the submarine hills and seamounts shaped by plate tectonics and seafloor spreading are usually uplifted, and the small polymetallic nodules and hydrothermal sulfides that may exist in the shallow part of the seafloor will produce static effect. If 3D numerical simulation ignores the effects of uplift terrain and static effect, it will cause large errors in data interpretation, which may further lead to the waste of data collection and an increase in exploration costs. For the forward modeling of submarine terrain, scholars have made some scientific achievements. Yutaka [23] uses the FD method to investigate the effect of 2D seafloor topography on 3D reservoir electromagnetic response and correct the topography by using the comparative method. Yang et al. [24] analyzes the influence of 2D submarine slope topography on the CSEM response of 3D high-resistivity reservoir based on the FV method. Yan and Han [25] realizes frequency-domain marine CSEM 3D forward modeling based on the FD method and discusses the influence of 2D mountain topography on electromagnetic response and the effect of topographic correction method. Yang et al. [26] uses the goal-oriented adaptive FE method to realize 3D marine CSEM modeling with anisotropy and topography. Therefore, it is important to study the impact of the topographic effect of 3D marine CSEM. For the forward modeling of static effect caused by small rocks and minerals on shallow surfaces, researchers have studied much in the numerical simulation of magnetotellurics and controlled-source audio-frequency magnetotellurics [27–31], but the 3D numerical simulation of marine CSEM considering static effect is very rare. In general, the complexity of the geological structure simulated by the FE method will increase, and the volume of calculations will also increase. A single inversion requires a large number of 3D simulations, and the FE method requires a large amount of memory, so calculation efficiency is limited and the calculation cost is greatly increased. The FD method can take into account calculation accuracy and efficiency. It is a practical method to simulate the 3D submarine uplift terrain and static effect.

In this paper, we carry out a numerical simulation study of the uplift terrain and static effect of 3D marine CSEM using the FD method in fictitious wave domain. We first derive the transformation formula between the governing equations in diffusive domain and the governing equations in fictitious wave domain, construct the Maxwell's equations in the fictitious wave domain, and introduce the fictitious emission source and the boundary condition of complex frequency shifted-perfectly matched layer (CFS-PML). We use the FD method to solve the CSEM response and the inverse transformation method to recover the electromagnetic response in the real diffusive domain, so as to realize the 3D marine CSEM numerical simulation based on the FD method in the fictitious wave domain. To verify the correctness and effectiveness of the algorithm, we then establish a three-dimensional model and a one-dimensional reservoir model, calculate the electromagnetic response of the above models, and compare with the analytic solutions in the frequency domain. Finally, through the electromagnetic response calculation of the 3D reservoir model of uplift terrain and static effect model, we analyze the influence characteristics of uplift terrain and static effect on electromagnetic response, which can provide reference for other scholars' subsequent research.

II. FICTITIOUS WAVE DOMAIN FD METHOD

To analyze and understand the influence characteristics of submarine terrain and static effect on marine CSEM propagation, and to achieve efficient and precise calculation of electromagnetic response of a complex reservoir model, this study proposes a 3D forward modeling method of submarine uplift terrain and a static effect based on the FD method in the fictitious wave domain. This method is mainly divided into three parts (as shown in Fig. 1). The first part is the construction of the governing equations in the fictitious wave domain, the second part is the solution of the electromagnetic response in the fictitious wave domain, including the discretization of the FD in the fictitious wave domain,

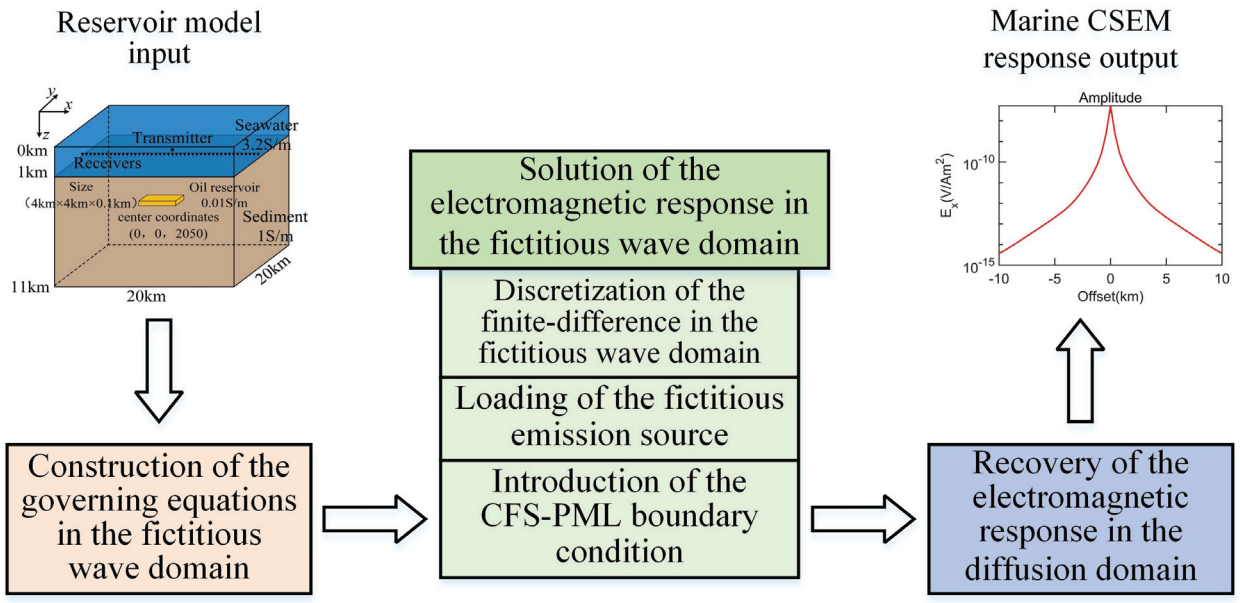

Fig. 1. Frame diagram of the FD method in the fictitious wave domain.

the application of the fictitious emission source and the CFS-PML boundary condition, and the third part is the recovery of the electromagnetic response in the diffusive domain. A frame diagram of the method is shown in Fig. 1.

A. Construction of the governing equations in the fictitious wave domain

We first design a submarine reservoir model according to the distribution characteristics of submarine topography and mineral resources. Next, we set the exploration simulation parameters, such as emission frequency and offset, according to the actual exploration situation. Finally, we transform the electromagnetic diffusive equations in the diffusive domain into electromagnetic wave equations in the fictitious wave domain through mathematical transformation. When the displacement current is neglected, the frequency domain expressions of quasi-static diffusive Maxwell's equations are:

$$-\nabla\times\mathbf{H}(\omega)+\sigma\mathbf{E}(\omega)=-\mathbf{J}(\omega), \tag{1}$$

$$\nabla\times\mathbf{E}(\omega)-i\omega\mu\mathbf{H}(\omega)=-\mathbf{K}(\omega), \tag{2}$$

where $\mathbf{E}$ and $\mathbf{H}$ are electric and magnetic vector fields, respectively. $\mathbf{J}$ is the electric current density. $\mathbf{K}$ is the magnetic current density. ω is the angular frequency in the diffusion domain. σ is the conductivity. μ is the magnetic permeability.

To transform Maxwell's equations in the diffusive domain into the fictitious wave domain, angular frequency ω' and dielectric permittivity ε' in the fictitious wave domain need to be defined as follows:

$$\omega'=(i+1)\sqrt{\omega\omega_0}, \tag{3}$$

$$\varepsilon'=\frac{\sigma}{2\omega_0}, \tag{4}$$

where $\omega_0=2\pi f_0$ is the scale parameter. The choice of ω_0 is in principle arbitrary, we use $f_0=1$ Hz.

By multiplying both sides of equation (1) by $\sqrt{-i\omega/2\omega_0}$ at the same time and substituting fictitious angular frequency and fictitious dielectric permittivity into equations (1) and (2), using the transformation relationship between fictitious wave domain and real diffusive domain, the frequency domain expressions of Maxwell's equations in fictitious wave domain can be obtained:

$$-\nabla\times\mathbf{H}'(\omega')-i\omega'\varepsilon'\mathbf{E}'(\omega')=-\mathbf{J}'(\omega'), \tag{5}$$

$$\nabla\times\mathbf{E}'(\omega')-i\omega'\mu\mathbf{H}'(\omega')=-\mathbf{K}'(\omega'), \tag{6}$$

where $\mathbf{E}'$ and $\mathbf{H}'$ are electric and magnetic vector fields in the fictitious wave domain. $\mathbf{J}'$ and $\mathbf{K}'$ are electric current and magnetic current densities in the fictitious wave domain.

Through the inverse Fourier transform, the time-domain expression of Maxwell's equations in the fictitious wave domain can be obtained:

$$-\nabla\times\mathbf{H}'(\mathbf{t}')+\varepsilon'\partial_{t'}\mathbf{E}'(\mathbf{t}')=-\mathbf{J}'(\mathbf{t}'), \tag{7}$$

$$\nabla\times\mathbf{E}'(\mathbf{t}')+\mu\partial_{t'}\mathbf{H}'(\mathbf{t}')=-\mathbf{K}'(\mathbf{t}'). \tag{8}$$

B. Solution of electromagnetic responses in the fictitious wave domain

The FDTD method is widely used in practical engineering. The form is simple and can simulate large

scale models numerically. Compared with the traditional FDTD method in the diffusive domain, the FDTD method in the fictitious wave domain is easier to meet the stability conditions of the iterative calculation, and a larger fictitious time step can be adopted to reduce the number of iterative and improve the computational efficiency [11]. In the specific solution, we introduce the fictitious emission source to avoid calculation of the initial electromagnetic field and the assumption of flat terrain in the diffusive domain. We apply CFS-PML absorption boundary conditions, which can efficiently absorb low frequency and late electromagnetic waves, reduce memory consumption, and further save computing time.

(a) Discretization of FD in the fictitious wave domain

After constructing the governing equations in the fictitious wave domain, it is necessary to solve the governing equations. Considering the accuracy and efficiency of the calculation, this study uses the FDTD method to solve Maxwell's equations. Yee grid [32] and the explicit Du Fort-Frankel method [33] are used to discretize the fictitious wave domain electric and magnetic fields in space and time, respectively, and the iterative formulas of 3D FD in the fictitious wave domain are obtained. Taking component E'_x as an example, the FD expression of the $n+1$ times iteration is given as:

$$E'^{n+1}_{x_{i+1/2,j,k}} = E'^{n}_{x_{i+1/2,j,k}} + \Delta t' \frac{2\omega_0}{\sigma} \left[\partial_y^- H'^{n+1/2}_{z_{i+1/2,j+1/2,k}} - \partial_z^- H'^{n+1/2}_{y_{i+1/2,j,k+1/2}} \right] - \Delta t' \frac{2\omega_0}{\sigma} J'_x, \tag{9}$$

where E' and H' are electric and magnetic fields responses in the fictitious wave domain. The electric current density in the fictitious wave domain is J'. The sampling time in the fictitious wave domain is $\Delta t'$. To ensure the stability of the iterative calculation of time-domain FD method, the time step $\Delta t'$ is required to satisfy Courant-Friedrichs-Lewy (CFL) condition:

$$\Delta t' \le \frac{1}{c_{\max}\sqrt{\frac{1}{\Delta x^2}+\frac{1}{\Delta y^2}+\frac{1}{\Delta z^2}}}, \tag{10}$$

where Δx, Δy and Δz are the cell grid dimensions. The maximum propagation speed of an electromagnetic wave in the fictitious wave domain is $c_{\max} = \sqrt{2\omega_0/\mu\sigma_{\min}}$.

(b) Application of the fictitious emission source

The selection of emission source signal in the virtual wave domain is flexible and not limited to a single function. However, in the selection process, it is necessary to ensure that the transmitted signal contains a large amount of spectrum, and the form should be easy to calculate. Therefore, in this study, the first derivative of Gaussian pulse is used as the fictitious emission source in the process of 3D numerical simulation. Adopting the above fictitious emission source can not only avoid the singularity of the source and the complex calculation of the initial electromagnetic field, but also break the assumption of flat terrain. The time-domain and frequency-domain expressions of the emission source are:

$$J(t) = -2\beta(t-t_0)\sqrt{\frac{\beta}{\pi}}e^{-\beta(t-t_0)^2}, \tag{11}$$

$$J(\omega) = i\omega e^{-\frac{\omega^2}{4\beta}} e^{-i\omega t_0}, \tag{12}$$

where $\beta = \pi f_{\max}^2$, $t_0 = \pi / f_{\max}$. The maximum frequency of the electromagnetic field transmission in the fictitious wave domain is $f_{\max}$. In the application of the emission source, the current direction in the fictitious wave domain is consistent with the inline direction in the real diffusive domain. The fictitious emission source is only related to the x and y components of the electric field, and the electric field component in the z-direction is zero.

(c) Introduction of the CFS-PML boundary condition

The CFS-PML absorbing boundary condition has a good absorption effect on electromagnetic wave propagation, which can greatly relieve the memory pressure on the computer and improve computational efficiency. Therefore, considering high efficiency computation, this paper introduces the CFS-PML boundary condition in the fictitious wave domain. Taking the electric field component E'_x as an example, its FD calculation expression in the fictitious wave domain is:

$$E'^{n+1}_{x_{i+1/2,j,k}} = E'^{n}_{x_{i+1/2,j,k}} + \Delta t' \frac{2\omega_0}{\sigma} \left[\partial_y^{-1} H'^{n+1/2}_{z_{i+1/2,j+1/2,k}} - \partial_z^{-1} H'^{n+1/2}_{y_{i+1/2,j,k+1/2}} \right] + \Delta t' \frac{2\omega_0}{\sigma} \left(\Psi^{n+1/2}_{e_{xy_{i+1/2,j,k}}} - \Psi^{n+1/2}_{e_{xz_{i+1/2,j,k}}} \right), \tag{13}$$

$$\Psi^{n+1/2}_{e_{xy_{i+1/2,j,k}}} = e^{-\left(\frac{\sigma_y}{k_y}+\alpha_y\right)\frac{\Delta t'}{\varepsilon'}} \Psi^{n-1/2}_{e_{xz_{i+1/2,j,k}}} + \frac{\sigma_y}{(\sigma_y k_y + k_y^2 \alpha_y)} \left(e^{-\left(\frac{\sigma_y}{k_y}+\alpha_y\right)\frac{\Delta t'}{\varepsilon'}} - 1 \right) \cdot \left(H'^{n+1/2}_{z_{i+1/2,j+1/2,k}} - H'^{n+1/2}_{y_{i+1/2,j-1/2,k}} \right) / \Delta_y, \tag{14}$$

$$\Psi^{n+1/2}_{e_{xz_{i+1/2,j,k}}} = e^{-\left(\frac{\sigma_z}{k_z}+\alpha_z\right)\frac{\Delta t'}{\varepsilon'}} \Psi^{n-1/2}_{e_{xz_{i+1/2,j,k}}} + \frac{\sigma_z}{(\sigma_z k_z + k_z^2 \alpha_z)} \left(e^{-\left(\frac{\sigma_z}{k_z}+\alpha_z\right)\frac{\Delta t'}{\varepsilon'}} - 1 \right) \cdot \left(H'^{n+1/2}_{y_{i+1/2,j+1/2,k}} - H'^{n+1/2}_{y_{i+1/2,j-1/2,k}} \right) / \Delta_z, \tag{15}$$

where $\Psi^{n+1/2}_{e_{xy_{i+1/2,j,k}}}$ and $\Psi^{n+1/2}_{e_{xz_{i+1/2,j,k}}}$ are two discrete variables. σ_i, k_i and $\alpha_i\,(i = x,y,z)$ are boundary parameters, which depend on the relative positions of the node and the target area, but are not fixed values:

$$\sigma_i = \sigma_{\max} \frac{|k-k_0|^m}{d^m}, i = x,y,z, \tag{16}$$

$$k_i = 1 + (k_{\max}-1)\frac{|k-k_0|^m}{d^m}, i = x,y,z, \tag{17}$$

$$\alpha_i = \alpha_{\max} \frac{|k-k_0|^m}{d^m}, i = x,y,z, \tag{18}$$

where $|k-k_0|$ is the distance from the calculation area to the absorption boundary. The polynomial parameter is m. The boundary layer thickness is d.

C. Recovery of electromagnetic response in the diffusive domain

After solving the time-domain electromagnetic response in the fictitious wave domain, it is transformed into the frequency-domain response result in the diffusive domain. The conversion relationship is as follows:

$$E_x(\omega)=\sqrt{\frac{-i\omega}{2\omega_0}}\int_0^T E_x'(t')e^{-\sqrt{\omega\omega_0}t'}e^{i\sqrt{\omega\omega_0}t'}dt', \quad (19)$$

$$J_x(\omega)=\int_0^T J'(t')e^{-\sqrt{\omega\omega_0}t'}e^{i\sqrt{\omega\omega_0}t'}dt', \quad (20)$$

where $T=n\Delta t'$ is the FD computation time in the fictitious wave domain. The sampling time in the fictitious wave domain is$\Delta t'$. The above electromagnetic response is excited by the emission source in the fictitious wave domain, not by the real emission source. To obtain the real electromagnetic response in the diffusive domain, it is necessary to construct Green's function or the impulse response function of the system according to different working devices. The marine CSEM emission source can be equivalent to a point source or a dipole source. The expression of its diffusive frequency domain Green's function is:

$$G_x(\omega)=\frac{E_x(\omega)}{J_x(\omega)}. \quad (21)$$

Through the derivation of Green's function formula in the full space diffusion frequency domain, we can see that Green's function has the following properties. Green's function in the diffusive domain becomes independent of the scale parameter$\omega_0$and the spectral width or maximum frequency that can be recovered in the diffusive domain is independent of the spectral width or maximum frequency in the fictitious wave domain [11].

We can use Green's function to recover the electromagnetic response in the real diffusive domain, obtain the marine CSEM response of the submarine reservoir model, and then analyze and understand the electromagnetic field propagation characteristics and rules of different models, so as to provide a theoretical basis for subsequent marine CSEM exploration under complex geological conditions.

III. ACCURACY VERIFICATION

A. 1D oil reservoir model

We chose a 1D oil reservoir model to verify the accuracy of our algorithm against the semi-analytical solutions given by Kong [34]. The first layer of the 1D model is a seawater layer with a thickness of 1 km and a conductivity of 3.2 S/m. The second layer is a seabed sedimentary layer with a thickness of 1 km and a conductivity of 1 S/m. The third layer is an oil layer with a thickness of 0.2 km and a conductivity of 0.01 S/m. The fourth layer is a downward extending sedimentary layer with a conductivity of 1 S/m. The size of the target area is 20×20×11 km. The transmitter and receivers are laid on the surface of the seabed. The 1D oil reservoir model adopts 100×100×100 m discrete grid. The simulation results of the FWD-FD method are compared with the semi-analytical solution, and the calculation results when the transmitting frequency is 0.1 Hz are shown in Fig. 2. It can be seen from Fig. 2 that the numerical solution of the electromagnetic field obtained by the FWD-FD method is basically consistent with the semi-analytical solution. When the offset is between 2 and 9 km, the amplitude relative error is less than 2.8%, which indicates that the proposed algorithm has high accuracy.

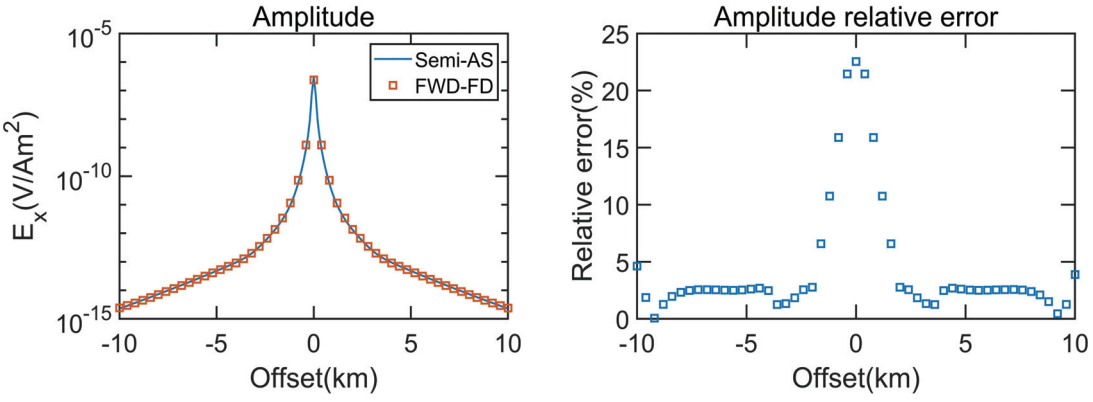

Fig. 2. Comparison of the electromagnetic response from this article with semi-analytical solution (semi-AS) for the 1D oil reservoir model: (a) amplitude curve and (b) relative error curve.

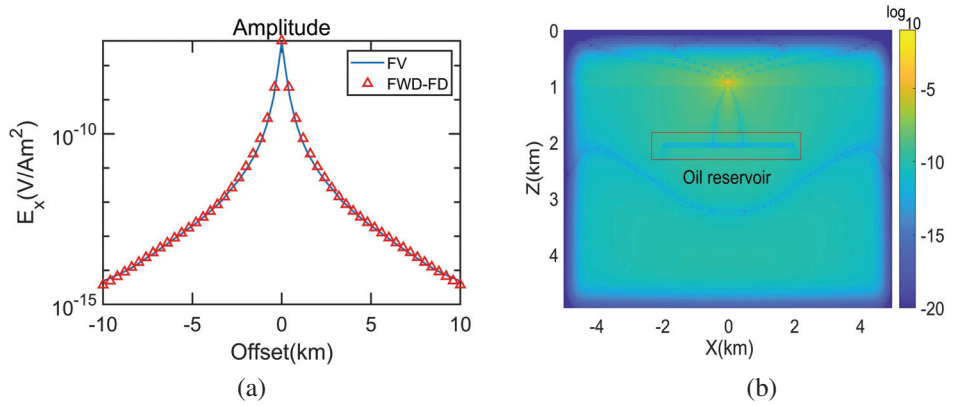

Fig. 3. (a) Comparison of the electromagnetic response of different algorithms for the 3D oil reservoir model and (b) snapshot of the induced current system in the fictitious wave field.

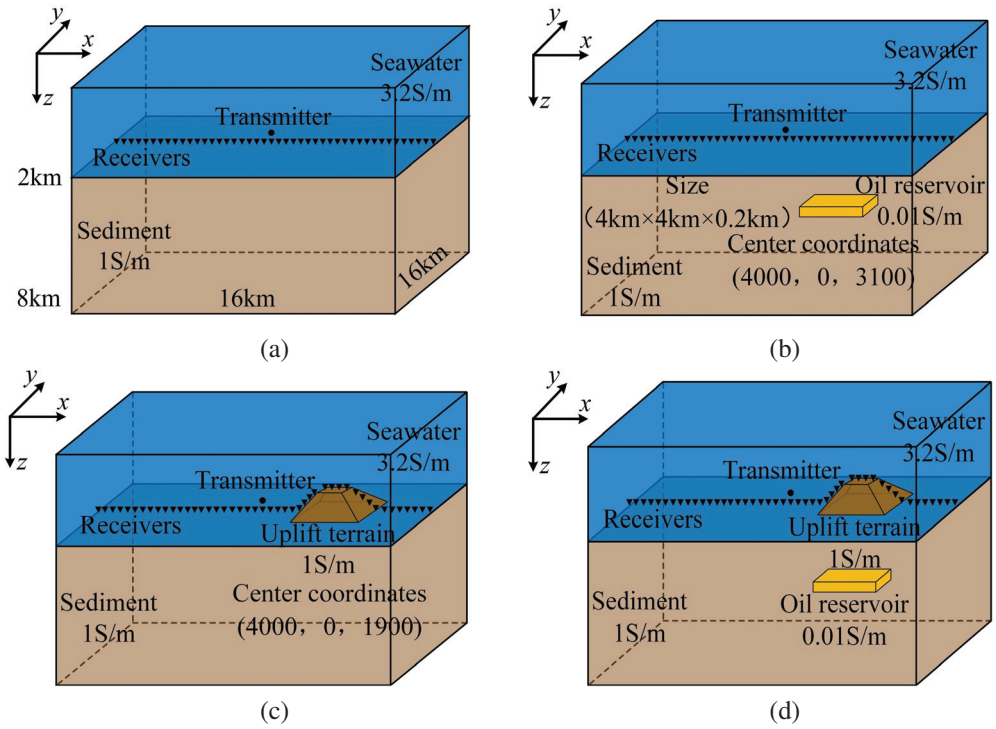

Fig. 4. 3D oil reservoir model under uplift terrain and comparison model: (a) flat terrain without oil reservoir model (M00), (b) flat terrain 3D oil reservoir model (M01), (c) uplift terrain without oil reservoir model (M02) and (d) uplift terrain 3D oil reservoir model (M03).

B. 3D oil reservoir model

A 3D oil reservoir model as shown in the upper left corner of Fig. 1 is constructed. The thickness of seawater layer is 1 km and the conductivity is 3.2 S/m. The conductivity of seabed sedimentary layer is 1 S/m. The oil and gas reservoir is located 1 km below the seabed, with a size of 4×4×0.1 km and a conductivity of 0.01 S/m. The size of the target area is 20×20×11 km. The transmitter is located directly above the oil and gas reservoir. The receiver is laid on the surface of the seabed. The 3D reservoir model adopts 100×100×100 m discrete grid. The numerical simulation results of the fictitious wave domain FD (FWD-FD) method and frequency domain FV method are compared. The amplitude curve of the electromagnetic response when the emission frequency is 0.1 Hz is shown in Fig. 3, and a snapshot of the induced current system in the fictitious wave domain is shown in Fig. 4. It can be seen from Fig. 3 that the calculation results of the above two algorithms are relatively consistent, which further verifies the

effectiveness of the calculation program of the FWD-FD method.

The number of grids for 3D simulation of the frequency domain FV method is 72×134×64, occupying 3.5 G memory. The maximum memory usage by the MUMPS direct solver for solving the coefficient matrix is 56.2 G, and the computation takes 48 min [35]. In this article, the number of grids for FD numerical simulation in the fictitious wave domain is 220×220×130, occupying 1.2 G memory. The number of iterations is 6000, the maximum memory usage during the computation is 2.1 G. The whole workflow of forward modelling mainly includes FWD-FD, time-frequency domain transformation of electromagnetic response and Green's function transformation, whose running time is 22 min, 4 min 12 s, 31 s, respectively, and the total execution time of the whole program is 27 min. The machine is configured as follows: CPU is Intel Core i5-7500 and main frequency is 3.4 GHz. Memory is 16 GB. It can be seen that the time domain difference method does not need to solve large linear equations, so it computes a much larger number of grids than the frequency domain FV method on a computer with the same memory. After solving the time domain electromagnetic response in the fictitious wave domain, all frequency domain electromagnetic responses less than $f_{\max}$ can be calculated quickly, and there is no need to simulate again. When the electromagnetic responses of multiple frequencies need to be calculated, the time domain FD method in the fictitious wave domain can save a lot of computation time, which proves the high efficiency of the proposed method.

IV. NUMERICAL EXPERIMENTS

In this section, uplift terrains with different parameters are studied first, followed by a static effect model under different conditions. Finally, a synthetic model including terrain and static effect is designed, and its responses are analyzed.

A. Uplift terrain model

To study the influence characteristics and laws of submarine uplift terrain on the marine CSEM response, we designed a 3D oil reservoir model containing uplift terrain and a comparison model (Fig. 4). In Fig. 4, M00 is a flat terrain without oil reservoir model, M01 is a flat terrain 3D oil reservoir model, M02 is an uplift terrain without oil reservoir model and M03 is an uplift terrain 3D oil reservoir model. We simulate the 3D marine CSEM response of the above model using the FD method in the fictitious wave domain, and calculate the relative influence of topography and the relative anomaly of oil reservoir. We first set the top width of the uplift terrain as 0.4 km, bottom width as 2 km, height as 0.2 km, center coordinate as (4000,0,1900), electrical conductivity as 1 S/m. There is a 3D oil reservoir directly below the uplift, the size of which is 4×4×0.2 km, the central coordinate is (4000,0,3100), and the conductivity is 0.01 S/m. The thickness of seawater layer is 2 km and the conductivity is 3.2 S/m. The conductivity of submarine sediment is 1 S/m. The size of the target area is 16×16×8 km, and the receiver is laid on the surface of the seabed along the uplift terrain.

The flat terrain without oil reservoir model, flat terrain 3D oil reservoir model, uplift terrain without oil reservoir model and uplift terrain 3D oil reservoir model adopt a 100×100×100 m discrete grid. The electromagnetic response calculation results of the four models at a frequency of 0.1 Hz, the relative effect of topography and the relative anomaly curves of oil reservoirs are shown in Fig. 5. It can be seen from the curves of M00 and M01 and their relative anomalies that the electromagnetic anomalies of oil reservoirs are obvious in the flat terrain 3D model. It can be observed from the curves of M00 and M02, M01 and M03 as well as the relative influence curves that the uplift terrain has a great influence on the electric field component. In addition, the M00 and M03 curves and their relative anomaly curves show

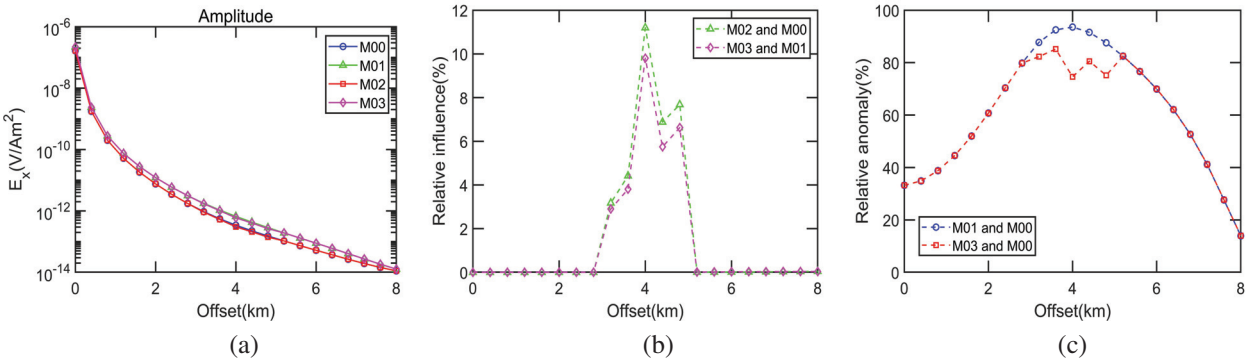

Fig. 5. Electromagnetic response of the uplift terrain model at a frequency of 0.1 Hz, the relative effect of topography and the relative anomaly curves of oil reservoirs: (a) electromagnetic response curve, (b) topography relative influence curve and (c) reservoir relative anomaly curve.

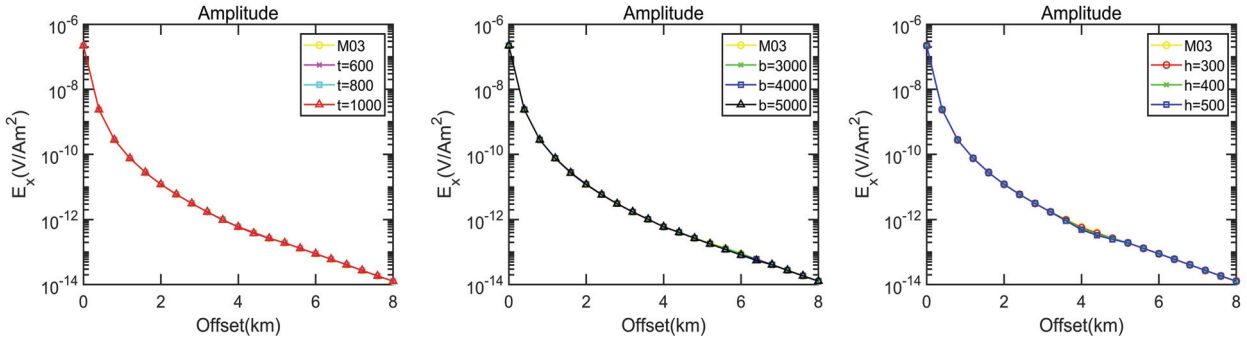

Fig. 6. Electromagnetic response curves of uplift terrain with different top widths, bottom widths and heights: (a) response curves with different top widths, (b) response curves with different bottom widths and (c) response curves with different heights.

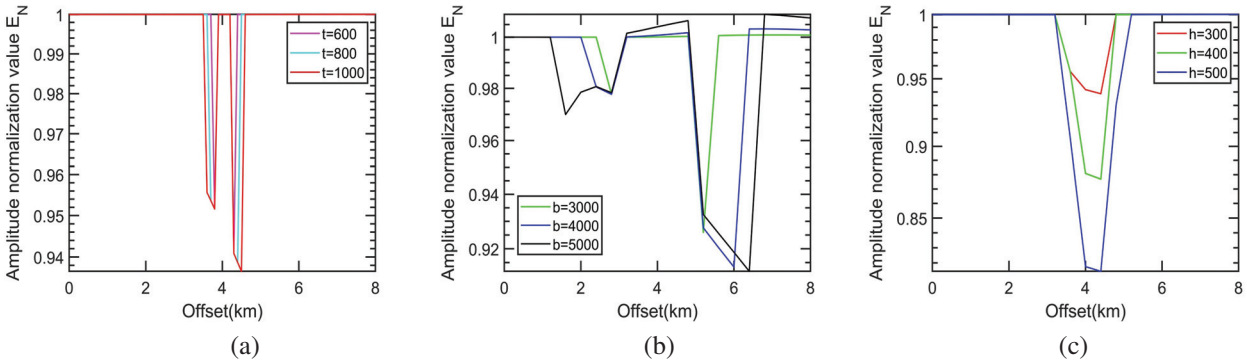

Fig. 7. Amplitude normalization curves of electromagnetic response for different top widths, bottom widths and heights of uplift terrain: (a) amplitude normalization curves for different top widths, (b) amplitude normalization curves for different bottom widths and (c) amplitude normalization curves for different heights.

that the uplift terrain will also weaken the electromagnetic anomalies generated by the reservoir. Therefore, when using the amplitude versus offset curve to qualitatively analyze potential oil reservoirs, it is necessary to consider the influence of uplift terrain on the CSEM response.

Let us now change the top width, bottom width and height of the uplift terrain, where the top width t is set to 600 m, 800 m and 1000 m, the bottom width b is set to 3000 m, 4000 m and 5000 m, and the height h is set to 300 m, 400 m and 500 m. The above models adopt 100×100×100 m discrete grid. The calculated electromagnetic responses at a frequency of 0.1 Hz are shown in Fig. 6, and the amplitude normalization values of the electromagnetic response curves and typical model electromagnetic response curves at different top widths, bottom widths and heights are shown in Fig. 7.

As can be seen from Fig. 6, the electromagnetic response curves of different top widths, bottom widths and heights are not distinct from those of typical terrain, indicating that the changes of top width, bottom width and height of uplift terrain have a weak influence on the electromagnetic response of the model. However, as can be seen from the amplitude normalization curve in Fig. 7, the uplift height has the greatest influence on the calculated results, followed by the bottom width and the top width. With the increase of height, bottom width and top width, the amplitude normalization values decrease gradually.

Finally, we change the volume of the uplift terrain, and set the top width, bottom width and height as (t, b, h) (400 m, 2000 m, 200 m), (600 m, 3000 m, 300 m), (800 m, 4000 m, 400 m) and (1000 m, 5000 m, 500 m). The grid size and scaling frequency adopted by the model are consistent with those in Fig. 5. The electromagnetic response calculation results when the frequency is 0.1 Hz are shown in Fig. 8 (a), and the amplitude normalization values of the electromagnetic response curves at different volumes of uplift terrain and typical terrain are shown in Fig. 8 (b).

As can be seen from Fig. 8 (a), there are differences between the electromagnetic response curves of uplift

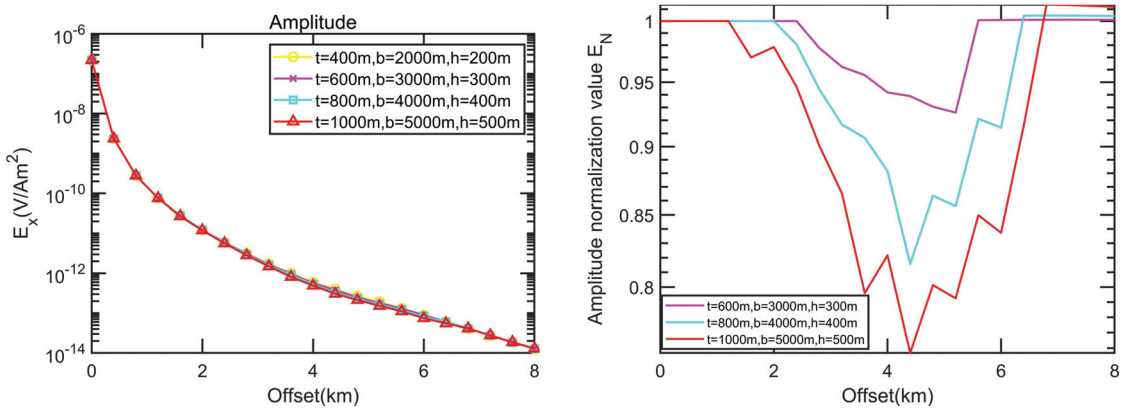

Fig. 8. Electromagnetic response curves and amplitude normalization curves of different volumes in the uplift terrain model: (a) electromagnetic response curves for different volumes of uplift terrain and (b) amplitude normalization curves of electromagnetic response for different volumes of uplift terrain.

terrain with different volumes and those of typical terrain, indicating that the change of uplift terrain volume has a strong influence on the electromagnetic response of the model. However, it can be seen from the amplitude normalization curves in Fig. 8 (b) that with the an increase of uplift terrain volume, the amplitude normalization values gradually decrease and, compared with the amplitude normalization curves of the electromagnetic response with different top width, bottom width and height in Fig. 7, the decrease trend of the amplitude normalization values are more significant, indicating that the volume change is more obvious than the single size change in the topographic effect.

B. Static effect model

To study the influence characteristics of static effects on the marine CSEM response, we designed a static effect model (M04) containing shallow anomalies (such as polymetallic nodules, hydrothermal sulfides) with deep oil reservoir (Fig. 9), where there is a shallow abnormal body B directly above the oil reservoir A. Reservoir A is 4×4×0.2 km in size, central coordinate is (4000,0,3100), and conductivity is 0.01 S/m. Abnormal body B is 0.5×0.5×0.1 km, and central coordinate is (4000,0,2050). The thickness of seawater layer is 2 km and conductivity is 3.2 S/m. The conductivity of sediments is 0.5 S/m. The size of the target area is 16×16×8 km, and the transmitter and receivers are arranged on the seabed surface.

We first set the conductivity of abnormal body B as 2 S/m, 0.2 S/m, 0.1 S/m, 0.02 S/m, 0.01 S/m, 0.008 S/m, 0.00625 S/m, 0.005 S/m and 0.002 S/m, respectively. The corresponding resistivity is 0.5Ω · m, 5Ω · m, 10Ω · m, 50Ω · m, 100Ω · m, 125Ω · m, 160Ω · m, 200Ω · m and 500Ω · m. The no abnormal body and oil reservoir

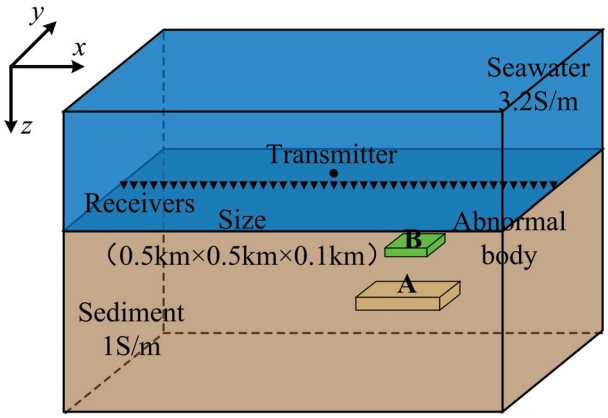

Fig. 9. Static effect model (M04).

model, reservoir model and abnormal body and reservoir model adopt 100 × 100 × 100 m discrete grid. The electromagnetic response calculated by the above model at a frequency of 0.1 Hz is shown in Fig. 10 .

As can be seen from Fig. 10, the curves of the 0.5Ω · m, 5Ω · m, 10Ω · m, 50Ω · m and 100Ω · m abnormal body and reservoir models nearly overlap with those of the reservoir models, indicating that the static effect of the above models is not obvious. However, the electromagnetic response calculation results of 125Ω · m, 160Ω · m, 200Ω · m and 500Ω · m models of abnormal body and reservoir show that when the resistivity of the abnormal body is larger than that of the oil reservoir, the amplitude of electromagnetic response curve decreases gradually with an increase of resistivity, and the deviation from the electromagnetic response curve of the reservoir model is larger. The static effect is more obvious.

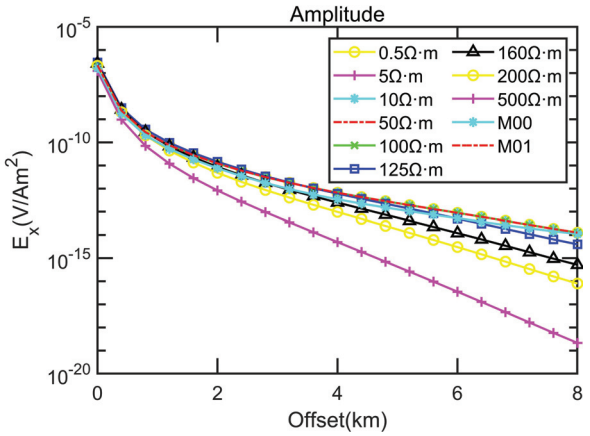

Fig. 10. Electromagnetic response curves of static effect model and comparison model at 0.1 Hz.

Next, we set the conductivity of abnormal body B as 0.005 S/m, that is, the resistivity is $200\Omega \cdot$ m. The center coordinates remain unchanged, and the length, width, thickness and depth of the abnormal body are changed, respectively. The length l of the abnormal body in the x direction is set as 1000 m, 1500 m, 2000 m, 2500 m and 3000 m . The width w of the abnormal body in the y direction is set as 1000 m, 1500 m, 2000 m, 2500 m and 3000 m . The thickness k of the abnormal body in the z direction is set to 200 m, 300 m, 400 m, 500 m and 600 m . The depth d is set to 100 m, 200 m, 300 m, 400 m and 500 m . The above models adopt $100 \times 100 \times 100$ m discrete grid. The electromagnetic response calculation results at an emission frequency of 0.1 Hz are shown in Fig. 11 (a). The amplitude normalization curves of the electromagnetic response curves for different lengths, widths, thicknesses and depths of the abnormal body B and the electromagnetic response curves for the original size of the abnormal body B are shown in Fig. 11 (b).

It can be seen from Fig. 11 (a) that the electromagnetic response curves of abnormal body B with different lengths, widths, thicknesses and depths almost overlap with those of abnormal body B with original dimensions, indicating that the changes of abnormal body length, width, thickness and depth have a very weak influence on the static effect of the model. In addition, it can be seen from the amplitude normalization curves in Fig. 11 (b) that the width of the abnormal body has the greatest influence on the calculated results, followed by the thickness of the abnormal body, the length of the abnormal body and the depth of the abnormal body. With the increase of width, thickness, length and depth, the amplitude normalization value increases gradually.

Finally, we assume that the conductivity and central coordinates of abnormal body B are constant, and only the volume of abnormal body is changed. The dimensions of abnormal body B along the x, y and z directions are set as (l, w, k) (500 m, 500 m, 100 m), (1000 m, 1000 m, 200 m), (1500 m, 1500 m, 300 m), (2000 m, 2000 m, 400 m), (2500 m, 2500 m, 500 m), (3000 m, 3000 m, 600 m) and (4000 m, 4000 m, 800 m). The grid size and scaling frequency adopted by the model are consistent with those in Fig. 10. The calculated electromagnetic response at the emission frequency of 0.1 Hz is shown in Fig. 12 (a), and the amplitude normalization curves of the electromagnetic response curves for different volumes of the abnormal body B and the electromagnetic response curves for the original volume of the abnormal body B are shown in Fig. 12 (b).

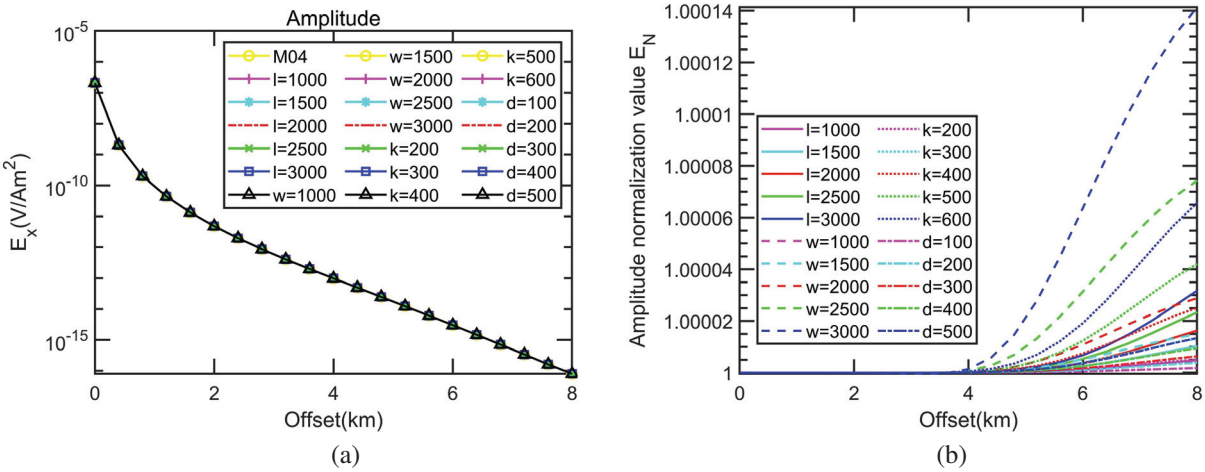

Fig. 11. Electromagnetic response curves and amplitude normalization curves of abnormal body B at different lengths, widths, thicknesses and depths in the static effect model: (a) electromagnetic response curves of abnormal body B at different lengths, widths, thicknesses and depths and (b) amplitude normalization curves of electromagnetic responses.

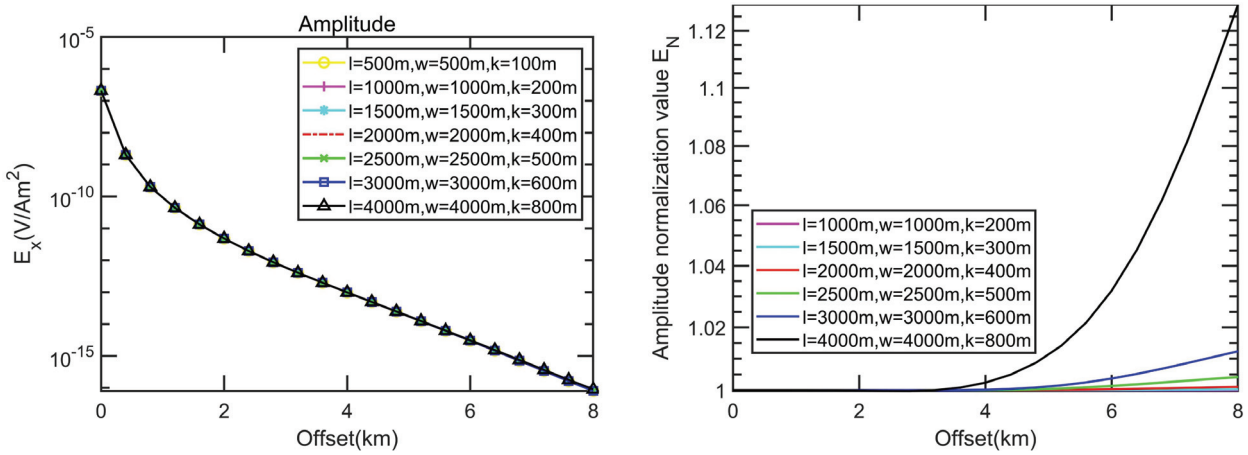

Fig. 12. Electromagnetic response curves and amplitude normalization curves of abnormal body B at different lengths, widths, thicknesses and depths in the static effect model: (a) electromagnetic response curves of abnormal body B at different volumes and (b) amplitude normalization curves of electromagnetic responses of abnormal body B with different volumes.

Figure 12 (a) shows that the electromagnetic response curves of abnormal body B with different volumes almost overlap with those of abnormal body B with original volumes, indicating that the change of abnormal body volume also has a weak influence on the static effect of the model. However, it is not difficult to find from the amplitude normalization curves in Fig. 12 (b) that with the increase of the volume of abnormal body B, the amplitude normalization value gradually increases and, compared with the amplitude normalization curves of electromagnetic responses at different lengths, widths, thicknesses and depths in Fig. 11 (b), the increase trend of the amplitude normalization value is stronger, indicating that the static effect caused by volume change is more obvious than that caused by single-direction extension.

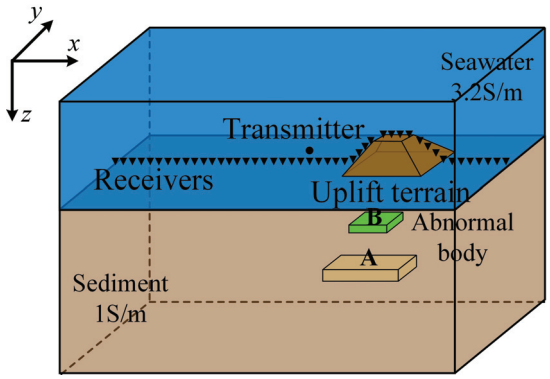

Fig. 13. Synthetic model of uplift terrain and static effect (M05).

C. Synthetic model of uplift terrain and static effect

To study the influence characteristics of terrain and static effects on the marine CSEM response, we designed a synthetic model (M05) including terrain and static effect (Fig. 13). The central coordinates and conductivity of the reservoir, terrain and abnormal body are the same as that shown in M03 and M04.

We changed the volume of the uplift terrain and set the volume parameters, mesh size and scaling frequency consistent with Fig. 8. The electromagnetic response at the emission frequency of 0.1 Hz and the amplitude normalization of the response curve for different volumes of the uplifted terrain and the electromagnetic response curve for the original volume of the uplifted terrain are shown in Fig. 14.

Then, we changed the volume of the abnormal body and set the volume parameters of abnormal body B, mesh size and scaling frequency consistent with Fig. 12. Electromagnetic response at the emission frequency of 0.1 Hz and amplitude normalization of the response curve for different volumes of abnormal body B and the electromagnetic response curve for the original volume of the abnormal body B are shown in Fig. 15. Finally, we changed both the volumes of uplifted terrain and the abnormal body and set the volume parameters of uplifted terrain and abnormal body B, mesh size and scaling frequency consistent with Figs. 8 and 12. The electromagnetic response at the emission frequency of 0.1 Hz and the amplitude normalization of the response curve for different volumes of the terrain and abnormal body B and the electromagnetic response curve for the original volume of the terrain and abnormal body B are shown in Fig. 16.

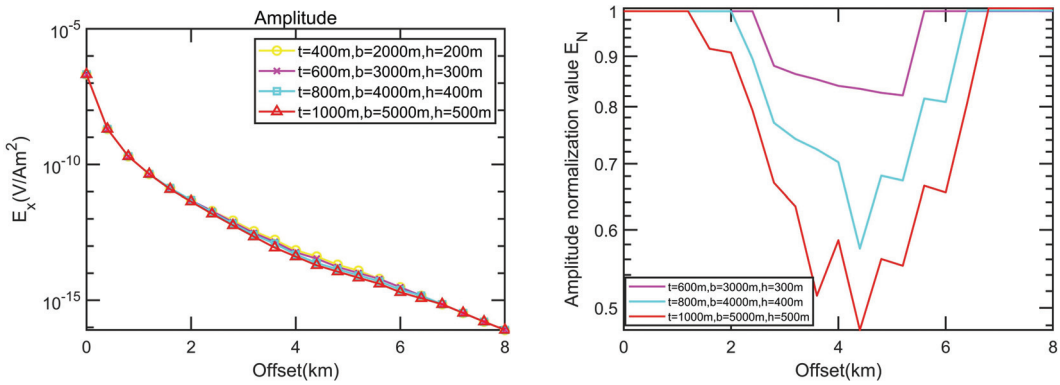

(a) (b)

Fig. 14. Electromagnetic response curves and amplitude normalization curves of different volume uplift terrain in the synthetic model: (a) electromagnetic response curves of uplift terrain at different volumes and (b) amplitude normalization curves of electromagnetic responses of uplift terrain with different volumes.

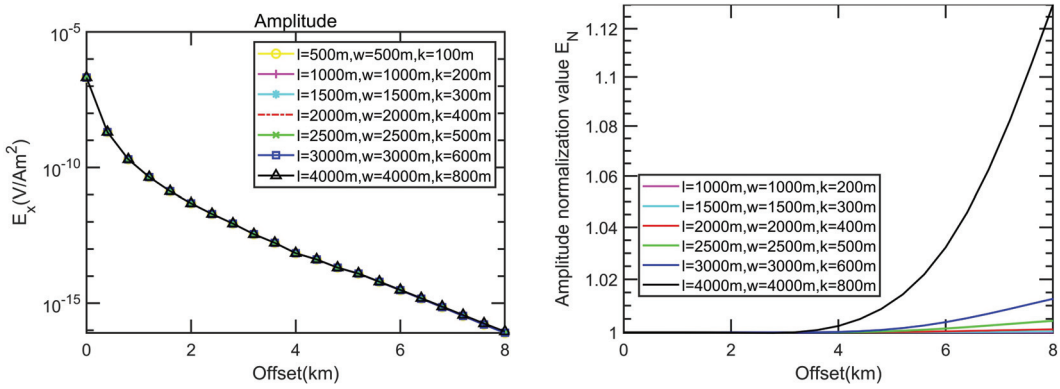

(a) (b)

Fig. 15. Electromagnetic response curves and amplitude normalization curves of different volume abnormal body in the synthetic model: (a) electromagnetic response curves of abnormal body at different volumes and (b) amplitude normalization curves of electromagnetic responses of abnormal body with different volumes.

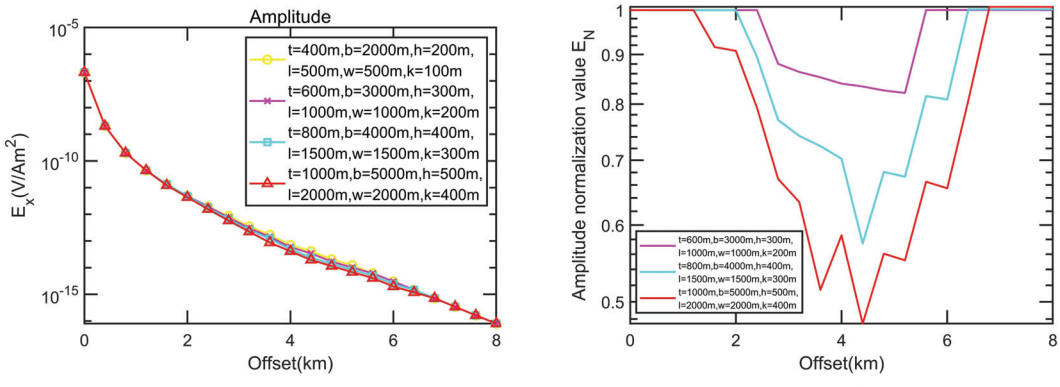

(a) (b)

Fig. 16. Electromagnetic response curves and amplitude normalization curves of the terrain and abnormal body at different volume in the synthetic model: (a) electromagnetic response curves of the terrain and abnormal body at different volumes and (b) amplitude normalization curves of electromagnetic responses of the terrain and abnormal body with different volumes.

It can be seen from Figs. 14 and 15 that the change of uplift terrain volume has a strong influence on the electromagnetic response of the synthetic model, and the amplitude normalization value gradually decreases with an increase of uplift terrain volume. The influence of the volume of abnormal body B on the static effect of the synthetic model is weak, but the amplitude normalization curve shows that the amplitude normalization value increases gradually with an increase of the volume of abnormal body B. The above results are similar to our previous conclusions. In addition, it can be seen from Fig. 16 that the influence of the simultaneous changes of terrain and abnormal body volume on the electromagnetic response of the synthetic model is equivalent to the superposition of the effects of the two changes separately.

V. CONCLUSION

In view of the uplift terrain such as submarine hills and seamounts shaped by plate tectonics and seafloor spreading and the static effect caused by polymetallic nodules and hydrothermal sulfide, this study adopts the FD method in fictitious wave domain to realize the 3D numerical simulation study of marine CSEM for the uplift terrain and static effect model. We compare the electromagnetic response of the whole-space model and the one-dimensional reservoir model with the analytical solution to verify the correctness and effectiveness of the algorithm.

We analyze and study the electromagnetic response through the forward simulation of the uplift terrain 3D reservoir model and the static effect model. The results show that the uplift terrain and the static effect produced by shallow abnormal body have different degrees of influence on the marine CSEM field. The uplift terrain distorts the electric field components and weakens the electromagnetic anomalies generated by oil reservoirs. In addition, compared with the top width, bottom width and height, the change of uplift terrain volume has a stronger influence on the electromagnetic response of the model. With an increase of the resistivity of the abnormal body, the influence of the static effect on the marine CSEM response increases gradually. Meanwhile, compared with length, width, thickness and depth, the static effect caused by a change of abnormal body volume is more obvious. Furthermore, results of the synthetic model corroborate the above conclusions, and the effect of the simultaneous change of terrain and abnormal body volume on the electromagnetic response of the synthetic model is equivalent to the superposition of the effect when the volume changes alone. Therefore, it is necessary to consider the effects of seafloor uplift terrain and static effects in marine CSEM exploration.

ACKNOWLEDGMENT

The authors would like to thank the anonymous reviewers and the editor for their valuable comments that greatly improved this article. This research was financially supported by the National Key Research and Development Program of China (Grant Number 2022YFC2807904).

REFERENCES

[1] S. Constable, "Ten years of marine CSEM for hydrocarbon exploration," *Geophysics*, vol. 75, no. 5, pp. 75A67-75A81, Oct. 2010.

[2] S. Constable, "Review paper: Instrumentation for marine magnetotelluric and controlled source electromagnetic sounding," *Geophys. Prospect.*, vol. 61 Suppl, pp. 505-532, Jan. 2013.

[3] J. Liu, T. Guo, B. Wang, and Z. Guo, "Review of marine electromagnetic methods for hydrocarbon exploration" [in Chinese], *Geophys. Prospect. Petro.*, vol. 60, no. 4, pp. 527-538, July 2021.

[4] E. Attias, K. Weitemeyer, S. Holz, S. Naif, T.A. Minshull, A.I. Best, A. Haroon, M. Jegen-Kulcsar, and C. Berndt, "High-resolution resistivity imaging of marine gas hydrate structures by combined inversion of CSEM towed and ocean-bottom receiver data," *Geophys. J. Int.*, vol. 214, no. 3, pp. 1701-1714, Sep. 2018.

[5] M. P. Miensopust, "Application of 3-D electromagnetic inversion in practice: Challenges, pitfalls and solution approaches," *Surv. Geophys.*, vol. 38, no. 5, pp. 869-933, Sep. 2017.

[6] Q. Wu, Y. Zhang, S. Guan, D. Li, and Y. Ji, "The 3D modeling of GATEM in fractured random media based on FDTD," *Appl. Comput. Electrom.*, vol. 36, no. 11, pp. 1401-1406, Nov. 2021.

[7] Y. Inoue and H. Asai, "Efficient electromagnetic simulation including thin structures by using multi-GPU HIE-FDTD method," *Appl. Comput. Electrom.*, vol. 33, no. 2, pp. 212-215, Feb. 2018.

[8] D. Yoon, M. S. Zhdanov, J. Mattsson, H. Z. Cai, and A. Gribenko, "A hybrid finite-difference and integral-equation method for modeling and inversion of marine controlled-source electromagnetic data," *Geophysics*, vol. 81, no. 5, pp. E323-E336, Oct. 2016.

[9] J. Tang, F. Zhou, Z. Ren, X. Xiao, L. Qiu, C. Chen, and H. Chen, "3-D forward modeling of the controlled-source electromagnetic problem based on the integral equation method with an unstructured grid," *Chin. J. Geophys.*, vol. 61, no. 4, pp. 1549-1552, Apr. 2018.

[10] R. Streich, "3D finite-difference frequency-domain modeling of controlled-source electromagnetic data: Direct solution and optimization for high

accuracy," *Geophysics*, vol. 74, no. 5, pp. F95-F105, Oct. 2009.

[11] R. Mittet, "High-order finite-difference simulations of marine CSEM surveys using a correspondence principle for wave and diffusion fields," *Geophysics*, vol. 75, no. 1, pp. F33-F50, Feb. 2010.

[12] H. Jahandari and C. G. Farquharson, "Finite-volume modelling of geophysical electromagnetic data on unstructured grids using potentials," *Geophys. J. Int.*, vol. 202, no. 3, pp. 1859-1876, July 2015.

[13] R. Peng, X. Hu, J. Li, and Y. Liu, "3D inversion of frequency-domain marine CSEM data in VTI media," *Chin. J. Geophys.*, vol. 62, no. 6, pp. 2165-2175, June 2019.

[14] V. Puzyrev, J. Koldan, J. de la Puente, G. Houzeaux, M. Vazquez, and J. M. Cela, "A parallel finite-element method for 3-D controlled-source electromagnetic forward modelling," *Geophys. J. Int.*, vol. 193, no. 2, pp. 678-693, May 2013.

[15] H. Chen, T. Li, B. Xiong, H. Wang, R. Zhang, and S. P. Li, "3D MCSEM modeling using an edge-based finite element method based on an unstructured grid and incremental model," *Chin. J. Geophys.*, vol. 61, no. 6, pp. 2560-2577, June 2018.

[16] R. U. Börner, "Numerical modelling in geo-electromagnetics: Advances and challenges," *Surv. Geophys.*, vol. 31, no. 2, pp. 225-245, Oct. 2009.

[17] K. H. Lee, G. Liu, and H. F. Morrison, "A new approach to modeling the electromagnetic response of conductive media," *Geophysics*, vol. 54, no. 9, pp. 1180-1192, Sep. 1989.

[18] A. T. de Hoop, "A general correspondence principle for time domain electromagnetic wave and diffusion fields," *Geophys. J. Int.*, vol. 127, no. 3, pp. 757-761, Dec. 1996.

[19] F. A. Maaø, "Fast finite-difference time-domain modeling for marine-subsurface electromagnetic problems," *Geophysics*, vol. 72, no. 2, pp. A19-A23, Feb. 2007.

[20] R. Mittet, "Seismic wave propagation concepts applied to the interpretation of marine controlled-source electromagnetics," *Geophysics*, vol. 80, no. 2, pp. E63-E81, Feb. 2015.

[21] J. Lu and Y. G. Li, "3-D marine CSEM modeling in fictitious wave domain," *Chin. J. Geophys.*, vol. 62, no. 8, pp. 3189-3198, Aug. 2019.

[22] Y. Ji, X. Meng, and G. Ren, "Shallow water three-dimensional transient electromagnetic modelling by using fictitious wave field methods," *Appl. Comput. Electrom.*, vol. 35, no. 1, pp. 72-81, Jan. 2020.

[23] S. Yutaka, "Bathymetric effects and corrections in marine CSEM data," *Geophysics*, vol. 76, no. 3, pp. F139-F146, Apr. 2011.

[24] B. Yang, Y. Xu, Z. He, and W. B. Sun, "3D frequency-domain modeling of marine controlled source electromagnetic responses with topography using finite volume method," *Chin. J. Geophys.*, vol. 55, no. 4, pp. 1390-1399, Apr. 2012.

[25] B. Yan and B. Han, "Bathymetric analysis and corrections for 3-D marine controlled-source electromagnetic field" [in Chinese], *Comput. Tech. Geophys. Geochem Explor.*, vol. 39, no. 1, pp. 9-16, Jan. 2017.

[26] X. Yang, M. Yue, D. Hu, Y. Li, and X. Wu, "Goal-oriented 3-D time-domain marine CSEM modeling with anisotropy and topography," *IEEE Trans. Geosci. Remote Sens.*, vol. 60, no. 1, pp. 1-14, Jan. 2022.

[27] T. V. Carlos and X. B. Francis, "Principles of spatial surface electric field filtering in magnetotellurics: Electromagnetic array profiling (EMAP)," *Geophysics*, vol. 57, no. 4, pp. 603-622, Apr. 1992.

[28] J. Tang and J. He, *Controlled-Source Audio-Frequency Magnetotelluric Method and its Application*. China: Central South University Press, 2005.

[29] L. Xia, "Response characteristic analysis and recognition and correction of static effect of MT sounding," M.S. thesis, School of Geophysics and Information Technology, China University of Geosciences (Beijing), Beijing, China, June 2016.

[30] Y. Li and M. Kris, "Denoising multicomponent CSEM data with equivalent source processing techniques," *Geophysics*, vol. 78, no. 3, pp. E125-E135, Apr. 2013.

[31] Y.Q. Yang, "Research on magnetotelluric static effect suppression and its application based on wavelet threshold," M.S. thesis, Faculty of Land Resources Engineering, Kunming University of Science and Technology, Kunming, Yunnan, China, May 2021.

[32] Y. Kane, "Numerical solution of initial boundary value problems involving maxwell's equations in isotropic media," *IEEE Trans. Antennas Propag.*, vol. 14, no. 3, pp. 302-307, May 1966.

[33] E. C. Du Fort and S. P. Frankel, "Stability conditions in the numerical treatment of parabolic differential equations," *Math. Tables Aids Comput.*, vol. 7, no. 43, pp. 135-152, May 1953.

[34] F. Kong, *Electromagnetic Field Calculation and MATLAB Implementation of Layered Media*. China: Jiangsu Phoenix Science and Technology Press, 2016.

[35] B. Han, X. Hu, Y. Huang, R. Peng, J. Li, and J. Cai, "3-D frequency-domain CSEM modeling using a parallel direct solver," *Chin. J. Geophys.*, vol. 58, no. 8, pp. 2812-2826, Aug. 2015.

Chunying Gu (Graduate Student Member, IEEE) received the M.S. degree from the College of Mechanical and Vehicle Engineering, Hunan University, Changsha, China, in 2011. She is currently pursuing the Ph.D. degree in detection technology and automation from Jilin University, Changchun, China. Her research interests include 3D marine controlled-source electromagnetic (CSEM) modeling and data processing.

Suyi Li (Member, IEEE) received her M.Sc. and Ph.D. degrees both from Jilin University in 2002 and 2009, respectively. From 2008 to 2009, she studied at the University of Illinois at Urbana-Champaign as a joint Ph.D. Now she is a professor in Jilin University. Her main research interests include computer applications and digital signal processing.

Wanyue Zhang (Graduate Student Member, IEEE) received the B.S. degree from the College of Instrumentation and Electrical Engineering, Jilin University, Changchun, China, in 2022, where she is currently pursuing the M.S. degree. She is primarily engaged in marine controlled-source electromagnetic (CSEM) data processing.

Silun Peng received the Ph.D. degree from the College of Automotive Engineering, Jilin University, Changchun, China, in 2014. He is currently a deputy senior engineer with Jilin University. His research interests include, but are not limited to, computer applications, digital signal processing and hardware system design.

Ultra Miniaturization and Transparency Frequency Selective Surface for Dual Band ISM Shielding

Dongming Guo and Huaxin Zhu

School of Science
Jiangnan University, Wuxi 214122, China
1422737299@qq.com, zhuhuaxin1312@163.com

Abstract – This article presents an ultraminiaturized frequency selective surface (FSS) for shielding 2.4 GHz and 5.8 GHz (ISM) signals. The unit cell size is 0.056λ × 0.056λ (λ is the free space wavelength at the first resonant frequency). It has smaller cell size and good transparency compared to previous ISM band studies, and transparency at 54%. The proposed FSS design consists of a wall structure and a compound square loop with 2.4 GHz and 5.8 GHz resonance frequencies for ISM band coverage. This FSS structure was fabricated on float glass with a dielectric constant of 8 by a photolithographic process. The fabricated FSS structure has excellent angular stability and polarization stability, which is further verified by experimentation. An easy optimization method is proposed to tune the independent resonant frequencies by optimizing the geometries individually. This FSS is interpreted by filtering through surface induced currents and equivalent circuit models. A prototype of the proposed FSS is fabricated and measured. The simulation results are in good agreement with the measured results. The proposed FSS has polarization insensitivity and 80° angle stability and is suitable for solving the EMI problem in ISM band.

Index Terms – frequency selective surface (FSS), ISM shielding, polarization stability, transparency, ultraminiaturized.

I. INTRODUCTION

With the rapid development of wireless communications, many unauthorized radios populate daily life, especially in the industrial, scientific and medical radio (2.4 GHz and 5.8 GHz ISM) bands. Interference in these frequency bands reduces communication performance and can even affect human health [1–8]. How to minimize interference and even protect your security in a complex wireless network environment is a critical issue. To solve this problem, indoor surfaces are usually converted to frequency selective surfaces (FSS) [9–15].

FSS consist of two dimensional planar or curved periodic arrays printed on dielectric substrates that exhibit frequency selection characteristics. FSS can effectively control the transmission and reflection of electromagnetic waves in order to screen electromagnetic waves of different frequencies [16]. Meanwhile, the filtering characteristics of FSS are affected by different geometry structures, dielectric substrates, and cell sizes. Based on the above characteristics, FSS is widely used in electromagnetic shielding [17], high impedance surfaces [18], radomes [19], and so on.

In recent years, miniaturized bandstop FSS for 2.4 GHz and 5.8 GHz have been widely studied. For example, a novel narrowband FSS hindering 2.4 GHz is mentioned in [20], achieving a narrower bandwidth and stable polarization response at 2.45 GHz by reducing the distance between the bottom legs and improving the three-legged periodic geometry. Reference [21] investigates the filtering properties of different geometries at 5.8 GHz, comparing the geometries of square, octagonal and hexagonal loops, and obtains a more stable FSS structure. However, but the above two FSS structures can only be used in a single frequency band, which is not able to satisfy the demand for dual-band in daily life. Furthermore, [22] used a double-layer convolution technique to obtain an FSS structure for shielding the 2.4 GHz and 5.8 GHz ISM bands with a miniaturization of 0.24λ×0.24λ. However, the double-layer structure increases the complexity of production. A miniaturized dual-bandstop FSS realized using geometrical nesting is proposed in [23]. The FSS structure consists of two complex geometries for hindering ISM bands. However, the angular stability of this FSS is 45°, which has limitations for higher angle applications. None of the above FSS structures for shielding ISM signals have explored optical transparency. This is difficult to apply indoors, so an ultraminiaturized FSS with optical transparency is urgently needed.

In this paper, we design and fabricate a single layer, optically transparent FSS structure for shielding ISM bands. The proposed FSS has better miniaturization and good optical transparency compared to other studies, with FSS cell sizes up to 0.056λ×0.056λ and 54%

Submitted On: May 28, 2024
Accepted On: August 27, 2024

https://doi.org/10.13052/2024.ACES.J.390605

transparency. In addition, the FSS structure has excellent polarization stability and large incidence angle stability. We also analyzed the surface induced currents of the proposed FSS and deduced the equivalent circuit model of the FSS. Finally, the prototype of this FSS was fabricated and measured in the field, and favorable reflections are obtained in all the desired frequency bands. Simulation and measurement results agree quite well.

II. STRUCTURE DESIGN

This paper proposes FSS printed on float glass [24] with a thickness of 1.6 mm and a dielectric constant of 8. It consists of a wall structure and a complex square loop. First step starts by designing the wall structure and the complex square loop in separate cells. The wall structure is an evolution of the square loop, and increases the effective electrical size by convolution, and makes it resonate at the first frequency and achieves miniaturization. The complex square loop is a modification of the square loop in order to achieve higher frequency resonance by adding four 45° diagonal arms to the square loop as well as eight triangular structures to optimize the internal geometry to a frequency slightly above 5.8 GHz. Finally, the two geometries are combined in the same cell to shield the ISM (2.4 GHz and 5.8 GHz) signals.

In addition, due to the mutual effect generated by stacking and nesting of the two structures, the distance between the two structures needs to be controlled to minimize interference, where the overall metal length and the operating frequency are in a specific relationship. FSS structures for individually shielded 2.4 GHz and 5.8 GHz are shown in Figs. 1 (a) and (b). Both structures are designed on a 7×7 mm^2 cell. Figure 1 (c) shows the dual-bandstop characteristic FSS. Table 1 shows the parameters of the optimized FSS.

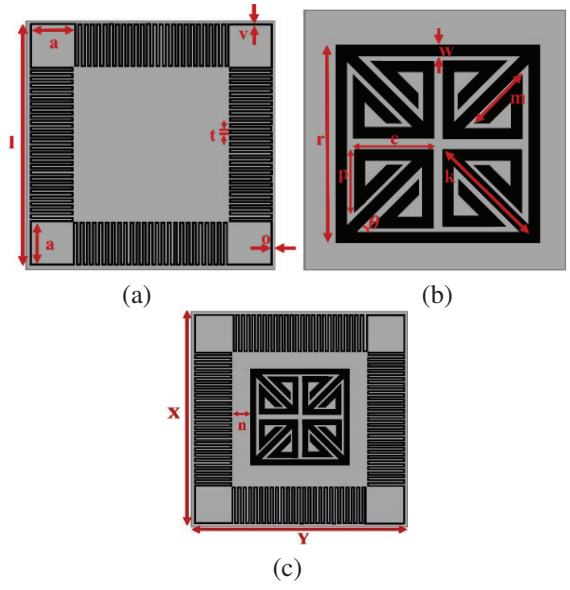

(a) (b)

(c)

Fig. 1. FSS geometries: (a) wall structure, (b) complex square loop, and (c) suggested dual-band FSS unit cell.

Table 1: The parameters of the optimized FSS

Parameter	**X**	**Y**	**n**	**l**	**a**
Value (mm)	7	7	0.1	6.92	1.44
Parameter	**v**	**t**	**o**	**r**	**w**
Value (mm)	0.04	0.12	0.04	3.8	0.2
Parameter	**p**	**e**	**k**	**m**	**θ**
Value (mm)	1.2	1.5	4.08	1.5	45°

Figure 2 shows the frequency response curves of the three structures and the frequency response curves of TE and TM polarized vertical incidence. From Fig. 2 (a), we can observe that the wall structure has bandstop characteristic at 2.3-2.6 GHz (−10 dB), which covers 2.4 GHz (WALN). The complex square loop has bandstop characteristic at 5.6-6 GHz (−10 dB), which covers 5.8 GHz (ISM). The proposed FSS has two transmission zeros at 2.4 GHz and 5.8 GHz with transmission coefficients up to −28.3 dB and one transmission pole at 3.16 GHz. This confirms that two different resonators can be individually optimized to achieve the desired filtering characteristics. From Fig. 2 (b), it is observed that the two curves of TE polarization and TM polarization overlap, showing that the 90° rotation-symmetric design provides a polarization-insensitive response.

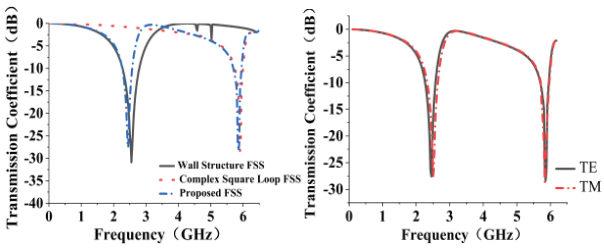

(a) (b)

Fig. 2. Simulated frequency response curve: (a) transmission coefficient for three structures and (b) TE and TM polarization for the proposed FSS.

III. SIMULATION ANALYSIS

A. Analysis of angular stability at different polarizations

It is particularly important for the FSS structure to work stably at different polarization and incidence angles, thus Fig. 3 shows TE and TM wave polarization at different angles. From Fig. 3, it can be seen that the proposed FSS can provide a stable response to different θ and φ angles under TE and TM polarization waves

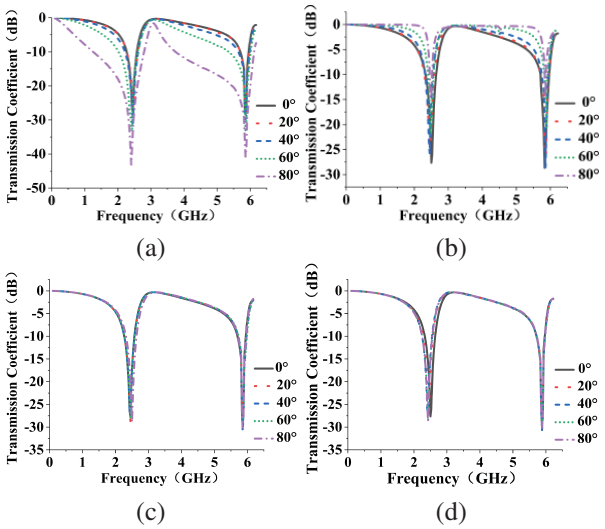

Fig. 3. Frequency curves for different polarizations and angles: (a) 0-80° θ angle TE polarization, (b) 0-80° θ angle TM polarization, (c) 0-80° φ angle TE polarization, and (d) 0-80° φ angle TM polarization.

without any significant change in transmission coefficients. The stability of the two polarizations is attributed to the compact periodic cell and symmetry of the periodic structure. Under TE polarization, the maximum frequency shift is 0.05 GHz (2%) at the first frequency and 0.01 GHz (0.17%) at the second frequency. Similarly, under TM polarization, the maximum frequency shift is 0.05 GHz (2%) at the first frequency and 0.049 GHz (0.8%) at the second frequency, which is due to the interactions that arise from the combination of two different structures. Interaction of the two different structures results in a weak shift of the resonance frequency.

In Figs. 3 (a) and (b), it can be seen that as the angle increases, the bandwidth of TE polarization increases and the bandwidth of TM polarization decreases. The wave impedance under TE polarization is $Z_{TE} = \frac{Z_0}{\cos\theta}$ and the angle change increases the wave impedance of TE polarization. Similarly, the wave impedance under TM polarization is $Z_{TM} = Z_0 \times \cos\theta$, and the angle change decreases the wave impedance of TM polarization [25]. Wave impedance is directly proportional to the quality factor, and the relationship between the quality factor and the bandwidth is shown in the equation (1), which is the reason for the above mentioned change in bandwidth.

$$Q = \frac{f}{BW}. \tag{1}$$

B. Analysis of current distribution and equivalent circuit

In order to have a deeper understanding of the working principle of FSS, the FSS current distribution as well as the equivalent circuit are further analyzed. Two transmission zeros at 2.4 GHz and 5.8 GHz are observed in Fig. 2 (b), and the vector current distribution at the two frequencies is shown in Fig. 4, where the colors and arrows denote the intensity and direction of the current, respectively. Figure 4 (a) shows the current distribution at frequency 2.4 GHz. The current flows in the walled structure and finally forms a closed loop, while there is little accumulation of current in the interior. Figure 4 (b) shows the current distribution at frequency 5.8 GHz. The current is mainly concentrated in the 45° diagonal arm as well as the square ring. It also proves that the two structures control the 2.4 GHz and 5.8 GHz ISM frequency bands, respectively. The equivalent circuit diagram of the FSS can be plotted from the current distribution graph and the complete equivalent circuit model is shown in Fig. 5.

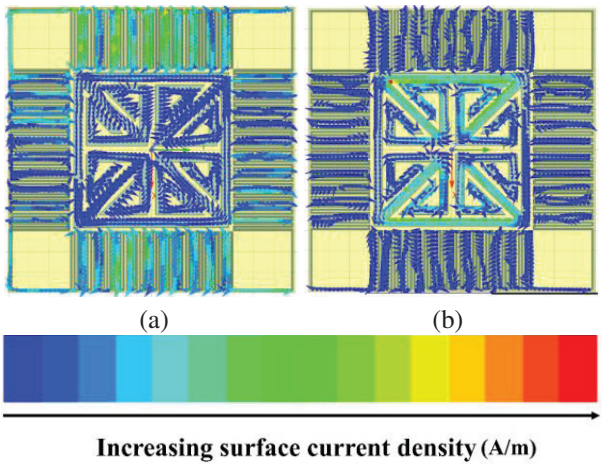

Fig. 4. FSS surface current distribution: (a) current distribution at frequency 2.4 GHz and (b) current distribution at frequency 5.8 GHz.

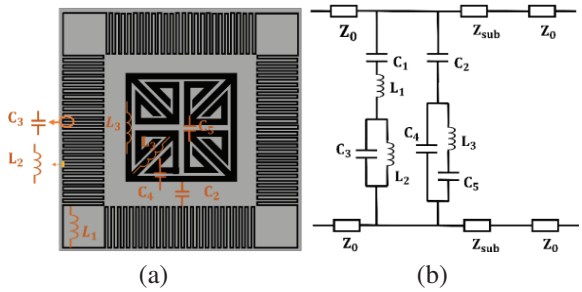

Fig. 5. LC model visualization and simplified equivalent circuit model of the proposed FSS: (a) visualization of LC model and (b) simplified equivalent circuit model.

Based on the metal gap equivalent as capacitance and the metal dipole equivalent as inductance, Fig. 5 (a) shows the LC model visualization of the proposed FSS. In Fig. 5 (b), Z_0 (Z_0= 377 Ω) is the wave impedance

in free space and Z_{sub} (Z_{sub}= 134 Ω) is the wave impedance of the dielectric substrate, where $Z_{sub} = \frac{Z_0}{\sqrt{\varepsilon_r}}$. At 2.4 GHz, the current is concentrated on the wall structure. Current is more concentrated on C_1, L_1, C_3 and L_2. The loop formed by these capacitive inductors exhibits low impedance, which leads to the mismatch of branch impedance. FSS exhibits band stopping characteristics, and the impedance of this FSS layer is $Z_{FSS}=\frac{1}{j\omega C_1}+j\omega L_1+\frac{j\omega L_2}{1-\omega^2 L_2 C_3}$. At 5.8 GHz, the reflection pattern of this FSS mainly involves a square loop, a 45° diagonal arm, and a triangular structure, so it is represented in the circuit by the series-parallel connection of C_2, C_4, L_3 and C_5. The impedance of this FSS layer is $Z_{FSS}=\frac{1}{j\omega C_2}+[\frac{(j\omega L_3+\frac{1}{j\omega C_5})\times\frac{1}{j\omega C_4}}{j\omega L_3+\frac{1}{j\omega C_5}+\frac{1}{j\omega C_4}}]$. The equivalent capacitance is mainly related to the gap and gap width of the periodic structure and the equivalent inductance value is related to the length and width of the periodic structure [26]. Equivalent circuit related equations are: $C_1 \propto \frac{X-2o}{o}$, L_1, $L_2 \propto \frac{a,t}{v}+M$, $C_3 \propto \frac{t}{v}$, $C_2 \propto \frac{r}{n}$, $L_3 \propto \frac{r}{w}+M$, C_4, $C_5 \propto \frac{e,p}{w}$. M is the interaction between the two structures (M ∝ n), which is important for higher order resonance. An increase in the values of 'a' and 't' parameters decreases the first resonant frequency (2.4 GHz). An increase in the values of 'o' and 'v' parameters increases the first resonant frequency. Similarly, an increase in the value of 'r' parameter decreases the second resonant frequency (5.8 GHz). An increase in the values of 'w' and 'n' parameters increases the second resonant frequency. A decrease in the value of 'n' parameter decreases the M value.

In order to obtain the capacitance and inductance values of the equivalent circuit, we fitted capacitance and inductance in ADS by transmitting zeros, transmitting poles as well as bandwidths. Table 2 shows the optimized capacitance and inductance values of the fitted optimized counterparts as shown in Fig. 6, where we observed that

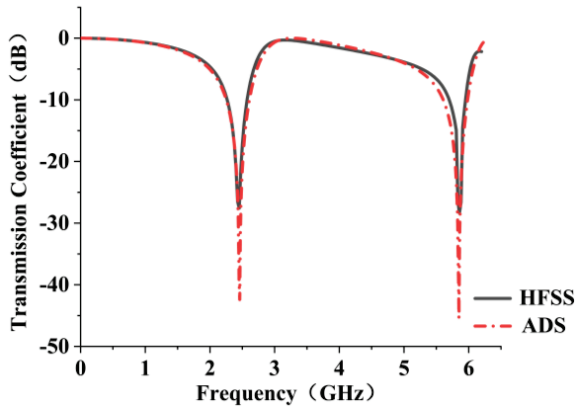

Fig. 6. ADS software and HFSS software transmission coefficient.

Table 2: Capacitive inductance values after fitting optimization

Parameter	C_1	L_1	C_2	L_2
Value (nH/pF)	0.495	4.95	0.504	0.682
Parameter	C_3	L_3	C_4	C_5
Value (nH/pF)	0.515	2.44	2.07	0.806

the two models are very close to each other, thus verifying the reliability of the equivalent circuit model.

IV. EXPERIMENTAL VERIFICATION

In the production of FSS prototypes, the float glass is first cleaned with alcohol. After a series of operations, such as spin-coating and drying, the float glass is placed inside the photolithography machine. The mask plate is placed on top of the photolithography machine, exposed using contact exposure, and finally dried and coated. The proposed FSS prototype is shown in Fig. 7 (a) A 90×90 mm^2 array of 12×12 cells is printed on float glass by photolithography process, which has the advantages of high transmittance and low cost and can be perfectly suitable for indoor use. The photolithography process ensures the accuracy of the printed lines. The wall structure has an area of 11.6 mm^2, and the complex square structure has an area of 11.3 mm^2. With an optical transparency of 54%, leaves and trees can be seen clearly through the FSS, making it perfectly suited for indoor use.

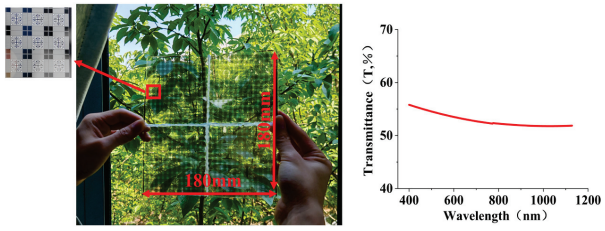

(a) (b)

Fig. 7. Prototype and optical transmission spectra of the proposed FSS: (a) prototype of proposed FSS array and (b) optical transmission spectra of FSS.

A collimated light path is built on the experimental bench. The outgoing beam is irradiated on the FSS prototype, and a fiber optic spectrometer is used to receive the light beam that transmits through the FSS prototype. The transmittance curve is obtained in Morpho software. Figure 7 (b) shows the transmittance of the FSS prototype at 350-1200 nm. The fabricated FSS has a transmittance of 52% in most of the range, and the measured results are more in line with the calculated results.

Figure 8 (a) shows the log periodic antennas model and Fig. 8 (b) shows the measurement setup. The measurement setup consists of BBHA 9120D log-periodic

antenna and a FieldFox N9918A handheld vector network analyzer. In measuring the transmission plot, calibration was performed at 1-10 GHz frequency. Since the horn aperture is 25×14 mm^2, four pieces of FSS prototypes were glued together with hot melt adhesive to cover the entire horn aperture and reduce diffraction. In order to improve the transmission efficiency of electromagnetic wave signals, an ordinary room is covered with wave absorbing cotton and the antenna speakers are placed at a calculated distance from each other. The sample is placed in the middle of the speakers during the measurement.

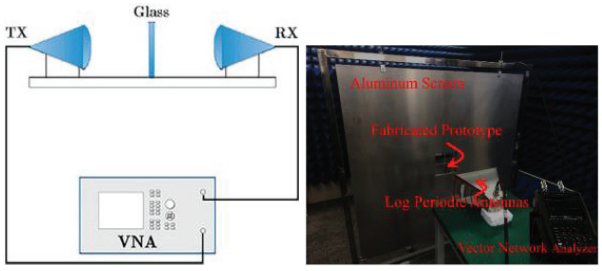

(a) (b)

Fig. 8. (a) Log periodic antennas model and (b) measurement setup.

According to the measurement results in Fig. 9 (a), it can be seen that the measured resonant frequency has a slight offset. The offset at first frequency is 130 MHz, and the offset at second frequency is 250 MHz. The main reason for this offset is that the test room is not a complete microwave darkroom, as well as the error of debugging the vector network analyzer during the measurement process, so this is acceptable. The FSS prototype was measured for stability of different polarization angles, and the measurement results are shown in Figs. 9 (b) and (c). The prepared FSS has a stable frequency response in 0-80°, and the resonance frequencies are more concentrated in 2.5 GHz and 6.1 GHz.

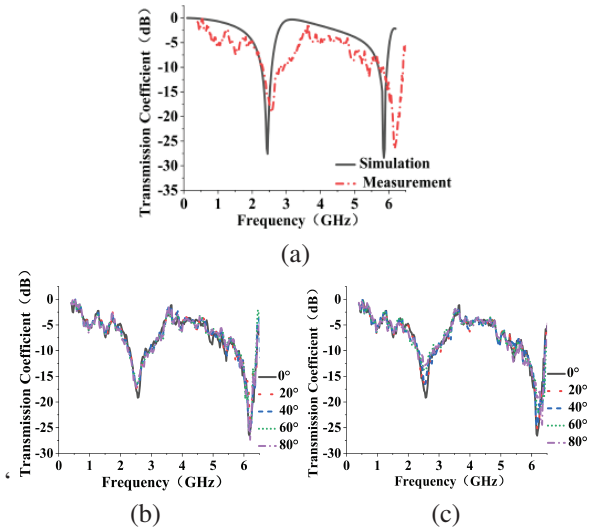

(a) (b) (c)

Fig. 9. Measured frequency response curve: (a) simulated and measured frequency response, (b) measurement curves of FSS at different incidence angles under TE polarization, and (c) measurement curves of FSS at different incidence angles under TM polarization.

To understand the advantages and disadvantages of the proposed FSS, information related to previous studies of miniaturized dual-band bandstop FSS is presented in Table 3, where "T" is the optical transparency, "λ" is the free-space wavelength at the first resonance frequency and "PFSS" is the proposed FSS.

We fabricated FSSs with smaller cell sizes. Some of the designs in Table 3 do not explore optical transparency nor polarization insensitivity, and most of the FSS structures have less angular stability than our designs. As can be seen in Table 3, our designed and printed FSS structures have single layer dual frequency operation, good transparency, ultraminiaturization, high level of polarization insensitivity and angular stability.

Table 3: Comparison of the proposed FSS structure with previous miniaturized dual-band bandstop FSS studies

REF	Operational Bands (GHz)	Transmission Coefficient (dB)	Bandwidths (MHz)	Polarization Insensitive	Angular Stability	Period of Unit Cell	λ (mm)	T%
[22]	2.4 and 5.8	−35 and −30	800 and 820	NO	60°	0.24 λ	125	NO
[23]	2.4 and 5.8	−43 and −30	1100 and 700	YES	45°	0.11 λ	125	NO
[27]	2.4 and 5.8	−37 and −20	900 and 400	YES	60°	0.22 λ	125	NO
[28]	2.4 and 5.8	−27 and −28	902 and 928	YES	45°	0.16 λ	125	NO
[29]	2.4 and 5	−49 and −50	550 and 400	YES	60°	0.21 λ	125	NO
[30]	2.4 and 5.4	−45 and −43	300 and 500	YES	45°	0.12 λ	125	70
[31]	2.5 and 5.3	−25 and −38	280 and 1770	YES	45°	0.16 λ	120	NO
[32]	9.8 and 10.7	−30 and −41	330 and 373	YES	30°	0.16 λ	30.6	NO
PFSS	2.4 and 5.8	−27 and −30	300 and 400	YES	80°	0.056 λ	125	54

V. CONCLUSION

In this paper, an ultraminiaturized and optically transparent FSS structure is proposed to shield 2.4 GHz and 5.8 GHz (ISM signals). The proposed design has polarization insensitivity and high angular stability. Surface current analysis and collector circuit modeling are further presented. The resonant frequency of this FSS can be tuned by individual optimization of geometry. The FSS structure was prototyped using photolithography and then measured using a horn antenna and a vector network analyzer. Measurement results show that this FSS exhibits good transparency, and it shows stable frequency response under both TE and TM polarizations, and angular stability up to 80°. Thus, the proposed FSS structure is an effective method to solve electromagnetic interference in the indoor ISM band.

ACKNOWLEDGMENT

This work was supported by the National Natural Science Foundation of China (61605067) and Open Fund of Key Laboratory of Optical System Advanced Manufacturing Technology, Chinese Academy of Sciences (KLOMT190103).

REFERENCES

[1] F. C. G. da Silva Segundo and A. L. P. S. Campos, "Compact frequency selective surface with dual-band response for WLAN applications," *Microw. Opt. Technol. Lett.,* vol. 57, pp. 265-268, 2015.

[2] S. Ahmed, F. A. Tahir, A. Shamim, and H. M. Cheema, "A compact Kapton-based inkjet-printed multiband antenna for flexible wireless devices," *IEEE Antennas Wireless Propag. Lett*., vol. 14, pp. 1802-1805, 2015.

[3] S. Manokaran, R. Sivasamy, V. H. Muthukaruppan, and E. K. Roshan, "Design of polycarbonate-based dual-band conformal frequency-selective surface for 4G/5G shielding applications," *Microw. Opt. Technol. Lett*., vol. 66, 2024.

[4] L. Tang, C. Wang, L. Yan, P. Gao, X. Zhao, and C. Liu, "Optically transparent and angularly stable broad-stopband frequency selective surface for millimeter wave electromagnetic interference mitigation," *Microw. Opt. Technol. Lett.*, vol. 66, 2024.

[5] S. M. Saeed, C. A. Balanis, and C. R. Birtcher, "Inkjet-printed flexible reconfigurable antenna for conformal WLAN/WiMAX wireless devices," *IEEE Antennas Wireless Propag. Lett*., vol. 15, pp. 1979-1982, 2016.

[6] M. Ikram, M. S. Sharawi, and A. Shamim, "A novel very wideband integrated antenna system for 4G and 5G mm-wave applications," *Microw. Opt. Technol. Lett*., vol. 59, no. 12, pp. 3082-3088, 2017.

[7] S. Balta and M. Kartal, "A novel double-layer low-profile multiband frequency selective surface for 4G mobile communication system," *Applied Computational Electromagnetics Society (ACES) Journal*, vol. 37, pp. 420-427, 2022.

[8] Y. Li, P. Ren, Z. Xiang, B. Xu, and R. Chen, "Design of dual-stopband FSS with tightly spaced frequency response characteristics," *IEEE Microwave and Wireless Components Letters*., vol. 32, pp. 1011-1014, 2022.

[9] M. Yan, S. Qu, J. Wang, J. Zhang, H. Zhou, H. Chen, and L. Zheng, "A miniaturized dual-band FSS with stable resonance frequencies of 2.4 GHz/5 GHz for WLAN applications," *IEEE Antennas Wirel. Propag. Lett.*, vol. 13, pp. 895-898, 2014.

[10] U. Farooq, M. F. Shafique, A. Iftikhar, and M. J. Mughal, "Polarization-insensitive triband FSS for RF shielding at normal and higher temperatures by retrofitting on ordinary glass windows," *IEEE Trans. Antennas Propag.*, vol. 71, pp. 3164-3171, 2023.

[11] M. Wang, L. Zhao, J. Wang, X. Liang, S. Zhang, Y. Li, and W. Yu, "A low-profile miniaturized frequency selective surface with insensitive polarization," *Applied Computational Electromagnetics Society (ACES) Journal*, vol. 33, pp. 1003-1008, 2018.

[12] A. Meredov, K. Klionovski, and A. Shamim, "Screen-printed, flexible, parasitic beam-switching millimeter-wave antenna array for wearable applications," *IEEE Open J. Antennas Propag*., vol. 1, pp. 2-10, 2020.

[13] M. Idrees, Y. He, S. Ullah, and S. Wong, "A dual-band polarization-insensitive frequency selective surface for electromagnetic shielding applications," *Sensors*, vol. 24, 3333, 2024.

[14] K. Klionovski, M. S. Sharawi, and A. Shamim, "A dual-polarization switched beam patch antenna array for millimeter-wave applications," *IEEE Trans. Antennas Propag.*, vol. 67, no. 5, pp. 3510-3515, 2019.

[15] R. Natarajan, M. Kanagasabai, S. Baisakhiya, R. Sivasamy, S. Palaniswamy, and J. K. Pakkathillam, "A compact frequency selective surface with stable response for WLAN applications," *IEEE Antennas Wirel. Propag. Lett*., vol. 12, pp. 718-720, 2013.

[16] J. C. Vardaxoglou, *Frequency Selective Surfaces: Analysis and Design*. New York: Research Studies Press, 1997.

[17] M. Bashiri, C. Ghobadi, J. Nourinia, and M. Majidzadeh, "WiMAX, WLAN, and X-band filtering mechanism: Simple-structured triple-band frequency selective surface," *IEEE Antennas Wireless Propag. Lett*., vol. 16, pp. 3245-3248, 2017.

[18] P. Deo, A. Methta, D. Mirshekar Syahkal, P. J. Massey, and H. Nakano, "High impedance surface-based square loop antenna with rf-absorber," *Microw. Opt. Technol. Lett*., vol. 53, pp. 481-485, 2011.

[19] H. Ahmad, M. Rahman, S. Bashir, W. Zaman, and F. C. Seman, "Miniaturized frequency selective radome operating in the X-band with wideband absorption," *Applied Computational Electromagnetics Society (ACES) Journal*, vol. 34, pp. 1915-1921, 2019.

[20] M. Kartal, S. K. Pinar, B. Doken, and I. Gungor, "A new narrow band frequency selective surface geometry design at the unlicensed 2.4-GHz ISM band," *Microw. Opt. Technol. Lett*., vol. 55, pp. 2986-2990, 2013.

[21] T. Hong, Y. Lee, F. Wee, Y. You, M. N. A. Karim, N. H. Ramli, H. Gan, and M. A. Jamlos, "Study of 5.8 GHz band-stop frequency selective surface (FSS)," *International Journal of Integrated Engineering*, vol. 11, pp. 244-251, 2019.

[22] B. Döken and M. Kartal, "Dual layer convoluted frequency selective surface design in the 2.4 and 5.8 GHz ISM bands," *Applied Computational Electromagnetics Society (ACES) Journal*, vol. 33, pp. 413-418, 2018.

[23] B. Döken and M. Kartal, "Dual-band frequency surface design by implementing a simple design technique," *IETE J Res*., vol. 68, pp. 2049-2054, 2019.

[24] Float Glass – Properties and Applications [Online]. Available: https://www.azom.com/properties.aspx?ArticleID=89.

[25] P. Wei, C. Chiu, and T. Wu, "Design and analysis of an ultraminiaturized frequency selective surface with two arbitrary stopbands," *IEEE Transactions on Electromagnetic Compatibility*, vol. 61, pp. 1447-1456, 2019.

[26] T. Liu and S. S. Kim, "Design of wide-bandwidth electromagnetic wave absorbers using the inductance and capacitance of a square loop-frequency selective surface calculated from an equivalent circuit model," *Opt. Commun*., vol. 359, pp. 372-377, 2016.

[27] B. Döken and M. Kartal, "Easily optimizable dual-band frequency selective surface design," *IEEE Antennas Wirel. Propag. Lett*., vol. 16, pp. 2979-2982, 2017.

[28] V. F. Barros, S. Segundo, A. L. P. Campos, S. G. da Silva, and A. Gomes Neto, "A novel simple convoluted geometry to design frequency selective surfaces for applications at ISM and UNII bands," *J Microw. Optoelectron. Electromagn. Appl*., vol. 16, pp. 553-563, 2017.

[29] M. A. Hussaini, M. I. Sulaiman, G. I. Kiani, and J. Khan, "Frequency selective window blinds for indoor WLAN shielding," *Microw. Opt. Technol. Lett*., vol. 66, issue 1, 2024.

[30] U. Farooq, A. Iftikhar, A. I. Najam, S. A. Khan, and M. F. Shafique, "An optically transparent dual-band frequency selective surface for polarization independent RF shielding," *Optics Communications*, vol. 546, 2023.

[31] R. V. D. Lira, B. S. da Silva, A. L. P. S. Campos, and A. G. Neto, "A dual-band complementary frequency selective surface combining structures that provides narrow and wide stop-band frequency responses," *Microw. Opt. Technol. Lett*., vol. 65, pp. 3107-3112, 2023.

[32] T. Qin, C. Huang, Y. Cai, and X. Lin, "Dual-band frequency selective surface with different polarization selectivity for wireless communication application," *Sensors*, vol. 23, no. 9, p. 4264, 2023.

Dongming Guo was born in QuanZhou, Fujian, China, in 2000. He received the B.S. degree from the Xiamen University of Technology, Xiamen, China, in 2022. Currently, he is focusing on antenna and microwave devices.

Huaxin Zhu received his Ph.D. degree in 2011. Since 2011, he has worked on optical thin film design, preparation and frequency selective surfaces. Currently, he is an Associate Professor in the Jiangnan University, School of Science.

An Accelerated Ray Tracing Method based on Embree3 Ray Tracing Library for Targets with Non-uniform Thickness Materials

Yi Zhu, Gao Wei, and Jianzhou Li

School of Electronics and Information
Northwestern Polytechnical University, Xi'an 710129, China
zy911@mail.nwpu.edu.cn, weigao.nwpu.edu.cn, ljz@nwpu.edu.cn

Abstract – This paper proposes an accelerated ray tracing method utilizing the Embree3 ray tracing library for targets with non-uniform thickness materials. In contrast to the traditional surface-based ray tracing, the proposed approach performs ray tracing within the materials, since surface tracing is ineffective for materials with non-uniform thickness. To ensure efficiency and handle the overlapping grids between different materials, the Embree3 ray tracing library is introduced to ray intersection. Numerical results confirm that the proposed method surpasses existing methods in terms of efficiency and applicability while maintaining accuracy.

Index Terms – Accelerated ray tracing method, electromagnetic scattering, thick materials.

I. INTRODUCTION

In recent years, the scattering of targets with materials has become a research hotspot. Numerous electromagnetic algorithms have been developed, such as the method of moments (MoM) [1], finite element method (FEM) [2], and finite difference time domain (FDTD) [3]. The common point of these numerical algorithms is high accuracy but low efficiency. For electrically large targets, a high-frequency algorithm is more suitable. The existing high-frequency algorithms mainly include the physical optics (PO) method and the shooting and bouncing ray (SBR) method. Both algorithms can be used for targets composed of uniformly thick materials. However, considering the shape design, some targets have non-flat surfaces, and the material is part of the structure rather than being a coating. This results in non-uniform thickness of the material. For non-uniform thickness materials, the PO method is not applicable, while the SBR method can only be applied through tracing inside the material, since it is impossible to determine the reflection coefficient without knowing the thickness of the material.

Ray tracing inside the material is the most suitable method for processing the electrically large target with non-uniform thickness materials. Several studies have been conducted on ray tracing inside materials, like [4] and [5]. Compared with the traditional SBR method, ray tracing inside the materials requires more intersection, making acceleration algorithms more critical. Although the existing acceleration algorithms can achieve a good acceleration ratio, they often have limitations. For instance, constructing an accelerated model using kd-tree [6] is computationally expensive and GPU computing [7] has certain hardware requirements. Further research is required to develop a more general and efficient acceleration method.

Furthermore, in contrast to the traditional SBR method with surface tracing, the overlapping grids at the interface of different materials cause issues. Figure 1 shows that it is difficult to identify the material on which the intersection occurs without processing the overlapping grids.

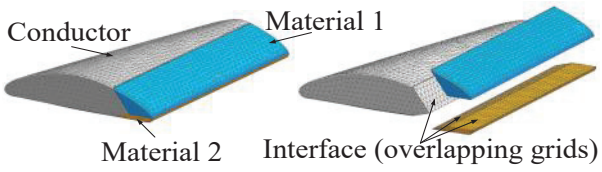

Fig. 1. Targets with non-uniform thickness materials.

To address the above-mentioned problems, an efficient and universal method is presented in this paper. Ray tracing is performed inside the material to obtain the radar cross-section (RCS) of targets with non-uniform thickness materials. Unlike the existing acceleration algorithms, the proposed approach employs the Embree3 ray tracing library, an open-source library specifically designed for image rendering, to realize model building and ray intersection. For overlapping grids at the interface, the intersection information is determined by tracing twice in multiple scenes, which avoids complex overlapping grid processing.

This paper successfully combines Embree3 with the SBR method. The introduction of Embree3 significantly improves the efficiency of ray tracing. Moreover, the problem of overlapping grids is ingeniously solved

Submitted On: April 19, 2024
Accepted On: August 27, 2024

https://doi.org/10.13052/2024.ACES.J.390606

through the multi-scene method. The proposed method has much higher efficiency and stronger applicability than the existing methods.

II. RAY TRACING INSIDE MATERIALS BASED ON EMBREE3

The common SBR method mainly includes modeling, ray tracing, field tracing, and far-field integration. The specific process of the SBR method based on Embree3 is as follows.

A. Modeling

In contrast to the traditional SBR method with surface tracing, internal ray tracing requires multiple sets of grids to differentiate between various materials. Besides, multiple scenes need to be created to solve the problem of overlapping grids.

There are three types of objects in Embree3, including device object (do), scene object (so), and geometry object (GO). Each object has an independent ID. As shown in Fig. 2, GO is the first level. Each GO corresponds to an independent set of grids, like GO 1, GO 2, and GO 3. The SOs are the second level, corresponding to different scenes. Each SO can include multiple GOs, like SO 1, SO 2, SO 3, and SO 4. DO is the third level. Each DO can include multiple SOs, like DO 1. Normally, the traditional SBR method with surface tracing requires only one scene (SO 1). However, tracing inside the materials requires multiple scenes (SO 1, SO 2, SO 3, and SO 4) to deal with the overlapping grids. The usage of multiple scenes will be described in Section IID.

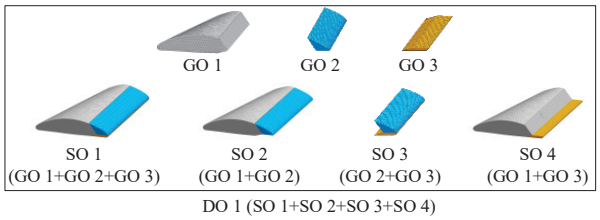

Fig. 2. Objects in Embree3.

B. Ray tracing

Ray tracing is the key to the accuracy and efficiency of the SBR method. The process of ray tracing based on Embree3 is described in detail below.

The first step is to determine the initial ray tube on the face of the bounding box, which is obtained through the function "RtcGetSceneBounds" defined in Embree3. The incident direction of the initial ray tube changes with coordinate rotation.

The second step is to find the intersections. Embree3 provides an efficient function "RtcIntersect" to obtain the intersection. The function "RtcIntersect" is based on the bounding volume hierarchy (BVH) algorithm [8] and the Möller-Trumbore algorithm [9].

Figure 3 shows that the BVH is a binary tree, where each node represents a bounding box containing grids. The root node represents the bounding box of the whole scene, and the other nodes represent the sub-bounding box. Intersection detection begins at the root node, checking if the ray overlaps with the bounding box. This process recursively continues until reaching the bounding box of the leaf node. In contrast to kd-tree, which divides regions based on space before intersection, BVH divides bounding boxes based on grids in the process of intersection. The Möller-Trumbore algorithm is a fast method to find the intersection of rays and triangles in space. It is used to obtain the actual intersection between the ray and the grids in the minimum bounding box.

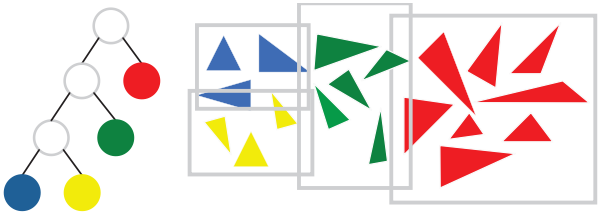

Fig. 3. BVH structure.

The combination of the BVH algorithm and the Möller-Trumbore algorithm significantly enhances the efficiency of ray intersection. Besides, Embree3 defines a structure "RTCRayHit" for storing incident and intersection information. As shown in Fig. 4, the structure "RTCRayHit" with incident information is passed as input to the function "RtcIntersect", and the intersection information is returned to the structure.

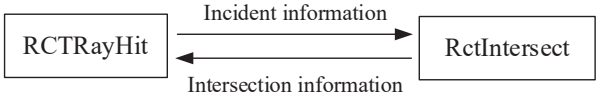

Fig. 4. Finding the intersections.

The third step is to determine the reflection and transmission information. Figure 5 shows that the intersection information in "RTCRayHit" is used to obtain reflection and transmission information employing equations (1)-(6).

As shown in Fig. 6, when a ray hits the interface between the free space (Region 0) and the material (Region 1), a transmitted wave and a reflected wave will be generated at the intersection. The incident wave vector

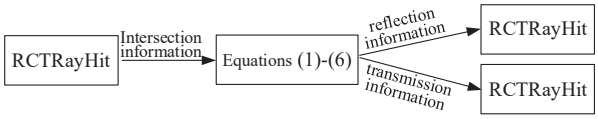

Fig. 5. Determining the reflection and transmission information.

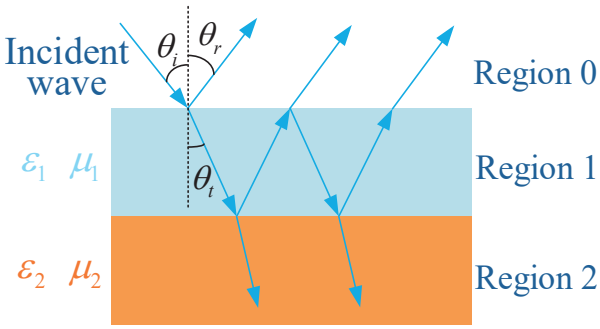

Fig. 6. Wave propagation inside the materials.

$\vec{k}^i$ and the transmitted wave vector $\vec{k}^t$ are:

$$\vec{k}^i = k_h^i \hat{h} + k_v^i \hat{v} = \left(k_0 \sin\theta^i\right)\hat{h} + \left(k_0 \cos\theta^i\right)\hat{v} = \omega\sqrt{\mu_0\varepsilon_0}, \tag{1}$$

$$\vec{k}^t = \bar{\beta}^t - j\bar{\alpha}^t = (\beta_h^t \hat{h} + \beta_v^t \hat{v}) - j(\alpha_h^t \hat{h} + \alpha_v^t \hat{v}) = \omega\sqrt{\mu_1\varepsilon_1}, \tag{2}$$

where θ^i is the incident angle, k_0 is the wave vector in free space, $\hat{h}$ is the transverse component, and $\hat{v}$ is the longitudinal component. According to the phase matching condition [10], the following can be obtained:

$$\left[\left(k_h^i\right)^2 + \left(\beta_v^t\right)^2\right] - \left[\left(\alpha_v^t\right)^2\right] = Re\left(\omega^2\mu_1\varepsilon_1\right), \tag{3}$$

$$2\beta_v^t\alpha_v^t = -Im\left(\omega^2\mu_1\varepsilon_1\right). \tag{4}$$

The transmission angle θ^t can be calculated after obtaining β_v^t by solving equations (3) and (4) with the following:

$$\theta^t = \tan^{-1}\left(\frac{k_0 \sin\theta^i}{\beta_v^t}\right). \tag{5}$$

According to the Snell's law, the reflection angle θ^r is equal to the incident angle θ^i:

$$\theta^r = \theta^i. \tag{6}$$

The fourth step is to determine whether to continue tracing. The maximum tracing times and the minimum energy limit are set as the end conditions. Moreover, ray tracing will also stop when there is no intersection. If the end condition is not met, the operation in the second step will be repeated by treating the reflected or transmitted ray as the new incident ray.

C. Field tracing and far-field integration

Field tracing and ray tracing are performed simultaneously. The attenuation coefficient $\bar{\alpha}^t$ of the material can be calculated using equations (3) and (4). The calculation method of the reflection and transmission coefficients is provided in [11] and listed as follows:

$$R_{TE} = \frac{\mu_0 k_v^i - \mu_1 k_v^t}{\mu_0 k_v^i + \mu_1 k_v^t}, T_{TE} = \frac{2\mu_1 k_v^i}{\mu_0 k_v^i + \mu_1 k_v^t}$$
$$R_{TM} = \frac{\varepsilon_0 k_v^i - \varepsilon_1 k_v^t}{\varepsilon_0 k_v^i + \varepsilon_1 k_v^t}, T_{TM} = \frac{2\varepsilon_1 k_z^t}{\varepsilon_0 k_v^i + \varepsilon_1 k_v^t} \tag{7}$$

where R_{TE}, R_{TM}, T_{TE}, and T_{TM} are the reflection and transmission coefficients of TE and TM waves, respectively. The reflected and transmitted electric fields at the intersection can be calculated as:

$$\begin{bmatrix}\bar{E}_{TE}\\ \bar{E}_{TM}\end{bmatrix}_{n+1}^{r} = \begin{bmatrix}R_{TE} & 0\\ 0 & R_{TM}\end{bmatrix}\begin{bmatrix}\bar{E}_{TE}\\ \bar{E}_{TM}\end{bmatrix}_{n}^{i}, \begin{bmatrix}\bar{E}_{TE}\\ \bar{E}_{TM}\end{bmatrix}_{n+1}^{t}$$
$$= \begin{bmatrix}T_{TE} & 0\\ 0 & T_{TM}\end{bmatrix}\begin{bmatrix}\bar{E}_{TE}\\ \bar{E}_{TM}\end{bmatrix}_{n}^{i}. \tag{8}$$

After performing ray tracing and field tracing for all ray tubes, the effective ray tubes are selected for far-field integration. Gordon's method is adopted in this paper for integration [12]. The RCS of the target can be obtained by superimposing the scattering field of all effective ray tubes.

D. Ray tracing in multiple scenes

Overlapping grids make it challenging to accurately and directly determine the correct material parameters required for reflection and transmission calculations. As shown in Fig. 7, there are four different intersections for a ray tube. Due to the overlapping grids at Point 2 and Point 3, all four intersections are located on the grid of GO 2, which affects the acquisition of correct material parameters. To ensure accurate and efficient ray tracing, the multiple scenes as shown in Fig. 2 are used to determine the precise GO where the intersection occurs. The specific process is as follows.

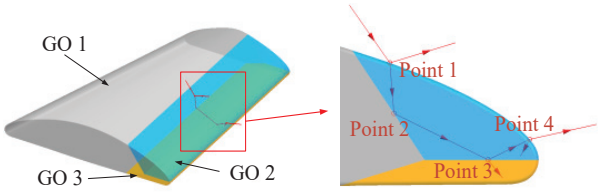

Fig. 7. Intersections of a ray tube.

In this multi-scene method, each ray tracing needs to be carried out twice in different SOs. As shown in Fig. 8, the intersection of the first tracing is on GO 2. Thus, the second tracing is made in SO 2, which does not contain GO 2. The distance d between the two intersections is calculated when both tracings have an intersection. According to the position of the second intersection and the distance d, the actual position of the intersection can be determined.

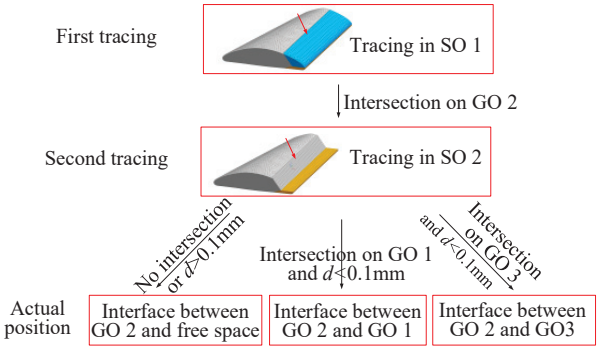

Fig. 8. Ray tracing in multiple scenes.

The multi-scene method effectively solves the problem of overlapping grids. Despite a significant increase in intersection points, the overall method remains efficient due to the powerful performance of Embree3 and the avoidance of overlapping grid processing. Furthermore, this multi-scene method is not limited by model shape and mesh quality.

III. SIMULATIONS AND DISCUSSION

The accuracy and efficiency of the proposed ray tracing method were investigated through the following four examples. All the simulations were performed on a workstation with two Intel (R) Xeon (R) CPU Gold-6248R.

A. SLICY model

A conductor SLICY model as shown in Fig. 9 was simulated first. The RCS from the SBR method in CST was compared with the proposed SBR method. The incident angle varied in the range of $\theta = 0° - 90°$ for $\varphi = 0°$, $\theta\theta$ polarization. The frequency was 10 GHz, and the electrical size was about $92\lambda \times 82\lambda \times 56\lambda$. The high degree of consistency between the two results shown in Fig. 10 validates the accuracy of the ray tracing method in this paper. Table 1 presents the computation cost, demonstrating the high efficiency of the proposed ray tracing method.

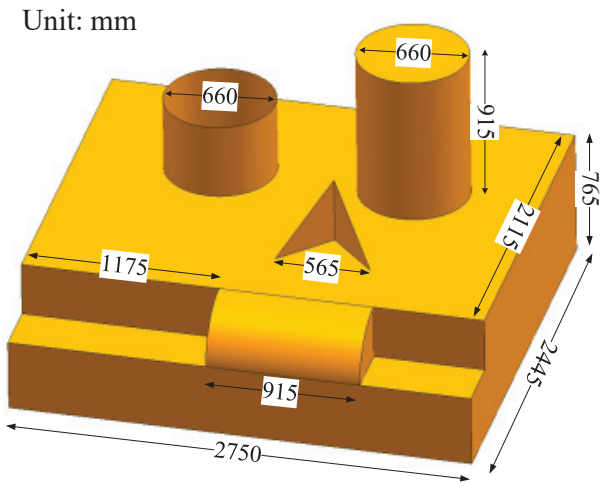

Fig. 9. Dimensions of the SLICY model.

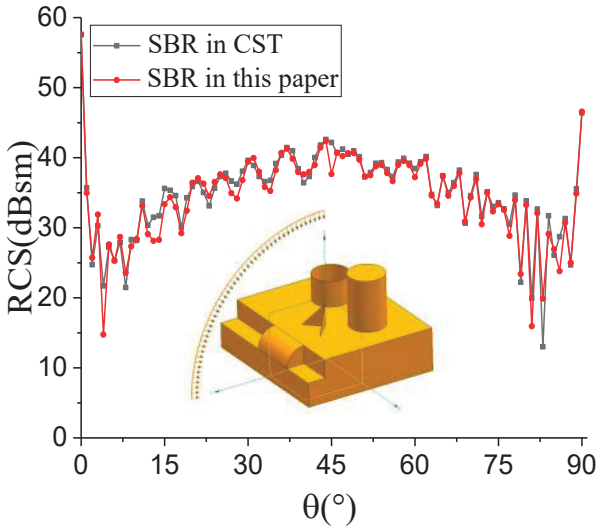

Fig. 10. RCS of the SLICY model.

Table 1: Computation time of the SLICY model

SLICY model	SBR in this paper	SBR in CST
Time	19 s	24 s

B. Trihedral coated with thick material

A $20\lambda \times 20\lambda \times 20\lambda$ trihedral coated by a material with a thickness of $1\ \lambda$ was analyzed. The parameters were $\varepsilon_r = 3 - j3$, $\mu_r = 1$. The incident angle varied in the range of $\theta = 0° - 90°$ for $\varphi = 45°$, $\theta\theta$ polarization, and the frequency was 6 GHz. Figure 11 compares the results of the SBR method in this paper with the FEM in HFSS. The results are quite consistent, demonstrating the accuracy of the SBR method in this paper when there is material in the target.

Table 2 compares the computation time of the SBR method in this paper with the SBR method in [5], which uses kd-tree for the same model. It can be seen that the efficiency of the proposed ray tracing is much higher than that of the traditional acceleration method.

Table 2: Computation time of coated trihedral

Coated trihedral	SBR in this paper	SBR in [5]	FEM
Time	16 s	2174 s	1.8 h

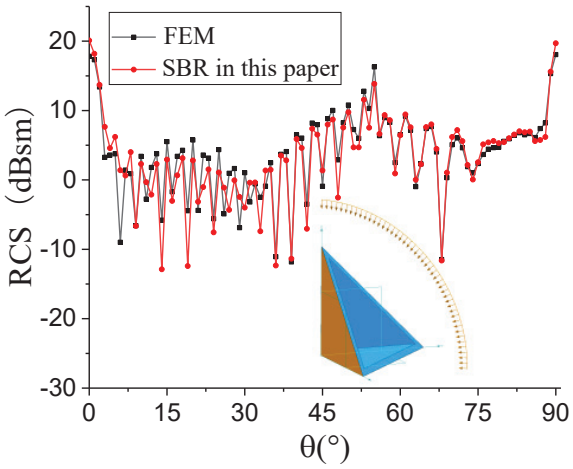

Fig. 11. RCS of coated trihedral.

C. Cube coated with thick materials

The RCS of a cube coated with thick materials was calculated. The size of the cube was $10\lambda \times 10\lambda \times 10\lambda$. Two different cases were considered. In one case, the cube was coated with a single layer of material, and the thickness was 0.5λ, $\varepsilon_r = 9.5 - j1$, $\mu_r = 1$. In the other case, the cube was coated with two-layer material, and the thickness of each layer was 0.5λ, $\varepsilon_r = 9.5 - j1$, $\mu_r = 1$ for the inner layer, and $\varepsilon_r = 2 - j1$, $\mu_r = 1$ for the outer layer. For both cases, the incident angle varied in the range of $\theta = 0° - 90°$ for $\varphi = 0°$, $\varphi\varphi$ polarization, and the frequency was 3 GHz. The RCS results of the two cases are shown in Fig. 12. The reference results are from the finite integration technique (FIT) in CST.

It can be seen from Fig. 12 that the results of the two methods are consistent, indicating that the SBR method proposed in this paper is still accurate when dealing with multi-layer thick materials. Table 3 shows that the computation time of the proposed SBR method is significantly lower than that of the FIT.

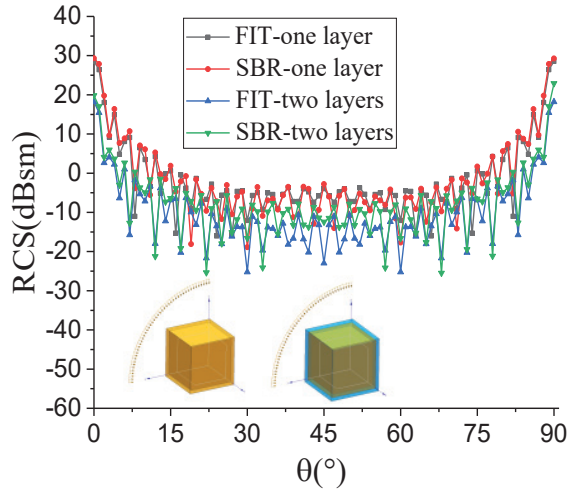

Fig. 12. RCS of a coated cube.

Table 3: Computation time of a coated cube

Coated Cube	One Layer		Two Layers	
	SBR	FIT	SBR	FIT
Time	13 s	3.5 h	20 s	4.6 h

D. Combination of conductor and materials

The fourth model was a combination of three parts. The size of the entire model was about $19\lambda \times 16\lambda \times 3\lambda$. Each part was of non-uniform thickness. There were two different cases. In case 1, all three parts were conductors. In case 2, part 1 was a conductor, part 2 was a material with $\varepsilon_r = 3 - j2$, $\mu_r = 1.5 - j1.2$, and part 3 was a material with $\varepsilon_r = 4 - j4$, $\mu_r = 1 - j0.5$. For both cases, the incident angle varied in the range of $\theta = 0° - 180°$ for $\varphi = 90°$, $\varphi\varphi$ polarization, and the frequency was 3 GHz.

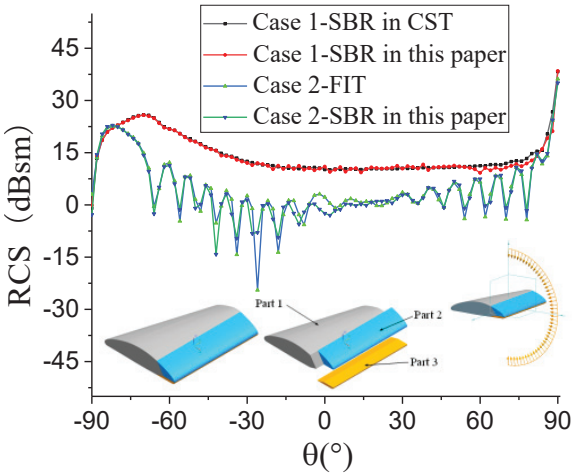

Fig. 13. RCS of three-part combination.

Figure 13 shows the RCS results of the three-part combination. The reference results are from the SBR method in CST for case 1 and the FIT in CST for case 2. It can be observed that the results are quite consistent for both cases. The computation time is shown in Table 4. This example further illustrates the accuracy and high

Table 4: Computation time of combination model

Combination	Case 1		Case 2	
	SBR	SBR in CST	SBR	FIT
Time	3 s	3 s	15 s	6.8 h

efficiency of the proposed SBR method when dealing with targets with non-uniform thickness materials since the SBR method in CST can only be used for conductor.

IV. CONCLUSION

An accelerated ray tracing method is studied in this paper. The scattering of target with non-uniform thickness materials is calculated by ray tracing inside the materials. The Embree3 ray tracing library is introduced to improve the efficiency of ray tracing. Moreover, a multi-scene method is proposed to determine the intersection position, which avoids overlapping grid hidden processing. Experimental results demonstrate and validate that the proposed method has higher efficiency and stronger applicability than the existing algorithms.

REFERENCES

[1] R. Gholami and V. Okhmatovski, "Surface–volume–surface EFIE formulation for fast direct solution of scattering problems on general 3-D composite metal–dielectric objects," *IEEE Trans. Antennas Propagat*., vol. 68, no. 7, pp. 5742-5747, July 2020.

[2] B. Stupfel, "Homogenization of a multilayer coating: Application to model-order reduction," *IEEE Trans. Antennas Propagat.*, vol. 69, no. 3, pp. 1528-1534, Mar. 2021.

[3] W. Chen, L. Wang, Z. Wu, M. Fang, Q. Deng, A. Wang, Z. Huang, X. Wu, L. Guo, and L. Yang, "Study on the electromagnetic scattering characteristics of high-speed target with non-uniform plasma via the FCC-FDTD method," *IEEE Trans. Antennas Propagat.*, vol. 70, no. 7, pp. 5744-5757, July 2022.

[4] Z. Xie, Z. Liang, H. Yue, and P. Gao, "A shooting and bouncing ray method for dielectric media," in *2017 International Applied Computational Electromagnetics Society Symposium (ACES)*, pp. 1-3, 2017.

[5] Y. Huang, Z. Zhao, X. Li, Z. Nie, and Q. H. Liu, "Volume equivalent SBR method for electromagnetic scattering of dielectric and composite objects," *IEEE Trans. Antennas Propagat*., vol. 69, no. 5, pp. 2842-2852, May 2021.

[6] H. Ding, P. Gao, Y. Tao, and H. Lin, "Kd-tree based fast facet visibility test in iterative physical optics," in *2013 IEEE Antennas and Propagation Society International Symposium (APSURSI)*, Orlando, FL, pp. 1788-1789, 2013.

[7] J. Huo, L. Xu, X. Shi, and Z. Yang, "An accelerated shooting and bouncing ray method based on GPU and virtual ray tube for fast RCS prediction," *IEEE Antennas Wireless Propagat. Lett.*, vol. 20, no. 9, pp. 1839-1843, Sep. 2021.

[8] H. Liu, B. Wei, and H. Wang, "A fast shooting and bouncing ray algorithm for electromagnetics scattering based on bounding volume hierarchy," in *2023 IEEE 7th International Symposium on Electromagnetic Compatibility (ISEMC)*, Hangzhou, China, pp. 1-3, 2023.

[9] T. Möller and B. Trumbore, "Fast, minimum storage ray-triangle intersection," *Journal of Graphics Tools*, vol. 2, no. 1, pp. 21-28, 1997.

[10] P. H. Pathak and R. J. Burkholder, *Electromagnetic Radiation, Scattering, and Diffraction.* Hoboken, NJ: Wiley-IEEE Press, 2022.

[11] W. C. Chew, *Waves and Fields in Inhomogeneous Media.* Hoboken, NJ: Wiley-IEEE Press, 1995.

[12] W. Gordon, "Far-field approximations to the Kirchoff-Helmholtz representations of scattered fields," *IEEE Trans. Antennas Propagat.*, vol. 23, no. 4, pp. 590-592, July 1975.

Yi Zhu was born in Sichuan, China, in 1996. He received the B.S. and M.S. degrees in electromagnetic field and microwave technology from Northwestern Polytechnic University, Xi'an, China, in 2018 and 2021, respectively, where he is currently pursuing the Ph.D. degree. His research interests include computational electromagnetics.

Gao Wei was born in Shandong, China, in 1963. He received the B.S. and M.S. degrees in electromagnetic field and microwave technology from Northwestern Polytechnic University, Xi'an, China. He is currently a professor with the School of Electronics and Information in Northwestern Polytechnic University. His current research interests include antenna theory and techniques, microwave measurement, and microwave application.

Jianzhou Li was born in Shaanxi, China, in 1972. He received the Ph.D. degree from Northwestern Polytechnic University, Xi'an, China, in 2005. He received a P.D. degree in Surrey Satellite Center in University of Surrey, UK, in 2009. He is currently an associate professor with the School of Electronics and Information in Northwestern Polytechnic University. His current research interests include antenna theory and techniques, and computational electromagnetics.

Efficient Electromagnetic Compatibility Optimization Design Based on the Stochastic Collocation Method

Xiaobing Niu, Shenglin Liu, and Runze Qiu

College of Marine Electrical Engineering
Dalian Maritime University, Dalian, 116026, China
emtf@dlmu.edu.cn, shaonian@dlmu.edu.cn, qiurunze321@163.com

Abstract **–** Nowadays, in the field of electromagnetic compatibility (EMC), numerical methods such as finite element analysis are often used for simulation analysis. These numerical methods take a long time to solve some complex simulation problems, which is not conducive to the optimal design of EMC. In particular, the intelligent optimization algorithm that needs continuous iterative calculation will not be realized because of the long optimization time. This paper realizes the innovative application of the uncertainty analysis method (Stochastic Collocation Method) in EMC optimization design. Two typical EMC optimization design problems, namely, the prediction of cable crosstalk and the design of shielding performance of metal boxes, are proposed to verify the effectiveness of the optimization algorithm. Meanwhile, its performance is compared with the classical intelligent optimization algorithms such as genetic algorithms and immune algorithms.

Index Terms **–** Efficient optimization design, electromagnetic compatibility, failure mechanism analysis, intelligent optimization algorithms, stochastic collocation method.

I. INTRODUCTION

Since the existence of the subject of Electromagnetic Compatibility (EMC), optimal design has been one of its important research contents. Due to the widespread randomness in the actual engineering environment, and the strong nonlinearity of the electromagnetic process, the optimization design of electromagnetic related performance is very difficult. In the 1990s, the International COMPUMAG Society presented the standard engineering problems, the Testing Electro-Magnetic Analysis Methods (TEAM), which are used to verify the correctness of electromagnetic field numerical analysis methods. Some of them involve optimization design about electromagnetic calculation, for example, TEAM 22 calculating example is the optimization design of superconducting magnetic energy storage systems, while TEAM 25 calculating example is the optimization design of magnetic field alignment die for anisotropic bonded permanent magnets [1, 2].

Around 2008 till now, intelligent optimization algorithms have been gradually introduced into EMC optimization design and achieved great success, such as particle swarm algorithm, genetic algorithm, immune algorithm and so on [3–6]. When the analytical method is used for forward prediction analysis or the single simulation time is short, intelligent optimization algorithms can get good optimization design results by virtue of their superior search ability. However, when the forward single simulation time is long, such as the complex EMC problem with finite element analysis method, intelligent optimization algorithms will lose competitiveness due to the long simulation time. Nowadays, with the requirements of multi-physical field coupling, uncertainty analysis and so on, the complexity of finite element analysis is increasing, which leads to the increase of various costs of EMC simulation prediction. At this time, intelligent optimization algorithms have no application.

Around 2014 till now, optimization algorithms based on surrogate model is becoming more and more popular in EMC simulation. The most representative methods are the Kriging model [7–9] and the surface response model based on radial basis function [10]. Their idea is to abstract the EMC prediction process into a substitute model, and then use intelligent optimization algorithms to optimize the agent model, so as to obtain the optimal design results. However, these methods have a fatal defect, that is, there is no accurate convergence judgment standard, which means the required EMC deterministic simulation times can only depend on the experience of the designers. When the number of EMC simulations is too low, the accuracy of optimal design is difficult to guarantee. When the number of EMC simulations is too high, it will cause a serious waste of computing resources.

Since 2013, uncertainty analysis is another hot research direction in the EMC field, and many methods have been successfully applied, such as the Monte Carlo

Submitted On: November 1, 2023
Accepted On: July 17, 2024

https://doi.org/10.13052/2024.ACES.J.390607

Table 1: Comparison of performance of electromagnetic optimization algorithms

	Intelligent Optimization Algorithms	**Surrogate Models**	**SCM**
Efficiency calculation	Low	High	High
Convergence	Poor	Relatively Poor	Good
Global search capability	Strong	Weak	Relatively Strong
Suboptimal search capability	Weak	Relatively Strong	Strong

Method [11, 12], the Stochastic Reduced Order Models [13], and so on. There are many potential applications of uncertainty analysis methods, one of which is the worst-case estimation. Its implementation process is similar to the optimization process based on agent model. Unlike intelligent optimization algorithm, the optimization process based on uncertainty analysis method does not need iteration, so it has higher computational efficiency. Unlike the optimization process based on traditional agent model, uncertainty analysis has a strict convergence judgment method [14, 15], so its calculation efficiency and accuracy are guaranteed.

The Stochastic Collocation Method (SCM) is a non-embedded uncertainty analysis method, which has the characteristics of high calculation accuracy and high calculation efficiency, so it is very suitable for the application of optimum design [16–18]. Therefore, this paper selects it as an extended application of uncertainty analysis method in optimization design, and discusses its optimum performance in detail.

Table 1 compares the electromagnetic optimum performance of Intelligent optimization algorithms, Surrogate models and SCM, the SCM algorithm is shown to be more innovative.

The structure of the paper is as follows: Principle of the SCM applied to optimal design is presented in Section II. Section III gives the limitation of the SCM and its improvement scheme. Example of crosstalk prediction in the cable cascade model is shown in Section IV. Section V offers an example of shielding performance design of metal box. Prospect of the proposed optimization design method is discussed in Section VI. Section VII summarizes this paper.

II. APPLICATION OF THE SCM IN OPTIMIZATION PROCESS

For the uncertainty analysis methods, the inputs of the EMC simulation are regarded as random variables instead of deterministic constants. In optimization process, the parameters to be optimized also change within a certain range. If the range is treated as a random variable with uniform distribution, the optimization process can be equivalent to an uncertainty analysis problem. The one-to-one correspondence between the value range $[A_{\min}, A_{\max}]$ and the random variable ξ_i is shown as follows:

$$A(\xi_i) = \frac{A_{\max} + A_{\min}}{2} + \frac{A_{\max} - A_{\min}}{2} \times \xi_i. \quad (1)$$

Where ξ_i is the random variable obeying the uniform distribution in the range of $[-1, 1]$.

According to the generalized polynomial chaos theory, the SCM uses the Legendre polynomials to deal with uncertainty analysis problems with random variables of uniform distribution. The first terms of Legendre polynomials in one dimension are as follows:

$$\begin{cases} \varphi_0(\xi_i) = 1 \\ \varphi_1(\xi_i) = \sqrt{3}\xi_i \\ \varphi_2(\xi_i) = \frac{\sqrt{5}}{2}\left(3\xi_i^2 - 1\right) \\ \varphi_3(\xi_i) = \frac{\sqrt{7}}{2}\left(5\xi_i^3 - 3\xi_i\right). \end{cases} \quad (2)$$

The principle formula of the SCM is as follows:

$$\mathrm{EMC}_{\mathrm{SCM}}(\xi) = \sum_{j_1=1}^{m_1} \cdots \sum_{j_n=1}^{m_n} \mathrm{EMC}(a_{j_1}, \cdots, a_{j_n}) \mathrm{Lag}(a_{j_1}, \cdots, a_{j_n}). \quad (3)$$

Where $\{a_{j_1}, \cdots, a_{j_n}\}$ are collocation points, which are the tensor product of zero points of chaotic polynomials like formula (2). $\mathrm{EMC}(a_{j_1}, \cdots, a_{j_n})$ means the EMC simulation result under the deterministic input parameters $\{a_{j_1}, \cdots, a_{j_n}\}$. $\mathrm{Lag}(a_{j_1}, \cdots, a_{j_n})$ is the calculation results of Multi-dimensional Lagrange Interpolation on collocation points, and $\mathrm{EMC}_{\mathrm{SCM}}(\xi)$ is the final results in the form of random variable polynomials . Finally, the uncertainty analysis results are obtained by sampling random variable polynomials $\mathrm{EMC}_{\mathrm{SCM}}(\xi)$. The results can be the expected values, the standard deviation results, the probability density function results, the worst-case estimation results and so on.

According to the above theory, the core idea of the SCM is using the random variable polynomials to replace the EMC simulation process, and then the agent model $\mathrm{EMC}_{\mathrm{SCM}}(\xi)$ can be sampled to obtain the uncertainty analysis results. For the optimization problem, we can also build a similar agent model, and then use the exhaustive method to obtain the optimum results. As the SCM has excellent computational efficiency, the establishment of the agent model only requires several forward EMC simulations, and the number of simulations is the number of collocation points. Unlike the traditional intelligent optimization algorithm, which requires repeated iterations, the efficiency of the proposed optimization algorithm is obviously better.

In uncertainty analysis, how to judge the convergence of the algorithm is an important topic, and the Mean Equivalent Area Method (MEAM) is an effective method to solve this problem [14, 15]. Back to this paper, our question is how to judge the order of chaotic polynomials in the SCM. In reference [14], there is a clear solution for the SCM: By increasing the order of polynomials, the MEAM is used to quantitatively calculate the similarity between adjacent order uncertainty analysis results, and then determine the convergence order of the SCM. This similarity must be in the "Excellent" level, namely, the MEAM value is larger than 0.95 at this time.

It is worth noting that the explicit convergence judgment basis is the unique advantage of the uncertainty analysis method different from the traditional agent model optimum design method, which is an important guarantee for the accuracy of optimum design and calculation efficiency.

The following is a typical multi-peak functional problem to preliminarily verify the accuracy of the proposed algorithm. Our goal is to identify its maximum value:

$$f(x_1,x_2) = e - e^{\frac{\cos(2\pi x_1)+\cos(2\pi x_2)}{2}} + 2\pi - 2\pi e^{-0.2\times\frac{\sqrt{x_1^2+x_2^2}}{2}}. \tag{4}$$

The value range of parameter x_1 to be identified is the range [4,8], and that of parameter x_2 is the range [8,10].

Zero points of the 5-th order Legendre polynomials are applied, and the selection of the collocation points in the form of tensor product is completed as follows:

$$\{a_{j_1}, a_{j_2}\} = \{9.91, 9.54, 9.00, 8.46, 8.09\} \otimes \{7.81, 7.08, 6.00, 4.92, 4.19\}. \tag{5}$$

The result of parameter identification calculated by the SCM is $\{9.5453, 7.5097\}$. Substituting the result into formula (4), the maximum predicted value is 7.4980. The preliminary verification of the optimization effect is shown in Fig. 1. There are 3000 blue points, which are brought into formula (4) by the exhaustive method to verify the effect of parameter identification. The red star is the optimization result given by the SCM, which is obviously in the region where the optimal value is located.

Sorting 3000 sampling results, the results of the top 10 maximum values are shown in Table 2. Obviously, it verifies the effectiveness of the SCM in this optimization example. In this example, the SCM only needs to perform 25 times forward calculations of the formula (4). High computational efficiency of this proposed optimization algorithm is due to high convergence of the generalized polynomial chaos theory.

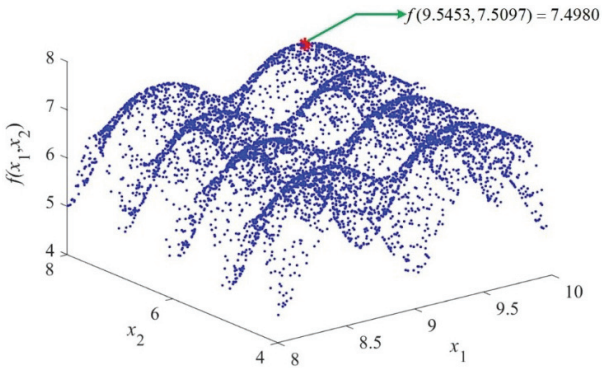

Fig. 1. Preliminary verification of the SCM in optimization effect.The red star is the maximum value position identified by SCM, and the blue dots represent the function value position of all grid points. It can be seen that the maximum value identified is consistent with the actual situation.

Table 2: Top 10 maximum values given by the exhaustive method

Order	Result
1	f(9.5073,7.5437)=7.4972
2	f(9.5589,7.5444)=7.4908
3	f(9.5463,7.4601)=7.4873
4	f(9.5975,7.5079)=7.4769
5	f(9.5975,7.5047)=7.4767
6	f(9.5534,7.5886)=7.4745
7	f(9.4821,7.4179)=7.4627
8	f(9.4154,7.5513)=7.4571
9	f(9.4169,7.5576)=7.4561
10	f(9.4466,7.4286)=7.4556

III. LIMITATION OF THE SCM AND ITS IMPROVEMENT SCHEME

In Section II, the effectiveness of the SCM in the optimization process has been preliminarily verified, especially its advantage of high computational efficiency.

However, choosing the collocation points in the form of tensor products will seriously affect the computational efficiency of the proposed optimization algorithm. The number of the collocation points is exponential with the number of random variables, which leads to the "curse of dimensionality". In this case, when there are many parameters to be identified, the times of the required forward simulations will increase explosively, and the SCM will lose its high computational efficiency. This is the limitation of the SCM, which suggests that the proposed optimization method is only applicable to a small number of parameters to be identified.

In uncertainty analysis, the sensitivity of different random variables can be predicted in advance in

the pretreatment stage. The random variables with low sensitivity can be replaced by the mean values to achieve the purpose of dimension reduction. With dimensionality the help of this idea, this section puts forward the improvement scheme of the SCM into the optimization process.

Firstly, the sensitivity calculation formula is as follows, which is proposed in reference [19]. It is a numerical approximate calculation method based on Richardson extrapolation method under the difference scheme, and has good nonlinear processing ability:

$$\begin{aligned} S_i = 2 \times & \frac{y_{EMC}\left(\overline{\xi_1}, \cdots \overline{\xi_i} + \frac{\delta_i}{2} \cdots, \overline{\xi_n}\right)}{\frac{\delta_i}{2}} \\ & - 2 \times \frac{y_{EMC}\left(\overline{\xi_1}, \cdots \overline{\xi_i} \cdots, \overline{\xi_n}\right)}{\frac{\delta_i}{2}} \\ & - \frac{y_{EMC}\left(\overline{\xi_1}, \cdots \overline{\xi_i} + \delta_i \cdots, \overline{\xi_n}\right)}{\delta_i} \\ & - \frac{y_{EMC}\left(\overline{\xi_1} \cdots \overline{\xi_i} \cdots, \overline{\xi_n}\right)}{\delta_i}, \end{aligned} \tag{6}$$

where $\overline{\xi_i}$ is the mean value of the random variable ξ_i, $y_{EMC}()$ indicates forward EMC simulation at the specific collocation point. δ_i is a small perturbation, and its value can be assumed to be $\frac{\max(\xi_i)-\min(\xi_i)}{2}$.

The improvement scheme of the SCM in the optimization process is as follows, and it divides the sensitivity into different levels before SCM calculation.

Step 1, according to formula (1), all parameters to be identified are transformed into random variables obeying the uniform distribution.

Step 2, according to formula (6), the sensitivity of every random variable is calculated, and it is used to classify random variables.

Step 3, random variables with low sensitivity are replaced by their mean values, and the SCM is used to carry out the optimization process on high sensitive random variables.

Step 4, random variables with high sensitivity are replaced by their optimal values calculated in the Step 3, and the SCM is used to carry out the optimization process a second time on low sensitivity random variables.

Step 5, the final results are the combination of all optimization parameters in the Step 3 and the Step 4.

Obviously, in this improvement scheme, the SCM optimizations are carried out twice for high sensitivity parameters and low sensitivity parameters respectively, so as to achieve the purpose of mitigating the "curse of dimensionality". For example, suppose that the number of parameters to be optimized is six, and the number of forward EMC simulations required for the normal SCM optimization is $5^6 = 15625$. Using the improvement scheme, this number is reduced to $2 \times 5^3 = 250$. In the process of sensitivity calculation, some forward EMC simulation times are added. Each random variable corresponds to the simulation of two perturbation quantities δ_i and $\frac{\delta_i}{2}$, plus the simulation at the mean value $\left(\overline{\xi_1}, \cdots \overline{\xi_i} \cdots \overline{\xi_n}\right)$, so the number of increases times is thirteen. The number of forward EMC simulations required for the improvement scheme is 263.

It is worth noting that the sensitivity of random variables can be divided into several levels, not just high level and low level, in order to improve the computational efficiency of the optimization process.

To sum up, the improvement scheme can effectively avoid the impact of the "curse of dimensionality" limitation of the SCM on the calculated efficiency of the optimization algorithm, which broadens the scope of application of the optimization algorithm proposed in this paper.

IV. EXAMPLE OF CROSSTALK PREDICTION IN THE CABLE CASCADE MODEL

In order to describe the geometric randomness caused by bundling or other factors, the cascaded transmission line model is usually used to model the cables [17]. According to the electromagnetic field theory, the closer the distance between cables, the stronger the electromagnetic coupling effect, and the greater the crosstalk between lines. According to this theorem, an optimization problem with known optimization results can be constructed through a cascade model, in order to verify the effectiveness of the proposed algorithm in this paper.

The schematic diagram of the cable cascade model is shown in Fig. 2. Two cables are laid flat on the ground aluminum plate, which are cascaded by six uniform transmission line models. The pink line is an interference emission line with a diameter of 0.07 m. The green line is the interference receiving line with a diameter of 0.09 m. According to the coordinate axis direction in Fig. 2, in

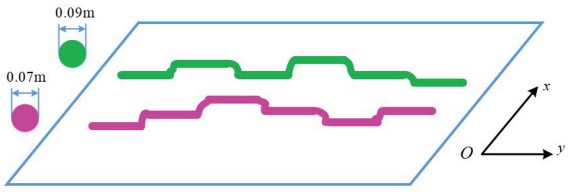

Fig. 2. Schematic diagram of the cable cascade model. The pink cable has electromagnetic interference, while the green one is the disturbed cable.

this example, the geometric position of the cable can be changed only in the x-axis direction.

Figure 3 shows the circuit schematic diagram of the crosstalk prediction problem. Both cables are 1m long and all load impedances are 50 Ω. The electromagnetic interference source is a sinusoidal excitation source with the amplitude of 1V and the frequency of 40 MHz. $U_{\text{crosstalk}}$ refers to the voltage crosstalk amplitude at the load end of the interference receiving line. The forward EMC simulation solver is the Finite Difference Time Domain method. The electrical parameters in the transmission line model are given by the image method and the electric axis method. Obviously, the ground heights of the two cables are their radius, namely 0.045 m and 0.035 m. Assume that the x-axis coordinates of the six transmission lines of the interference emission line are fixed, which are {2.5 m, 5.5 m, 5.7 m, 8.2 m, 6.9 m, 2.8 m}. The x-axis coordinates of the six transmission lines of the interference receiving line are parameters to be optimized. The optimization objective is to maximize the crosstalk value $U_{\text{crosstalk}}$. More information about crosstalk calculation is consistent with reference [17].

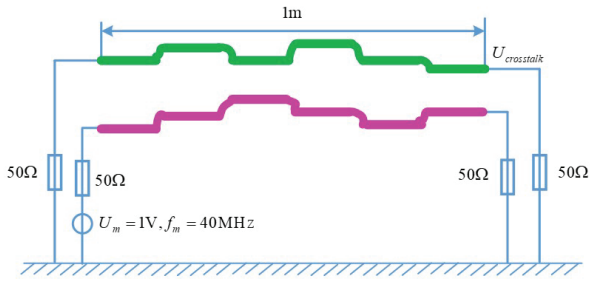

Fig. 3. Schematic diagram of the cable cascade model. The pink cable has electromagnetic interference, while the green one is the disturbed cable.

The value range of parameters to be optimized is from 1 m to 10 m. Obviously, the answer to this optimization problem is known. That is, when the two cables coincide, the crosstalk value is the largest, so the answer to the optimal design is {2.5 m, 5.5 m, 5.7 m, 8.2 m, 6.9 m, 2.8 m}. At this time, the crosstalk value is 0.0163 V. Since the cables in the example are solid (with radius), they cannot be completely coincident. Therefore, when calculating the distance between cables in the image method, when it is less than the sum of the radius of two cables $0.045 + 0.035 = 0.08$ m, the distance is directly equal to 0.08 m.

This article primarily aims to identify the optimal value of the simulation model, which is independent of the actual test results; therefore, no corresponding test results are provided.

Using the improved optimization algorithm mentioned in Section III, the optimization result is {2.5869 m, 5.5014 m, 5.6186 m, 8.0243 m, 7.4948 m, 2.7990 m}. The crosstalk value under this result is 0.0056 V.

The genetic algorithm and the immune algorithm are compared to verify the performance of the proposed algorithm. In the immune algorithm, 40 chromosome individuals are used for three generations of evolution, and the total number of forward EMC simulations required is 883. The final optimization result of the immune algorithm is {9.4595 m, 3.8242 m, 5.6702 m, 8.2771 m, 6.9049 m, 2.7770 m}, and its crosstalk value is 0.0037 V. The number of forward EMC simulation required by the SCM is only 263, less than one-third of 883, but its optimization result is better than that of the immune algorithm.

For the genetic algorithm, 60 chromosomes are used for 20 iterations, and the results are shown in Table 3. The final identification result of the SCM is better than that of the first 14 generations of the genetic algorithm. Similarly, the number of forward EMC simulations required is less than one-third of that of the genetic algorithm.

The intelligent optimization algorithm needs to obtain the optimal solution through repeated iterative evolution, while the SCM only completes

Table 3: Optimization results of genetic algorithm in crosstalk prediction example

Iteration Times	Simulation Times	Crosstalk Value
1	120	0.0011V
2	180	0.0011V
3	240	0.0017V
4	300	0.0017V
5	360	0.0023V
6	420	0.0023V
7	480	0.0024V
8	540	0.0032V
9	600	0.0032V
10	660	0.0032V
11	720	0.0033V
12	780	0.0034V
13	840	0.0040V
14	900	0.0049V
15	960	0.0059V
16	1020	0.0062V
17	1080	0.0063V
18	1140	0.0063V
19	1200	0.0063V
20	1260	0.0063V

the identification through a single operation without an iterative process. Therefore, the SCM can quickly obtain the local optimal solution because of its high convergence, but its ability to obtain the global optimal solution is obviously inferior to the intelligent optimization algorithm. Table 3 shows the ability of the genetic algorithm to seek the global optimal solution in the process of continuous iteration. It means that the SCM is more suitable for optimization problems where a single forward EMC simulation takes too long. The reason is that the intelligent optimization algorithm cannot be used because of its low computational efficiency. When the single EMC simulation time is short, the intelligent optimization algorithm is still the first choice.

V. EXAMPLE OF SHIELDING PERFORMANCE DESIGN OF METAL BOX

In order to verify the practicability of the proposed algorithm, this chapter applies it to the electromagnetic protection design example of metal box, and its design details are shown in Fig. 4. The size of the anechoic chamber is $3.9 \times 3.9 \times 3.3\text{m}^3$. The shielding material is carbon-loaded foam with low conductivity. There is a biconical antenna at the center of the darkroom, and this position is also assumed to be the coordinate origin. The details of the coordinate axis are also shown on the right side of Fig. 4. The antenna emits the spherical wave at the frequency of 10 MHz, other settings of the model are consistent with those shown in reference [20].

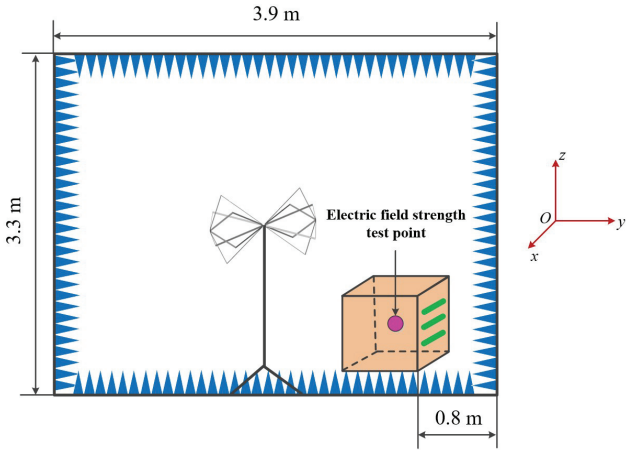

Fig. 4. Schematic diagram of shielding performance design. The green lines represent the strip cooling holes, which are supposed to be facing away from the antenna to achieve the best electromagnetic shielding effect.

There is an aluminum box 0.8 m away from the right wall of the anechoic chamber, and this position is fixed. The size of the box is $0.6 \times 0.6 \times 0.6\text{m}^3$ with a thickness of 0.02 m. There is an electromagnetic-sensitive device in the middle of the aluminum box. Therefore, the electric field strength at this location needs to be predicted, and the value should be minimized in the design process.

Similarly, there are six parameters to be optimized in this example. The first two parameters are the position parameters of the aluminum box in the x-axis and z-axis directions. Take the center point (pink test point) of the aluminum box in Fig. 4 as the reference point, and the value ranges of their coordinates are both $[-0.8\text{ m}, 0.8\text{ m}]$.

There are three cooling holes on the right side of the metal box, and its enlarged view is shown in Fig. 5. The lengths of the three holes are the parameters to be identified, and their value ranges are [0.36 m,0.44 m]. The width of the holes is assumed to be 0.01 m. The last parameter to be identified is the distance between the hole at both ends and the hole in the middle. It is assumed that the distance between the center and both ends is the same, that is, $h_1 = h_2$. Its value range is [0.06 m, 0.1 m]. Similarly, this example exclusively presents the optimization results derived from the simulation model.

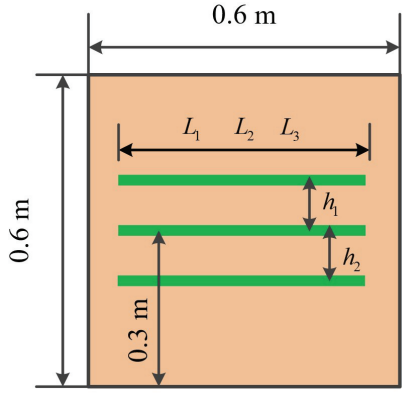

Fig. 5. Enlarged view of position information of cooling holes in the aluminum box. The length and relative position of the cooling holes are parameters to be optimized.

Using the optimization algorithm proposed in Section III, third order Legendre polynomials are selected, so the number of forward EMC simulations is $2 \times 3^3 + 2 \times 6 + 1 = 67$. The determination method of the order will be discussed in the next section. The final optimization result of the SCM is {-0.7991 m, 0.5456 m, 0.3970 m, 0.3600 m, 0.3609 m, 0.0609 m}, and the electric field strength value at this time is 3.0765×10^{-5} V/ m.

Table 4 shows the comparative optimization results of the genetic algorithm. A total of 60 chromosomes are used for 10 iterations. The SCM identification result is better than the results of the first two generations. In this case, the number of forward EMC simulations

Table 4: Optimization results of genetic algorithm in crosstalk prediction example

Iteration Times	Simulation Times	Crosstalk Value
1	120	3.5658×10^{-5} V/m
2	180	3.3418×10^{-5} V/m
3	240	2.4779×10^{-5} V/m
4	300	2.4779×10^{-5} V/m
5	360	2.4779×10^{-5} V/m
6	420	2.4779×10^{-5} V/m
7	480	2.4779×10^{-5} V/m
8	540	2.4779×10^{-5} V/m
9	600	2.4779×10^{-5} V/m
10	660	2.4779×10^{-5} V/m

required in the SCM is less than one-third of that of the genetic algorithm. However, after three generations of iteration, the genetic algorithm can quickly identify the global optimal solution. Therefore, the conclusion obtained through comparison is consistent with that in Section IV, that is, the SCM is better at finding the suboptimal solution quickly, while the genetic algorithm is inefficient but can find the global optimal solution.

It is worth noting that the genetic algorithm has converged in the third generation, but it cannot be determined that it has converged until the tenth generation. Therefore, in the practical application, the optimization design method based on the SCM has greater advantages in computational efficiency.

In order to further demonstrate the accuracy of the SCM, the optimization results of the exhaustive method are proposed for comparison. Sorting 500 sampling results, the optimization results of the top five minimum electric field strength values are shown in Table 5. Obviously, the optimization result given by the SCM is better than 500 sampling results in the exhaustive method. This is enough to prove the accuracy of the SCM in the optimization process.

Table 5: Optimization results of genetic algorithm in crosstalk prediction example

Order	Parameters [m]	Electric Field Intensity
1	−0.7991, −0.3189, 0.3757, 0.3908, 0.4276, 0.0888	3.3811×10^{-5} V/m
2	0.7845, −0.2846, 0.3799, 0.3733, 0.3796, 0.0972	3.4548×10^{-5} V/m
3	0.7131, −0.0191, 0.3720, 0.4344, 0.3800, 0.0964	3.5168×10^{-5} V/m
4	0.7946, 0.5739, 0.4131, 0.3665, 0.3848, 0.0743	3.5791×10^{-5} V/m
5	0.6650, 0.5878, 0.4023, 0.4335, 0.4123, 0.0958	3.5996×10^{-5} V/m

VI. PROSPECT OF THE PROPOSED OPTIMIZATION DESIGN METHOD

Prospect 1: Relationship between the number of sensitivity categories and the performance of optimization algorithm.

In this paper, sensitivity is only divided into high level and low level, but it can be divided into many categories. In the future work, especially in the multi-parameter optimization design problem, how to select the number of levels scientifically and reasonably will be discussed. Among them, the relationship between the number of the levels and the accuracy of the SCM, and how to allocate this number to maximize the calculation efficiency of the SCM are both worth discussing.

Prospect 2: Application of the proposed optimization algorithm in robust optimal design.

Due to the existence of manufacturing error and randomness in the actual engineering environment, the suboptimal solution with low sensitivity is sometimes more practical than the optimal solution with high sensitivity. Therefore, the concept of robust optimal design has been proposed in recent years [21, 22]. The optimization algorithm proposed in this paper can quickly find the suboptimal solution, so it is expected to be well applied in robust optimization design, especially in some cases where online identification is required.

VII. CONCLUSION

In this paper, the SCM, which is originally an uncertainty analysis method, is creatively applied to EMC optimization design to solve low computational efficiency problems of traditional intelligent optimization algorithms when single forward simulation takes a long time. Combined with the sensitivity approximate calculation method based on the Richardson extrapolation, an improved optimization scheme considering multiple sensitivity levels is proposed to avoid the adverse impact of the "curse of dimensionality" problem of the SCM with the optimum performance. Based on professional background of the EMC, two typical examples are designed. They are crosstalk prediction of cable cascade model and shielding performance design of metal box. The optimal design results of the SCM are quantitatively compared with those of genetic algorithm and immune algorithm, and the following conclusions are drawn. The SCM can quickly find the sub optimal solution or locally optimal solution. On the premise that it can only carry out finite forward simulations, the optimum performance of the SCM is better than that of the intelligent optimization

algorithm. However, the search ability of the SCM is not as good as that of intelligent optimization algorithm, so when the time of single forward simulation is short or the cost of single simulation is small, intelligent optimization algorithm is still a better choice.

REFERENCES

[1] C. Salvatore, L. Antonino, and F. F. Riganti, "TEAM problem 22 approached by a hybrid artifificial life method," *COMPEL The International Journal for Computation and Mathematics in Electrical and Electronic Engineering*, vol. 31, no. 3, pp. 816-826, May 2012.

[2] R. Jauregui, M. Aragon, and F. Silva, "The role of uncertainty in the feature selective validation (FSV) method," vol. 55, no. 1, pp. 217-220, Feb. 2013.

[3] K. R. Ali, Y. Shiyou, and K. Shafiullah, "A multimodal improved particle swarm optimization for high dimensional problems in electromagnetic devices," *Energies*, vol. 14, no. 24, p. 8575, Dec. 2021.

[4] O. U. Rehman and S. Yang, "A quantum particle swarm optimizer with enhanced strategy for global optimization of electromagnetic devices," *IEEE Transactions on Magnetics*, vol. 55, no. 8, pp. 1-4, May 2019.

[5] T. Zheng and S. Yang, "A robust methodology for design optimizations of electromagnetic devices under uncertainties," *International Journal of Applied Electromagnetics and Mechanics*, vol. 59, no. 1, pp. 71-78, Mar. 2019.

[6] S. An and L. Liu, "A preference-based physical programming method for multi-objective designs of electromagnetic devices," *EEE Transactions on Magnetics*, vol. 56, no. 3, pp. 1-4, Mar. 2020.

[7] A. Bingler, S. Bilicz, and M. Csörnyei, "Global sensitivity analysis using a Kriging metamodel for EM design problems with functional outputs," *IEEE Transactions on Magnetics*, vol. 58, no. 9, pp. 1-4, Apr. 2022.

[8] Y. Li and S. Xiao, "A dual Kriging approach with improved points selection algorithm for memory efficient surrogate optimization in electromagnetics," *IEEE Transactions on Magnetics*, vol. 52, no. 3, pp. 1-4, Mar. 2016.

[9] J. Bai, B. Hu, and Z. Xue, "EMC uncertainty simulation method based on improved Kriging model," *IEEE Letters on Electromagnetic Compatibility Practice and Applications*, vol. 5, no. 4, pp. 127-130, July 2023.

[10] T. Akhtar and C. A. Shoemaker, "Multi objective optimization of computationally expensive multi-modal functions with RBF surrogates and multi-rule selection," *Journal of Global Optimization*, vol. 64, no. 1, pp. 17-32, Jan. 2016.

[11] G. Spadacini and S. A. Pignari, "Numerical assessment of radiated susceptibility of twisted-wire pairs with random nonuniform twisting," *IEEE Transactions on Electromagnetic Compatibility*, vol. 55, no. 5, pp. 956-964, Oct. 2013.

[12] C. Jullien and P. Besnier, "Advanced modeling of crosstalk between an unshielded twisted pair cable and an unshielded wire above a ground plane," *IEEE Transactions on Electromagnetic Compatibility*, vol. 55, no. 1, pp. 183-194, Feb. 2013.

[13] Z. Fei and Y. Huang, "Uncertainty quantification of crosstalk using stochastic reduced order models," *IEEE Transactions on Electromagnetic Compatibility*, vol. 59, no. 1, pp. 228-239, Aug. 2017.

[14] J. Bai and L. Wang, "Validity evaluation of the uncertain EMC simulation results," *IEEE Transactions on Electromagnetic Compatibility*, vol. 59, no. 3, pp. 797-804, June 2017.

[15] J. Bai and J. Sun, "Convergence determination of EMC uncertainty simulation based on the improved mean equivalent area method," *Applied Computational Electromagnetics Society (ACES) Journal*, vol. 36, no. 11, pp. 1446-1452, Dec. 2021.

[16] P. Manfredi and D. V. Ginste, "Stochastic transmission line analysis via Polynomial Chaos Methods: An overview," *IEEE Electromagnetic Compatibility Magazine*, vol. 6, no. 3, pp. 77-84, Nov. 2017.

[17] J. Bai and G. Zhang, "Performance comparison of the SGM and the SCM in EMC simulation," *IEEE Transactions on Electromagnetic Compatibility*, vol. 58, no. 6, pp. 1739-1746, Dec. 2016.

[18] J. Bai and G. Zhang, "Dimension-reduced sparse grid strategy for a stochastic collocation method in EMC software," *IEEE Transactions on Electromagnetic Compatibility*, vol. 60, no. 1, pp. 218-224, Feb. 2018.

[19] J. Bai and G. Zhang, "Uncertainty analysis in EMC simulation based on improved Method of Moments," *IEEE Transactions on Electromagnetic Compatibility*, vol. 31, no. 1, pp. 66-71, Dec. 2021.

[20] COMSOL. (2023, Oct.) Anechoic electromagnetic wave absorption [Online]. Available: http://cn.comsol.com/model/anechoicchamber-absorbing-electromagnetic-waves-38681

[21] Z. Ren and J. Ma, "Managing uncertainties of permanent magnet synchronous machine by adaptive Kriging assisted weight index Monte Carlo simulation method," *IEEE Transactions on Electromagnetic Compatibility*, vol. 35, no. 4, pp. 2162-2169, Dec. 2020.

[22] M. Xia and D. Sun, "A novel methodology for robust topology optimization considering manufacturing errors and topology deviations," *IEEE Transactions on Electromagnetic Compatibility*, vol. 58, no. 9, pp. 1-4, Sep. 2022.

Xiaobing Niu received the B.S. degree in electrical engineering and the M.E. degree in electrical drive and its automation from Dalian Maritime University, Dalian, China, in 1991 and 1998, respectively. He is currently an Associate Professor with the School of Marine Electrical Engineering, Dalian Maritime University. His current research interests include motor control theory and its applications, energy transformation and its EMC problem.

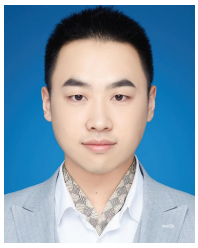

Shenglin Liu received the B.S. degree in marine electronic and electrical engineering from Dalian Maritime University, Dalian, China, in 2015. He is currently working toward the M.E. degree in Dalian Maritime University. His current research interests include modular multilevel converters control theory with applications to high voltage direct current and design of power electronic interfaces.

Runze Qiu received the B.S. degree in electrical engineering and automation from Hohai University, Nanjing, China, in 2022.He is currently pursuing the master's degree in electrical engineering at Dalian Maritime University, Dalian, China.His current research interests include modular multilevel converters in marine electrical systems, and transmission systems for offshore wind power.

A Spoof Surface Plasmon Polaritons Filter with Controllable Negative Slope Equalization Based on Surface Resistance

Chenhao Wang[1], Junjie Dong[1], Xiaomin Shi[2], and Hailong Yang[3]

[1]Xi'an Key Laboratory of Intelligence
Xi'an Technological University, Xi'an 710021, China
wangchenhao@xatu.edu.cn, xxhrlle@163.com

[2]Department of Communication Engineering
Xi'an Shiyou University, Xi'an 710065, China
xmshi@xsyu.edu.cn

[3]School of Electronic Engineering
Xi'an University of Posts and Telecommunications, Xi'an 710100, China
yanghl68@163.com

Abstract – This paper presents a novel spoof surface plasmon polariton (SSPP) filter integrated with controllable negative slope equalization. Different from traditional microwave filters, two microwave functions - amplitude compensation and interference suppression - are integrated into one device by depositing a lossy indium tin oxide (ITO) film on the rectangular corrugated stub of the SSPP unit. The key point of negative slope equalization benefits from the surface resistance of the ITO film, and the circuit model and behavior are analyzed in detail. Based on the principle, a prototype of a SSPP filter operating from S to C band is designed and fabricated. The measurement results show that the attenuation in the passband increases almost linearly from 3.5 GHz (−4.8 dB) to 6.9 GHz (−15.4 dB), indicating that −10.6 dB equalization is achieved. The improved S_{21} is attributed to the good impedance matching by sputtering the ITO film on the rectangular metal strip rather than the central strip. Due to the natural low-pass property of SSPPs, the high-order parasitic band is suppressed above the cut-off frequency of 8.5 GHz. The analyses, simulations and measurements show that the proposed SSPP filter is provided with an additional ability to compensate for positive amplitude fluctuation in wideband antennas.

Index Terms – equalization, indium tin oxide, low-pass filter, spoof surface plasmon polaritons.

I. INTRODUCTION

The amplitude compensation of frequency domain is a perpetual topic in microwave wideband systems. Although most microwave systems experience a negative slope response, where the gain decreases with increasing frequency, positive slope response is common due to chip process or device characteristics. For example, the radiation efficiency of the high-frequency band of a wideband antenna is higher than that of the low-frequency band, which requires a negative slope equalizer to smooth fluctuations.

In recent years, various types of equalizers have been proposed to smooth the system gain curves [1–5]. In [1], a substrate-integrated-waveguide (SIW) equalizer operating in millimeter wave is investigated by spraying tantalum nitride on the substrate. The positive slope transmission curves with different equalizing values of 2.8, 5.6 and 9 dB are synthesized over the whole Ka band. In [2], a gain equalizer based on periodic spiral-shaped defected ground structure is proposed, which achieved good isolation effects due to the confinement of the electric field by the grounded coplanar waveguide. Further, in order to regulate attenuation, micro-electro-mechanical system (MEMS) switches are used to achieve a reconfigurable microwave equalizer, realizing four different attenuations of 7.0, 6.6, 5.9 and 5.6 dB [3]. A number of other different equalizing structures, such as active SiGe heterojunction bipolar transistor [4] or stepped impedance resonator [5], have enabled the realization of various equalizing curves. However, due to the inherent resonance structure, the high-order periodic response of the existing microwave equalizer will deteriorate the suppression performance out of the passband of broadband systems, which is imperceptible. Additional measures need to be studied to alleviate this situation.

Spoof surface plasmon polaritons (SSPPs) are a highly confined surface mode at the interface between a dielectric and periodic metal structure, which has

Submitted On: November 23, 2023
Accepted On: August 12, 2024

https://doi.org/10.13052/2024.ACES.J.390608

attracted extensive attention. Since Pendry theoretically proved the existence of SSPPs [6] in 2004 and Hibbins experimentally confirmed the surface mode [7] in 2005, many investigations have been conducted on microwave devices based on SSPPs, such as filter [8], antenna [9] and power divider [10]. Due to inherent dispersion, surface waves higher than the asymptotic frequency cannot propagate in SSPPs, that is, the natural low-pass filter. Although the insertion loss of SSPPs is larger than other transmission structures, it provides a method to suppress the periodic response of microwave devices.

In view of the above two key points, this paper presents a novel SSPP filter with controllable negative slope equalization. The equalization and low-pass properties are explained in detail. To validate the method, a prototype is designed, simulated and measured. The results show that the proposed SSPP filter achieves a linear equalization from 3.5 GHz to 6.9 GHz with −10.6 dB equalizing value. Periodic response does not occur in the upper stopband from 8.5 GHz to 15 GHz. Compared with existing SSPP filters, the proposed filter has obvious advantages in realizing equalization and filtering functions simultaneously, which can smooth the positive slope gain response caused by higher radiation efficiency in the high-frequency band, such as wideband antennas.

II. CIRCUIT MODEL OF THE UNIT CELL

The SSPPs unit cell of the proposed filter is shown in Fig. 1 (a). The double-sided corrugated strip is coated on the transparent polyethylene terephthalate (PET) film, with relative dielectric constant $\varepsilon_r = 3$ and thickness t = 100 μm. In contrast to regular SSPP unit cells, indium tin oxide (ITO) conductive material is uniformly sputtered on the rectangular corrugated strip instead of ideal metal thin layer, as indicated by the gray region in Fig. 1 (a). The residual center metal strip is shown by the yellow region. The main parameters of the unit cell during the analysis are set as follows: the width and length of the ITO strip are h=26 mm, b=1.5 mm; the width and length of the metal strip are w=1.4 mm, l=3 mm; and the period of the unit cell is p=6 mm, respectively.

The equalization and filtering properties can be analyzed by the equivalent model of the SSPP unit cell. Since the unit cell in Fig. 1 (a) is a single conductor structure, the ground plane can be defined at infinity, that is, the RLC network as depicted in Fig. 1 (b) can be extracted and calculated using the method provided in [11]. It should be noted that the equivalent resistance R_s depends on the surface impedance Z_s of the ITO film, which can be calculated by (1):

$$\mathrm{R_s} = \frac{\mathrm{Z_s(h/2)}}{\mathrm{b}}. \tag{1}$$

Combining the structure parameters mentioned above with the setting of Z_S=2.5 Ω/□, each element is calculated as L_m=3.44 nH, L_s=0.58 nH, L_i=0.04 nH,

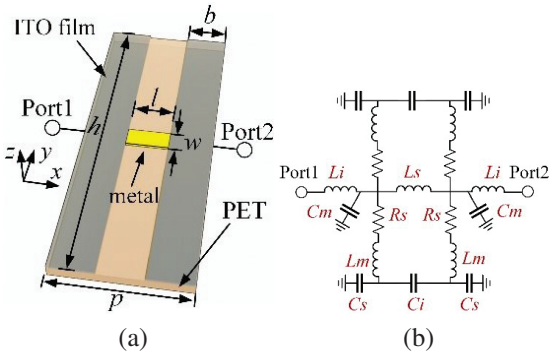

Fig. 1. Layout (a) and equivalent circuit (b) of the SSPP unit cell.

C_s=540 fF, C_m=258 fF, C_i=77 fF and R_s=20 Ω. When the surface transverse magnetic (TM) energy flows across a period length p of the unit cell, the phase and amplitude of the propagating surface wave increases and decays by a constant, respectively, which can be defined in the ABCD matrix as follows:

$$\begin{bmatrix} V_n \\ I_n \end{bmatrix} = [\mathrm{A}_M] \begin{bmatrix} V_{n-1} \\ I_{n-1} \end{bmatrix} = \begin{bmatrix} e^{\gamma_x p} V_{n-1} \\ e^{\gamma_x p} I_{n-1} \end{bmatrix}, \tag{2}$$

where $[\mathrm{V_n}, \mathrm{I_n}]$ and $[\mathrm{V_{n-1}}, \mathrm{I_{n-1}}]$ are the voltage-current pairs on both sides of the unit cell, $\gamma_x = \alpha_x + i\beta_x$ is the propagation constant in the x-direction of surface wave propagation, with α_x being the attenuation constant and β_x the phase constant. $[\mathrm{A_M}]$ is the transmission matrix of the RLC-network in Fig. 1 (b), which can be expressed in terms of R_s, L_i, L_s, L_m, C_i, C_s and C_m. For a symmetric network, the elements A, B, C and D in matrix $[\mathrm{A_M}]$ satisfy $A{\cdot}D - B{\cdot}C = 1$, hence, $\gamma_x$can be expressed as:

$$\gamma_x = \alpha_x + i\beta_x = \frac{\mathrm{arcosh(A)}}{\mathrm{p}}. \tag{3}$$

The real-part α_x and imaginary-part β_x in (3) describe the equalization and dispersion properties of the unit cell, respectively. For ease of understanding, Fig. 2 depicts the two characteristic curves. In Fig. 2 (a), similar to the lossless SSPPs, all dispersion curves obviously deviate from the light as β_x gradually increases. As the width of ITO strip h gradually decreases from 26 mm to 14 mm, the asymptotic frequency of the proposed unit cell increases from 3.5 GHz to 6.9 GHz, indicating that dispersion ability is maintained even though the ITO film is loaded and the transmission of the confined TM surface is still supported. In Fig. 2 (b), the curve of attenuation constant α_x exhibits an additional energy fading of the unit cell along with the frequency, which is manifested by the increase in the modulus of α_x. The equalization band is defined as the corresponding frequency when α_x is between a certain value and 0. For ease of understanding, an example of $\alpha_x = 26$ is provided for illustration in Fig. 2 (b). The equalization bands of the three curves start from direct current ($\alpha_x = 0$) and end

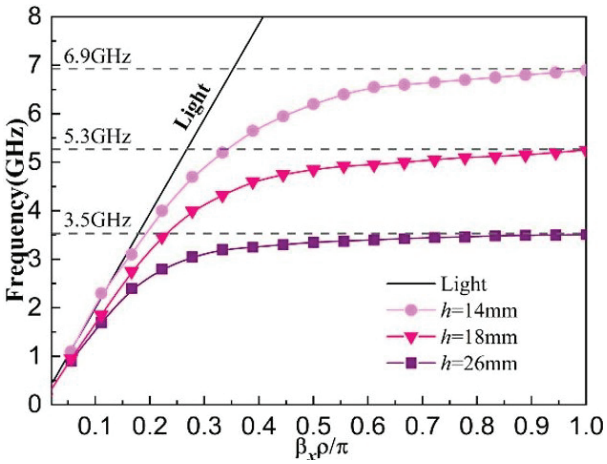

(a)

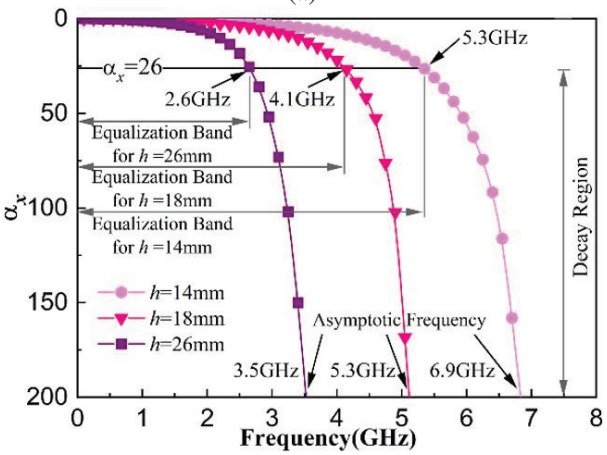

(b)

Fig. 2. Dispersion curves (a) and attenuation curves (b) of the SSPP unit cell with various widths h.

at 2.6 GHz, 4.1 GHz and 5.3 GHz ($\alpha_x = 26$) with the almost linear negative decay slopes of −9.7 Np/GHz, −6.5 Np/GHz and −5.0 Np/GHz, respectively. By converting the unit of voltage attenuation multiple to logarithm, an equalizing value of −1.35 dB can be achieved within the period length p=6 mm of a unit cell to compensate for the positive amplitude fluctuations. In addition, it can be observed that all curves converge to the constant $\alpha_x = 26$ near each asymptotic frequency. This is important because it provides an effective mean for tuning the bandwidth of the filter while maintaining a fixed equalizing value.

Furthermore, in order to investigate how well the controllable equalization of the SSPP unit cell meets different compensation requirements, the equalizing curves with various values of R_s under a fixed h=18 mm are shown in Fig. 3. All curves terminate at the same asymptotic frequency of 5.3 GHz. With R_s increasing from 5 Ω to 40 Ω, the equalizing values increase slowly, resulting in the slopes of −1.40 Np/GHz, −2.72 Np/GHz, −4.84 Np/GHz and −6.83 Np/GHz in the equalization band from 0.4 GHz to 4.0 GHz, respectively. The slope is linearly proportional to R_s, namely, the controllable amplitude compensation is achieved by the surface impedance of the ITO film. Especially when R_s decreases to 0 Ω, the ITO thin film strip degenerates into an ideal conductor, and the attenuation curve of R_s=0 Ω returns to the traditional lossless SSPPs as shown in Fig. 3, with the equalization ability no longer provided.

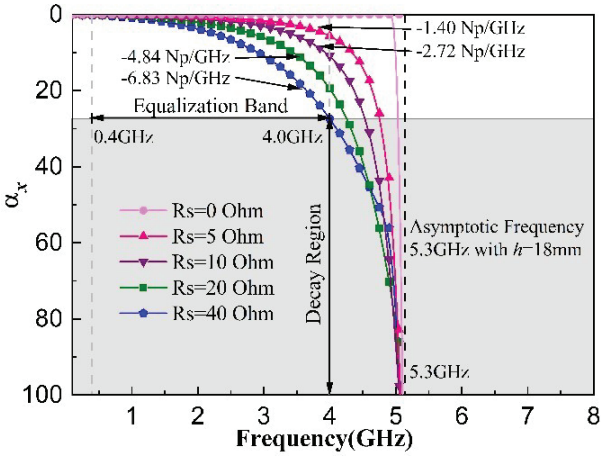

Fig. 3. Attenuation curves of the SSPP unit cell with various surface impedance Z_s.

III. THE DESIGN AND MEASUREMENT OF THE SSPP FILTER

Based on the analysis described above, a SSPP filter with controllable negative slope equalization is proposed. Figure 4 exhibits the geometry of the filter which consists of three regions: (1) coplanar waveguide (CPW) region, (2) transition region and (3) SSPP waveguide region. The geometric parameters are set as: p=6 mm, w=1.4 mm, l=3 mm, h=14 mm, d=1.2 mm and Z_S=5 Ω/□. The CPW transmission line supports transverse electro-magnetic (TEM) mode and provides 50 Ω connection node for external systems. The conversion

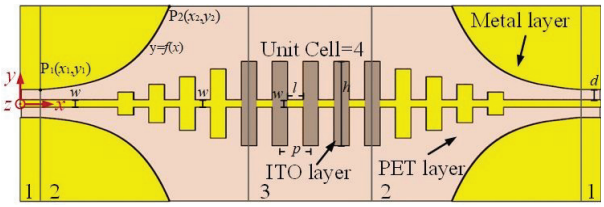

Fig. 4. Geometric configuration of the proposed SSPP unit cell consists of three regions: (1) coplanar waveguide region, (2) transition region and (3) SSPP waveguide region.

structure is used to complete smooth momentum and impedance conversion between TEM and TM mode [12]. As shown in Fig. 4, the conversion structure includes flared ground and gradient grooves, increasing the groove width from w=1.4 mm to h=14 mm in increments of 2.52 mm, and the outline of the flared ground is characterized as:

$$y = f(x) = C_1 e^{ax} + C_2, \tag{4}$$

where $x_1 \le x \le x_2$, $P_1(x_1, y_1)$ and $P_2(x_2, y_2)$ are the origin and destination of the outline, $C_1 = \frac{y_2 - y_1}{e^{ax_2} - e^{ax_1}}$, $C_2 = \frac{y_1 e^{ax_2} - y_2 e^{ax_1}}{e^{ax_2} - e^{ax_1}}$, the optimal values are a=0.14, $|x_2 - x_1| = 25\ mm$,$|y_2 - y_1| = 16.05\ mm$.

The SSPP waveguide region mainly determines the performance of the filter. As shown in Fig. 5 (a), the frequency characteristic of the SSPP filter depends on the width of the ITO strip. As h increases from 11 mm to 16 mm, the cut-off frequency decreases from 8.1 GHz to 5.3 GHz with the −10 dB equalizing bandwidth of 4.9 GHz, 2.9 GHz and 1.7 GHz, respectively. Due to the SSPP filter being a single conductor structure, the insertion loss below 3.6 GHz is relatively large, which can be improved by employing grounded SSPPs. According to the analysis in Section II, the adjustment of the equalizing value in the passband can be realized by regulating the surface resistance Z_s of the ITO film. Figure 5 (b) depicts the relationship between Z_s and the transmission curve with h=14 mm. As expected, the equalizing values within the equalization band from 3.5 GHz to 6 GHz are 8 dB, 11.5 dB, 13.6 dB and 15.6 dB, respectively, along with Z_s increases from 5 Ω to 10 Ω, 15 Ω and 20 Ω. The higher the surface resistance, the greater the response that can be compensated. These adjustable parameters provide sufficient flexibility in practical negative response, which can be applied in microwave systems with positive fluctuations such as wideband antennas.

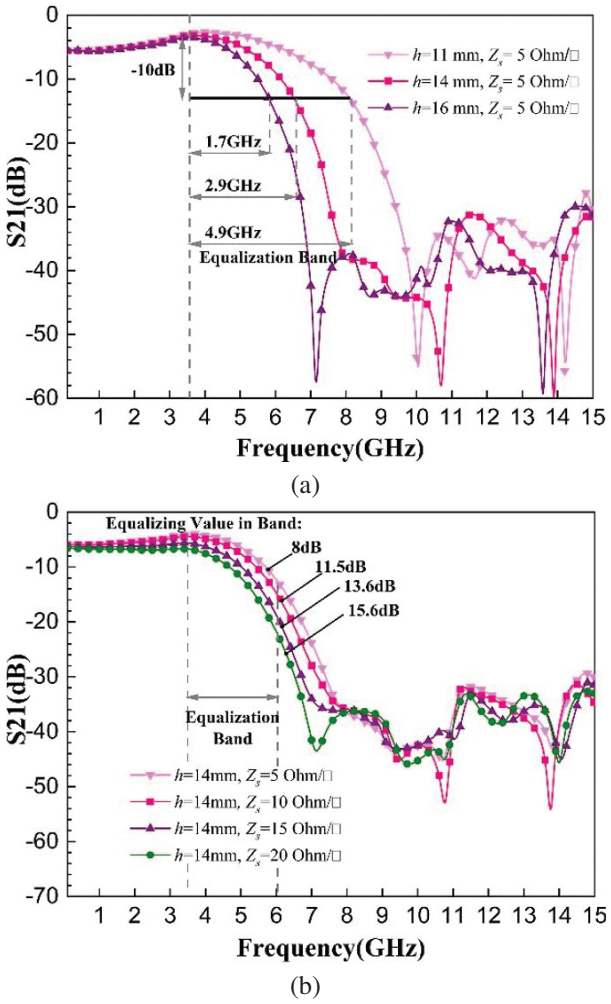

Fig. 5. (a) h-dependency of S_{21} curves and (b) Z_s-dependency of S_{21} curves.

To validate the above analysis, a prototype of the proposed SSPP filter with controllable negative slope equalization is manufactured. The flexible PET film is selected as the substrate with relative dielectric constant ε_r= 3 and layer thickness t = 100 μm. Figure 6 shows the vertical view and measurement results of the filter. The dimensions mentioned in Fig. 4 are optimized as: p=6 mm, w=1.4 mm, l=3 mm, h=14.7 mm, d=1.2 mm, $Z_S = 5\ \Omega/\square$, the coefficient a in (4) is 0.14.

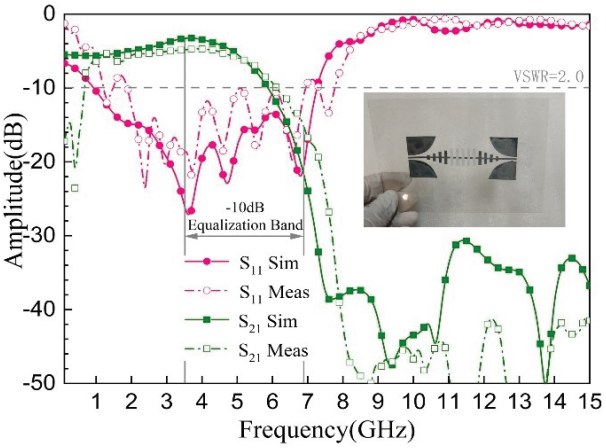

Fig. 6. Measurement and simulation results of the SSPP filter with negative slope equalization.

Before measurement, conductive silver paste is used to bond the SMA connector to the two ports of the filter. The measurement results are obtained by vector network analyzer P5008A of Keysight. It can be seen that the low-pass cut-off frequency of the filter is 8.5 GHz, and negative slope equalization is realized in the passband. The −10 dB equalization band starts at 3.5 GHz (IL = −4.8 dB) and ends at 6.9 GHz (IL = −15.4 dB).

The average reflection coefficient is −13 dB, which is superior to the filter in [13]. The suppression of the upper stopband up to 15 GHz is better than −41 dB, thus the interference can be eliminated effectively. Since the loss of the PET substrate is relatively larger in application compared to theoretical calculation, the insertion loss of the measured curve is greater than the simulated one. However, the advantage of the PET substrate is that it brings the flexibility of the filter in applications, which enables it to be assembled with conformal surfaces and it occupies less volume.

Table 1 compares the performance of the proposed SSPP filter with similar works. It can be observed that the proposed SSPP filter is provided with filtering and negative slope equalization simultaneously, which can compensate for positive fluctuations, such as wideband antenna.

Table 1: Performance comparison with recent reported works

Ref. No.	**Function**		**IL or EV (dB)**	**FBW**	**Slope**	**Struc**
	F	E				
[1]	N	Y	9	42%	Positive	SIW
[2]	N	Y	8	50%	Neg.Seg	CPW
[5]	N	Y	8.6	78%	Neg.Seg	Microstrip
[8]	Y	N	1.1	174%	NA	SSPP
[14]	Y	N	1.6	200%	NA	SSPP
This work	**Y**	**Y**	**10**	**65%**	**Negative**	**SSPP**

F=Filter, E=Equalization, N=No, Y=Yes, IL=Insert Loss, EV=Equalizing Value, Struc=Structure, Neg.Seg=Negative Segment, FBW=Fractional Bandwidth

IV. CONCLUSION

In this paper, a SSPP filter with controllable negative slope equalization based on surface resistance of ITO film is designed, fabricated and measured. The dispersion and equalization properties of the SSPP cells are analyzed in detail. Subsequently, a SSPP filter equipped with amplitude equalization is proposed by employing the unit cell, and controlling the cut-off frequency and equalizing value by the width and surface impedance of an ITO strip. Compared with other published works, the verified properties show that the proposed SSPP filter possesses filtering and negative slope equalization properties simultaneously.

ACKNOWLEDGMENT

This work was supported in part by the Natural Science Basic Research Program of Shaanxi Province under Grant 2023-JC-QN-0500, in part by the Scientific Research Program Funded by Education Department of Shaanxi Provincial Government under Grant 23JK0485, 21JK0847, and in part by the National Science Foundation of China under Grant 62301428.

REFERENCES

[1] H. Peng, F. J. Zhao, J. Dong, S. O. Tatu, Y. Liu, N. J. Lin, and T. Yang, "Substrate integrated waveguide equalizers and attenuators with surface resistance," *IEEE Trans. Microw. Theory Techn.*, vol. 68, no. 4, pp. 1487-1495, Apr. 2020.

[2] X. Pang, L. Xia, and J. N. Jiao, "A gain equalizer based on grounded coplanar waveguide with spiral-shaped defected ground," in *2022 IEEE 9th Int. Sym. Microw. Antenna Propag. EMC Technol. Wireless Commun. (MAPE)*, Chengdu, China, pp. 15-19, Aug. 2022.

[3] L. Han, "A reconfigurable microwave equalizer with different maximum attenuations based on RF MEMS switches," *IEEE Sensors J.*, vol. 16, no. 1, pp. 17-18, Jan. 2016.

[4] Y. Itoh and H. Takagi, "L-band SiGe HBT active differential equalizers with variable inclination and position of the positive or negative gain slopes," *46th Eur. Microw. Conf.*, London, UK, Oct. 2016.

[5] T. F. Zhou, Z. G. Wang, W. Huan, and R. M. Xu, "Design of microwave wave gain equalizer using microstrip shorted SIR," in *Int. Conf. Microw. Millim. Wave Technol.*, Shenzhen, China, May 2012.

[6] J. B. Pendry, L. Martín-Moreno, and F. J. Garcia-Vidal, "Mimicking surface plasmons with structured surfaces," *Science*, vol. 305, pp. 847-848, Aug. 2004.

[7] A. P. Hibbins, B. R. Evans, and J. R. Sambles, "Experimental verification of designer surface plasmons," *Science*, vol. 308, pp. 670-672, Apr. 2005.

[8] M. Wang, S. Sun, H. F. Ma, and T. J. Cui, "Supercompact and ultrawideband surface plasmonic bandpass filter," *IEEE Trans. Microw. Theory Techn.*, vol. 68, no. 2, pp. 732-740, Feb. 2020.

[9] J. Wang, K. X. Xu, X. L. Kong, R. F. Xu, and L. Zhao, "Wide-angle beam-scanning leaky-wave antenna array based on hole array SSPPs," *IEEE Antennas Wireless Propag. Lett.*, vol. 22, no. 7, pp. 1731-1735, July 2023.

[10] B. C. Pan, P. Yu, Z. Liao, F. Zhu, and G. Q. Luo, "A compact filtering power divider based on spoof surface plasmon polaritons and substrate integrated waveguide," *IEEE Microw. Wireless Compon. Lett.*, vol. 32, no. 2, pp. 101-104, Feb. 2022.

[11] A. Kianinejad, Z. N. Chen, and C. W. Qiu, "Design and modeling of spoof surface plasmon modes-based microwave slow-wave transmission line," *IEEE Trans. Microw. Theory Techn.*, vol. 63, no. 6, pp. 1817-1825, June 2015.

[12] H. F. Ma, X. P. Shen, Q. Cheng, W. X. Jiang, and T. J. Cui, "Broadband and high-efficiency conversion from guided waves to spoof surface plasmon polaritons," *Laser Photon. Rev.*, vol. 8, no. 1, pp. 146-151, 2014.

[13] C. H. Wang, X. M. Shi, H. L. Yang, and X. L. Xi, "A flexible amplitude equalizing filter based on spoof surface plasmon polaritons," *IEEE Trans. Antennas Propag.*, vol. 71, no. 7, pp. 5777-5785, July 2023.

[14] Y. L. Wu, L. D. Pan, W. M. Wang, Y. H. Yang, Y. W. Wei, H. P. Wu, and L. Ma, "A new self-packaged substrate integrated air-filled spoof surface plasmon polaritons line with inherent low loss and deep upper frequency suppression," *IEEE Trans. Plasma. Sci.*, vol. 48, no. 10, pp. 3516-3523, Oct. 2020.

Chenhao Wang was born in Shaanxi province, China, in 1988. He received the B.S., M.S. and Ph.D. degrees in electromagnetic field and microwave technology from Xi'an University of Technology, Xi'an, China, in 2011, 2014 and 2022, respectively. He currently works at Xi'an Technological University, Xi'an, China. His current research interests include spoof surface plasmon polaritons and novel metamaterial functional devices, including theoretical design and experimental realization.

Junjie Dong received the B.S. degree from China West Normal University, Nanchong, China, in 2021. He is currently pursuing the M.S. degree at Xi'an Technological University, Xi'an, China. His research interests include metamaterial and microwave filters.

Xiaomin Shi received the B.S., M.S. and Ph.D. degrees in electromagnetic field and microwave technology from Xi'an University of Technology, Xi'an, China, in 2006, 2010 and 2017, respectively. She joined the Department of Communication Engineering, Xi'an Shiyou University, in 2017. Her current research interests include microwave circuits and graphene-based devices.

Hailong Yang received the B.S. in communicating engineering from Heze University, Heze, China, in 2012, and M.S and Ph.D. degrees in communicating engineering from Xi'an University of Technology, Xi'an, China, in 2015 and 2019. He joined the faculty of Electronic Engineering Department, Xi'an University of Posts and Telecommunications, in 2019. His research interests include wave propagation and antenna design.

A Low-profile Dual-band Frequency Selective Surface with High Selectivity at its Higher Passband

Jian Jiao[1], Nianxi Xu[2], and Jinsong Gao[3]

[1]School of Physics
Changchun Normal University, Changchun 130032, China
xinhe7hl@126.com

[2]Key Laboratory of Optical System Advanced Manufacturing Technology
Changchun Institute of Optics, Fine Mechanics and Physics, Chinese Academy of Sciences
Changchun 130033, China
xnxlzhy999@126.com

[3]Jilin Provincial Key Laboratory of Advanced Optoelectronic Equipment and Instruments Manufacturing Technologies
Changchun 130033, China
gaojs@ciomp.ac.cn

Abstract – In order to meet the requirements for multi-band communication, a dual-band passband frequency selective surface (FSS) with low-profile and high selectivity at its higher passband is proposed in this paper. The proposed FSS is a three-layer structure. An arc-cross patch (ACP) and four quarter-circular patches (QCP) are introduced on the outer layers to produce two transmission nulls of the higher passband, which result in high selectivity of higher passband. The inductively complementary structure on the middle layer is introduced to manipulate the coupling between layers which contribute to the low-profile and angular stability. The segmental study method is used to establish the equivalent circuit model (ECM) and analyze its mechanism. The proposed dual-band FSS, whose high selectivity was verified by experiment, is low-profile and shows good polarization insensitivity and angular stability. A feasible FSS design solution is provided for dual-band communication.

Index Terms – Complementary structure, dual-band, frequency selective surfaces, high selectivity, low-profile.

I. INTRODUCTION

Frequency selective surfaces (FSSs) are two-dimensional periodic structures which can control the propagation of electromagnetic waves and are widely used in antenna [1], radome [2], satellite communication [3], electromagnetic shielding [4], and so on. With the development of communication technology, the demands of multi-band communication systems have increased. Therefore, the study of FSSs that meet the application requirements of multi-band communication systems is of great significance [5][6].

In previous studies, various techniques have been proposed to develop multiband performance. In [7], a dual-band 3D FSS with close band spacing were designed based on SCW structure. One modified parallel-plate waveguide propagation path and one SCW propagation path are responsible for dual passband, and the counteraction between them contributes to transmission zeros, resulting in a high selectivity of 2.65 at the higher passband. Nevertheless, its thickness is $0.145\lambda_{10}$, where λ_{10} refers to the free-space wavelength corresponding to the center frequency of the lower passband. In [8], based on an interlaced grid arrangement, a 3D dual-band FSS with large band ratio is proposed. Grating structures form higher passbands, and the additional wire-grid polarizers form the lower passband. It has poor selectivity. Its thickness is $0.139\lambda_{10}$, and its upper passband response is not stable when the incident angle increases to 40°. In [9], the proposed unit cell is evolved from a cross-shaped structure surrounded by an inductive grid. Diagonal feed networks are proposed to accomplish the dc bias, and different transmission poles are produced by soldering different varactors to diagonal units. It is angular stable, and its thickness is only $0.007\lambda_{10}$. However, it shows poor selectivity, and lumped elements would introduce large insertion loss. Cascaded FSSs is the most popular approach to design multi-band FSSs [10][11]. The FSS proposed in [10] is a three-layer structure. One metallic cross-shaped grid

Submitted On: February 18, 2024
Accepted On: August 27, 2024

https://doi.org/10.13052/2024.ACES.J.390609

layer is sandwiched by two metallic layers with a split ring-shaped slot. The slots in the outer layer are responsible for the lower passband, and the three-layer FSS forms a second order hybrid resonator at higher bandpass. Its thickness is $0.017\lambda_{10}$ and its *SF* value is 2.14 at higher passband. In [11], a frequency-selective rasorber is presented. The lossy layer is a combination of a loop with loaded resistors and three folded loops, and the FSS layer consists of double hexagon loop slots. Its two transmission poles are generated by two parallel LC circuits. Its thickness is $0.16\lambda_{10}$ and its *SF* value is 2.71 at higher passband. The performance of the FSSs in the above literatures are compared with this work in Table 1.

In this paper, a novel dual-band passband FSS with low-profile and high selectivity at higher passband is presented. The lower passband has one transmission pole whereas the higher passband has two transmission poles. Its thickness is reduced to $0.015\lambda_{10}$ and the performance of selectivity is improved to 1.85. The structure consists of three metallic layers and two thin dielectric substrates. An arc-cross patch (ACP) and four quarter-circular patches (QCP) are introduced in the outer layer to generate two transmission nulls which are the key factors in forming fast roll-off characteristics of the higher passband. A complementary structure of the outer layer is introduced in the middle layer to regulate the coupling between layers, which plays an important role in forming the low-profile and angular stability. The proposed FSS, which is insensitive to polarization, can be a potential candidate for multiband applications.

Table 1: Comparison of this work with previously reported FSS

FSS	f_{10} & f_{20} (GHz)	Angular Stability	Thickness (λ_{10})	*SF*
[9] 2022	1.43/2.09	60°	0.007	7.5/ 9.72
[8] 2022	2.5/15.5	40°	0.139	6.0/ 5.0
[11] 2019	6.1/10.1	30°	0.16	2.86/ 2.71
[7] 2019	5.46/7.15	45°	0.145	12.6/ 2.65
[10] 2018	3.2/6.7	45°	0.017	5.71/ 2.14
This work	8.4/13.7	45°	0.015	4.28/ 1.85

$SF = \frac{BW_{-30dB}}{BW_{-3dB}}$ is the property of roll-off, where BW_{-30dB} refers to the bandwidth of -30 dB passband and BW_{-3dB} refers to the bandwidth of -3 dB passband [12].

II. DUAL-BAND FSS DESIGN AND CIRCUIT ANALYSIS

A. Design description

Figure 1 shows the proposed dual-band bandpass FSS structure which consists of three metallic layers separated from one another by two thin dielectric substrates. The unit cell of the top and bottom layers consists of an ACP at the center with four QCP (forming circular patches in a periodic array) present at each corner. The unit cell of the middle layer is the complementary structure of the outer layers.

The relative permittivity of the two thin substrates is 2.2 (ignoring its loss tangent in simulation) and the optimized thickness of them is d = 0.35 mm. Other optimized dimensional parameters of the unit cell are given as follows: $D_x = D_y = 10$ mm, $r_1 = 3.4$ mm, $w_1 = 1.0$ mm, $r_0 = 3.5$ mm, and $w_0 = 1.0$ mm.

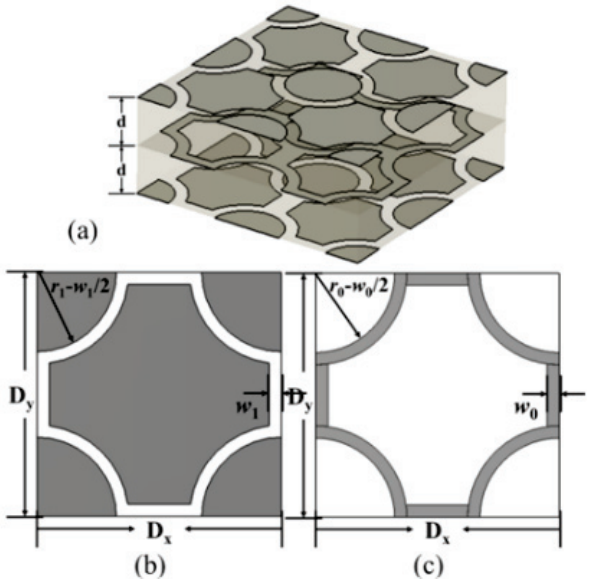

Fig. 1. FSS geometry: (a) 3D view of a 2×2 array, (b) unit cell of the top and bottom layers, and (c) unit cell of the middle layer.

B. Circuit analysis and mechanism

To better understand the operation of this structure, its ECM is shown in Fig. 2 (a). The ACP and QCP in the top and bottom layers can be modeled as a parallel of two series LC resonators (L_1-C_1 and L_2-C_2) [13]. The metallic wire in the middle layer acts as a shunt inductance L. The magnetic coupling between outer layers and middle layer is taken into account. The coupling changes the values of self-inductance into L′, L_1′, and L_2′. The semi-infinite free space on both sides of the FSS is represented by intrinsic wave impedance $Z_0 = 377\ \Omega$. The two dielectric substrate layers can be modeled as the

same short piece of transmission line whose characteristic impedance is $Z_C = Z_0/\sqrt{\varepsilon_r}$. Its equivalent circuit is a series inductor L_T and shunt capacitor C_T, which is shown in Fig. 2 (b).

Two hybrid LC resonators are coupled to one another by inductor L_m after converting the T-network composed of inductors L_T and $L\prime$ into a π-network composed of L_m and $L_T\prime$, as shown in Fig. 2 (c).

The segmental study method is used to analyze its mechanism. At the lower passband, the parallel $L_T\prime$-C_T resonators are the dominant resonant mechanism, and the filter can be reduced to two parallel resonators, as shown in Fig. 2 (d). The equivalent impedance Z_L of the proposed FSS working at lower passband can be expressed as:

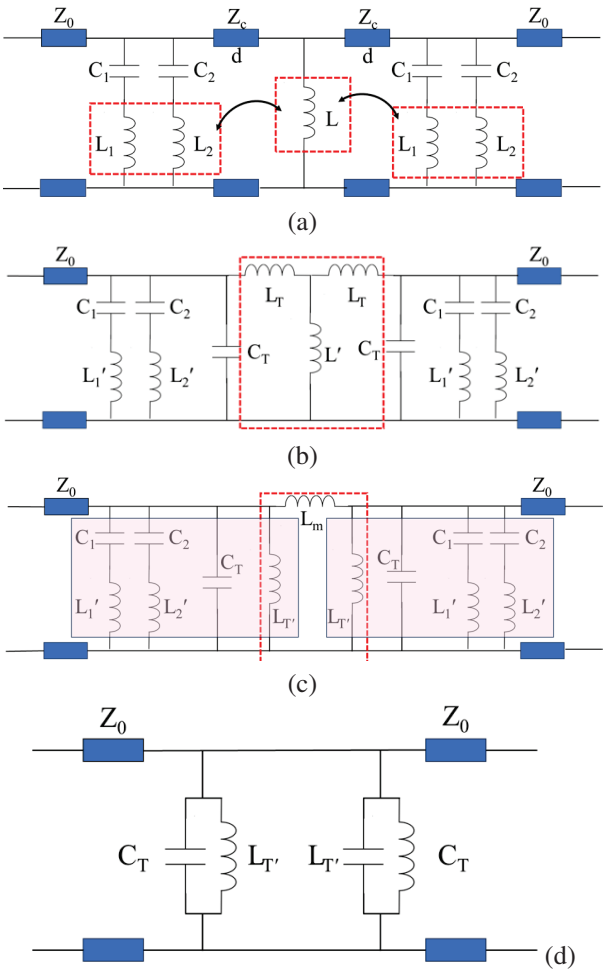

Fig. 2. ECM of the proposed FSS (a) with transmission lines, (b) using series inductor L_T and shunt capacitor C_T instead of transmission lines, (c) after converting the T-network into a π-network, and (d) equivalent circuit at its lower passband.

$$Z_L = \frac{1}{2(j\omega C_T + \frac{1}{j\omega L_T'})}. \tag{1}$$

Thus, one transmission pole f_{pole-1} can be obtained when Z_L goes to infinity, which means that the FSS would transmit the EM wave at that frequency value. Based on this analysis, the transmission pole at the lower passband can be expressed as:

$$f_{pole-1} = \frac{1}{2\pi\sqrt{L_T' C_T}}. \tag{2}$$

A second order coupled-resonator bandpass filter with inductive coupling shown in Fig. 2 (c) is responsible for the higher passband. The impedance of the hybrid LC resonator as shown in the shaded area in Fig. 2 (c) is:

$$Z = \frac{Z_1' Z_2' Z_3'}{Z_2' Z_3' + Z_1' Z_3' + Z_1' Z_2'}. \tag{3}$$

Here, Z_1', Z_2', and Z_3' are:

$$Z_1' = j\omega L_1' + \frac{1}{j\omega C_1}, \tag{4}$$

$$Z_2' = j\omega L_2' + \frac{1}{j\omega C_2}, \tag{5}$$

$$\frac{1}{Z_3'} = j\omega C_T + \frac{1}{j\omega L_{T'}}. \tag{6}$$

The equivalent impedance Z_H of the proposed FSS working at higher passband can be expressed as [14]:

$$Z_H = \frac{1}{\frac{1}{Z} + \frac{1}{Z + j\omega L_m}}. \tag{7}$$

For the hybrid LC resonator, if the series resonator $L_1\prime$-C_1 resonates, a transmission zero will be formed at f_{null-1}. Similarly, another transmission zero will be formed at f_{null-2} when the series resonator $L_2\prime$-C_2 resonates. The EM wave would be reflected by the proposed FSS at these two resonant frequencies which can be expressed as:

$$f_{null-1} = \frac{1}{2\pi\sqrt{L_1' C_1}}, \tag{8}$$

$$f_{null-2} = \frac{1}{2\pi\sqrt{L_2' C_2}}. \tag{9}$$

Two transmission poles would be formed when Z_H goes to infinite [15], and expressed as:

$$f_{pole-2} = \frac{-b - \sqrt{b^2 - 4ac}}{2a}, \tag{10}$$

$$f_{pole-3} = \frac{-b + \sqrt{b^2 - 4ac}}{2a}, \tag{11}$$

where the variables a, b, and c are expressed as:

$$a = 3L_m L_1' C_1 L_2' C_2 L_T' C_T, \quad (12)$$

$$b = -2[L_m \left(L_T' C_1 L_2' C_2 + L_T' C_2 L_1' C_1 + L_1' C_1 L_T' C_T + L_2' C_2 L_T' C_T + L_1' C_1 L_2' C_2\right) + 2L_T' L_1' C_1 L_2' C_2], \quad (13)$$

$$c = 2L_T' \left(L_1' C_1 + L_2' C_2\right) + L_m \left(L_T' C_1 + L_T' C_2 + L_T' C_T + L_1' C_1 + L_2' C_2\right). \quad (14)$$

f_{null-1} and f_{null-2} located outside f_{pole-2} and f_{pole-3} could regulate the fast roll-off characteristics of sidebands at higher passband.

The simplified ECMs shown in Figs. 2 (c) and (d) are good approximations for us to understand its mechanism which has been validated in the Agilent Advanced Design System (ADS) research presented in Section IIIA.

III. SIMULATION RESULTS

A. Normal incidence

Simulations are conducted with the structure parameters provided in Section IIA by using CST Microwave Studio. Figure 3 presents the simulated S_{21}. The structure is polarization insensitive. The proposed FSS exhibits dual-band bandpass response with lower passband ($S_{21} >$ -3 dB) from 7.17 GHz to 9.71 GHz, and higher passband ($S_{21} >$ -3 dB) from 12.8 GHz to 14.5 GHz. The lower passband exhibits the first-order response, and its transmission pole exists at 8.4 GHz. Meanwhile, the higher passband exhibits second-order response with a sharp roll-off at sidebands, and its two peaks exist at 13.25 GHz and 14.1 GHz between which a valley exists at 13.7 GHz.

The segmental study method is used to analyze the ECMs of the proposed FSS by the ADS. The ECM shown in Fig. 2 (c) characterizes the higher passband of the proposed FSS from about 11 GHz to 15.5 GHz. The ECM shown in Fig. 2 (d) characterizes the lower passband of the proposed FSS before about 11 GHz. The values of $L_T\prime$ and C_T could influence the quality factor of the two passband simultaneously, hence the values of $L_T\prime$ and C_T in Figs. 2 (c) and (d) should be the same.

The optimized values of the circuit parameters in Figs. 2 (c) and (d) are $L_T\prime = 2.276$ nH, $C_T = 0.155$ pF, $L_1\prime = 9.95$ nH, $L_2\prime = 25.6$ nH, $C_1 = 0.0175$ pF, $C_2 = 0.0043$ pF, and $L_m = 2.96$ nH. That C_T is larger than theoretical value is attributed to the strong electric field located at the gap between the metallic patches. The circuit simulation result of S_{21} is also presented in Fig. 3 and a good match is found with full-wave simulation. There is some discrepancy around 11-12 GHz, because 11-12 GHz is the critical range between two ECMs. The discrepancy is a little larger after 15.5 GHz, but it is outside the working band. The discrepancy of lower transmission null between ADS and CST is 0.15 GHz, and that of higher transmission null is 0.09 GHz. These discrepancies mean that these circuit parameters need finer optimization, and our circuit models need improvements. However, the ECMs in Figs. 2 (c) and (d) are sufficient to explain the mechanism of the proposed FSS.

B. Oblique incidence

The calculated S_{21} of the proposed FSS to the angle of incidence is shown in Fig. 4. Figure 4 (a) shows the frequency response of the FSS for TE polarization. As the angle of incidence increases, the bandwidth of the two passbands does not considerably change, but the band ripple of the higher passband increases. For the TM incidence as shown in Fig. 4 (b), the bandwidth of the higher passband increases and the passband ripple decreases, as the angle of incidence increases.

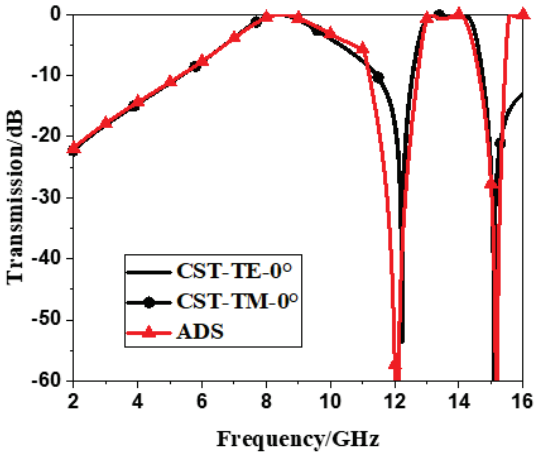

Fig. 3. Transmission characteristics of the proposed dual-band FSS.

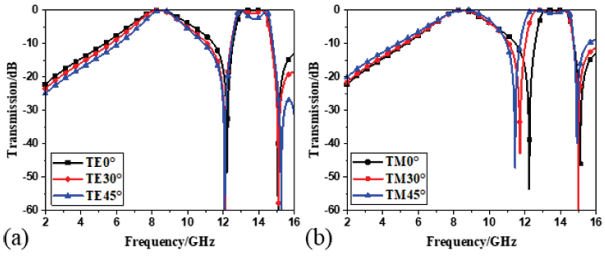

Fig. 4. Calculated transmission coefficients of the proposed FSS for different incidence angles: (a) TE polarization and (b) TM polarization.

The lower passband shows better angular stability with incidence angle variation than the higher passband. The frequency response of the proposed FSS is relatively stable at 45° for both TE and TM polarizations.

As the angle of incidence varies, the variations observed in the bandwidth of the structure can be attributed to the change of wave impedance, which in turn will change the loaded quality factor of the coupled resonators [16]. For TE incidence, the wave impedance changes as $Z/cos\theta$. The quality factor Q_H of the hybrid resonators shown in Fig. 2 (c) increases for large incidence angles. The bandwidth corresponding to each transmission pole of the higher passband is reduced and consequently the passband ripple is increased. For TM incidence, the wave impedance changes as $Z/cos\theta$. Therefore, that Q_H decreases for large incidence angles results in the broadening of the FSS bandwidth.

IV. EXPERIMENTAL VERIFICATION

A prototype of the proposed FSS with 400×400 array was fabricated with the printed circuit board technique. The substrate is F4BM220 with a relative permittivity of 2.2 and a loss tangent of 0.001 and the thickness that the supplier can provide is 0.254 mm. Other structure parameters of the prototype unit cell are the same as that given in Section IIA.

To improve alignment accuracy, the top and middle layers were printed on both sides of the substrate. The bottom layer was printed on one side of another substrate. Meanwhile, five asymmetric location holes were drawn on the four edges of each board. They were used to improve alignment accuracy when the two boards are bonded together by a layer of EVA glue with a thickness of 0.045 mm, a dielectric constant of 3, and a loss tangent of 0.005. Hence, the physical dimensions of the prototype are 405 mm × 405 mm × 0.553 mm ($0.015\lambda_{10}$).

The free space measurement technique was used to measure S_{21}. An Agilent N5224A vector analyzer and three pairs of horn antennas covering 6-18 GHz were used to measure the proposed prototype. The experimental setup and the fabricated FSS prototype are shown in Fig. 5.

The performance of the proposed FSS has been verified experimentally under oblique incident wave. The measured and simulated transmission coefficients are plotted, derived from the simulation in Figs. 6 (a-d).

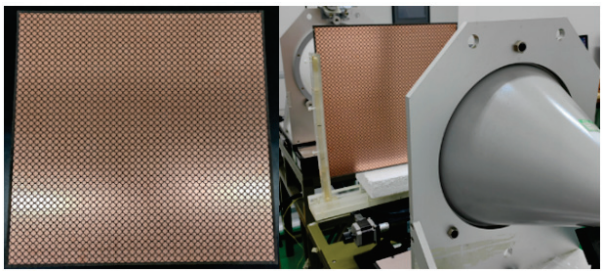

Fig. 5. FSS sample and measurement setup.

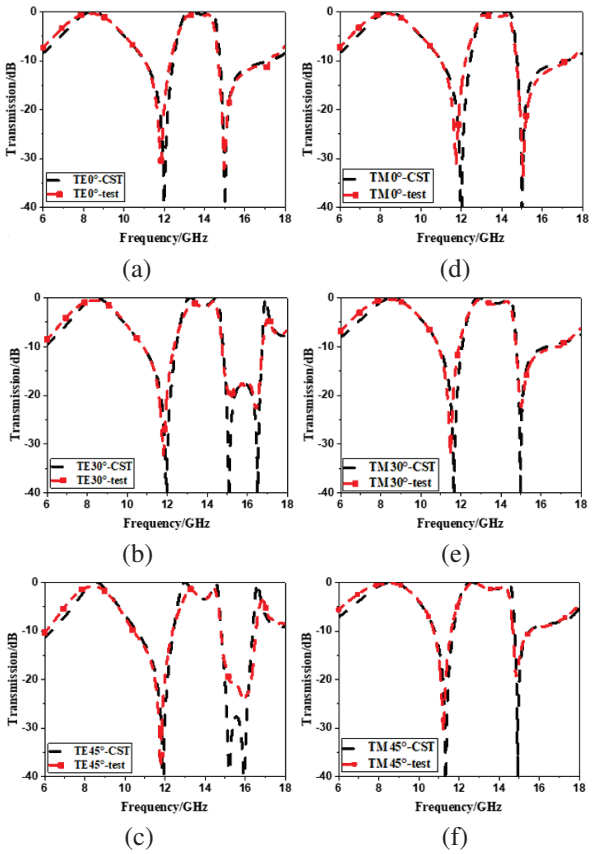

Fig. 6. Measured transmission coefficients of the FSS sample under (a)-(c) TE polarization and (d)-(f) TM polarization.

They show good agreement with the simulated ones. There is a slight downshift for the lower transmission null whose maximum deviation is 0.25 GHz compared with simulation. The lower passband, whose maximum deviation of -3 dB bandwidth is 0.3 GHz, is a little broader than the simulated one. The deviations may be caused by a machining error of ACP and an alignment error between the two boards during bonding.

V. CONCLUSION

In this paper, a new dual-band FSS structure with low-profile and high selectivity at upper passband is presented. The segmental study method and equivalent circuit approach is used to establish its ECM and analyze its filtering mechanism. Two parallel LC resonators are responsible for the lower passband, whereas two hybrid LC resonators are series inductively coupled via L_m at the higher passband. A prototype of the proposed dual-band FSS has been fabricated and its performance has been verified through experiment. The proposed low-profile FSS with high selectivity has potential applications in designing low-frequency devices for dual-band communication.

ACKNOWLEDGMENT

The authors would like to acknowledge the support of Natural Science Foundation of Jilin Province, China (Grant No. YDZJ202301ZYTS378) and the Science and Technology Project of the Education Department of Jilin Province, China (Grant No. JJKH20230903KJ).

REFERENCES

[1] P. Jha, A. Kumar, A. De, and R. K. Jain, "Super ultra-wideband planar antenna with parasitic notch and frequency selective surface for gain enhancement," *Applied Computational Electromagnetics Society (ACES) Journal*, vol. 37, no. 7, pp. 757-764, Dec. 2022.

[2] H. Ahmad, M. Rahman, S. Bashir, W. Zaman, and F. C. Seman, "Miniaturized frequency selective radome operating in the X-band with wideband absorption," *Applied Computational Electromagnetics Society (ACES) Journal*, vol. 34, no. 12, pp. 1915-1921, Dec. 2019.

[3] Ş. Balta and M. Kartal, "A novel double-layer low-profile multiband frequency selective surface for 4G mobile communication system," *Applied Computational Electromagnetics Society (ACES) Journal*, vol. 37, no. 4, pp. 420-427, Apr. 2022.

[4] M. Idrees, S. Buzdar, S. Khalid, and M. A. Khalid, "A miniaturized polarization independent frequency selective surface with stepped profile for shielding applications," *Applied Computational Electromagnetics Society (ACES) Journal*, vol. 31, no. 5, pp. 531-536, Aug. 2021.

[5] M. S. Samani, R. S. Shirazi, and G. Moradi, "Multiband frequency selective surface design based on idea of clusters in cellular communication systems," *Applied Computational Electromagnetics Society (ACES) Journal*, vol. 30, no. 10, pp. 1079-1082, Aug. 2021.

[6] E. C. Braz and A. L. P. S. Campos, "A new multifractal geometry for design of frequency selective surfaces with dual band response," *Applied Computational Electromagnetics Society (ACES) Journal*, vol. 30, no. 7, pp. 799-803, Aug. 2021.

[7] Z. Yu, X. Yang, W. Tang, J. Zhu, and C. Wang, "Three-dimensional dual-band frequency selective surface with close band spacing," in *CSQRWC Conference*, Taiyuan, China, pp. 1-3, 2019.

[8] P. Jiang, W. Jiang, W. Hu, and S. Gong, "An interlaced grid dual-band dual-polarized bandpass FSS with a large band ratio," *IEEE Antennas Wireless Propag. Lett.*, vol. 21, no. 5, pp. 1027-1031, May 2022.

[9] Y.-H. Ma, D.-W. Wang, Y. Yu, and W.-S. Zhao, "Design of dual-band frequency-selective surfaces with independent tunability," *IEEE Trans. Antennas Propag.*, vol. 70, no. 12, pp. 12381-12386, Dec. 2022.

[10] A. Chatterjee, G. Ali Sarkar, and S. K. Parui, "A multi-layered frequency selective surface-based wireless filter with dual bandpass response," in *IEEE MTT-S Int. Microwave and RF Conference*, Kolkata, India, pp. 1-4, 2018.

[11] X. Zhang, W. Wu, J. Huang, W. Zhang, Y. Ye, and N. Yuan, "Dual-polarized frequency selective rasorber with two transmission bands," *IEEE Access*, vol. 7, pp. 139795-139801, Sep. 2019.

[12] B. Q. Hu, L. M. Zhan, C. Z. Chen, and W. G. Li, "Theoretical analysis and simulation of shape factor of bandpass filter," *Ship Electronic Engineering*, vol. 39, no. 8, pp. 100-107, Aug. 2019.

[13] F. Costa, A. Monorchio, and G. Manara, "An overview of equivalent circuit modeling techniques of frequency selective surfaces and metasurfaces," *Applied Computational Electromagnetics Society (ACES) Journal*, vol. 29, no. 12, pp. 960-976, Aug. 2021.

[14] D. Li, T. W. Li, R. Hao, H. S. Chen, W. Y. Yin, H. C. Yu, and E. P. Li, "A low-profile broadband bandpass frequency selective surface with two rapid band edges for 5G near-field applications," *IEEE Trans. Electromagnetic Compatibility*, vol. 59, no. 2, pp. 670-676, Apr. 2017.

[15] M. Hussein, J. Zhou, Y. Huang, and B. Al-Juboori, "A low-profile miniaturized second-order bandpass frequency selective surface," *IEEE Antennas Wireless Propag. Lett.*, vol. 16, pp. 2791-2794, Aug. 2017.

[16] M. Al-Joumayly and N. Behdad, "A new technique for design of low-profile, second-order, bandpass frequency selective surfaces," *IEEE Trans. Antennas Propagat.*, vol. 57, no. 2, pp. 452-459, Feb. 2009.

Jian Jiao received the Ph.D. degree in Optics from Changchun Institute of Optics, Fine Mechanics and Physics, Chinese Academy of Sciences, China, in 2015. She joined the School of Physics, Changchun Normal University, China, in 2019. Her research interests include frequency selective surface and artificial electromagnetic material.

Nianxi Xu received the Ph.D. degree in Optics from Changchun Institute of Optics, Fine Mechanics and Physics, Chinese Academy of Sciences, China, in 2012. He joined Changchun Institute of Optics, Fine Mechanics and Physics, Chinese Academy of Sciences, in 2012. His research interests include frequency selective surfaces and functional thin films.

Jinsong Gao received the Ph.D. degree in Optics from Changchun Institute of Optics, Fine Mechanics and Physics, Chinese Academy of Sciences, China, in 2005. He has been the director Jilin Provincial Key Laboratory of Advanced Optoelectronic Equipment and Instruments Manufacturing Technologies since 2017. His research interests include optical thin films, frequency selective surfaces, and functional thin films.

Comparative Study of High-speed Permanent Magnet Synchronous Motors with In-line Slot Conductors and Equidirectional Toroidal Windings

Yinjun Sun[1], Peixin Wang[1], Rui Nie[1], Fuquan Nie[2], Peng Gao[3], and Jikai Si[1]

[1]Department of Electrical and Information Engineering
Zhengzhou University, Zhengzhou 450001, China
syjxixinyidian163.com, wangpeixin509@126.com, nierui@zzu.edu.cn, sijikai527@126.com

[2]Department of Henan Institute of Science and Technology
Xinxiang, Henan 453000, China
976028398@qq.com

[3]Department of Henan United Electric Power Technology Co. Ltd.
Zhengzhou 450001, China
15290418261@qq.com

***Abstract* –** The high-speed permanent magnet synchronous motor (HSPMSM) plays an important role in a wide range of engineering fields due to its high power density, high efficiency, and light weight. In this paper, a HSPMSM equipped with in-line slot conductors (I-LSC) is proposed and compared with one equipped with equidirectional toroidal winding (ETW). Firstly, the differences between them are revealed, including topology, back-electromotive force (EMF), slot fill factor, copper loss, and torque. Secondly, two-dimensional finite element method (2D-FEM) tools are used to obtain more precise performance such as air-gap field, back-EMF, torque characteristics, efficiency maps, and the unbalanced magnetic force (UMF). Considering the end-windings of copper loss of ETW and the end ring copper loss of I-LSC, the losses and efficiency of two motors are simulated by three-dimensional finite element method (3D-FEM). Finally, the simulation results validate the feasibility of the newly proposed winding and indicate that in-line slot conductors have superiority in power density due to the high slot fill factor.

***Index Terms* –** Equidirectional toroidal winding, high fill factor, high-speed permanent magnet synchronous motor, in-line slot conductor, power density.

I. INTRODUCTION

The demands for high-speed (HS) motor technologies are continuously evolving, with a focus on achieving high power density, enhanced efficiency, and energy conservation in the engineering applications such as automobiles, aircraft, and flywheel energy storage [1–3]. According to the operation principle, they can principally be divided into HS switched reluctance, induction, and permanent magnet synchronous motors [3–5]. Notably, high-speed permanent magnet synchronous motors (HSPMSM) with diverse stator and rotor structures stand out for their exceptional performance. HSPMSMs not only demonstrate remarkable efficiency and power density but also boast a broader range of applications and quicker dynamic response capabilities. Hence, HSPMSM can be a good candidate in the HS application field [6].

In the past few decades, the motor has been vigorously researched and promoted to seek the maximize power density, which put very high requirements on the design of the rotor/stator [6, 7]. The influence of the rotor structure on power density has been emphasized previously [8]. Another important factor for power density is the stator winding. For example, the fractional slot concentrated windings (FSCW) in conventional permanent magnet (PM) motors possess high power density while the multiphase motors with integral slot distributed windings can offer much higher torque than the FSCW [9]. The motor end-windings should be designed shorter, otherwise excessive axial length leads to low torque density as outlined in [10]. HSPMSMs with hairpin structures can have high torque but the slot shape is always parallel as demonstrated in [11]. Here follows an overview concerning diverse windings.

HSPMSM generally can be configured with [12]:

(1) overlapping windings: Fig. 1 (a) is a representative example that uses a full pitch overlapping windings with six slots [13]. Hence, HSPMSM with overlapping windings have a relatively high winding factor. However, regardless of the single layer and double layer, these overlapping windings need to be set

Submitted On: November 8, 2023
Accepted On: July 23, 2024
https://doi.org/10.13052/2024.ACES.J.390610

up in a crisscross arrangement, which makes the motor not only display bulk end-windings but also increases copper consumption. Moreover, the end-windings result in a long axial length with a consequent reduction in power density [13].

(2) Non-overlapping windings sometimes can be involved in concentrated windings, such as tooth-wound and yoke-wound. Compared with overlapping windings, tooth-wound windings have the advantage of short end-windings, low copper loss, and shorter motor axial length [14]. As depicted in Figs. 1 (b) and (c), single-layer and double-layer windings are sleeve windings that have been extensively utilized in permanent magnet motors. Taking 3s2p as an example, the winding factor for Figs. 1 (b) and (c) is 0.866 [15–17]. Halbach winding is also a type of non-overlapping winding, which can achieve the effect of enhancing and weakening the magnetic field on one side in PMs. But the winding factor is also 0.866 [18]. The equidirectional toroidal windings (ETW) are subordinate to yoke-wound windings and have been proven to have a conductor factor of 1 [19]. Furthermore, the utilization rate of windings has been improved by utilizing a dual-rotor structure to address end-winding [20]. ETW can significantly enhance torque density in various types of motors, such as axial flux PMs, radial flux PMs, and linear motors [21–23]. However, single rotor radial flux PMs with ETW has the disadvantage of low winding utilization rate [24]. Hence, the new topology, the in-line slot conductor (I-LSC), is envisaged and proposed in this paper. In this way, this type of winding can be seen as the ETW where the end-windings are omitted, and the myriads of winding conductors are infinitely approximated to a whole conductor that is placed in the stator slot in Fig. 1 (d). The I-LSC can improve winding utilization and have a high slot fill factor in a single rotor motor. Besides crucial merits, I-LSC can reduce copper consumption. It can be predicted to be suitable for HS motors due to the low number of turns. The influence of ETW configuration has been studied on HS operation but I-LSC has not been systematically investigated [25].

The major objective of this paper is to evaluate and confirm the merits and demerits of the new proposed I-LSC and the existing ETW in HSPMSM by a fair comparison. The constructions and operation principles of I-LSC and ETW are introduced in Section II. Then, the main performance of similarities and differences between the two motors is revealed in Section III. Finally, a summary of this paper as well as directions for future research work are presented in Section IV.

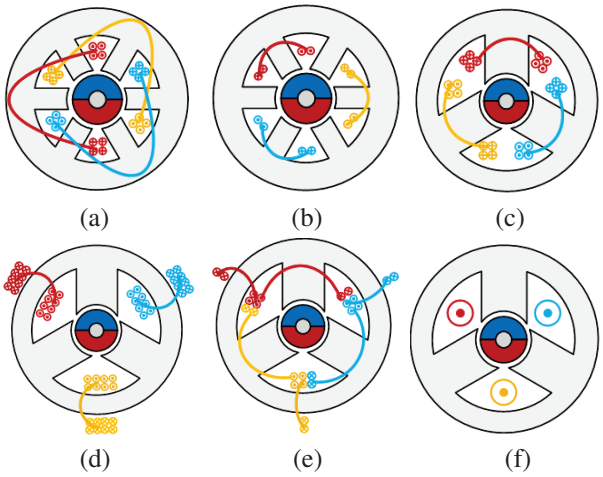

Fig. 1. Various winding types: (a) distributed winding, (b) single layer winding, (c) double layer winding, (d) ETW, (e) Halbach winding, and (f) I-LSC.

II. STRUCTURE AND OPERATION PRINCIPLES

The construction of the mentioned motor with ETW and the proposed motor with I-LSC are named ETW-HSPMSM and I-LSC-HSPMSM, respectively, as shown in Fig. 2. What they have in common is the 3s2p topologies to reduce the operating frequency and minimize switching losses. The same rotors are external-installed with PMs (N30SH) which can be diametrically magnetized. Furthermore, all other parameters are the same for comparison purposes, except that ETW-HSPMSM has more outer teeth and end-windings than I-LSC-HSPMSM.

A. Structure

The differences between the two motors are mainly on the stator side. Firstly, the two stators have similar inside teeth and slots. However, ETW-HSPMSM is equipped with external teeth to place the outside conductors, as shown in Fig. 2. Secondly, the windings of ETW-HSPMSM are wound around the stator yoke but I-

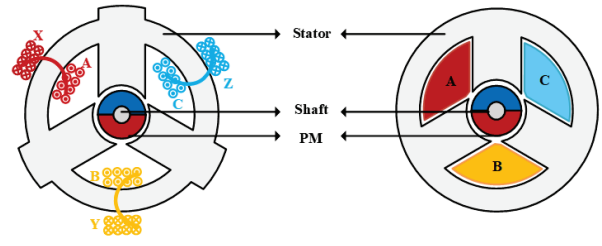

Fig. 2. 3s2p motor topology: (a) ETW-HSPMSM and (b) I-LSC-HSPMSM.

LSC-HSPMSM is inserted into the stator slots. In addition, the positive sides (A, B, and C) of the ETW are positioned inside the stator core, while the negative sides (X, Y, and Z) are situated on the outside, as illustrated in Fig. 2 (a). Only the positive sides (A, B, and C) can be considered as effective edges. However, I-LSC only has the positive sides (A, B, and C) without negative sides. In ETW-HSPMSM, the incoming line terminals (A, B, and C) need to be linked to a three-phase power source, while the outgoing terminals (X, Y, and Z) are connected together by a wye configuration. Conversely, for I-LSC-HSPMSM, solid copper blocks (A, B, and C) are inserted into the stator slots and connected to the end ring. By contrast, there are no end-windings for I-LSC which reduces the invalid length to diminish the size of I-LSC-HSPMSM. The shape of the conductor can be made even closer to the shape of the slot to improve the slot fill factor.

B. Operation principle

To illustrate the operation principle of HSPMSMs with ETW and I-LSC clearly, it is analyzed by using the minimum unit motor as an example. Two motors are shown to be fed square wave currents to maintain consistency, which ETW had been reported in [20]. It is necessary to observe the operating principles of the two motors for their subsequent performance analysis. In Fig. 3, two motors are excited by the square wave current source, and the current during this period of one electrical cycle is divided into six intervals, each corresponding to specific three-phase current directions, as displayed in Table 1.

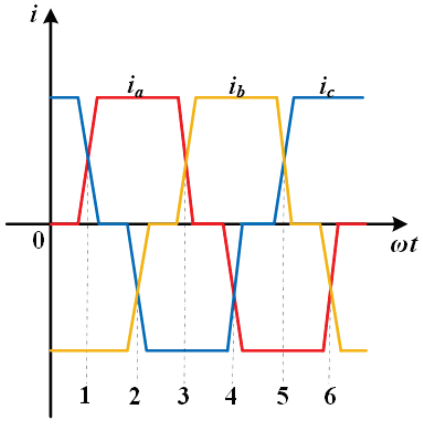

Fig. 3. Three-phase square waveform current.

The notation '+' denotes current outflow the plane of windings, while '-' signifies current inflow the plane, as indicated in Table 1. The current through the windings of ETW-HSPMSM and I-LSC-HSPMSM in a period will generate an armature magnetic field. The armature magnetic field rotates periodically with time and forms a periodical rotating magnetic field. Under the effect of the rotating magnetic field, the rotor core subsequently rotates. The armature magnetic field of two motors at three moments in sequence is selected successively to compare its distribution of magnetic field lines with the armature magnetic field at moment 0 in Fig. 4. Each time elapsed, N or S will undergo a counterclockwise rotation of 120 degrees. Thus, the armature magnetic field alternates in a periodic manner, forming a pair of poles.

Table 1: Three-phase winding current directions at different times

Current	Times						
	0	1	2	3	4	5	6
i_a	0	+	+	+	-	-	-
i_b	-	-	-	+	+	+	-
i_c	+	+	-	-	-	+	+

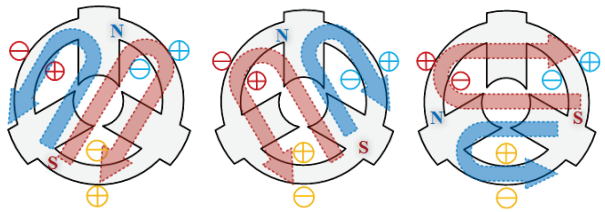

Fig. 4. Armature reaction field of ETW-HSPMSM: (a) time 2, (b) time 3, and (c) time 4.

Figure 5 demonstrates that the armature magnetic field of I-LSC-HSPMSM rotates counterclockwise which exhibits the same rotational direction as ETW-HSPMSM. However, ETW-HSPMSM has an effect of magnetic leakage because of the existence of end-windings.

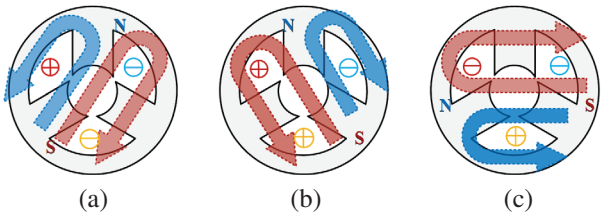

Fig. 5. Armature reaction field of I-LSC-HSPMSM: (a) time 2, (b) time 3, and (c) time 4.

The structure and materials of the PMs of the two motors are identical, and the parallel direction are all magnetized uniformly. Thus, the flux distribution generated by the PMs in both motors is identical. Consequently, this ensures that the magnetic load of the two

motors is identical, enabling a fairer comparison of their performance in subsequent analyses.

C. No-load back-EMF

The no-load back-electromotive force (EMF) is generated when the external rotor permanent magnet rotates around the Z-axis. Only the phase-EMF of positive sides (E_A, E_B, and E_C) are effective edges for the two motors due to the unique coil arrangement of ETW and I-LSC. The pitch factor (k_p) is the coefficient of reduction in the phase-EMF, which is always 0.5 [19]. The winding distributed coefficients (k_d) of the two motors are 1. The fundamental EMF component is E_0, which is given by:

$$E_0 = 2.22 f N_s \Phi_1, \tag{1}$$

where N_s is the number of turns per phase, f is the motor frequency, and ϕ_1 is the fundamental flux generated by PM at each pole.

For ETW-HSPMSM and I-LSC-HSPMSM, E_0 is proportional to the number of turns and the fundamental flux.

D. Fill factor

According to stator tooth width and yoke height, the cross-sectional area of stator slot and conductor (A_{cond}) can be determined for slot fill factor. A high slot fill factor (k_{fill}) decreases the motor volume by reducing the unnecessary area of the slot, which can be calculated by:

$$k_{fill} = \frac{A_{cond} N_s}{S_{slot}}, \tag{2}$$

where A_{cond} is the cross-sectional area of one conductor while S_{slot} is the stator slot.

I-LSC has arranged the winding as close to the slot shape as feasible after removing the thickness of the insulating paper. However, for ETW, there will be a gap between the round-copper wires no matter how they are placed.

E. Torque

The electromagnetic torque on the rotor in a synthetic magnetic field can be expressed as:

$$T_e = \frac{2.22 m f N_s \Phi_1 I_{RMS} \cos\Phi_0 \eta}{2\pi f}, \tag{3}$$

where m is the phase number of the motor, Φ_0 is the angle formed by the current and back-EMF, and η is the efficiency of the motor.

The current per phase (I_{RMS}) is affected by current density (J_s). When stator slot area (S_{slot}) is determined, slot fill factor is also a principal element to affects I_{RMS}, which is given by:

$$I_{RMS} = J_s A_{cond}, \tag{4}$$

$$I_{RMS} = J_s \frac{S_{slot} k_{fill}}{N_s}. \tag{5}$$

Torque can be also expressed as:

$$T_e = 1.11 m B_g l_a D_{air} J_s k_{fill} S_{slot} \eta, \tag{6}$$

where l_a is stator active length, D_{air} is average value of the sum of the stator inner and outer diameters, and B_g is peak value of air-gap flux density. According to the above equation, if the mechanical structure of the motors and the materials of the PMs are determined, the torque will be proportional to the slot fill factor (k_{fill}) under the same current density.

F. Copper loss

Total copper loss (P_{TCL}) includes DC loss (P_{DC}) and AC loss (P_{AC}) [26]. In calculating DC copper loss, the end-windings of the ETW in the out slot should be taken into account in copper loss, while I-LSC has only one effective edge, which is given by:

$$P_{TCL} = P_{AC} + P_{DC}, \tag{7}$$

$$P_{DC} = 3\rho_{cu} I^2_{RMS} \frac{2(l_a + h_{sy}) N_s}{A_{cond}}, \tag{8}$$

where ρ_{cu} is the resistivity of copper, N_s is the number of in-series turns per phase, and h_{sy} is stator yoke height.

To verify the rationality of the proposed motor with I-LSC, the common and distinct characteristics of I-LSC-HSPMSM and ETW-HSPMSM are compared. At the same time, it is demonstrated that I-LSC-HSPMSM will have a higher torque than ETW-HSPMSM due to high slot fill factor. Moreover, due to its smaller volume, I-LSC-HSPMSM has a higher power density compared to ETW-HSPMSM. The following section will verify these conclusions by two-dimensional finite element method (2D-FEM) and three-dimensional finite element method (3D-FEM). Designing the two motors requires adhering to specific preconditions and constraints to ensure a fair comparison.

(1) Both motors possess identical dimensions and materials of the stators, PMs, and rotors. Magnetizing direction of PMs in both motors is identical.

Table 2: Optimized design parameters for two HSPMSM

	ETW-HSPMSM	**I-LSC-HSPMSM**
Stator out diameter D_0(mm)	54	54
Stator inner diameter D_i(mm)	16.2	16.2
Stator active length l_a(mm)	9.1	9.1
Air-gap length l_g(mm)	1.25	1.25
Shaft radius R_{shaft}(mm)	0.3	0.3
Number of series turns per phase N_s	36	1
Outer tooth height h_{ot}(mm)	3.3	0
Stator yoke height h_{sy}(mm)	6.3	6.3
Inner tooth width w_{it}(mm)	12.5	12.5
Current density J_s(mm)	9.7	9.7
Rated speed (krpm)	110	110
DC copper loss P_{dc}	6.78	2.65

(2) Air-gap length remains consistent between the two motors.

(3) The two motors are excited by the same current density. Based on these principles, the primary parameters of the two motors are presented in Table 2 [27].

III. ELECTROMAGNETIC CHARACTERISTICS OF TWO MOTORS

Each motor, ETW-HSPMSM and I-LSC-HSPMSM, is composed of a three-phase winding and a pair of magnets as its minimum unit. According to the aforementioned parameters and analysis, the electromagnetic performance of ETW-HSPMSM is consistent with what is presented in [25] firstly. It will be seen that there are some common points and differences in the electromagnetic performance by considering both no-load and on-load situations, respectively.

A. Air-gap flux density

The waveforms of air-gap flux density produced by two PMs of both motors exhibit similarity as depicted in Fig. 6 (a), which is due to the fact that the two motors ensure the same magnetic load conditions. It demonstrates that the outer teeth do not affect the air gap magnetic density. In Fig. 6 (b), it is illustrated that the amplitudes of the fundamental harmonic of the air-gap flux density in both motors are 0.85 T, with total harmonic distortions (THD) of 7.01% for each.

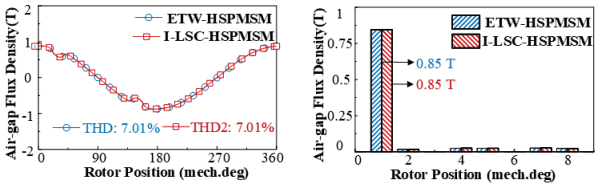

(a) (b)

Fig. 6. Air-gap flux density of ETW-HSPMSM and I-LSC-HSPMSM: (a) waveforms and (b) harmonic spectra.

B. Open-circuit flux linkage

The detailed flux density distribution of the two motors at the same rated speed of 110 krpm is depicted in Fig. 7, and the peak flux density is specifically located at the tip of the stator teeth. The flux linkage waveforms are shown in Fig. 8 (a), the peak value of ETW-HSPMSM is 2.0 mWb while I-LSC-HSPMSM is 0.056 mWb. There is an apparent difference in amplitudes for the two motors which can be mainly attributed to the different turns. The number of turns for ETW is 36 whereas I-LSC is only 1. The ratio of the maximum values of the flux linkage between the two motors is equal to the ratio of their respective numbers of turns. It is worth noting that the fundamental amplitude of ETW-HSPMSM is 2.32 mWb while I-LSC-HSPMSM is 0.05 mWb.

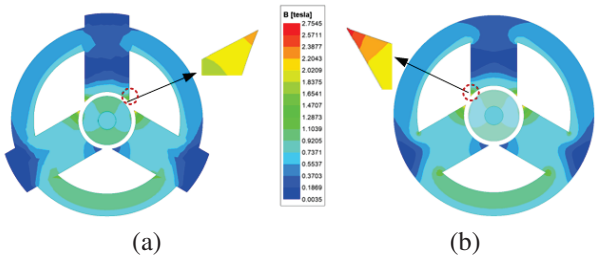

(a) (b)

Fig. 7. Equal potential and flux distributions of high-speed motors: (a) ETW-HSPMSM and (b) I-LSC-HSPMSM.

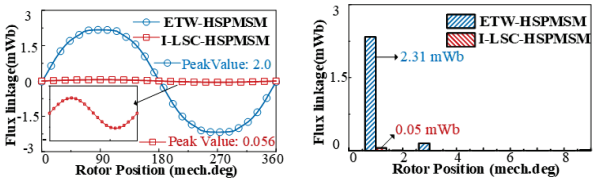

(a) (b)

Fig. 8. Flux linkage and its harmonic spectra of ETW-HSPMSM and I-LSC-HSPMSM: (a) waveforms and (b) harmonic spectra.

C. Back-EMF

The no-load back-EMF of the two motors with the rated speed of 110 krmp is shown in Fig. 9. It is evident that the peak values of no-load back-EMF in ETW-HSPMSM and I-LSC-HSPMSM are 24.52 V and 0.66 V, respectively. The basic harmonic amplitude of ETW-HSPMSM is 26 V, while that of I-LSC-HSPMSM is 0.63 V, which is shown in Fig. 9 (b). I-LSC-HSPMSM has 36 times lower back-EMF than ETW-HSPMSM because the number of turns is 36 times less than ETW-HSPMSM according to equation (1). THD of ETW-HSPMSM and I-LSC-HSPMSM is 3.84% and 0.24%, respectively. In particular, the 3rd harmonic of the phase back-EMF in both motors cannot be ignored. However, this 3rd harmonic is effectively eliminated in the line back-EMF, as illustrated in Fig. 10.

D. Armature reaction fields

Figure 11 illustrates the windings armature field of the two motors when subjected to square wave excitation under identical current density. I_{RMS} of I-LSC-HSPMSM is 576.1 A, and that of ETW-HSPMSM is 12.02 A. I-LSC has 1 turn while ETW has 36 turns. Peak value of I-LSC-HSPMSM is 0.151 T while peak value of ETW-HSPMSM is 0.114 T as shown in Fig. 11 (a).

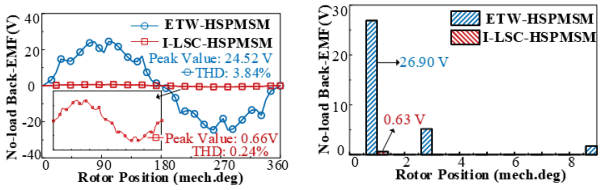

(a) (b)

Fig. 9. No-load back-EMF and its harmonic spectra of ETW-HSPMSM and I-LSC-HSPMSM: (a) waveforms and (b) harmonic spectra.

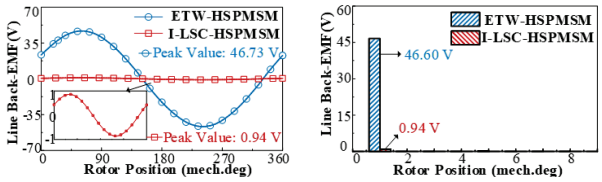

(a) (b)

Fig. 10. No-load line back-EMF of ETW-HSPMSM and I-LSC-HSPMSM: (a) waveforms and (b) harmonic spectra.

Therefore, the ratio of peak values of the armature magnetic fields of the two motors is approximately equal to the ratio of the incoming current of the two motors. In Fig. 11 (b), the main fundamental values of ETW-HSPMSM and I-LSC-HSPMSM are 0.05 T and 0.072 T, respectively.

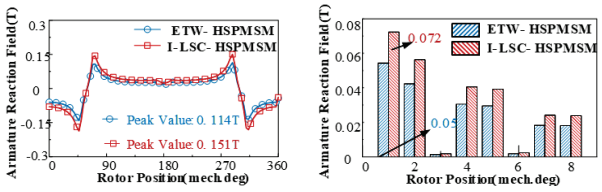

(a) (b)

Fig. 11. Armature field of ETW-HSPMSM and I-LSC-HSPMSM: (a) waveforms and (b) harmonic spectra.

E. On-load torque characteristics

With a conductor cross-sectional area of 1.24 mm^2 and a slot area cross-sectional of 73.50 mm^2, ETW-HSPMSM can theoretically achieve a maximum slot fill factor of 60.71%. As for I-LSC-HSPMSM, the winding shape is close to the stator slot and k_{fill} of I-LSC can extend up to 80.00%. Under square-wave excitation with the same current density, the average torque of the two motors is 47.84 mNm and 63.52 mNm, respectively, demonstrated in Fig. 12. It can be observed that the torque ratio of the two motors and the slot fill factor ratio are the same. The output torque of I-LSC-HSPMSM is 24.68% higher than that of ETW-HSPMSM. Meanwhile, torque ripple is 1.30% lower than that of ETW-HSPMSM.

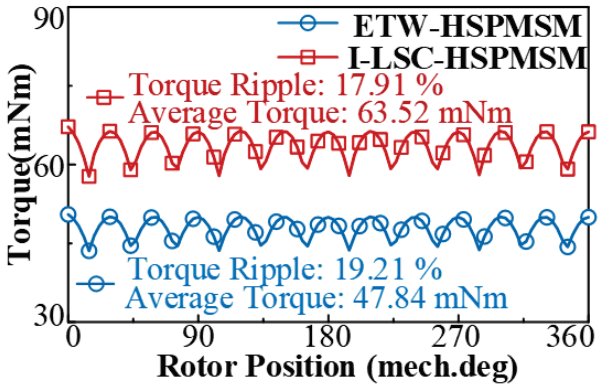

Fig. 12. Torque waveforms of ETW-HSPMSM and I-LSC-HSPMSM under rated load conditions.

F. Loss and efficiency map

In HSPMSMs, the main losses are stator iron loss and copper loss. The application of 3D-FEM can be applied for a more comprehensive analysis of motor losses, including the calculation of the losses of end-windings. Iron loss accounts for the main component of total loss due to the high frequency of the HSPMSM, which is shown in Fig. 13. Copper loss is obtained by integrating the current density over one electrical cycle for both motors. AC loss is determined by subtracting the calculated DC copper loss from this total loss.

Two motors have different losses due to the different currents which are fed into the windings at the same current density. Iron core loss of ETW-HSPMSM is 88.5 W, while that of I-LSC-HSPMSM is 76.4 W. I-LSC-HSPMSM has a larger cross-sectional area of the conductor and lower resistance, resulting in DC

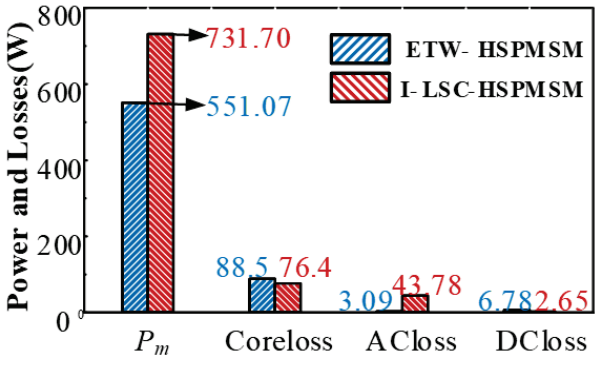

Fig. 13. Comparison of on-load losses at rated speeds.

loss of 2.65 W compared to ETW-HSPMSM's DC loss of 6.78 W. It is worth mentioning that AC loss of I-LSC-HSPMSM reaches 43.78 W due to the skin effect, whereas AC loss of ETW-HSPMSM is only 3.09 W. At high frequencies, AC copper loss of I-LSC-HSPMSM is high because of the skin effect. According to equation (9), output power of ETW-HSPMSM is 551.07 W, while that of I-LSC-HSPMSM is 731.70 W (see Fig. 13). However, the efficiency of ETW-HSPMSM is 84.85%, and that of I-LSC-HSPMSM is 85.63%, as calculated by equation (10):

$$P_m = T_e \frac{2\pi n}{60}, \tag{9}$$

$$\eta = \frac{P_{\mathrm{m}}}{P_{\mathrm{m}} + P_{AC} + P_{\mathrm{core}} + P_{DC}} \times 100\%, \tag{10}$$

where P_m is the output mechanical power, P_{core} is the stator core loss, and n is the rated speed.

The output torque will be affected because of different excitations. Under sinusoidal excitation, the output torque is 9% smaller than the square wave excitation. The efficiency map should be generated under the sinusoidal excitation as shown in Fig. 14.

When the two motors are in the bus voltage of 35.04 V and the current density is 0-12 J/mm^2, the highest efficiency of both motors is 85.02%. Under the same current density, the output torque of I-LSC-HSPMSM is still higher than that of ETW-HSPMSM. Core loss of the two motors increases much faster than the increment of the output power, which leads to a high-efficiency area not at the point of inflection. However, in the range of 200 krmp, output torque of I-LSC-HSPMSM only declines by 7.82%, while ETW-HSPMSM drops to 49.39% at 200 krmp. Therefore, I-LSCHSPMSMs are more suitable for high-speed applications than ETW-HSPMSMs.

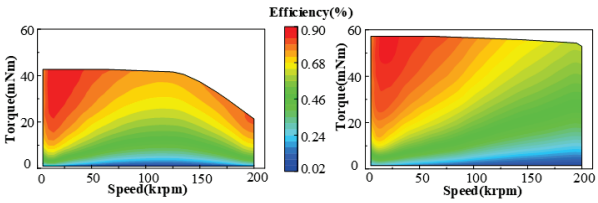

(a) (b)

Fig. 14. Efficiency map of two motors: (a) ETW-HSPMSM and (b) I-LSC-HSPMSM.

G. Unbalanced magnetic force

In addition to output power, unbalanced magnetic force (UMF) is also an important performance index for HS operation. UMF significantly affects vibration, noise level, and life of bearings, which can be calculated by [28]:

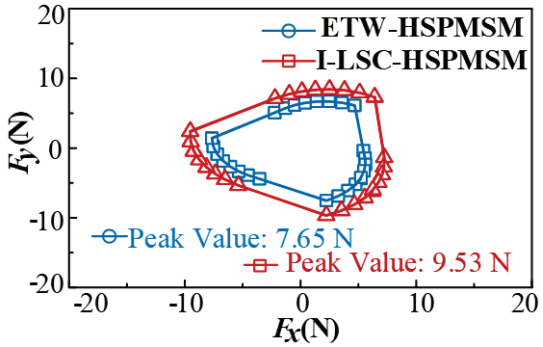

Fig. 15. Orthogonal components of unbalanced magnetic force.

$$F_x = \frac{r_{ag} l_a}{2\mu_0} \int_0^{2\pi} [(B_t^2 - B_r^2)\cos\theta + 2B_r B_t \sin\theta] d\theta, \tag{11}$$

$$F_y = \frac{r_{ag} l_a}{2\mu_0} \int_0^{2\pi} [(B_t^2 - B_r^2)\cos\theta - 2B_r B_t \sin\theta] d\theta, \tag{12}$$

where F_x and F_y are two orthogonal components of UMF, r_{ag} is radius of the air-gap, μ_0 is permeability of a vacuum, and B_r and B_t are radial and tangential components of air-gap flux density.

No matter the ETW and I-LSC, they both have the UFM shown in Fig. 15. Maximum value of ETW-HSPMSM is 7.65 N and of I-LSC-HSPMSM is 9.53 N. UMF will appear in the 3s2p motors at rated high speed due to asymmetric stator structure. Therefore, future work should change the pole-slot combination to offset UMF.

IV. CONCLUSION

In this paper, an HSPMSM with I-LSC is proposed and compared with ETW. It can be seen that the proposed motor (I-LSC-HSPMSM) has superiority in output torque due to a high slot fill factor at the same speed. Comparative studies on the two motors also show that the power density of I-LSC-HSPMSM is higher than ETW-HSPMSM due to high power and small volume. Compared with ETW, the I-LSC can be an excellent choice in HS motors from the point of maintaining a high torque at high speed. Moreover, I-LSC-HSPMSM has the advantages of dealing with the problem of the end-windings of ETW in the radial motor. However, I-LSC-HSPMSM inevitably has higher AC loss at high speeds due to skin effects. It can be concluded that I-LSC has a bright future and new challenges which should be solved in HS applications. As for unbalanced magnetic force, it can be known that the two motors both exist, which will be investigated in future studies for an appropriate structure. Subsequently, a motor prototype will be fabricated to verify the correctness of the ideas and simulations.

ACKNOWLEDGMENT

This work was supported by the National Natural Science Foundation of China under Grant 52307070, 52277069, and 52207067, the Postdoctoral Fellowship Program of China Postdoctoral Science Foundation under Grant GZC20232386, and the Major Special Project for Collaborative Innovation in Zhengzhou under Grant 20XTZX12023, and the Henan Province Key R&D and promotion projects under Grant 232102221016.

REFERENCES

[1] C.-W. Lin, J. F. Tu, and J. Kamman, "An integrated thermo-mechanical-dynamic model to characterize motorized machine tool spindles during very high speed rotation," *International Journal of Machine Tools and Manufacture,* vol. 43, no. 10, pp. 1035-1050, 2003.

[2] D. J. Tao, K. L. Zhou, F. Lv, Q. P. Dou, J. X. Wu, Y. T. Sun, and J. B. Zou, "Magnetic field characteristics and stator core losses of high-speed permanent magnet synchronous motors," *Energies,* vol. 13, no. 3, Feb. 2020.

[3] D. Gerada, A. Mebarki, N. L. Brown, C. Gerada, A. Cavagnino, and A. Boglietti, "High-speed electrical machines: Technologies, trends, and developments," *IEEE Transactions on Industrial Electronics,* vol. 61, no. 6, pp. 2946-2959, June 2014.

[4] G. Buticchi, D. Gerada, L. Alberti, M. Galea, P. Wheeler, S. Bozhko, S. Peresada, H. Zhang, C. M. Zhang, and C. Gerada, "Challenges of the optimization of a high-speed induction machine for naval applications," *Energies,* vol. 12, no. 12, June 2019.

[5] N. Bianchi, S. Bolognani, and F. Luise, "Potentials and limits of high-speed PM motors," *IEEE Transactions on Industry Applications,* vol. 40, no. 6, pp. 1570-1578, Nov.-Dec. 2004.

[6] A. Toba and T. A. Lipo, "Generic torque-maximizing design methodology of surface permanent-magnet vernier machine," *IEEE Transactions on Industry Applications,* vol. 36, no. 6, pp. 1539-1546, Nov.-Dec. 2000.

[7] G. Liu, Y. Wang, X. Xu, W. Ming, and X. Zhang, "The optimal design of real time control precision of planar motor," *The Applied Computational Electromagnetics Society Journal (ACES),* vol. 32, no. 10, pp. 948-954, Oct. 2017.

[8] M. Kimiabeigi, R. Long, J. D. Widmer, and Y. Gao, "Comparative assessment of single piece and fir-tree-based spoke type rotor designs for low-cost electric vehicle application," *IEEE Transactions on Energy Conversion,* vol. 32, no. 2, pp. 486-494, June 2017.

[9] L. Xu, G. Liu, W. Zhao, J. Ji, H. Zhou, W. Zhao, and T. Jiang, "Quantitative comparison of integral and fractional slot permanent magnet vernier motors," *IEEE Transactions on Energy Conversion,* vol. 30, no. 4, pp. 1483-1495, 2015.

[10] T. R. He, Z. Q. Zhu, F. Xu, H. Bin, D. Wu, L. M. Gong, and J. T. Chen, "Comparative study of 6-slot/2-pole high-speed permanent magnet motors with different winding configurations," *IEEE Transactions on Industry Applications,* vol. 57, no. 6, pp. 5864-5875, 2021.

[11] S. Balasubramanian, N. Langmaack, and M. Henke, "Evaluation and loss estimation of a high-speed permanent magnet synchronous machine with hairpin windings for high-volume fuel cell applications," *Elektrotechnik und Informationstechnik,* vol. 138, no. 6, pp. 415-423, Oct. 2021.

[12] T. He, Z. Q. Zhu, F. Xu, Y. Wang, H. Bin, and L. Gong, "Electromagnetic performance analysis of 6-slot/2-pole high-speed permanent magnet motors with coil-pitch of two slot-pitches," *IEEE Transactions on Energy Conversion,* vol. 37, no. 2, pp. 1335-1345, June 2022.

[13] M. Merdzan, J. J. H. Paulides, and E. A. Lomonova, "Comparative analysis of rotor losses in high-speed permanent magnet machines with different winding configurations considering the influence of the inverter PWM," in *2015 Tenth International Conference on Ecological Vehicles and Renewable Energies (EVER),* 2015.

[14] Z. Q. Zhu, Z. Y. Zhao, Y. W. Liu, F. R. Liang, D. W. Huang, and H. L. Liu, "Effect of end-winding on electromagnetic performance of fractional slot and Vernier PM machines with different slot/pole number combinations and winding configurations," *IEEE Access,* vol. 10, pp. 49934-49955, 2022.

[15] Y. Xu, Z. Xu, H. Wang, and W. Liu, "Research on magnetic-fluid-thermal-stress multi-field bidirectional coupling of high speed permanent magnet synchronous motors," *Case Studies in Thermal Engineering,* vol. 54, Feb. 2024.

[16] G. Chen, J. Si, R. Nie, J. Liang, and Y. Hu, "Analysis of armature magnetic field of slotless permanent magnet machine with arbitrary-phase equidirectional toroidal winding," *Energy Reports,* vol. 9, pp. 350-358, Apr. 2023.

[17] J. H. Park and S. G. Min, "Power-constrained design optimization of PM machines for low-power low-voltage and high-torque applications," *IEEE Transactions on Transportation Electrification,* pp. 1-1, 2023.

[18] X. Liang, M. Wang, P. Zheng, J. Gao, and W. Li, "Research and analysis of toroidal and conventional windings in permanent magnet synchronous

machine," in *IEEE International Magnetic Conference*, pp. 1-2, 2023.

[19] J. Si, T. Zhang, R. Nie, C. Gan, and Y. Hu, "Comparative study of dual-rotor slotless axial-flux permanent magnet machines with equidirectional toroidal and conventional concentrated windings," *IEEE Transactions on Industrial Electronics,* vol. 70, no. 2, pp. 1216-1228, Feb. 2023.

[20] Y. Wei, J. Si, Y. Han, Y. Li, and C. Gan, "Comparative analysis between slotless axial flux permanent magnet motor with equidirectional toroidal winding and integral-slot winding," *IEEJ Transactions on Electrical and Electronic Engineering,* vol. 17, no. 12, pp. 1790-1797, Dec. 2022.

[21] X. Chai, J. Si, Y. Hu, Y. Li, and D. Wang, "Characteristics analysis of double-sided permanent magnet linear synchronous motor with three-phase toroidal windings," *The Applied Computational Electromagnetics Society (ACES) Journal,* vol. 36, no. 8, pp. 1099-1107, Aug. 2021.

[22] Y. Wang, W. Zhang, R. Nie, J. Si, W. Cao, and Y. Li, "Analysis of a sinusoidal rotor segments axial flux interior permanent magnet synchronous motor with 120-degree phase belt toroidal windings," *The Applied Computational Electromagnetics Society (ACES) Journal,* vol. 37, no. 4, pp. 507-515, Apr. 2022.

[23] C. Gao, M. Gao, J. Si, Y. Hu, and C. Gan, "A novel direct-drive permanent magnet synchronous motor with toroidal windings," *Energies,* vol. 12, no. 3, Art. 432, Feb. 2019.

[24] J. K. Si, T. X. Zhang, Y. H. Hu, C. Gan, and Y. S. Li, "An axial-flux dual-rotor slotless permanent magnet motor with novel equidirectional toroidal winding," *IEEE Transactions on Energy Conversion,* vol. 37, no. 3, pp. 1752-1763, Sep. 2022.

[25] F. Xu, T. R. He, Z. Q. Zhu, Y. Wang, S. Cai, H. Bin, D. Wu, L. M. Gong, and J. T. Chen, "Influence of slot number on electromagnetic performance of 2-pole high-speed permanent magnet motors with toroidal windings," *IEEE Transactions on Industry Applications,* vol. 57, no. 6, pp. 6023-6033, Nov. 2021.

[26] L. J. Wu, Z. Q. Zhu, D. Staton, M. Popescu, and D. Hawkins, "Analytical model of eddy current loss in windings of permanent-magnet machines accounting for load," *IEEE Transactions on Magnetics,* vol. 48, no. 7, pp. 2138-2151, July 2012.

[27] F. Xu, T. R. He, Z. Q. Zhu, Y. Wang, S. Cai, H. Bin, D. Wu, L. M. Gong and J. T. Chen, "Influence of slot number on electromagnetic performance of 2-pole high-speed permanent magnet motors with toroidal windings," *Fifteenth International Conference on Ecological Vehicles and Renewable Energies (EVER)*, pp. 7, 2020.

[28] J. T. Chen and Z. Q. Zhu, "Comparison of all- and alternate-poles-wound flux-switching PM machines having different stator and rotor pole numbers," *IEEE Transactions on Industry Applications,* vol. 46, no. 4, pp. 1406-1415, July-Aug. 2010.

Yinjun Sun was born in Nanyang, Henan, China. She received B.S. degree in electrical engineering and automation from Xuzhou University of Technology, Xuzhou, China, in 2022. She is currently pursuing the M.S. degree with the College of Electrical Engineering of Zhengzhou University, Zhengzhou, Henan, China. Her current research interests include design, analysis and control of high-speed permanent magnet motors.

Peixin Wang received the B.Sc. and M.Sc. degrees from the School of Electrical Engineering and Automation, Henan Polytechnic University, Jiaozuo, China, in 2016 and 2018, respectively, and the Ph.D. degree from the Department of Electrical Engineering, Southeast University, Nanjing, China, in 2022. Since 2023, he has joined the School of Electrical and Information Engineering, Zhengzhou University as a research fellow. His research interests include permanent magnet and 2DoF machine systems.

Rui Nie received the B.S. degree in electrical engineering from Henan Polytechnic University, Jiaozuo, China, in 2015, and the Ph.D. degree in electrical engineering from the China University of Mining and Technology, Xuzhou, China, in 2020. She is currently a Post-Doctoral Researcher with the School of Electrical and Information Engineering, Zhengzhou University. Her current research interests include linear motor design and control, and renewable energy generation technology.

Fuquan Nie received the B.S. degree in mechanical and electrical from Henan Institute of Science and Technology, Xinxiang, China, and the M.S. degree from Henan University of Science and Technology, Luoyang, China. He is currently Dean of the mechanical and electrical department of Henan Institute of Science and Technology. He has authored and co-authored over 400 technical articles. His main research interests include the theory, application, and control of the crane. He was named the national ten thousand program leading talents, national innovation talents promotion project of science and technology innovation talents.

Peng Gao received B.S. degree in electrical engineering and automation from Zhengzhou University, Zhengzhou, China, in 2014. He works in Henan United Electric Power Technology Co. Ltd., Zhengzhou, China. He engages in grid source coordination, power engineering debugging and transformation, thermal control professional technical supervision.

Jikai Si received the B.S. degree in electrical engineering and automation from the Jiaozuo Institute of Technology, Jizaozuo, China, in 1998, the M.S. degree in electrical engineering from Henan Polytechnic University, Jizaozuo, in 2005, and the Ph.D. degree from the School of Information and Electrical Engineering, China University of Mining and Technology, Xuzhou, China, in 2008. He is currently a Distinguished Professor with Zhengzhou University, Zhengzhou, China. He has authored and co-authored over 160 technical articles. His main research interests include the theory, application, and control of special motor. Prof. Si is a member of the Green Motor System Professional Committee, China.